

N O T I C E

THIS DOCUMENT HAS BEEN REPRODUCED FROM
MICROFICHE. ALTHOUGH IT IS RECOGNIZED THAT
CERTAIN PORTIONS ARE ILLEGIBLE, IT IS BEING RELEASED
IN THE INTEREST OF MAKING AVAILABLE AS MUCH
INFORMATION AS POSSIBLE

VOLUME II - APPENDICES

**DEVELOPMENT OF
CO₂ LASER DOPPLER INSTRUMENTATION
FOR
DETECTION OF CLEAR AIR TURBULENCE**

**FINAL REPORT
10 FEBRUARY 1972 - 27 DECEMBER 1978**

ER78-4392-2

September 1979

**Under NASA Contract
NAS8-28424**

**Prepared for
GEORGE C. MARSHALL SPACE FLIGHT CENTER
NASA
HUNTSVILLE, ALABAMA 35812**

**By
C. E. Harris
A. V. Jelalian**

**RAYTHEON COMPANY
Equipment Division
Equipment Development Laboratories
Electro-Optics Systems Laboratory
Wayland, Massachusetts 01778**

VOLUME II

TABLE OF CONTENTS

APPENDIX

PAGE

A.	CAT Transmitter Shock and Vibration and Flight Crash Safety Mounting Analysis	A-1
B.	CAT Transmitter and Telescope Assembly - Safety of Flight Analysis	B-1
C.	Determination of CO₂ Laser Attenuation Coefficients in Atmosphere	C-1
D.	CAT LIDAR Wind Shear Studies	D-1
E.	CAT Flight A Tests Data Analysis	E-1
F.	CAT Flight B Tests Data Analysis	F-1
G.	Detailed Operating Instructions and CAT System Adjustment	G-1

APPENDIX A

**CAT TRANSMITTER SHOCK AND VIBRATION
AND FLIGHT CRASH SAFETY
MOUNTING ANALYSIS**



FORM 10-0007 10-001 0000

DIVISION MISSILE SYSTEMS
Operation Bedford Laboratories
Department Mechanical Systems Lab

To: P. Roberts

From: W. Shivitz

Subject: C.A.T. Transmitter Shock
and Vibration and Flight
Crash Safety Mounting
Analysis

Classification

Contract No.

Distribution aa

File No.

Memo No. MS Lab 72-166

Date 18 April 1972

- Reference:**
- (a) Raytheon Memo AC-71-11 dated 29 July 1971
 - (b) Raytheon Memo MS Lab 72-125 dated 22 March 1972
 - (c) NASA CV990 Airborne Laboratory Experimenters' Handbook
 - (d) Raytheon Drawings WSSK 32472-1 and JDSK 32472-2, 3 and 4 - C.A.T. Transmitter Support Frame and Mount Supports
 - (e) "Handbook of Engineering Fundamentals", Eshbach, Second Edition, 1952
 - (f) "Formulas for Stress and Strain", Roark, Fourth Edition, 1965

- Enclosures:**
- (1) Plot, "Deflection Vs. Static Load, Lord BTR-8350-39 Mount"
 - (2) Sketch of C.A.T. Transmitter Assembly and Mounting Arrangement
 - (3) Detailed Mounting Support Flight Crash Safety Analysis

I. Summary - Analyses of the mounting and mount support systems verify that satisfactory shock and vibration isolation will be attained. The mount support structure will conform to flight crash safety requirements with relatively high margins of safety. Restraint cables will reinforce the mounts in the critical loaded forward direction limiting maximum forward system deflection to 1 1/4 inches.

II. Mounting Description - The mounting design consists of four Lord BTR-8350-39 elastomer shear mounts which are

**MISSILE SYSTEMS DIVISION
Bedford Laboratories
Mechanical Systems Lab**

oriented at 50° in the vertical plane and at 70° inward toward the overall system center of gravity from the longitudinal direction in the horizontal plane. The mounts are geometrically balanced about the center of gravity and the mounting system is approximately focalized in the vertical, transverse and roll and also in the longitudinal and pitch planes. Thus, the transverse-roll and longitudinal-pitch modes are relatively uncoupled.

Restraint cables are located near each of the four mounts to prevent excessive motion of and to fully captivate the C.A.T. Transmitter system. The cables will limit deflection in the critical 9g forward flight crash safety condition to approximately 1 1/4 inches. The mounts will limit crash safety load deflections in all other directions to less than one inch.

The principal natural frequencies of the mounted transmitter system are calculated as follows:

<u>Mode</u>	<u>Frequencies</u>
Vertical	9.8 Hz
Transverse	8.4 Hz
Longitudinal/Pitch	5.7 Hz
Pitch	8.9 Hz
Transverse/Roll	4.9 Hz
Yaw	6.5 Hz

The highly damped BTR elastomer will allow only small resonant magnification at the above frequencies and vibration isolation should be achieved above 15 Hz.

The maximum physical motions which will be allowed by the BTR-8350-39 mounts under normal environmental conditions are:

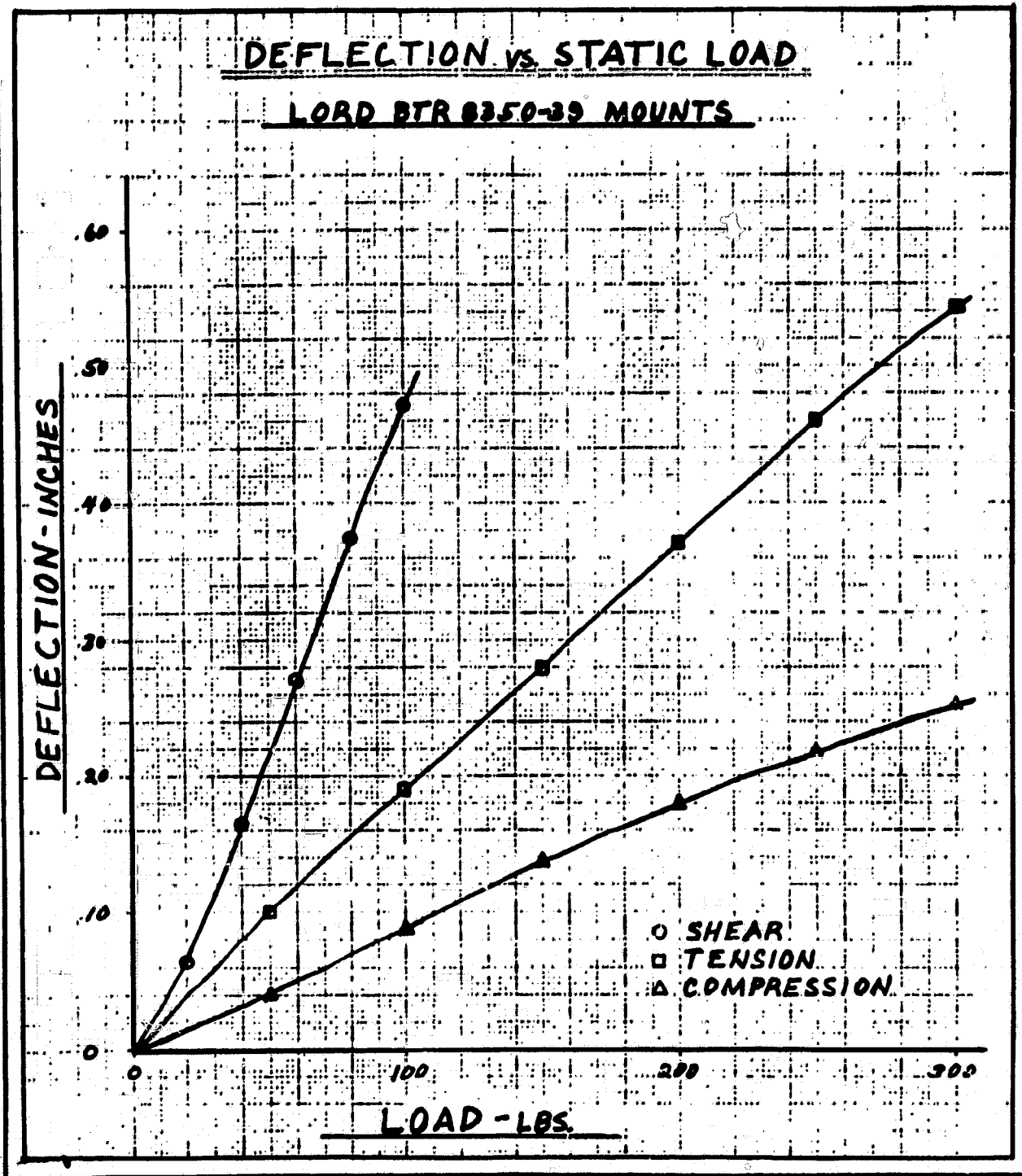
<u>Direction</u>	<u>Load</u>	<u>Deflection</u>
Vertical up	0g	0 In.
Vertical Down	3.0g	.31 In.
Forward	0.5g	.15 In.
Aft	0.2g	.06 In.
Transverse	$\pm 0.2g$	$\pm .03$ In.

**MISSILE SYSTEMS DIVISION
Bedford Laboratories
Mechanical Systems Lab**

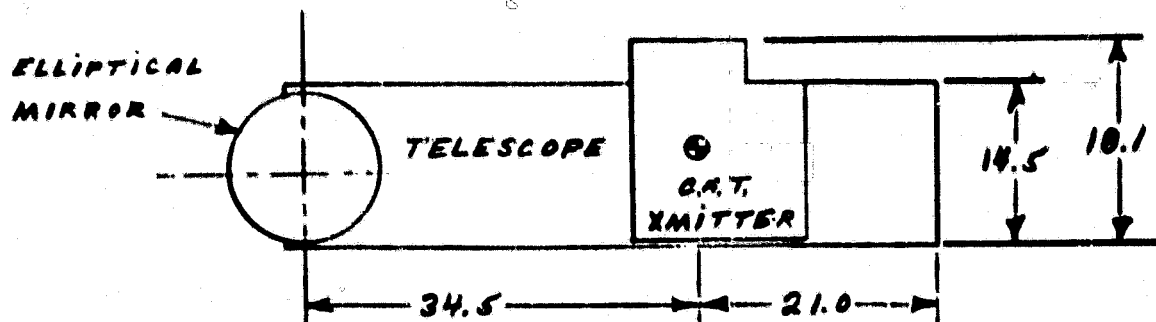
III. Mounting Support Structure - The four mounts are supported by a frame structure which bridges across two NASA supplied "Low Boy" equipment racks. These racks and also the transmitter cabinet and telescope assembly are assumed to have been analyzed elsewhere for flight safety conditions. Detailed structural analyses of the mounting support frame which verify its conforming to flight crash safety requirements are given in Enclosure (3).

Enclosure 1 to MS Lab Form #72-1/66

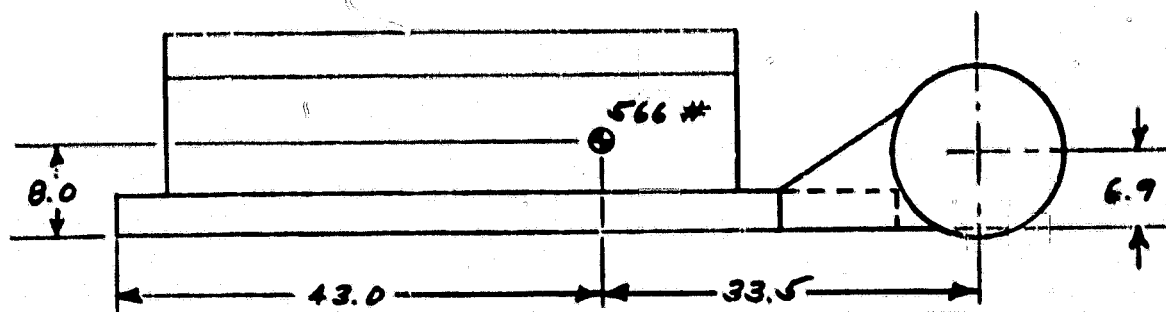
ENGINEER W SHIVITZ	RAYTHEON COMPANY	PAGE NO.
CHECKER	MISSILE SYSTEMS DIVISION	REPORT NO.
DATE 7 MAR 72		MODEL NO.



ENGINEER W SHIVITE	RAYTHEON COMPANY	PAGE NO.
CHECKER	MISSILE SYSTEMS DIVISION	REPORT NO.
DATE	C.A.T. TRANSMITTER	MODEL NO.



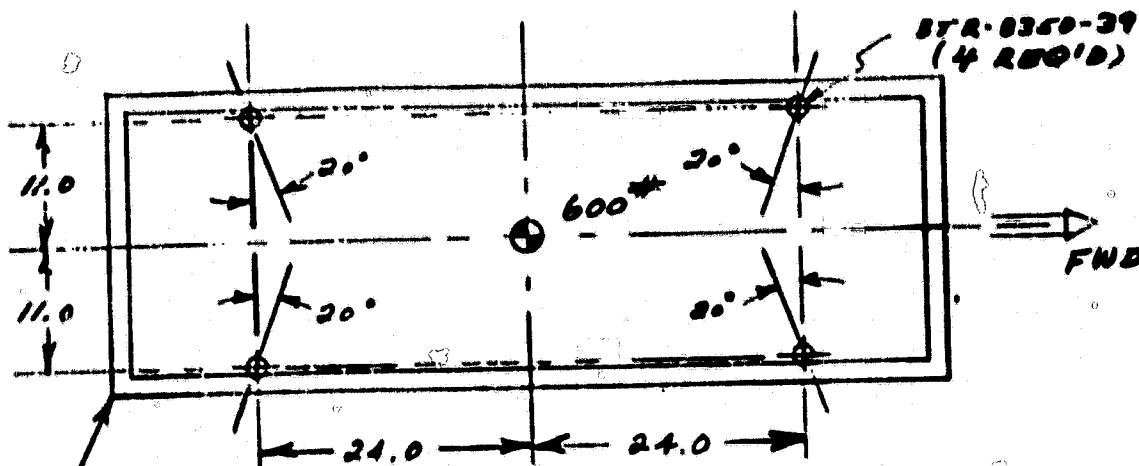
VIEW LOOKING FORWARD



VIEW LOOKING TO PORT

ENGINEER W SHVITZ	RAYTHEON COMPANY	PAGE NO.
CHECKER	MISSILE SYSTEMS DIVISION	REPORT NO.
DATE		MODEL NO.

BTR 0350-39 MOUNT PLAN-LAYOUT



SUPPORT FRAME

4 x 1.647 x .247 STANDARD 6061-T6 CHANNELS

NOTE: BTR-0350-39 MOUNTS ARE INCLINED 50° IN THE VERTICAL PLANE

NOTE: ABOVE DIMENSIONS REFER TO MOUNT TOP SURFACE CENTERLINES.

ENCLOSURE (3)
FLIGHT CRASH SAFETY
ANALYSIS

INTRODUCTION

The mounting framework is constructed primarily of standard channels and bent plate structure welded or bolted together. This flight safety analysis will cover the relatively critical areas of the mounting support structure. Analysis of the transmitter frame and the "Low Boy" equipment racks is considered not to be the responsibility of this department.

This analysis will assure that no part of the system connected directly to the mounting supports will become separated from its attach points and create a flying object hazard to personnel or aircraft under crash conditions.

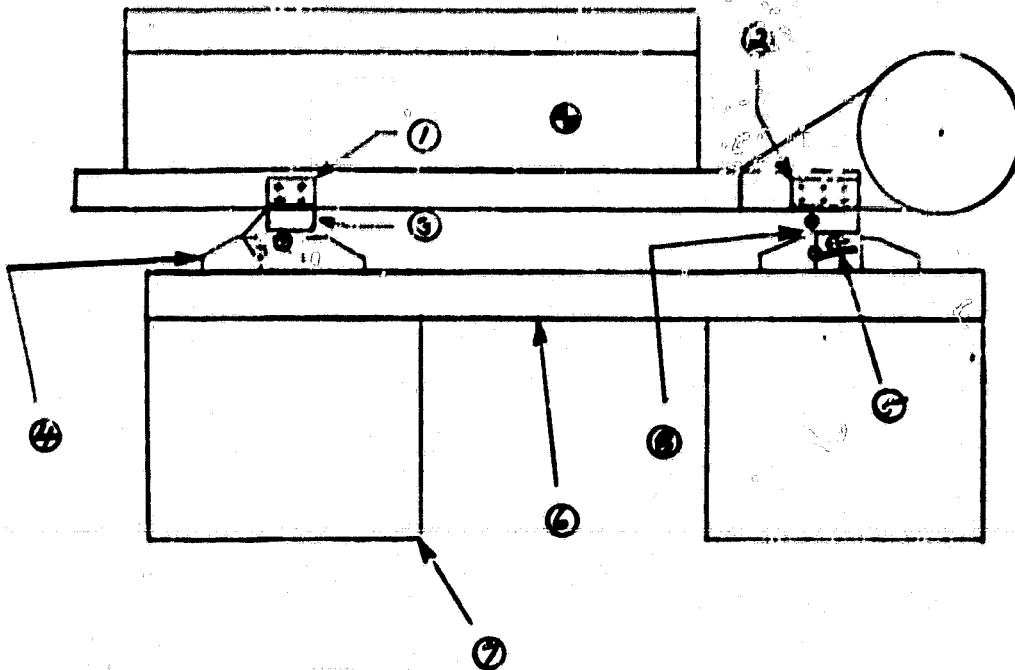
DESIGN LOAD FACTORS

The design criteria for this analysis is based on those guidelines set forth in section 5.1 of Reference (c). The criteria dictates that the following load factors, when applied one at a time, must not produce a stress in any element of the structure beyond the accepted yield point for the construction material. A safety factor of 1.5 is used in the determination of the margin of safety.

<u>Load Direction</u>	<u>Load Factor</u>	
	<u>Yield</u>	<u>Ultimate</u>
Forward	9.0g	13.5g
Down	7.0g	10.5g
Up	2.0g	3.0g
Side	1.5g	2.25g
Aft	1.5g	2.25g

ENGINEER W. SHIVITZ	RAYTHEON COMPANY	PAGE NO.
CHECKER	MISSILE SYSTEMS DIVISION	REPORT NO.
DATE	CAT TRANSMITTER	MODEL NO.

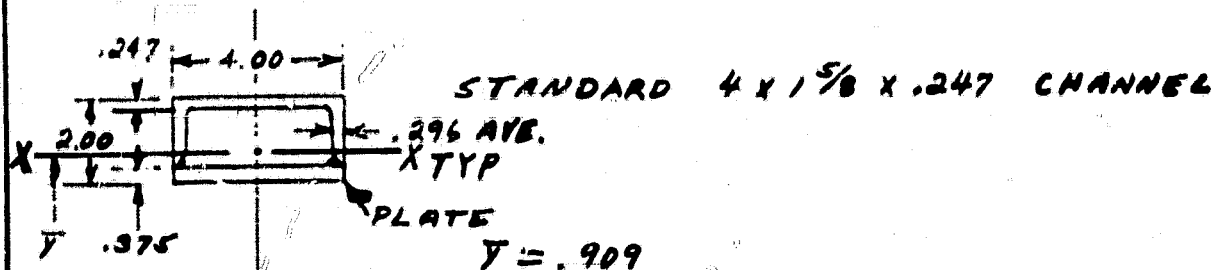
MOUNT SUPPORT COMPONENT BREAKDOWN



<u>COMPONENT</u>	<u>DESCRIPTION</u>	<u>NO. REQUIRED</u>
①	2 1/2 x 2 x 1/4 BRACKET	2
②	2 1/2 x 2 x 1/4 BRACKET	2
③	UPPER MOUNT SUPPORT	2
④	LOWER MOUNT SUPPORT	2
⑤	BTR-B350-39 MTS.	4
⑥	MOUNT SUPPORT FRAME	1
⑦	"LOW BOY" RACKS	2
⑧	RESTRAINT CABLES	4

ENGINEER W SHIVITE	RAYTHEON COMPANY	PAGE NO.
CHECKER	MISSILE SYSTEMS DIVISION	REPORT NO.
DATE	C.A.T. TRANSMITTER	MODEL NO.

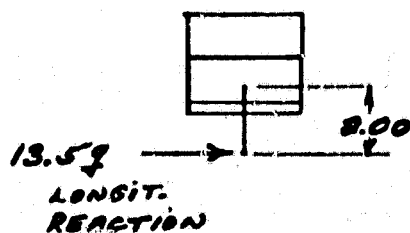
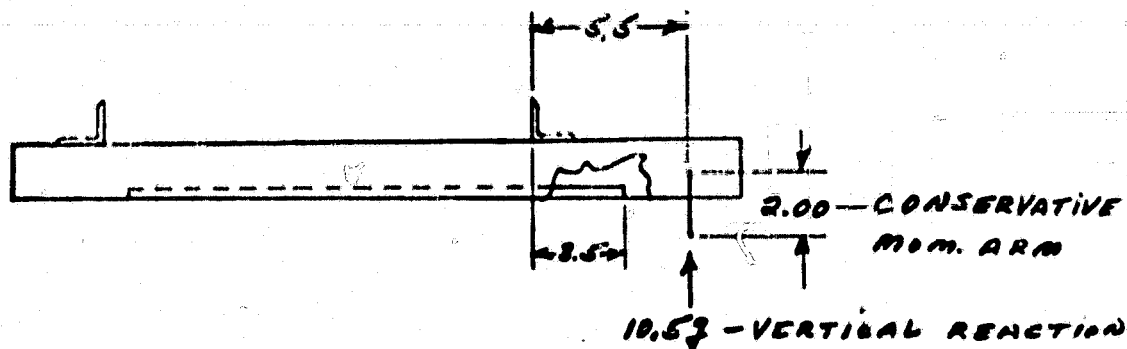
UPPER CHANNEL MOUNT SUPPORT



$$I_{xx} = 1.87 \text{ in.}^4$$

$$I_{yy} = 6.12 \text{ in.}^4$$

AFT SUPPORT MOST CRITICAL

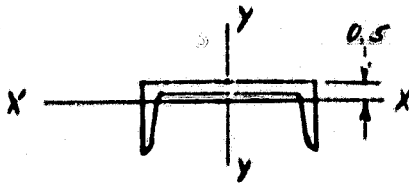


$$\frac{600}{4} = 150 \text{ LBS / SUPPORT}$$

$$10.5(150) = 1575 \text{ LBS.}$$

$$13.5(150) = 2025 \text{ LBS.}$$

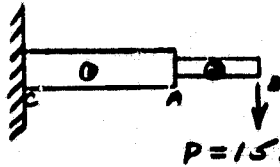
ENGINEER W. SHIVITZ	RAYTHEON COMPANY	PAGE NO.
CHECKER	MISSILE SYSTEMS DIVISION	REPORT NO.
DATE	C.A.T. TRANSMITTER	MODEL NO.



$$I_{xx} = .40 \text{ in.}^4$$

$$I_{yy} = 4.17 \text{ in.}^4$$

10.5.2 VERTICAL REACTION



$$P = 1575 \text{ LBS.}$$

$$I_1 = 1.87 \quad l_1 = 3.5$$

$$I_2 = .40 \quad l_2 = 2.0$$

$$\delta_p = \frac{P(l_2)^3}{3EI_2} + \frac{P(l_1)^3}{3EI_1} + \frac{P(l_1)(l_2)^2}{2EI_1}$$

$$= \frac{1575}{(10)^7} \left[\frac{(2.0)^3}{3(.40)} + \frac{(3.5)^3}{3(1.87)} + \frac{(3.5)^2}{2(1.87)} \right]$$

$$= .0041 \text{ in.} \rightarrow 388,000 \text{ LB/in.}$$

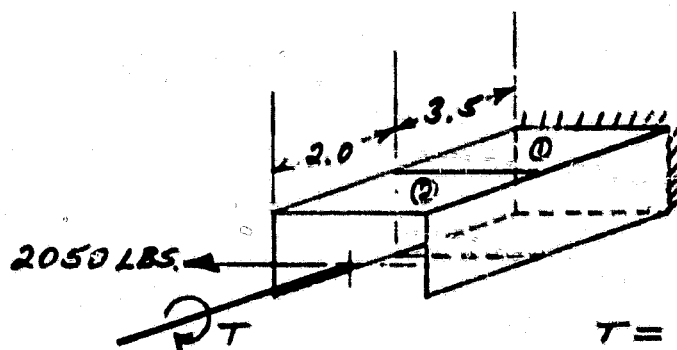
$$S_{A \text{ max}} = \frac{(1575)(2)(1.147)}{.40} = 9033 \text{ PSI}$$

$$MS = \frac{60,000}{9033} - 1 = 5.64 \text{ OK}$$

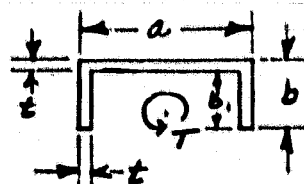
$$S_{B \text{ max}} = \frac{(1575)(5.5)(1.09)}{1.87} = 5049 \text{ PSI}$$

$$MS = \frac{60,000}{5049} - 1 = 10.88 \text{ OK}$$

ENGINEER W SHIVITZ	RAYTHEON COMPANY	PAGE NO.
CHECKER	MISSILE SYSTEMS DIVISION	REPORT NO.
DATE	C.A.T. TRANSMITTER	MODEL NO.

13.5 LONGITUDINAL REACTION

$$T = 2050(2.00) = 4100 \text{ IN.-LBS.}$$

SECTION ②

$$\theta = \frac{36.2 T l J}{A^4 G} \quad \tau = \frac{9 T}{2 t^2 (a + 3b)}$$

$$\begin{aligned} a &= 4.0 \text{ IN.} & J &= I_x + I_y = 4.57 \text{ IN.}^4 \\ b &= 1.625 \text{ IN.} & l &= 2.0 \text{ IN.} \\ t &\approx .25 \text{ IN.} & G &= 3.87 (10)^6 \text{ PSI} \\ A &\approx 1.688 \text{ IN.}^2 \end{aligned}$$

TORSION

$$\theta_2 = \frac{(36.2)(4100)(2.0)(4.57)}{(1.688)^4 (3.87)(10)^6} = .0432 \text{ RAD} \approx 2.5^\circ$$

$$\rightarrow R = 94,960 \text{ IN.-LB/RAD}$$

$$\tau_{2u} = \frac{9(4100)}{2(.25)^2(4 + 3(1.625))} = 43,412 \text{ PSI}$$

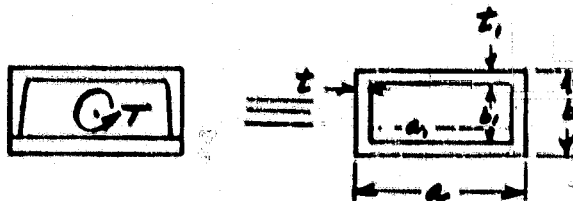
NOTE: THIS STRESS WILL ACTUALLY BE MUCH LOWER SINCE THE SOLID MOUNT SUPPORT BLOCK WHICH IS SEATED IN THIS OPEN

* REF (c)

Form No. V-1028

ENGINEER W. SHIVITZ	RAYTHEON COMPANY	PAGE NO.
CHECKER	MISSILE SYSTEMS DIVISION	REPORT NO.
DATE	C.A.T. TRANSMITTER	MODEL NO.

END OF THE UPPER CHANNEL PROVIDES A RIGID DEFORMATION RESTRAINT TO THIS SECTION. THE SOLID BLOCK IS ALSO WELDED DIRECTLY TO THE ADJACENT BOX SECTION ①. FIFTY PERCENT OF THE ABOVE SHEARING STRESS WOULD STILL BE CONSIDERED UNREALISTICALLY HIGH. SECTION ①



* TORSION

$$\tau = \frac{T}{2t(a-t)(b-t)}$$

$$\theta = \frac{TL(a+bt, -t^2 - t_1^2)}{2t_1(a-t)^2(b-t)^2 G}$$

$$T = 4100 \text{ IN-LBS.}$$

$$a = 4.0 \text{ IN.}$$

$$b = 2.0 \text{ IN.}$$

$$a_1 \approx 3.41 \text{ IN.}$$

$$b_1 \approx 1.4 \text{ IN.}$$

$$t \approx .296 \text{ AVE.}$$

$$t_1 \approx .30 \text{ AVE.}$$

$$L = 5.5 \text{ (CONSERVATIVE)}$$

$$G = 3.87 \text{ (IN)}^6 \text{ PSI}$$

$$\theta = \frac{(4100)(5.5)([4][.296] + [2][.30] - [.296]^2 - [.30]^2)}{2(.296)(.30)(4-.296)^2(2-.30)^2(3.87)(10)^6}$$

$$= .00133 \text{ RAD.} \approx .08^\circ$$

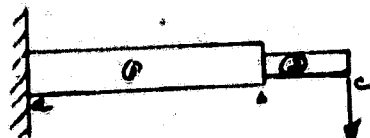
$$\tau = \frac{4100}{2(.296)(4-.296)(2-.30)} = 1100 \text{ PSI}$$

* REF. (6)

Form No. V-1028

ENGINEER W. SHIVITE	RAYTHEON COMPANY	PAGE NO.
CHECKER	MISSILE SYSTEMS DIVISION	REPORT NO.
DATE	C.A.T. TRANSMITTER	MODEL NO.

1359 LOAD (2025 LBS.)

 $P = 2025$

$$I_1 = 6.12 \quad l_1 = 5.5 \text{ (CONSERV.)}$$

$$I_2 = 4.17 \quad l_2 = 2.0$$

$$\begin{aligned} \delta &= \frac{P(l_2)^3}{3EI_2} + \frac{P(l_1)^3}{3EI_1} + \frac{P(l_1)(l_2^2)}{2EI_1} \\ &= \frac{2025}{(10)^3} \left[\frac{(2)^3}{3(4.17)} + \frac{(5.5)^3}{3(6.12)} + \frac{(5.5)^3}{2(6.12)} \right] \\ &= .0047 \text{ IN.} \rightarrow 429,295 \text{ LB/IN.} \end{aligned}$$

$$S_{BTH} = \frac{(2025)(2)(2)}{4.17} = 1942 \text{ PSI}$$

$$S_{a_{max}} = \frac{(2025)(7.5)(2)}{6.12} = 4963 \text{ PSI}$$

ENGINEER W SHIVITE	RAYTHEON COMPANY	PAGE NO.
CHECKER	MISSILE SYSTEMS DIVISION	REPORT NO.
DATE		MODEL NO.

COMBINING STRESSES

$$S_{\max} = \frac{1943}{2} + \sqrt{\left(\frac{1943}{2}\right)^2 + [(1.5)(43,412)]^2}$$

$$= 22,699 \text{ PSI}$$

$$M.S. = \frac{60,000}{22,699} - 1 = \underline{1.64 \text{ OK}}$$

$$S'_{\max} \text{ (SHEAR)} = \pm \sqrt{\left(\frac{1943}{2}\right)^2 + [(1.5)(43,412)]^2} = 21,728 \text{ PSI}$$

$$M.S. = \frac{45,000}{21,728} - 1 = \underline{1.07 \text{ OK}}$$

$$S_{\max} = \frac{4963}{2} + \sqrt{\left(\frac{4963}{2}\right)^2 + (1100)^2} = 5196 \text{ PSI}$$

$$M.S. = \frac{60,000}{5196} - 1 = \underline{10.54 \text{ OK}}$$

$$S'_{\max} \text{ (SHEAR)} = \sqrt{\left(\frac{4963}{2}\right)^2 + (1100)^2} = 2714 \text{ PSI}$$

$$M.S. = \frac{45,000}{2714} - 1 = \underline{15.50 \text{ OK}}$$

ENGINEER W. SHIVITE	RAYTHEON COMPANY	PAGE NO.
CHECKER	MISSILE SYSTEMS DIVISION	REPORT NO.
DATE	C.A.T. TRANSMITTER	MODEL NO.

EACH LOWER MOUNT SUPPORT IS ATTACHED TO THE FRAME BY AT LEAST TEN $\frac{1}{4}$ INCH BOLTS. IF ONLY HALF THE TOTAL TWENTY BOLTS WERE EFFECTIVE

$$M.S. = \frac{10(3600)}{13.5(600)} - 1 = 3.54 \quad OK$$

THE MOUNT SUPPORT FRAME IS TO BE BOLTED TO THE "LOW BOY" RACKS WITH TWENTY 10-32 BOLTS AT EXISTING RACK BOLT HOLE LOCATIONS. IF ONLY THE OUTER EIGHT BOLTS ARE ASSUMED TO BE EFFECTIVE

$$M.S. = \frac{8(2125)}{13.5(600)} - 1 = 1.10 \quad OK$$

THE REMAINING STRUCTURAL MEMBERS OF THE MOUNTING ASSEMBLY SUCH AS THE CHANNELS, BRACKETS, WELDED SUPPORT PLATES, AND RESTRAINT CABLES HAVE HIGH MARGINS OF SAFETY BY INSPECTION.

ENGINEER W SHIVITE	RAYTHEON COMPANY	PAGE NO.
CHECKER	MISSILE SYSTEMS DIVISION	REPORT NO.
DATE	C.A.T. TRANSMITTER	MODEL NO.

**BRACKET ATTACHMENTS TO TRANSMITTER
CABINET AND UPPER MOUNT SUPPORTS**

THE UPPER MOUNT SUPPORTS ARE ATTACHED TO THE TRANSMITTER CABINET BY MEANS OF FOUR $2\frac{1}{2} \times 2 \times \frac{1}{4}$ STRUCTURAL BRACKETS. EACH BRACKET IS BOLTED TO THE TRANSMITTER CABINET BY A MINIMUM OF FOUR $\frac{5}{16}$ INCH BOLTS WITH AN ULTIMATE SHEAR STRENGTH OF 5750* EACH. THE BRACKETS ARE ALSO FASTENED TO THE UPPER MOUNT SUPPORTS WITH THREE $\frac{3}{8}$ BOLTS PER BRACKET OF 8280* SHEAR STRENGTH EACH.

THE CRITICAL CONDITION FOR THESE ATTACH LOCATIONS WOULD BE FOR A 9g FORWARD CRASH LOAD.

CONSIDER ONLY TWO BRACKETS TO BE EFFECTIVE:

$$MS_{\frac{5}{16}} = \frac{8(5750)}{8100} - 1 = 4.68 \quad OK$$

$$MS_{\frac{3}{8}} = \frac{6(8280)}{8100} - 1 = 5.13 \quad OK$$

Enclosure (3) to MS Lab Memo #72-166

ENGINEER W. SHIVITZ	RAYTHEON COMPANY	PAGE NO.
CHECKER	MISSILE SYSTEMS DIVISION	REPORT NO.
DATE	C.A.T. TRANSMITTER	MODEL NO.

STRESSING IN THE REMAINING CRASH
LOADING DIRECTIONS IS NOT CRITICAL AND
THE STRUCTURAL MARGIN OF SAFETY IS
HIGH BY INSPECTION.

APPENDIX B

**CAT TRANSMITTER
AND
TELESCOPE ASSEMBLY**

SAFETY OF FLIGHT ANALYSIS

Introduction

The following is a safety of flight analysis of the C.A.T. transmitter and telescope assembly. The transmitter structure consists of an aluminum base channel and aluminum plates. The channel acts as the main support member while the plates act as intermediate supports and enclose the transmitter. The telescope assembly is supported at one end of the base channel.

The main concern of this analysis is to insure that no parts under crash conditions will tear loose and create a hazard to the aircraft or personnel on board.

Design Criteria

The design loads for this analysis are taken from Section 5.1 of the NASA CV 990 Airborne Laboratory Experimenters Handbook and are summarized in the table below. A factor of 1.5 is used to determine the ultimate load factors.

<u>Load Direction</u>	<u>Load Factor (Yield)</u>	<u>Load Factor (Ultimate)</u>
Forward	9.0	13.5
Down	7.0	10.5
Up	2.0	3.0
Side	1.5	2.25
Aft	1.5	2.25

Summary and Conclusions

The analysis of the transmitter structure shows it to be structurally sound with high margins of safety. An investigation of the telescope housing, support rings, support plates, and associated hardware show that the telescope and its installation are also structurally sound for flight safety.

C.A.T. TRANSMITTER

THE BASE CHANNEL IS ASSUMED TO BE THE FIXED SUPPORT. EXAMINATION OF THE CHANNEL SHOWS THAT BECAUSE OF OPTICAL REQUIREMENTS FOR A RIGID PLATFORM THE STRENGTH OF THE CHANNEL FAR EXCEEDS THAT REQUIRED FOR SAFETY OF FLIGHT. THE METHOD OF ATTACHMENT OF THE CHANNEL TO THE AIRCRAFT SUPPORT STRUCTURE HAS NOT BEEN ANALYZED AND IS ASSUMED NOT TO BE OUR RESPONSIBILITY.

THE TRANSMITTER OUTER STRUCTURE CONSISTS OF ALUMINUM PLATES (.25-.50THK.) WHICH UNDER CRASH CONDITIONS WILL CONTAIN ANY INTERNAL COMPONENTS WHICH MAY TEND LOOSE.

THE ATTACHMENT OF THE TRANSMITTER TO THE BASE CHANNEL IS ACCOMPLISHED BY $\frac{1}{8}$ INCH DIAMETER STEEL PINS AND 6-32 SCREWS.

FOR $\frac{1}{8}$ DIAMETER PINS $f_{su} = 75000 \text{ psi}$

$$P_{su} = \frac{\pi (.125)^2}{4} (75000) = 920 \text{ lbs / PIN.}$$

FOR #6-32 SCREWS $f_{tu} = 80,000 \text{ psi}$

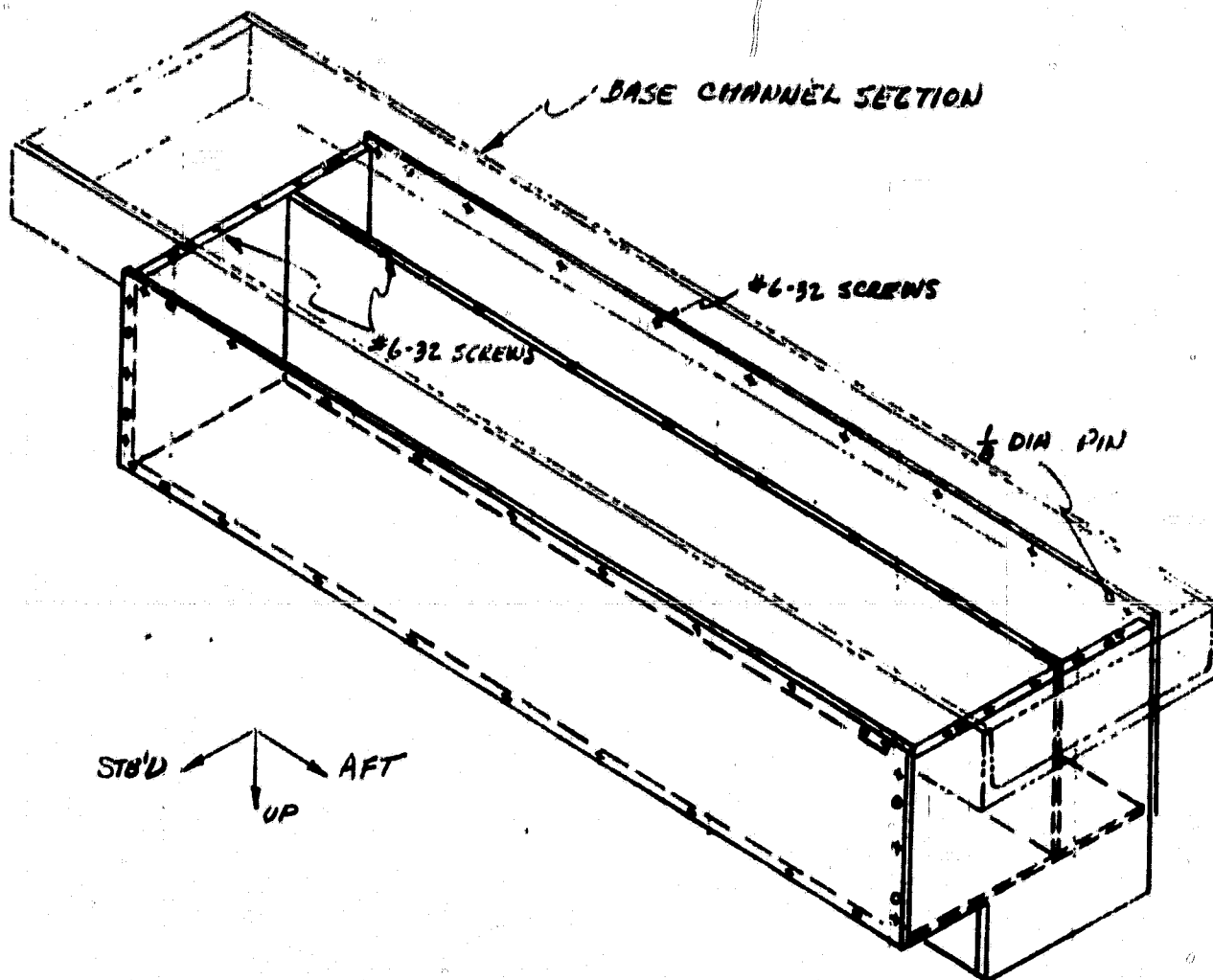
$$P_{tu} = 730 \text{ lbs / SCREW}$$

$$P_{su} = .6 (730) = 438 \text{ lbs}$$

FORM NO. 46-0389



CALC. <i>EC Wong</i>	REV	DATE	RAYTHEON COMPANY EQUIPMENT DIVISION WAYLAND LABORATORY, WAYLAND, MASS.	CLASSIF.
CHK.				MODEL
				REPORT NO.
DATE				PAGE NO. 3



ORIGINAL PAGE IS
OF POOR QUALITY

C.A.T. TRANSMITTER STRUCTURE

CALC. <i>ECWong</i>	REV	DATE	RAYTHEON COMPANY EQUIPMENT DIVISION WAYLAND LABORATORY, WAYLAND, MASS.	CLASSIF.
CHK.				MODEL
				REPORT NO.
DATE				PAGE NO. <i>4</i>

FOR FORWARD LOADING TEN (10) $\frac{1}{8}$ DIA PINS AND THIRTY-SEVEN (37) 6-32 SCREWS REACT THE TRANSMITTER ASSEMBLY IN SHEAR.

FOR $\frac{1}{8}$ PINS ONLY (VERY CONSERVATIVE)

$$P_{sa} = 10 \times 920 = 9200 \text{ lbs}$$

$$F_x = 300 \times 13.59 = 4050 \text{ lbs}$$

$$M.S. = \frac{9200}{4050} - 1 = +1.27$$

FOR PINS & SCREWS

$$P_{sa} = 9200 + 37(438) = 25400 \text{ lbs}$$

$$M.S. = \frac{25400}{4050} - 1 = +5.27$$

FOR UP LOADING NINETEEN 6-32 SCREWS SECURE THE TRANSMITTER TO THE BASE.

$$P_{sa} = 19(730) = 13870 \text{ lbs}$$

$$F_z = 300 \times 39 = 900 \text{ lbs}$$

$$M.S. = \frac{13870}{900} - 1 = +14.4$$

FORM NO. 48-9380



CALC. <i>EC Wong</i>	REV	DATE	RAYTHEON COMPANY EQUIPMENT DIVISION WAYLAND LABORATORY, WAYLAND, MASS.	CLASSIF.
CHK.				MODEL
				REPORT NO.
DATE				PAGE NO. 5

FOR SIDE LOADING SIX (6) $\frac{1}{8}$ DIA. PINS AND NINETEEN (19)
6-32 SCREWS RESIST THE TRANSMITTER IN SHEAR.

FOR $\frac{1}{8}$ DIA. PINS ONLY (VERY CONSERVATIVE)

$$P_{sa} = 6 \times 920 = 5520 \text{ lbs}$$

$$F_y = 2.25(300) = 675 \text{ lbs}$$

$$M.S. = \frac{5520}{675} - 1 = 7.18$$

THE LOADING IN THE OTHER DIRECTIONS ARE SEEN TO
BE LESS CRITICAL BY INSPECTION.

FORM NO. 49-9300



CALC. <i>ECWmg</i>	REV	DATE	RAYTHEON COMPANY EQUIPMENT DIVISION WAYLAND LABORATORY, WAYLAND, MASS.	CLASSIF.
CHK.				MODEL
				REPORT NO.
DATE				PAGE NO. 6

C.A.T. TRANSMITTER TELESCOPE

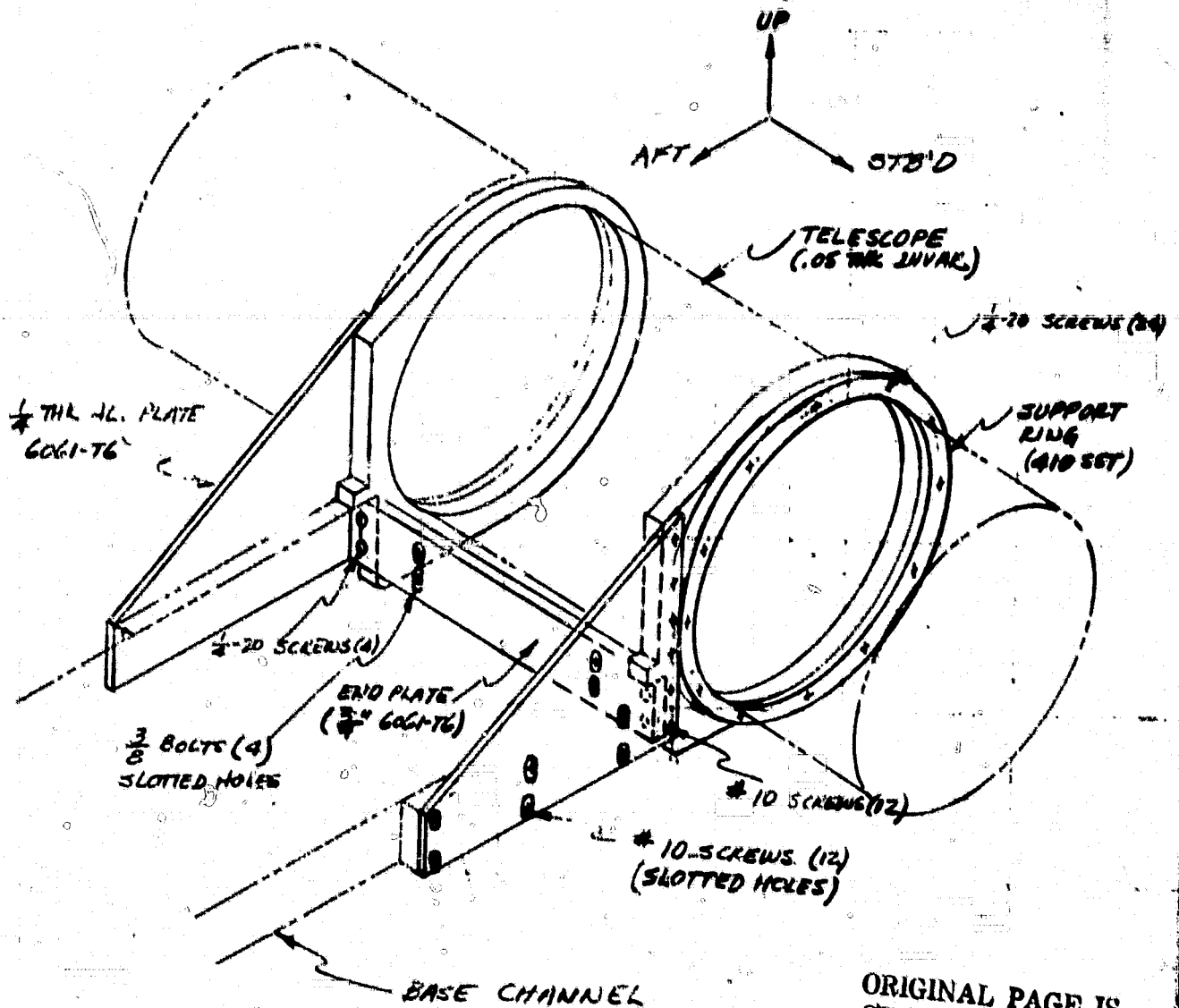


FIG. 1

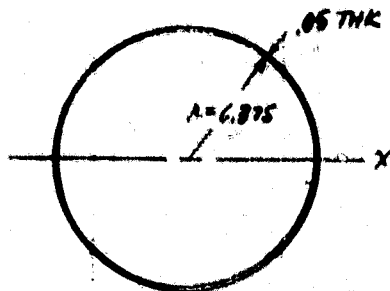
ORIGINAL PAGE IS
OF POOR QUALITY

CALC. <i>ECWing</i>	REV	DATE	RAYTHEON COMPANY EQUIPMENT DIVISION WAYLAND LABORATORY, WAYLAND, MASS.	CLASSIF.
CHK.				MODEL
				REPORT NO.
DATE <i>9/29/71</i>				PAGE NO. 7

TELESCOPE SUPPORT RING

TWELVE $\frac{1}{2}$ -20 AIRCRAFT BOLTS SECURE EACH OF THE TWO TELESCOPE RING FLANGES TO THE SUPPORT RINGS. THE RING FLANGES ARE WELDED TO THE TELESCOPE HOUSING WHICH IS MADE OF .050 INVAR.

TELESCOPE HOUSING STRESSES



$$I_x = \frac{\pi(6.425^4 - 6.375^4)}{4} = 41.178 \text{ in}^4$$

REF: BRUNN FIG. C6-12

$$\frac{L}{r} = \frac{6.425}{.05} = 128.5$$

$$C_b = .22$$

$$f_{bc} = C_b E \left(\frac{L}{r} \right)^2 = .22 (21 \times 10^6) \left(\frac{.05}{6.425} \right)^2 = 35950 \text{ psi} > f_{cy}$$

$$f_{cy} = 24000 \text{ psi}$$

$$M_c = \frac{f_{cy} I}{c} = \frac{24000 (41.178)}{6.425} = 153816 \text{ in lbs}$$

MAXIMUM BENDING MOMENT IS APPROXIMATELY

$$M_b = 99 (60 \times 20) = 10800 \text{ in lbs}$$

$$A.I.S. = \frac{153,816}{10800} - 1 = +13.24$$

FORM NO. 48-9280



CALC. E.C. Wong	REV	DATE	RAYTHEON COMPANY EQUIPMENT DIVISION WAYLAND LABORATORY, WAYLAND, MASS.	CLASSIF.
CHK.				MODEL
				REPORT NO.
DATE 9/23/71				PAGE NO. 8

RING WELD STRESSES

$$A_w = 2(\pi D)(.707t) = 2(\pi)(12.55)(.707)(.05) = 2.854 \text{ in}^2$$

$$F_s = 2.25g(140) = 315 \text{ lbs}$$

$$f_s = \frac{F_s}{A_w} = \frac{315}{2.854} = 110 \text{ psi}$$

$$M.S. = \frac{14400}{110} - 1 = \text{HIGH}$$

RING BOLT LOADS

$$F_s = 13.5g(140) = 1890 \text{ lbs}$$

$$P_s = \frac{1890}{24} = 79 \text{ lbs / screw}$$

$$M.S. = \frac{1970}{79} - 1 = \text{HIGH}$$

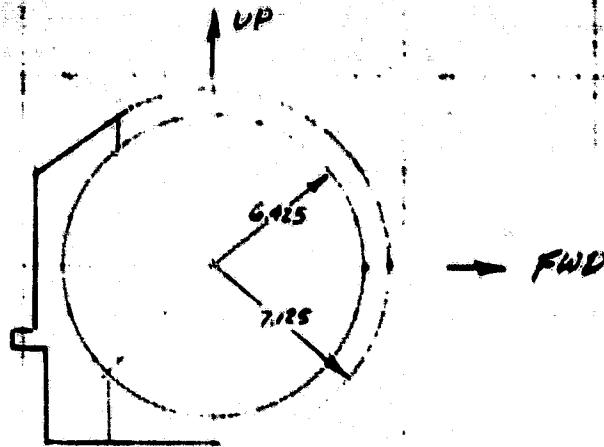
FORM NO. 42-0380



CALC. <i>E. Wong</i>	REV	DATE	RAYTHEON COMPANY EQUIPMENT DIVISION	CLASSIF.
CHK.				MODEL
			WAYLAND LABORATORY, WAYLAND, MASS.	REPORT NO.
DATE				PAGE NO. 9

SUPPORT RING STRESSES

REF. 2. SECT B6.0



$$\frac{e}{D} = \frac{7.125}{12.85} = .55$$

$$\frac{W}{D} = \frac{14.25}{12.85} = 1.1$$

$$\frac{D}{t} = \frac{12.85}{.8125} = 15.8$$

$$A_{br} = 12.85(.8125) = 10.44 \quad A_t = (14.25 - 12.85)(.8125) = 1.138 \text{ in}^2$$

$$P'_{br} = K_{br} F_{ux} A_{br} \\ = .08(60,000)(10.44) = 50,112 \text{ lbs}$$

$$P'_{tu} = K_t F_{tu} A_t \\ = .99(60000)(1.138) = 67,600 \text{ lbs}$$

$$P'_y = K_{by} A_{br} F_{uy} \\ = .1(10.44)(32000) = 33,408 \text{ lbs}$$

$$P = 1.5(140) = 210 \text{ lbs}$$

$$M.S. = \frac{33408}{210} - 1 = \text{HIGH}$$

FORM NO. 48-5389

CALC. E.C. Wong.	REV	DATE	RAYTHEON COMPANY EQUIPMENT DIVISION WAYLAND LABORATORY, WAYLAND, MASS.	CLASSIF.
CHK.				MODEL
				REPORT NO.
DATE				PAGE NO. 10

FOR DOWNWARD LOADING

$$A_{av} = \frac{6}{\frac{3}{A_1} + \frac{1}{A_2} + \frac{1}{A_3} + \frac{1}{A_4}} = \frac{6(8125)}{\frac{3}{2.5} + \frac{1}{.7} + \frac{1}{.7} + \frac{1}{1}} = .964$$

$$\frac{A_{av}}{A_{br}} = \frac{.964}{10.44} = .092$$

$$P_{en} = K_{en} A_{br} F_{enx} \\ = .12(10.44)(60000) = 75,168 \text{ lbs}$$

$$P'_y = K_{ey} A_{br} F_{eyx} \\ = .12(10.44)(32000) = 40,090 \text{ lbs}$$

$$P = 7(140) = 980 \text{ lbs}$$

$$M.S. = \frac{40090}{980} - 1 = \text{HIGH}$$

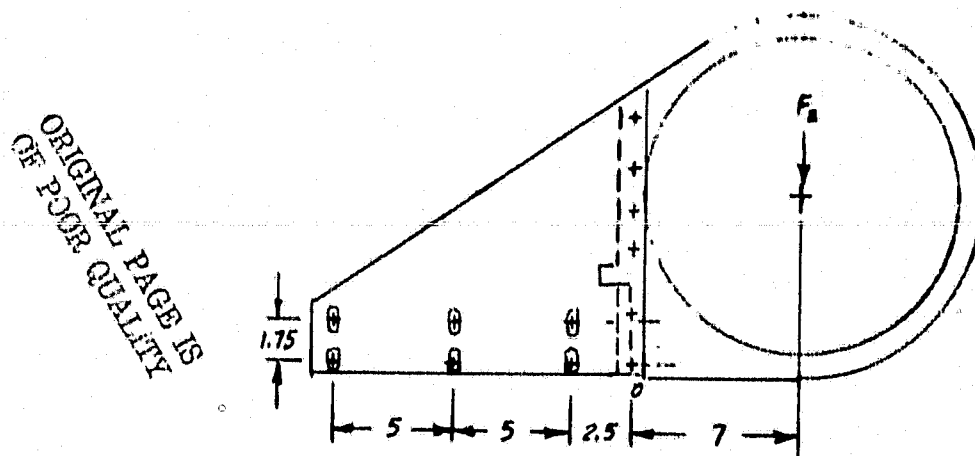
FORM NO. 48-9390



CALC. <i>EC Wong</i>	REV	DATE	RAYTHEON COMPANY EQUIPMENT DIVISION WAYLAND LABORATORY, WAYLAND, MASS.	CLASSIF.
CHK.				MODEL
				REPORT NO.
DATE				PAGE NO. //

TELESCOPE SUPPORT RING INSTALLATION

THE $\frac{1}{4}$ INCH THICK ALUMINUM PLATES WHICH HELP SUPPORT THE RING TO THE CHANNEL HAVE SLOTTED HOLES. THESE SLOTTED HOLES ARE NOT EFFECTIVE IN THE VERTICAL DIRECTION EXCEPT THRU FRICTION OF THE SCREWS OR WHEN THEY ULTIMATELY BOTTOM IN THEIR SLOTS.



DUE TO THE NON SYMMETRICAL LOCATION OF THE CENTER OF GRAVITY BETWEEN THE SUPPORT RING 75% OF THE TOTAL TELESCOPE WEIGHT COULD BE DISTRIBUTED TO ONE SUPPORT RING.

FORM NO. 48-0380



CALC. ECWang	REV	DATE	RAYTHEON COMPANY EQUIPMENT DIVISION WAYLAND LABORATORY, WAYLAND, MASS.	CLASSIF.
CHK.				MODEL
				REPORT NO.
DATE				PAGE NO. 12

ASSUME THE VERTICAL FORCES ARE RESISTED ONLY BY THE TWO
 $\frac{1}{4}$ -20 SCREWS AT THE LOWER PORTION OF THE SUPPORT
 RING.

$$F_2 = .75(10.5g)(140) = 1102 \text{ lbs}$$

$$P_3 = \frac{1102}{2} = 551 \text{ lbs/SCREEN}$$

$$M.S. = \frac{.6(1750)}{551} - 1 = +.9 \text{ (CONSERVATIVE)}$$

THE MOMENT CREATED BY A VERTICAL FORCE IS REACTED
 ABOUT POINT "O" AND IS RESISTED BY FRICTION IN THE SIX (6)
 10-32 SCREWS AT THE SLOTTED HOLES AND IN TENSION BY THE
 TWO $\frac{1}{4}$ -20 SCREWS AT THE LOWER PORTION OF THE SUPPORT RING.

$$M = .75(10.5g)(140)(7) = 7718 \text{ in lbs.}$$

FRICTIONAL RESISTANCE OF 10-32 SCREWS

$$P_{fr} = \frac{M/r}{3(x^2+y^2)} = \frac{7718 [12.5^2 + 2.25^2] \frac{1}{2}}{2[2.5^2 + 7.5^2 + 12.5^2] + 3[.5^2 + 2.25^2]} = 216 \text{ lbs (FRICTION)}$$

FOR #10 SCREW WITH A RECOMMENDED MINIMUM TORQUE OF

$$20 \text{ in-lbs} \quad P_t = 412 \text{ lbs}$$

$$P_{fr} = \mu P_t = .61(412) = 251 \text{ lbs}$$

$$M.S. = \frac{251}{216} - 1 = +.16 \text{ (FRICTION SLIPPAGE)}$$

CALC. ECL Wong	REV	DATE	RAYTHEON COMPANY EQUIPMENT DIVISION WAYLAND LABORATORY, WAYLAND, MASS.	CLASSIF.
CHK.				MODEL
				REPORT NO.
DATE				PAGE NO. 13

FOR THE CASE JUST CONSIDERED THE MOMENT RESISTING CAPABILITY OF THE TWO $\frac{1}{2}$ -20 SCREWS HAS NOT BEEN TAKEN INTO ACCOUNT. ALSO EVEN IF FRICTION IS IGNORED THE TELESCOPE WILL ONLY BOTTOM IN THE SLOTTED HOLES. WHEN THIS OCCURS THE ALLOWABLE SHEAR FORCE ON THE SCREWS BECOMES A FUNCTION OF THE ULTIMATE SHEAR STRESS OF THE SCREW MATERIAL.

ASSUME THE TWO SCREWS AT THE FAR LEFT BOTTOM AND RESIST THE MOMENT CAUSE BY VERTICAL LOADING

$$P_3 = \frac{M}{d} = \frac{7718}{12.5} = 617 \text{ lbs}$$

$$M.S. = \frac{.6(1400)}{(617/2)} - 1 = +1.72 \quad (\text{NO FRICTION, CONSERVATIVE})$$

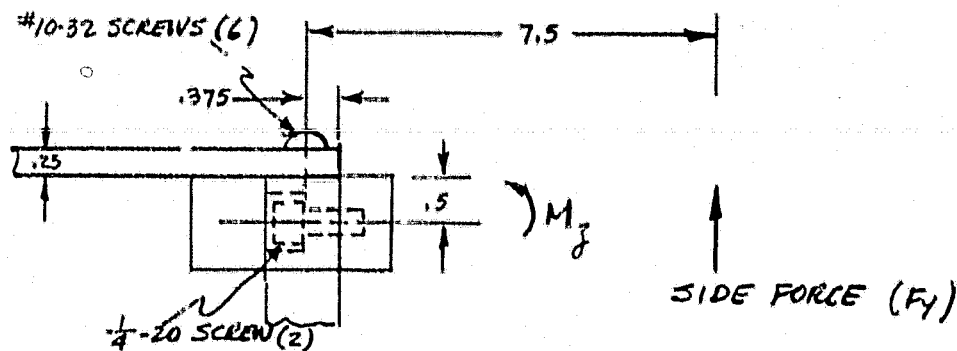
FOR LOADING IN THE LONGITUDINAL DIRECTION THE LARGE NUMBER OF SUPPORTING SCREWS MAKE THE INSTALLATION ADEQUATE BY INSPECTION.

FORM NO. 48-0380



CALC. <i>EC'Wing</i>	REV	DATE	RAYTHEON COMPANY EQUIPMENT DIVISION WAYLAND LABORATORY, WAYLAND, MASS.	CLASSIF.
CHK.				MODEL
				REPORT NO.
DATE				PAGE NO. 14

FOR LOADING IN THE PORT AND STARBOARD DIRECTIONS THE RELATIVE STIFFNESSES OF THE TELESCOPE TO SUPPORT RINGS WILL IN REALITY CAUSE VERY LITTLE BENDING MOMENT TO OCCUR AT THE SUPPORT RING AND CHANNEL INTERFACE. HOWEVER FOR A CONSERVATIVE ANALYSIS ASSUME THE LOADING FROM THE TELESCOPE ARE DISTRIBUTED EQUALLY BETWEEN THE TWO RINGS.



$$F_y = \left(\frac{40}{2}\right)(2.25) = 157.5 \text{ lbs}$$

ORIGINAL PAGE IS
OF POOR QUALITY

$$M_j = F_y (7.5) = 1181 \text{ in lbs}$$

$$P_t = \frac{M_j r A}{\sum r^2 A} = \frac{1181 (.375) (.0152)}{6 (.375)^2 (.0152) + 2 (.5)^2 (.0281)} = 250 \text{ lbs} \quad (\#10-32)$$

$$P_t = \frac{1181 (.5) (.0281)}{6 (.375)^2 (.0152) + 2 (.5)^2 (.0281)} = 617 \text{ lbs} \quad (1/4-20)$$

CALC.	REV	DATE	RAYTHEON COMPANY EQUIPMENT DIVISION WAYLAND LABORATORY, WAYLAND, MASS.	CLASSIF.
CHK.				MODEL
				REPORT NO.
DATE				PAGE NO. 15

$$M.S. = \frac{1400}{250} - 1 = +4.6 \quad (10-32)$$

$$M.S. = \frac{1750}{617} - 1 = +1.83 \quad (\frac{1}{4}-20)$$

ALUMINUM PLATE ($\frac{1}{4}$ THK)

$$f_b = \frac{6M}{bt^2} = \frac{6(1181)}{10.38(.25)^2} = 10922 \text{ psi}$$

$$M.S. = \frac{42000}{10922} - 1 = +2.84$$

FOR LOADING IN THE VERTICAL DIRECTION TWELVE 10-32
SCREWS AND FOUR $\frac{3}{8}$ -16 BOLTS SECURE THE TELESCOPE
SUPPORT RING ASSEMBLY TO THE BASE CHANNEL. THESE
FASTENER HOLES ARE SLOTTED. HOWEVER UNDER CRASH
CONDITIONS IF FRICTION IS NOT SUFFICIENT THE SCREWS
WILL BECOME FULLY EFFECTIVE ONCE THE BOTTOM IN THEIR
SLOTS. THE MARGIN OF SAFETY IS HIGH BY INSPECTION.

FORM NO. 48-0360



CALC. <i>ECWay</i>	REV	DATE	RAYTHEON COMPANY EQUIPMENT DIVISION WAYLAND LABORATORY, WAYLAND, MASS.	CLASSIF.
CHK.				MODEL
				REPORT NO.
DATE				PAGE NO. 16

REFERENCES

1. BREUHN, E. F. ANALYSIS & DESIGN OF FLIGHT VEHICLE STRUCTURES
TRI-STATE OFFSET COMPANY, CINCINNATI, OHIO.
2. NASA (GEORGE C MARSHALL SPACE FLIGHT CENTER)
ASTRONAUTICS STRUCTURES MANUAL.
3. NASA CV 990 AIRBORNE LABORATORY EXPERIMENTERS HANDBOOK

FORM NO. 48-0380



CALC.	REV	DATE	RAYTHEON COMPANY EQUIPMENT DIVISION WAYLAND LABORATORY, WAYLAND, MASS.	CLASSIF.
CHK.				MODEL
				REPORT NO.
DATE				PAGE NO. 17

APPENDIX C

DETERMINATION OF ATTENUATION COEFFICIENTS



FORM 10-2007 10-001 0000

DIVISION EQUIPMENT
Operation EDL - SUDBURY
Department Electro-Optics

To: Distribution

From: D. A. Kawachi

Subject: Atmospheric Attenuation of CO₂
Laser Radiation in Clear
Weather

Classification UNCLASSIFIED

Contract No.

Distribution As Listed

File No. EM77-0348

Memo No. DAK:77:08

Date 13 July 1977

Determination of Attenuation Coefficients

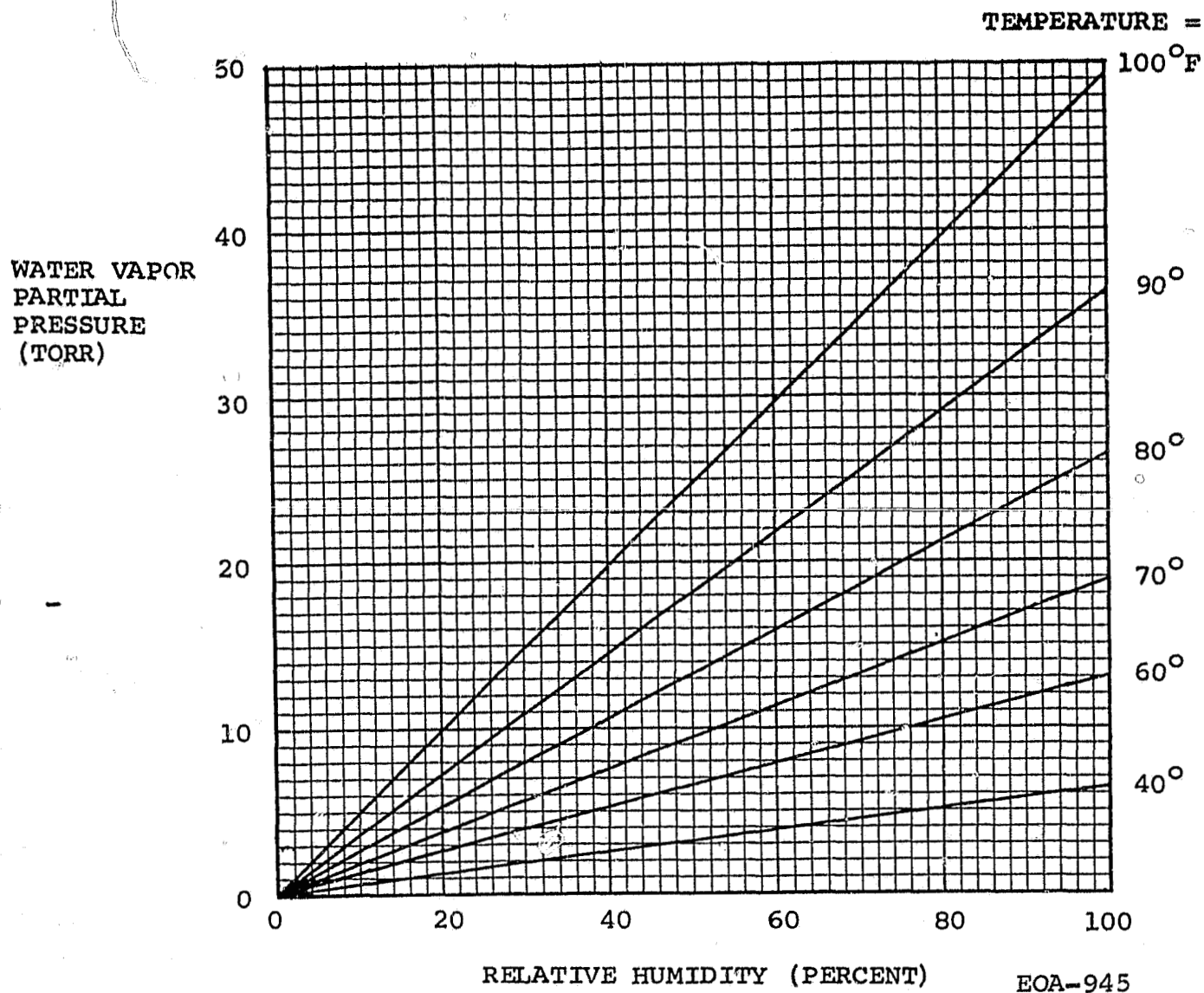
Various researchers have measured the attenuation of CO₂ laser radiation in clear weather. McCoy, Rensch and Long⁽¹⁾² measured specifically the attenuation due to water vapor which is the attenuator of most interest for this analysis, but the measurements of Shumate et al⁽²⁾ are for more recent and appear to have been made under more carefully controlled conditions. Therefore, the data of the latter were used for the attenuation due to water vapor. For the CO₂ attenuation, the values presented by S. Murty⁽³⁾ based upon the measurements of P. Yin and R. Long⁽⁴⁾ were included. Finally, the aerosol attenuation values were taken from McClatchey's data⁽⁵⁾ extrapolated to a visibility of 12 km.

The relationship of water vapor pressure to temperature and humidity is shown in Figure C-1. It is apparent that the water vapor pressure during the summer is often above the highest pressure of the Shumate measurements which was 15 Torr. For example, a temperature of 95°F and a relative humidity of 95 percent produces a water vapor pressure of 40 Torr. Therefore, the data had to be extrapolated to the pressures of interest, but in order to do it accurately, the relationship between attenuation and pressure must be known. The relationship is assumed to be quadratic.

$$\mu = Ap + Bp^2 \quad (1)$$

where μ is the attenuation coefficient, p is the water vapor partial pressure, and the coefficients A and B depend upon the total pressure.

Atmospheric Attenuation of CO₂ Laser Radiation in Clear Weather



ORIGINAL PAGE IS
OF POOR QUALITY

Figure C-1. Water Vapor Pressure as Function of Temperature and Humidity. One cm of H₂O/km ≈ 10 Torr.

Atmospheric Attenuation of CO₂ Laser Radiation in Clear Weather

The atmospheric attenuation coefficients were determined for selected emission lines of the CO₂ laser in clear weather as a function of temperature and relative humidity at sea level. The lines of specific interest for this analysis are the P(16), P(18), P(20), P(22), P(24) and P(26) lines of the 10.4 micron branch, but other lines were also briefly examined.

The conclusions of the analysis are:

1. Attenuation coefficients for the P(18), P(20), P(22), P(24) and P(26) lines are generally within 0.5 dB/km (each way) of each other, with the P(20) line the worst and the P(26) line the best of this group. The P(16) line, however, attenuates by a somewhat greater amount - 0.5 to 2 dB/km more depending upon humidity - and should be avoided. Figures C-2 and C-3 compare the attenuation for different P-lines.
2. Typical attenuation values vary from 1 dB/km each way in an 11 Torr water vapor pressure atmosphere (e.g., T = 70°F, R.H. = 60%) to 6 dB/km each way in a 40 Torr atmosphere (e.g., T = 95°F, R.H. = 95%). For a 5 km path the corresponding atmospheric losses range from 10 to 60 dB round trip. Figure C-4 shows the variation of atmospheric attenuation with range. Figures C-5 and C-6 show the variation with temperature and humidity for two specific P-lines, P(20) and P(26), which bracket the attenuation for the five lines from P(18) to P(26).
3. Under humid conditions, water vapor is the dominant attenuator. In a clear dry atmosphere, CO₂ is the dominant attenuator. Finally, under foggy conditions the aerosol scatter becomes dominant, but note that the fog must be

Atmospheric Attenuation of CO₂
Laser Radiation in Clear
Weather

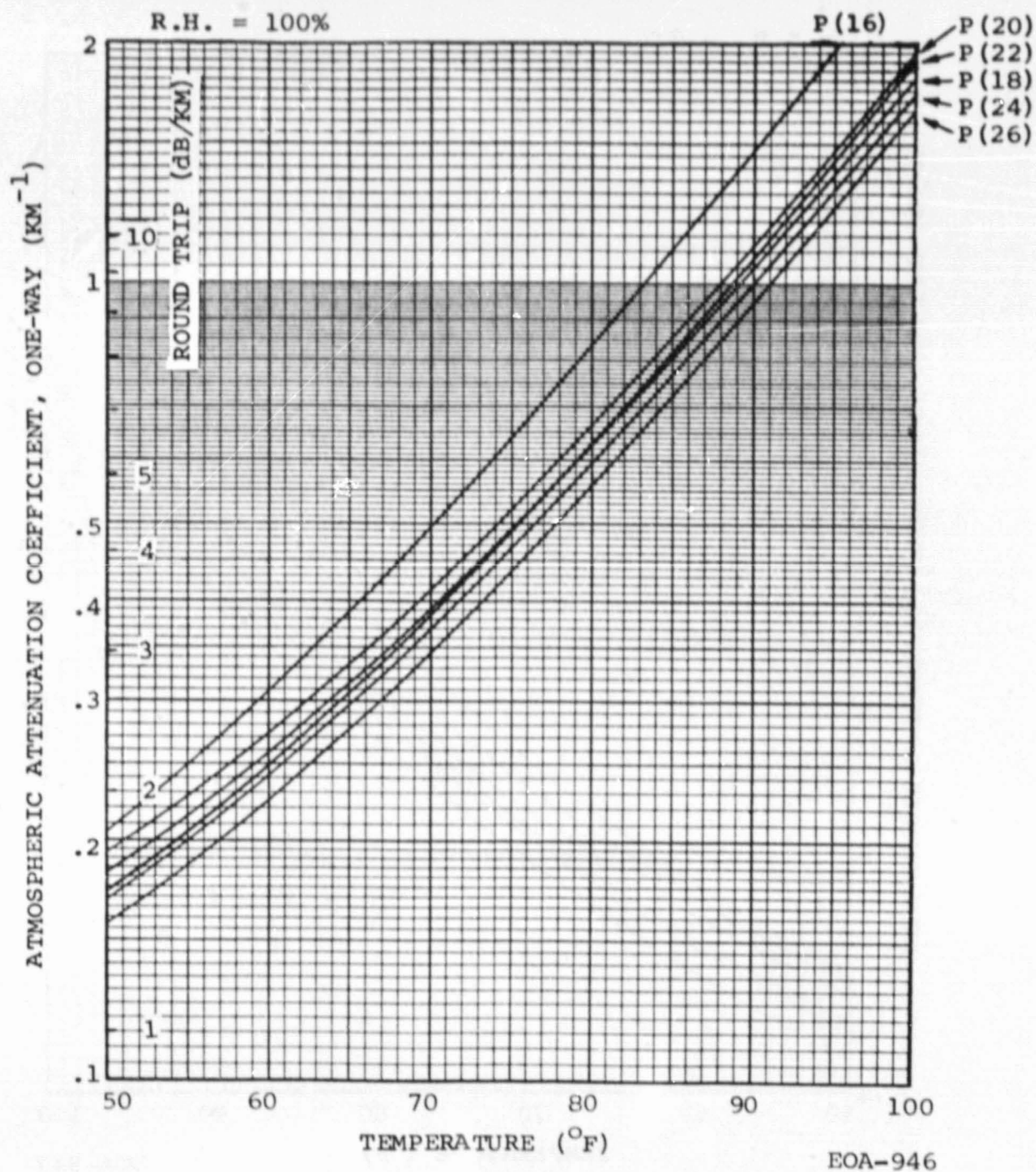


Figure C-2. Atmospheric Attenuation Coefficient for
10.6 Micron CO₂ Laser Lines at Sea Level,
100% Relative Humidity

Atmospheric Attenuation of CO₂
Laser Radiation in Clear
Weather

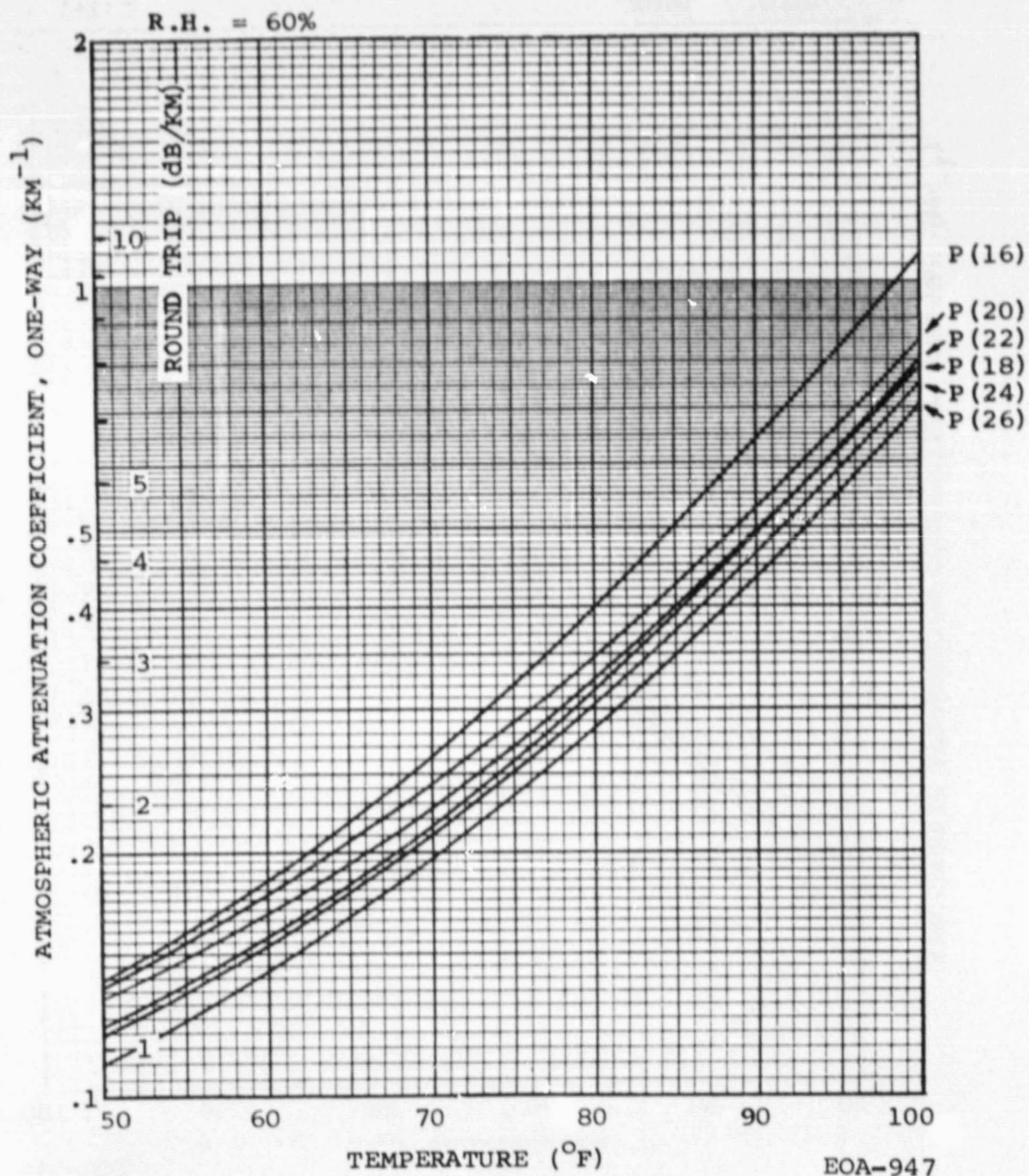


Figure C-3. Atmospheric Attenuation Coefficient for
10.6 Micron CO₂ Laser Lines at Sea Level,
60% Relative Humidity

Atmospheric Attenuation of CO₂ Laser Radiation in Clear Weather

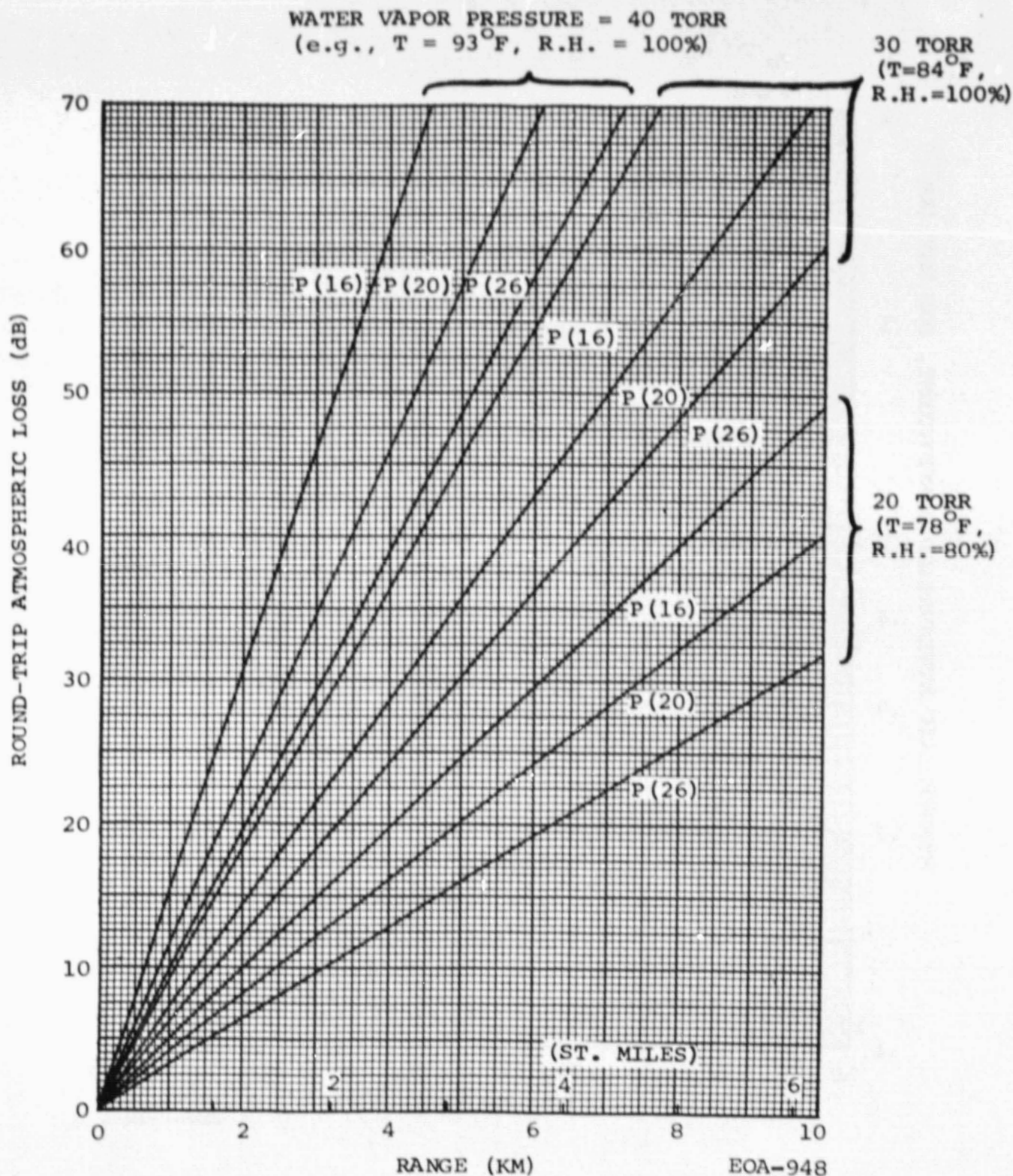


Figure C-4. Atmospheric Loss for Different
10.6 Micron CO₂ Laser Lines as
Function of Range at Sea Level

ORIGINAL PAGE IS
OF POOR QUALITY

Atmospheric Attenuation of CO₂
Laser Radiation in Clear
Weather

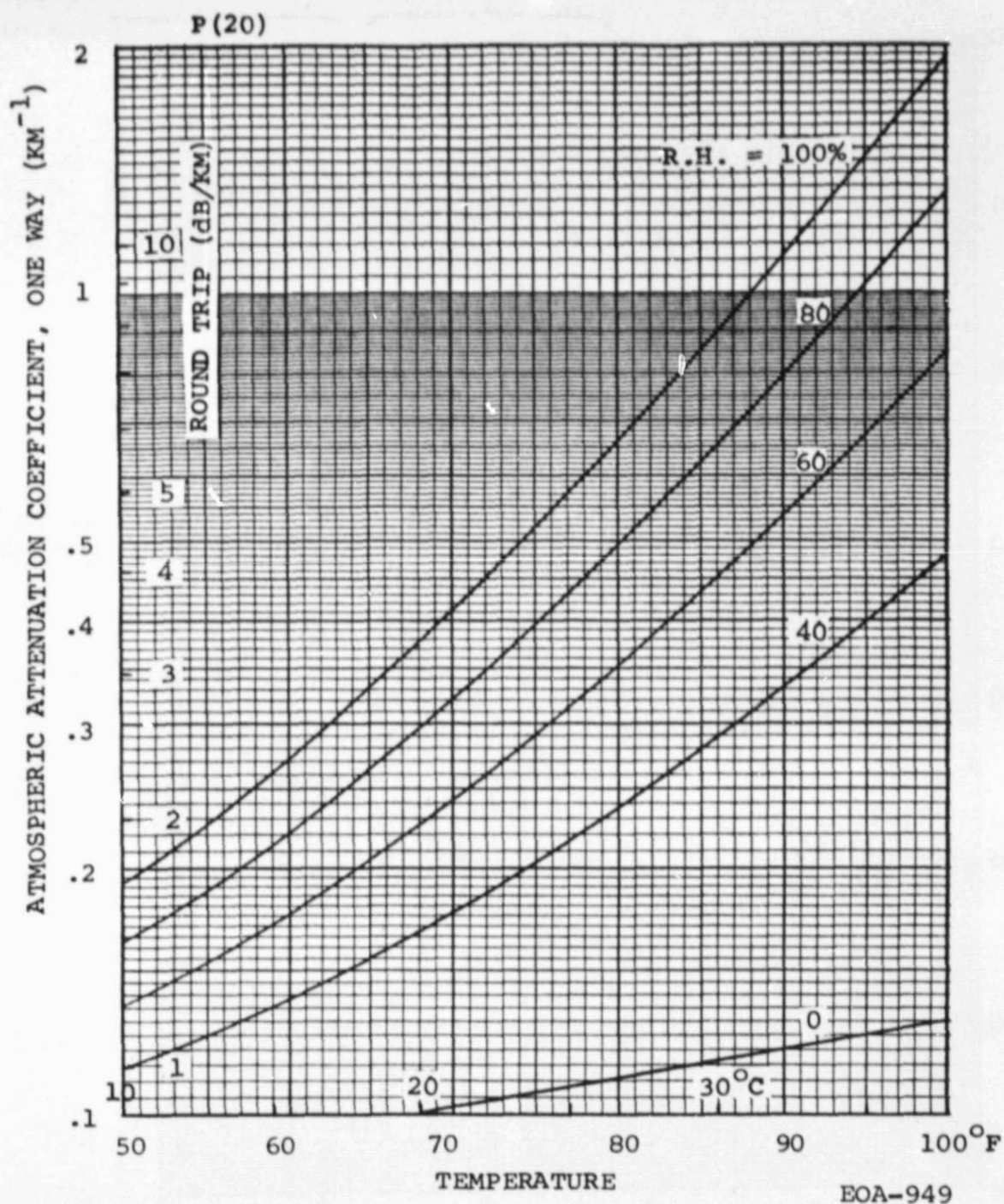


Figure C-5. Atmospheric Attenuation Coefficient for
P(20) Line of CO₂ Laser at Sea Level

Atmospheric Attenuation of CO₂ Laser Radiation in Clear Weather

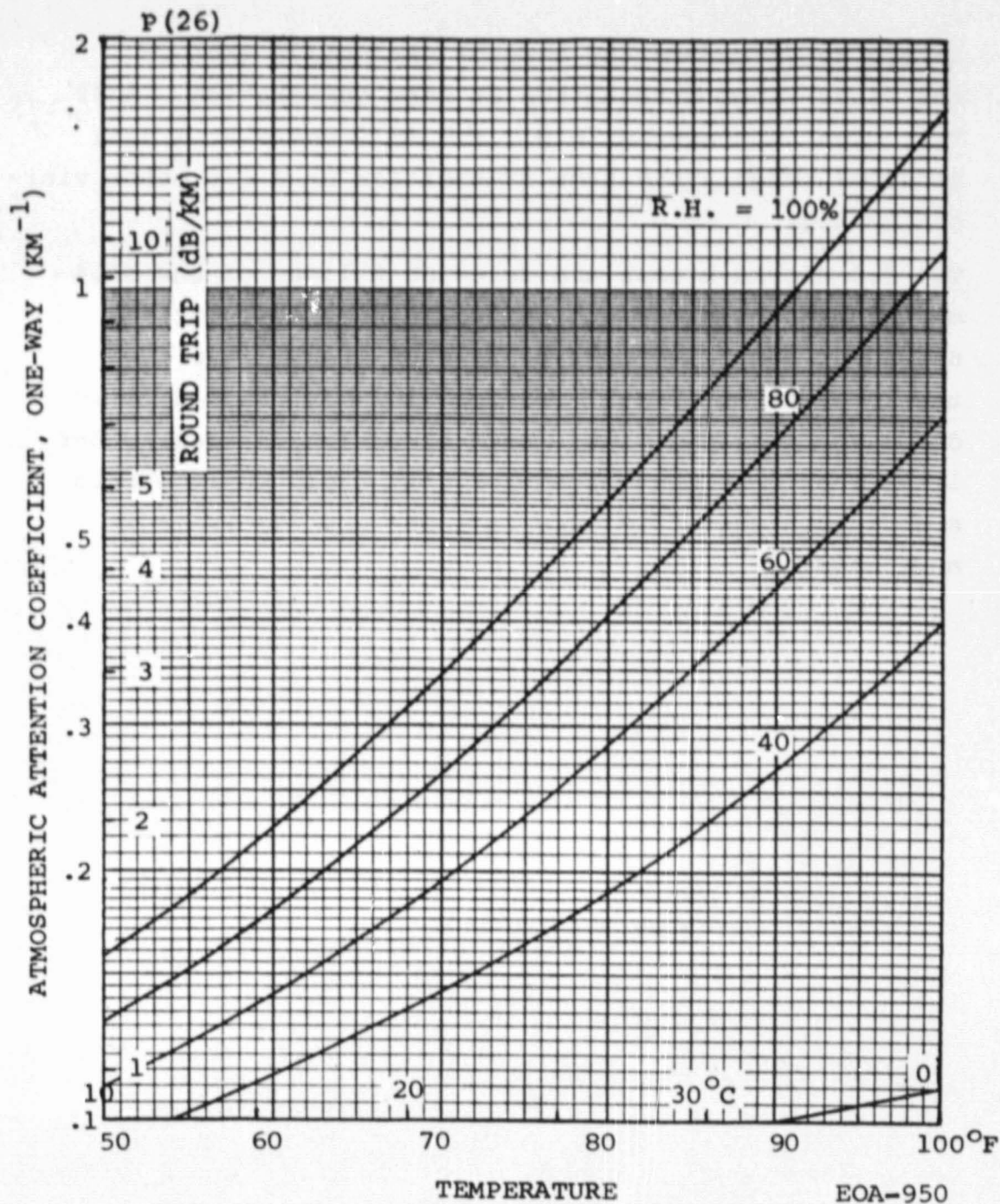


Figure C-6. Atmospheric Attenuation for P(26)
Line of 10.6 Micron CO₂ Laser at
Sea Level

Atmospheric Attenuation of CO₂ Laser Radiation in Clear Weather

fairly thick before the aerosol extinction exceeds the water vapor attenuation at warm temperature. A 40 Torr clear atmosphere (e.g., $T = 95^{\circ}\text{F}$ and $\text{R.H.} = 95\%$) produces roughly the same attenuation as a 150 meter visibility fog.

4. The 9.4 micron branch and selected R lines of the 10.4 micron branch suffer substantially less attenuation under hot and humid conditions than the P lines of the 10.4 micron branch. Differences may reach 5 to 10 dB/km round trip. Thus, laser operation on these other lines should be considered for hot, humid environments even though the efficiency is lower and the laser is more complex.

References:

1. J. McCoy, D. Rensch and R. Long, App. Op., Vol. 8, No. 7
7/69 pp. 1471-8.
2. M. Shumate, R. Menzies, J. Margolis and L. Rosengren,
App. Op., Vol. 15, No. 10, 10/76, pp. 2480-8.
3. S. S. R. Murty, "Atmospheric Transmission of CO₂ Laser
Radiation with Application to Laser Doppler System," NASA
Tech. Memo TM X-64987, 11/75.
4. P. Yin and R. Long, App. Op., Vol. 7, No. 8, 8/68, pp. 1551-3.
5. R. McClatchey and J. Selby, AFCRL-72-0611, Envir. Res. Paper
#419.

APPENDIX D

CAT LIDAR WIND SHEAR STUDIES

CAT LIDAR WIND SHEAR STUDIES

1. INTRODUCTION

Three major commercial aircraft accidents occurring during the past several years, and linked by the National Transportation Safety Board to wind shear, have demonstrated the serious threat this phenomenon represents to safe aircraft operations in the terminal area. These accidents were: Iberian Airlines DC10-30, Logan International Airport, December 17, 1973 (accident occurred on landing)⁽¹⁾; Eastern Airlines, B727-225, JFK International Airport, June 24, 1975 (accident occurred on landing)⁽²⁾; and Continental Airlines B727-224, Stapleton Airport, August 7, 1975 (accident occurred on takeoff)⁽³⁾.

Remote ground-based sensing of wind field characteristics represents a possible solution to the wind shear hazard. Ground-based equipment has the advantage over airborne equipment of (1) providing information to general aviation aircraft for which airborne wind shear avionics may be economically unfeasible and (2) alerting the pilot prior to takeoff or prior to entry into hazardous shear (on landing) thus avoiding the hazard completely or allowing a timely go-around maneuver.

CO₂ pulse Doppler LIDAR has been recognized as a viable candidate for the remote ground based detection of wind fields. As part of the CAT system improvement studies, the application of the MSFC CAT LIDAR (and improved versions of this sensor) have been examined as possible wind shear sensors.

The studies have considered the major meteorological factors producing wind shear, methods to define and classify wind shear in terms significant from an aircraft perturbation standpoint, the significance of sensor location and scan geometry on the detection and measurement of wind shear and the tradeoffs involved in sensor performance such as range/velocity resolution, update frequency and data averaging interval. This memo summarizes the study results.

2. SHEAR PRODUCING WEATHER CONDITIONS

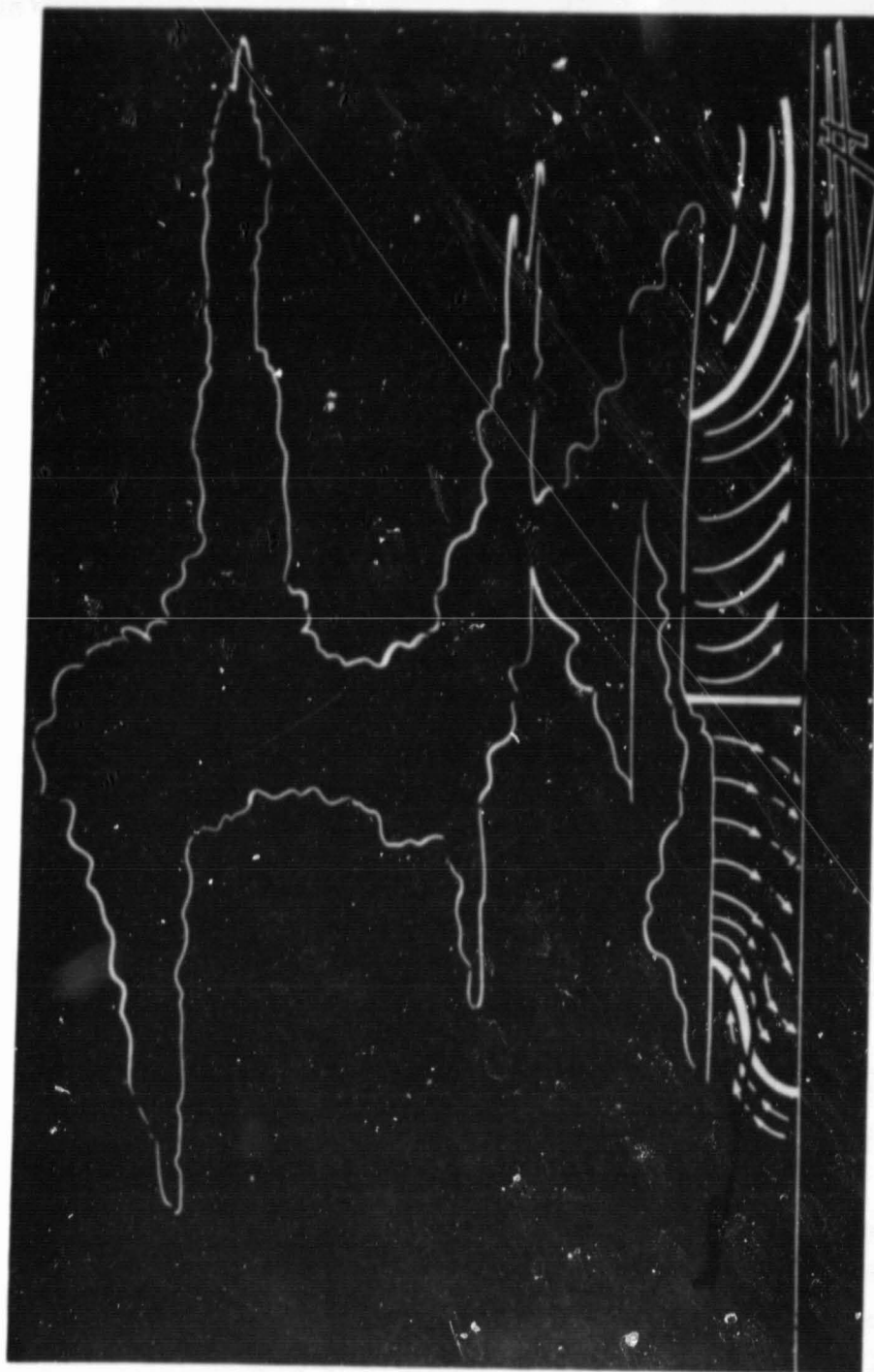
The three most significant weather phenomena causing hazardous wind shear are thunderstorms, frontal systems and low level temperature inversions. The flow fields accompanying these phenomena are characterized in Figures D-1, D-2 and D-3.

The gust front preceding a thunderstorm is characterized by high turbulence, strong updrafts and downdrafts and large shear producing windshifts. Moreover, the gust front can precede the storm itself by 10 or more miles.

Frontal systems are dangerous to aircraft when they are moving at speeds greater than 30 knots and have temperature differences across the front of 10°F or greater. Wind shifts occurring across and along the frontal surface produce wind shear. Normally the most severe shear from a cold front occurs just after frontal passage, conversely, the shear created by a warm front occurs just prior to passage of the front, (i.e., on the cooler side of the front in both cases). Warm fronts are normally much shallower in slope than cold fronts. This fact is discussed more completely in a later section, but essentially it results in warm front shears being encountered with a vertical change in position (approximate horizontal striation of the air mass) and cold front shear being encountered with a horizontal change in position (approximate vertical striation of the air mass).

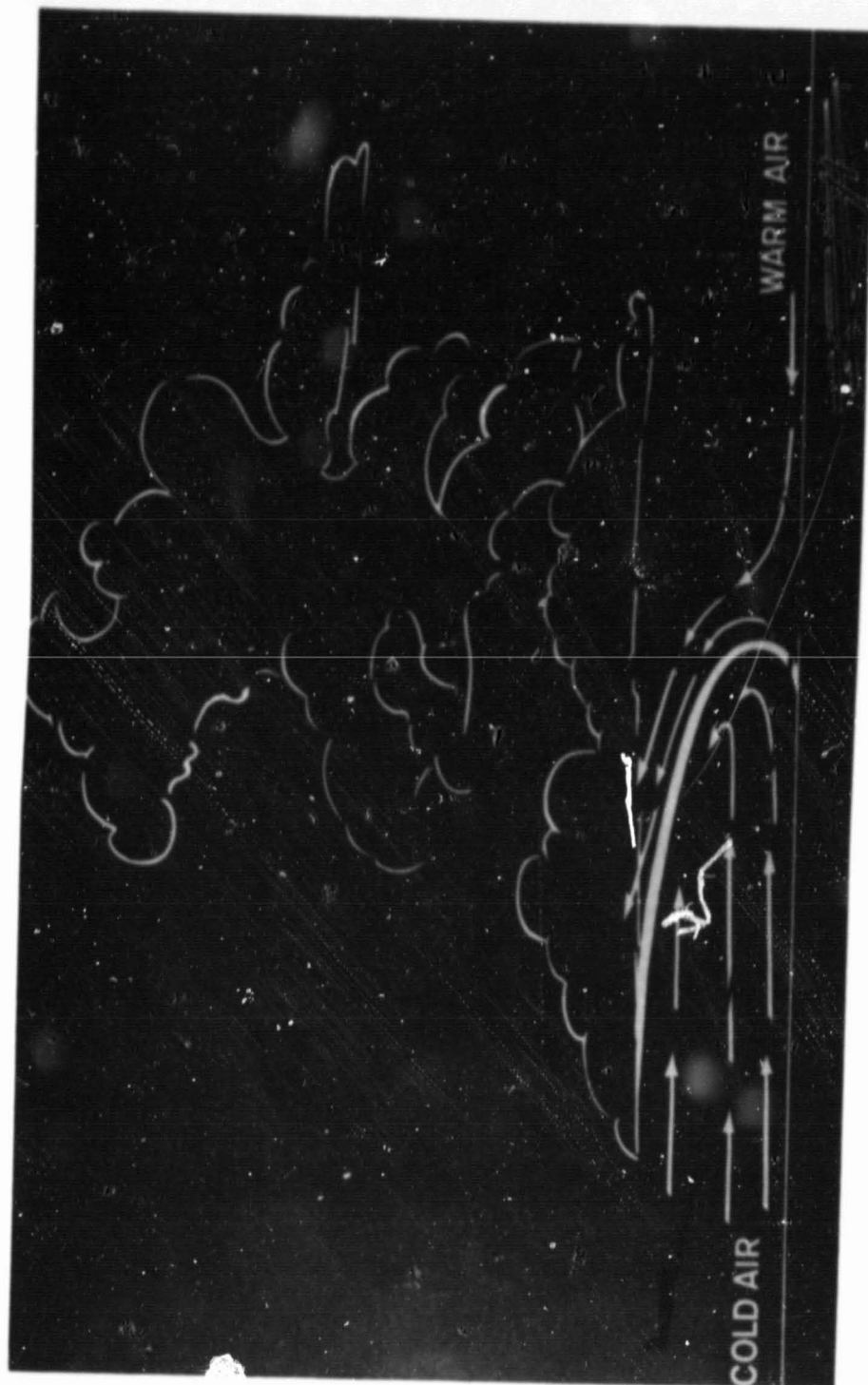
3. WIND SHEAR DEFINITION

In general, wind shear is a change in wind velocity with position or time. Since wind shear is normally measured by instrumented towers, it is commonly given as the change in horizontal wind speed occurring over some height interval. From an aircraft performance standpoint the concern is with the change in aircraft airspeed induced by changes in the wind field occurring between points on the flight path. This is true whether the aircraft is landing, flying level or climbing out as shown in Figure D-4.



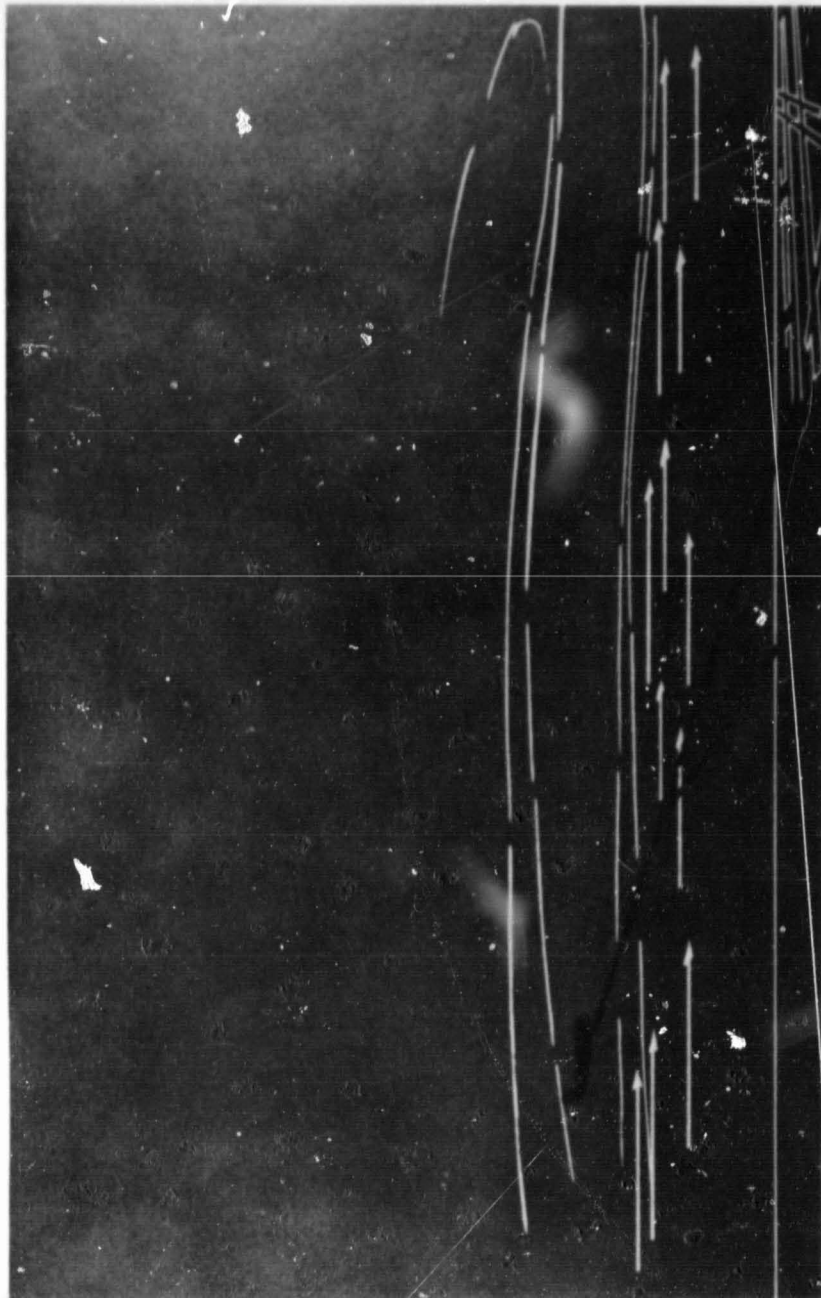
EO-583

Figure D-1. Typical Thunderstorm Threat.



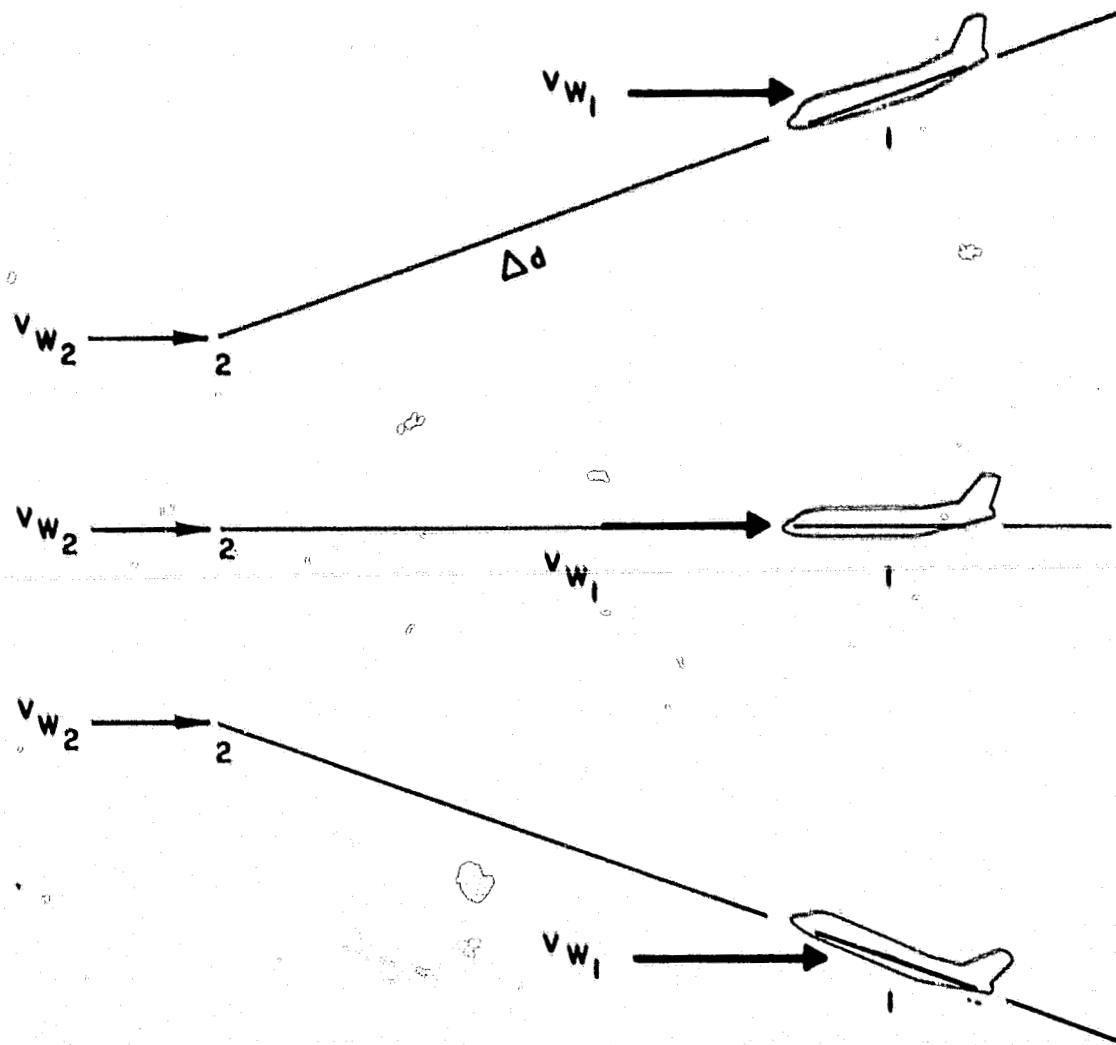
EO-584

Figure D-2. Typical Front Threat.




EO-585

Figure D-3. Typical Inversion Threat.



EOA-999

Figure D-4. Aircraft Related Shear



Compared to the component of wind along the flight path, the other components are lesser concern to the pilot since they do not directly affect airspeed. These are the cross wind component (causes lateral drift) and the vertical component (updraft/downdraft). The latter are known to be severe in conjunction with major thunderstorm activity and probably were significant in the Eastern crash at Kennedy International Airport⁽²⁾.

If we assume that the aircraft in Figure D-4 is trimmed for un-accelerated flight at point one, and is accelerated by the wind variation between points one and two; the airspeed change or wind shear between points one and two is equal to the difference between the vector wind at one and two projected along the flight path, ΔV_f . Fichtl⁽⁴⁾ gives the following expression for ΔV_f :

$$\Delta V_f = (\Delta \bar{u} + \Delta u') \sin \gamma \cos \theta + \Delta v' \sin \gamma \sin \theta + \Delta w' \cos \gamma \quad (1)$$

where

$$\Delta \bar{u} = \bar{u}(z_2) - \bar{u}(z_1)$$

$$\Delta u' = u'(x_2, y_2, z_2, t_2) - u'(x_1, y_1, z_1, t_1)$$

$$\Delta v' = v'(x_2, y_2, z_2, t_2) - v'(x_1, y_1, z_1, t_1)$$

$$\Delta w' = w'(x_2, y_2, z_2, t_2) - w'(x_1, y_1, z_1, t_1)$$

and $\bar{u}(z)$ = the mean wind speed at height (z)
 u', v', w' are the x, y, z components of the turbulent velocity vector.

Equation (1) is the total wind change between points one and two along the aircraft's flight path. As previously mentioned, wind shear is normally expressed as the change in horizontal wind between two different heights; in the aircraft case (where the aircraft can be flying level, climbing or descending) a more suitable measure is the wind change, ΔV_f , divided by either the time of flight between points one and two or the distance along the flight path between points one and two (Δd) as shown on Figure D-4. In the former case, the wind shear would be the wind change (or airspeed change induced by the wind) expected per unit time, while in the latter case, the shear would be the wind change per unit distance along the flight path.

$$\begin{aligned} (WS)_t &= \frac{\Delta V_f}{(t_2 - t_1)} \\ (WS)_d &= \frac{\Delta V_f}{(d_2 - d_1)} \end{aligned} \quad (2)$$

For convenience of reporting, shears could be referenced to some convenient value of time or distance, e.g., 1 min. or 1000 meters,

$$\begin{aligned} (\overline{WS})_t &= \left(\frac{\Delta V_f}{(t_2 - t_1)} \right) \cdot 60 \text{ sec} \\ (\overline{WS})_d &= \left(\frac{\Delta V_f}{(d_2 - d_1)} \right) \cdot 1000 \text{ m} \end{aligned} \quad (3)$$

Equations (3) are suggested as appropriate indices for expressing wind shear magnitudes. They are particularly well suited to being measured by glide slope scanning sensors.

The above wind shear indices are compared with the ICAO standard wind shear categories in Table D-1, for an aircraft landing along a

three degree glide slope at 125 kts (64.4m/sec). The ICAO wind shear categories are related to the variation of the horizontal wind (m/sec) in a 30 meter height interval.

TABLE D-1
INDICES FOR WIND SHEAR SEVERITY

ICAO Category	Wind Shear Parameter		
	Height Related m/sec/30m alt.	Aircraft Related $(WS)_t$, m/sec/60 sec	$(WS)_d$, m/sec/1000 m range
Light	0 - 2.5	0 - 16.9	0 - 4.4
Moderate	2.5 - 4.5	16.9 - 30.4	4.4 - 7.9
Strong	4.5 - 6.0	30.4 - 40.6	7.9 - 10.5
Severe	>6.0	>40.6	>10.5

Describing shear in terms of the wind change that occurs over some distance along the flight path or over some elapsed time appears more suitable than using the ICAO standard approach. The shear so described relates directly to aircraft performance changes and is readily obtained from the output of a glide slope or quasi glide slope sensor. The method is not as compatible with vertical probe (VAD) type sensors, that generate information similar to tower data. The glide path indices can be computed from vertical probe data provided horizontal homogeneity of the wind field is assumed.

4. AIRCRAFT PERTURBATIONS DUE TO SHEAR

In order to assess aircraft glide slope excursions due to wind shear without resorting to numerical integration of the aircraft equations of motion a simplified model for computing these excursions was derived.

The algorithm, which gives reasonable predictions for short duration flight (10-15 sec maximum) in uniform shear, assumes that

the headwind/tailwind varies linearly over some altitude or equivalent glide slope distance.

The perturbations are computed along (s) and normal (n) to the glide slope as shown in Figure D-5. The aircraft is flying at a velocity of V_{ac} and is assumed to be trimmed for unaccelerated flight along the glide slope. The perturbational acceleration (\ddot{n}) in a direction normal to the glide slope experienced by an aircraft in wind shear relative to an aircraft experiencing zero shear is given by:

$$\ddot{n} = \left(\frac{g}{w} \right) \frac{1}{2} C_L \rho S \left(V_{a\text{SHEAR}}^2 - V_{a\text{NO SHEAR}}^2 \right) \quad (4)$$

where g = the gravitational acceleration

w = the aircraft weight

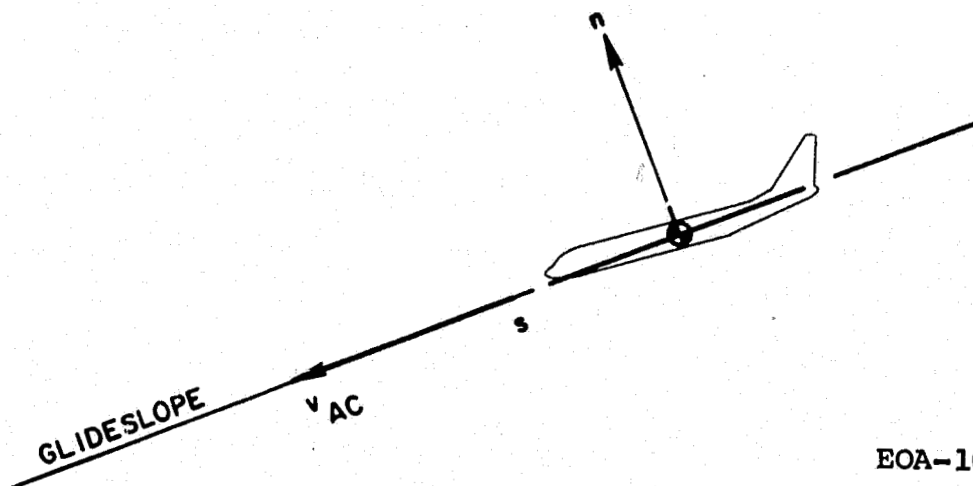
C_L = the aircraft lift coefficient

ρ = the atmospheric density

S = the aircraft reference area

$V_{a\text{SHEAR}}$ = the aircraft airspeed in a wind shear environment

$V_{a\text{NO SHEAR}}$ = the aircraft airspeed in a zero wind shear environment



EOA-1000

Figure D-5. Perturbation Model Geometry

In a wind shear that varies linearly with altitude or distance along a shallow glide slope (typically -3°), the aircraft airspeed variation can be written:

$$V_{aS} = V_{aNS} - \dot{V}_w t \quad (5)$$

where \dot{V}_w is the rate of change of tailwind speed with time (dV_w/dt)

Substituting Equation 5 into 4 and simplifying

$$\ddot{n} = g \left(\frac{L}{W} \right) \left[-2 \frac{\dot{V}_w}{V_{aNS}} t + \left(\frac{\dot{V}_w}{V_{aNS}} t \right)^2 \right] \quad (6)$$

integrating

$$n = g \left(\frac{L}{W} \right) \left[-\frac{1}{3} \left(\frac{\dot{V}_w}{V_{aNS}} \right) t^3 + \frac{1}{12} \left(\frac{\dot{V}_w}{V_{aNS}} \right)^2 t^4 \right] \quad (7)$$

For an aircraft trimmed for landing $L/W \approx 1$ and since the second term in brackets is \ll the first term, Equation (7) can be simplified to

$$n = g \left[-\frac{1}{3} \left(\frac{\dot{V}_w}{V_{aNS}} \right) t^3 \right] \quad (8)$$

Furthermore, since $\dot{V}_w = \frac{dV_w}{dt} = \frac{dV_w}{ds} \cdot \frac{ds}{dt}$, and

$$\frac{ds}{dt} \approx V_{aNS}$$

$$\dot{V}_w = \frac{dV_w}{ds} \cdot V_{aNS} \approx \frac{\Delta V_w}{\Delta s} \cdot V_{aNS} \quad (9)$$

Substituting Equation (9) into (8)

$$n = g \left[-\frac{1}{3} \left(\frac{\Delta V_w}{\Delta s} \right) t^3 \right], \quad t < 10-15 \text{ sec} \quad (10)$$

Equation (10) is an approximate expression for the short term departure of an aircraft above or below the glide slope, for a linear change in tailwind, expressed as the change in tailwind (ΔV_w) over some distance (Δs) along the glide slope. For the sign convention assumed, ΔV_w is positive for an increase in tailwind (decrease in headwind) and vice versa. Equation (10) has been used for assessing critical glide slope departures due to shear.

5. CO₂ DOPPLER LIDAR DEPLOYMENT ALTERNATIVES

CO₂ Doppler LIDAR systems for use at airports for wind shear detection can be sub-divided into short and long range applications. Short range applications include the operation of CW Doppler LIDAR in a VAD mode. For long range applications pulse-Doppler systems are applicable. Pulsed Doppler LIDARS (of primary concern in this memo) can be further sub-divided into glide slope or quasi glide slope wind scanning systems and central airport wind shear surveillance systems. A surveillance sensor would present data similar to a weather radar, but presenting wind Doppler information. Shear surveillance data would be obtained by scanning continuously in azimuth or over a selected azimuth sector at a shallow elevation angle.

6. SYSTEM MEASUREMENT TRADEOFFS

Involved in the design of a wind shear system are questions concerned with data averaging and (for pulsed systems) the choice of a pulse length which gives a reasonable compromise between system velocity and range resolution.

A hypothetical glide slope wind measuring system might consist of an array of anemometers mounted on towers spaced evenly along the aircraft flight path. Neglecting for the moment the impracticality of such a system, data collected from the anemometers would represent

an average based upon some time interval. The time interval would be chosen as long as possible in the interest of smoothing noise, but not so long as to disguise the minimum size wind variations of interest. Also, the anemometer spacing would be chosen to include wind variation wavelengths that significantly affect the aircraft flight path.

The tradeoffs for a LIDAR system scanning the glide slope are concerned with similar questions, choices of data integration and averaging intervals as well as velocity and range resolution. A LIDAR system looking up the glide slope would be required to resolve shear gusts (changes in wind along the aircraft path) that result in significant aircraft departures from the glide slope.

Although incomplete at this time, some data does exist on the history of maximum wind shears observed at particular stations. Page 319 of Reference 5 contains applicable data including the effects of averaging interval on the maximum recorded shear. This data presented in Figure D-6 was assumed to be typical of what might be observed at an airport.

For each interval, the average shear listed can be interpreted as the maximum average shear over the interval. The product of this maximum average shear and the averaging interval (Δt), $\left(\frac{dv_w}{dh}\right) \Delta t$, can be considered the maximum wind shear "gust impulse" that an aircraft would experience in that time interval.

This data can be easily converted to the expected air speed change if a homogeneous atmosphere is assumed and the glide slope and aircraft speed are known. Furthermore, through the simplified equation for predicting aircraft perturbations in shear (Equation 10) the maximum aircraft glide slope departure as a function of averaging interval can be determined. A minimum significant averaging interval can then be defined.

Figure D-7 presents the maximum glide slope departure (from Equation 10), obtained as a function of averaging interval for the worst shear data of Figure D-6.

An allowable aircraft glide slope departure was assumed to be a 1/2 scale deflection of the glide slope needle at a distance from touchdown of 1/2 nmi. This corresponds to a 19 ft. glide slope departure

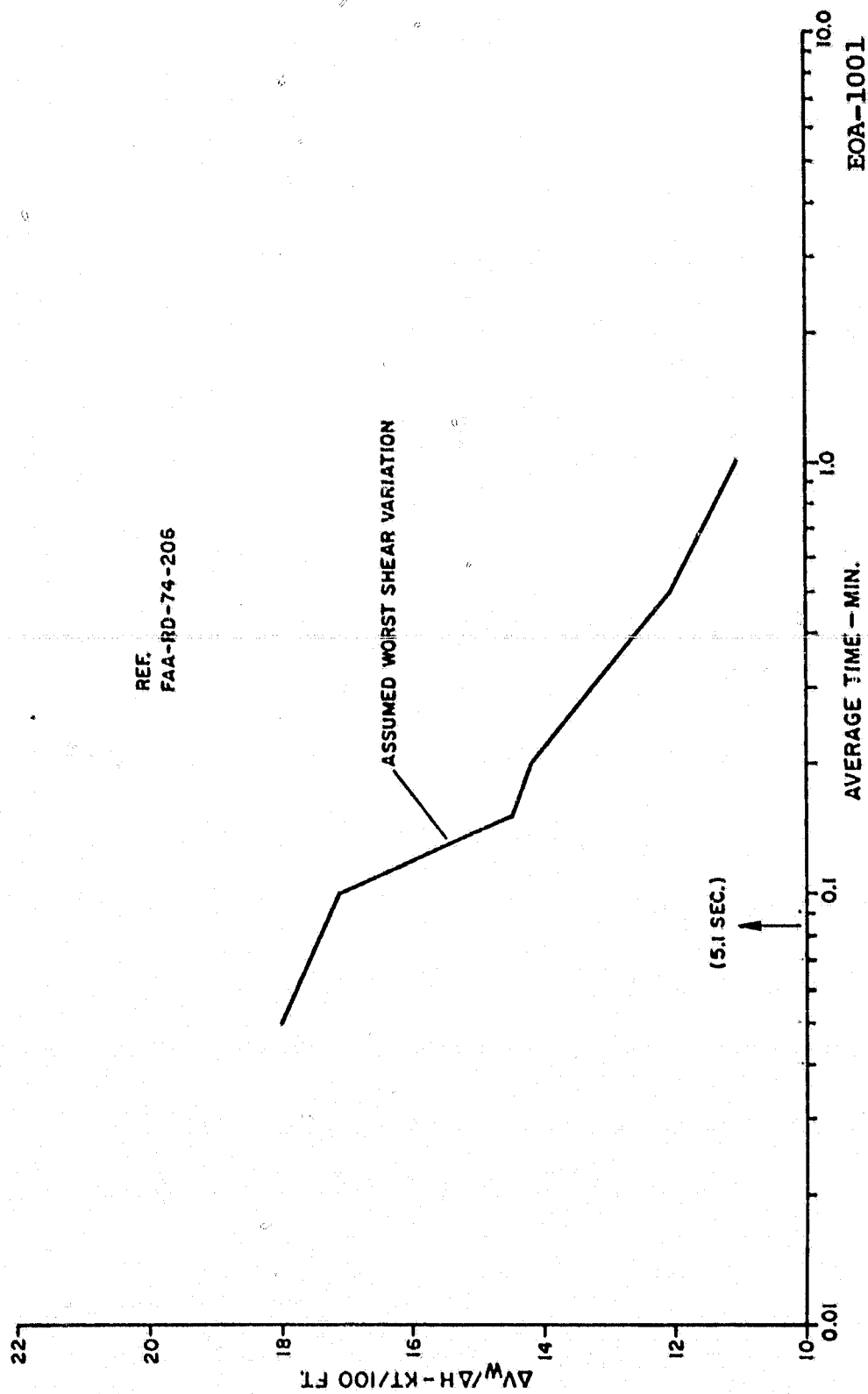
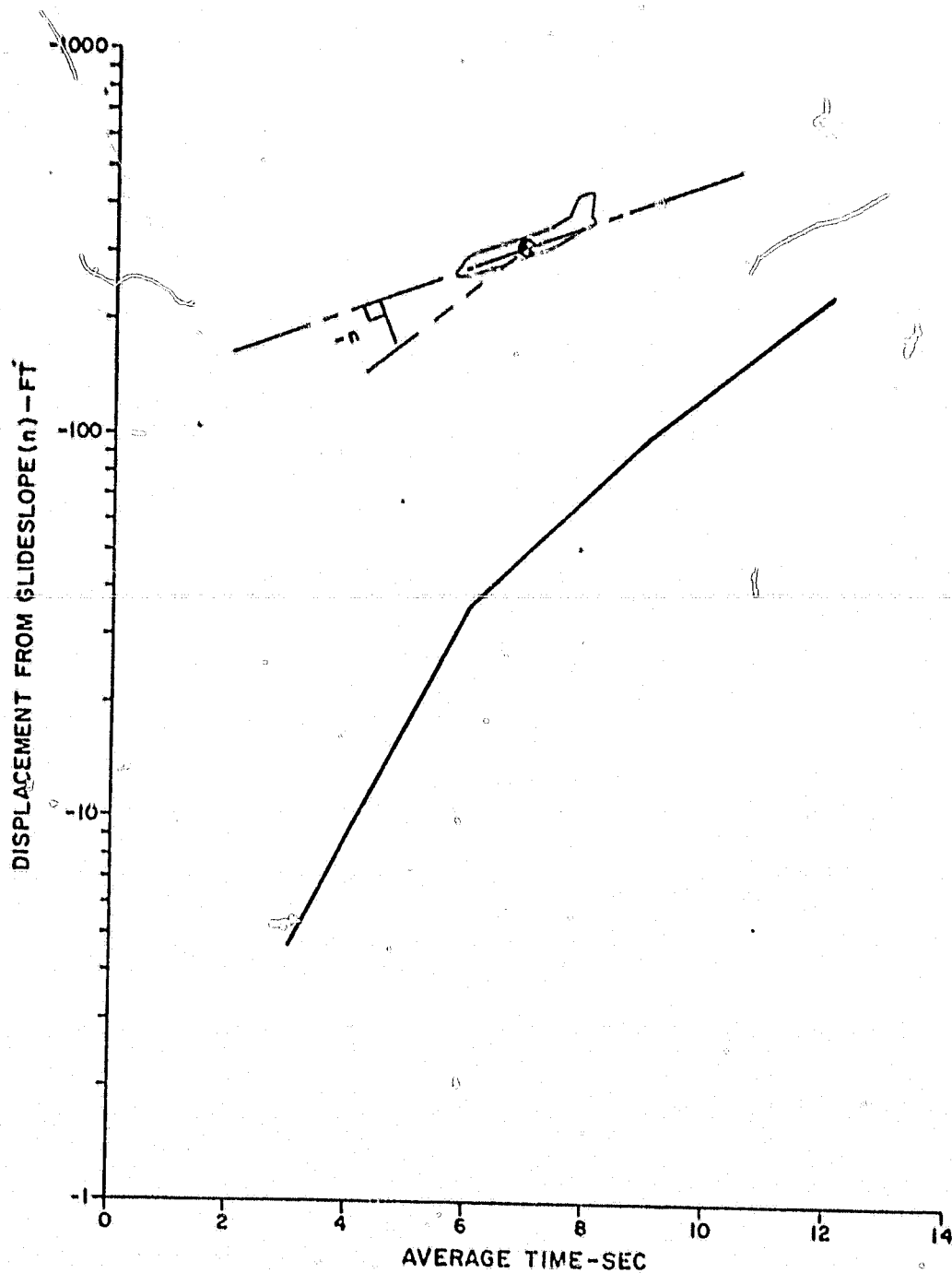


Figure D-6. Maximum Shear vs. Averaging Time



EOA-1002

Figure D-7. Maximum Glide Slope Departure vs. Averaging Time

or an averaging time of 5.1 seconds based on the data of Figure D-7. This means that, if an aircraft flying at 125 knots encounters the maximum average shear measured in the data of Figure D-6 for a 5.1 second interval, a glide slope departure of 19.1 feet will occur. If the data are averaged over an interval greater than 5.1 seconds, wind changes will be excluded that can produce departures of greater than 19 feet. If data are averaged over an interval less than 5.1 seconds, wind changes will be measured to a resolution greater than the assumptions require.

In 5.1 seconds at 125 knots, an aircraft will travel 328 meters. From Figure D-6, the sensor must be capable of resolving a shear of 17.4 ft/sec/100 ft (altitude). Along a glide slope inclined at 3 degrees, this amounts to a wind shear of 3 m/sec in 328 meters (9.1 m/sec/1000 meters).

At the CO₂ wavelength, a 2 μ sec pulse length corresponds to a range resolution of 300 m and a velocity resolution of 2.65 m/sec. Therefore, a pulse Doppler LIDAR (including the present CAT system) operating at a pulse length of 2 μ sec is reasonably compatible with the required resolution requirements. Processing to improve velocity resolution over the unprocessed 2.65 m/sec value would be desirable to improve accuracy. Using a system with a shorter pulse and matched filters would result in reduced signal-to-noise ratios as a result of the smaller sample volume. It is desirable to utilize the longest pulse consistent with the laser technology and the resolution desired. It happens in this application that the technology and the system requirements resolution coincide at approximately 2 μ sec.

To summarize, a preliminary analysis has shown that a CO₂ pulse Doppler LIDAR operating in a glide slope mode must be capable of resolving wind gust impulses of approximately 3 m/sec over a range cell of 300 meters in order to detect wind changes causing glide slope departures equivalent to a 1/2 scale deflection of the glide slope instrument at a distance 1/2 nmi from touchdown. Data may be averaged for up to 5 seconds and still identify wind shear gusts to the required resolution.

No attempt was made to examine the processing required to extract the change in wind or Doppler velocity within a resolution cell. One

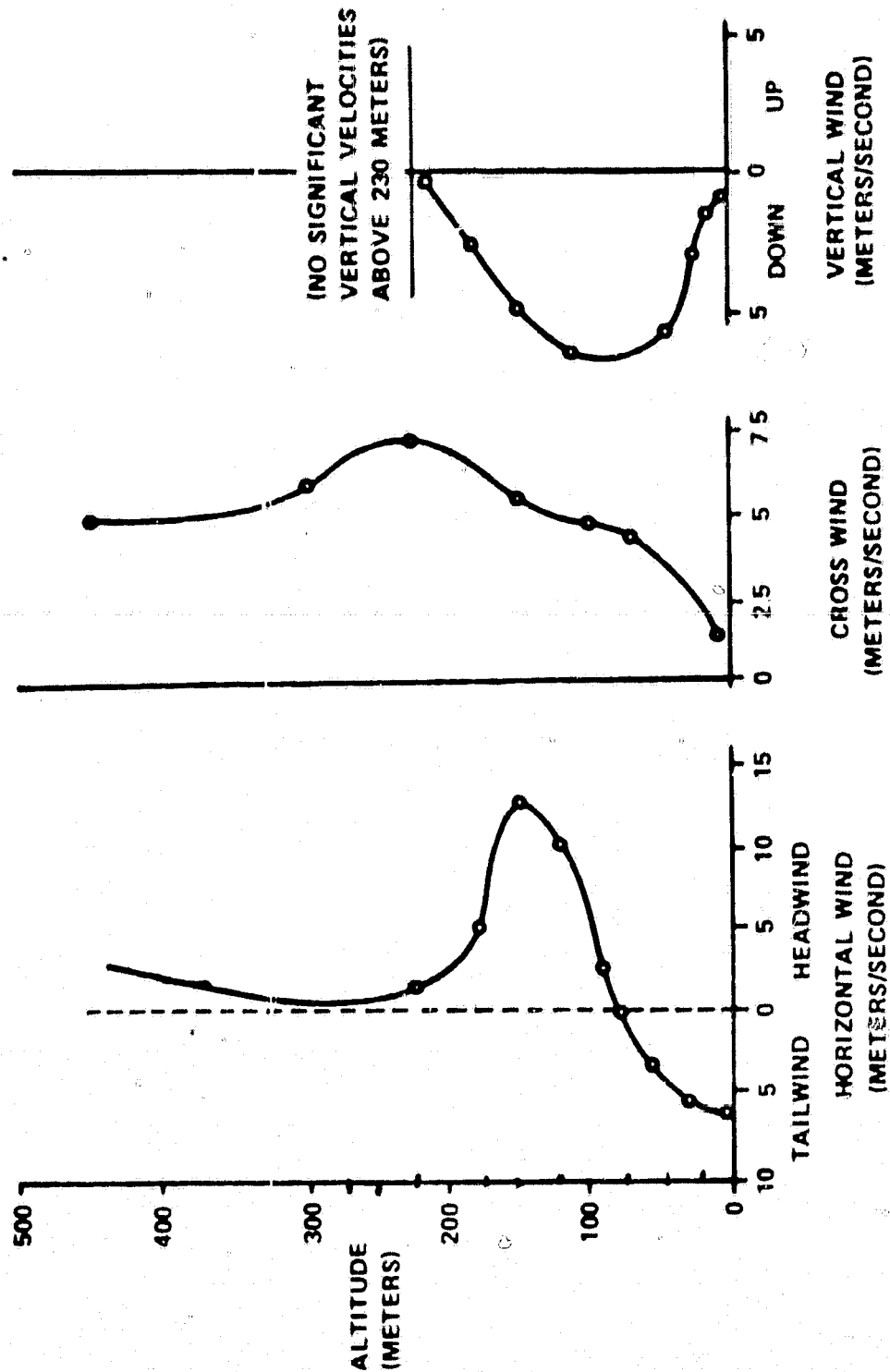
method would be to difference the mean Doppler from adjacent resolution cells. Likewise, within a resolution cell, it may be possible to extract the change in Doppler based on knowledge of the mean and higher data moments.

Useful information concerning the applications and requirements for a CO₂ pulse Doppler LIDAR wind shear sensor can be obtained if the Doppler returns from realistic wind fields are examined as a function of system parameters such as sensor location, scan geometry, scan update interval, etc.

To provide this insight, the returns measured by a sensor situated at the touchdown location and looking up the glide slope, as well as a sensor displaced from this location, but still looking in the general glide slope direction have been examined.

Two wind fields were selected. The first, shown in Figure D-8, is representative of the thunderstorm gust front outflow model used by the FAA in studies of aircraft perturbations due to shear. This wind field is horizontally homogeneous and stationary and, therefore, the wind characteristics are independent of horizontal position (x,y) and time and vary only with altitude (z). As pointed out by Fichtl⁽⁴⁾ these conditions are rarely realized in the atmospheric boundary layer because of significant variations in surface roughness and heat-transfer properties in the horizontal.

The second model wind field was selected from Reference (6) and represents the actual wind field measured in a plane defined by an instrumented tower and the mean wind velocity during the passage of a thunderstorm front. The temporal variation of the three components of wind measured at several heights along the tower were recorded and smoothed to produce two-dimensional contour plots of the 3-components of velocity, temperature and the streamline geometry. The temporal data was converted to spatial data using Taylor's hypothesis. This wind field data (case G of the reference) are shown in Figure D-9.



EOA-1003

Figure 2-8. Thunderstorm Cold Air Outflow (Gust Front)

1 KM



EOA-1004

D-20

The two model wind fields represented in Figures D-8 and D-9 were used to analyze the Doppler velocity measured along the sensor line-of-sight (LOS) as it was directed up the glide slope, and also as the LOS was directed in the general glide slope direction, but with the sensor displaced from the touchdown location in the down runway direction. Doppler data were also examined for both sensor locations when the beam was scanned laterally (windfield of Figure D-8 only). For simplicity, the sensor was kept aligned with the runway centerline in all cases. The effects of laterally offsetting the sensor from the runway centerline by an amount meeting FAA installation standards are expected to be small.

Figure D-10 was developed from the data of Figure D-9 assuming a glide slope angle of 3 degrees and an aircraft speed of 125 knots. The figure compares the Doppler experienced by the aircraft as it flies down the glide slope (heavy curve) with that measured by a glideslope sensor located at the touchdown point and directed up the glide slope. The four lighter curves represent the Doppler observed by the sensor at zero time when the aircraft is at a distance of 7.5 kilometers from touchdown and at times of 1, 2 and 3 minutes.

For the gust front examined, the tailwind observed by the aircraft begins at a distance of 7500 m with a value of approximately 18 m/sec, increases slightly at first to a value of 22 m/sec before dropping sharply to a tailwind of 4 m/sec at touchdown. This variation in tailwind causes an initial drop below the glide slope, followed by an increase in airspeed (decrease in tailwind) causing a performance increase or a rise above the glide slope.

The magnitude of the shear experienced is shown by the slope of the shear magnitude scale in the lower right hand portion of the figure. As shown, the performance increasing change in tailwind would be classified as a severe shear by ICAO standards and would obviously precipitate a go-around maneuver.

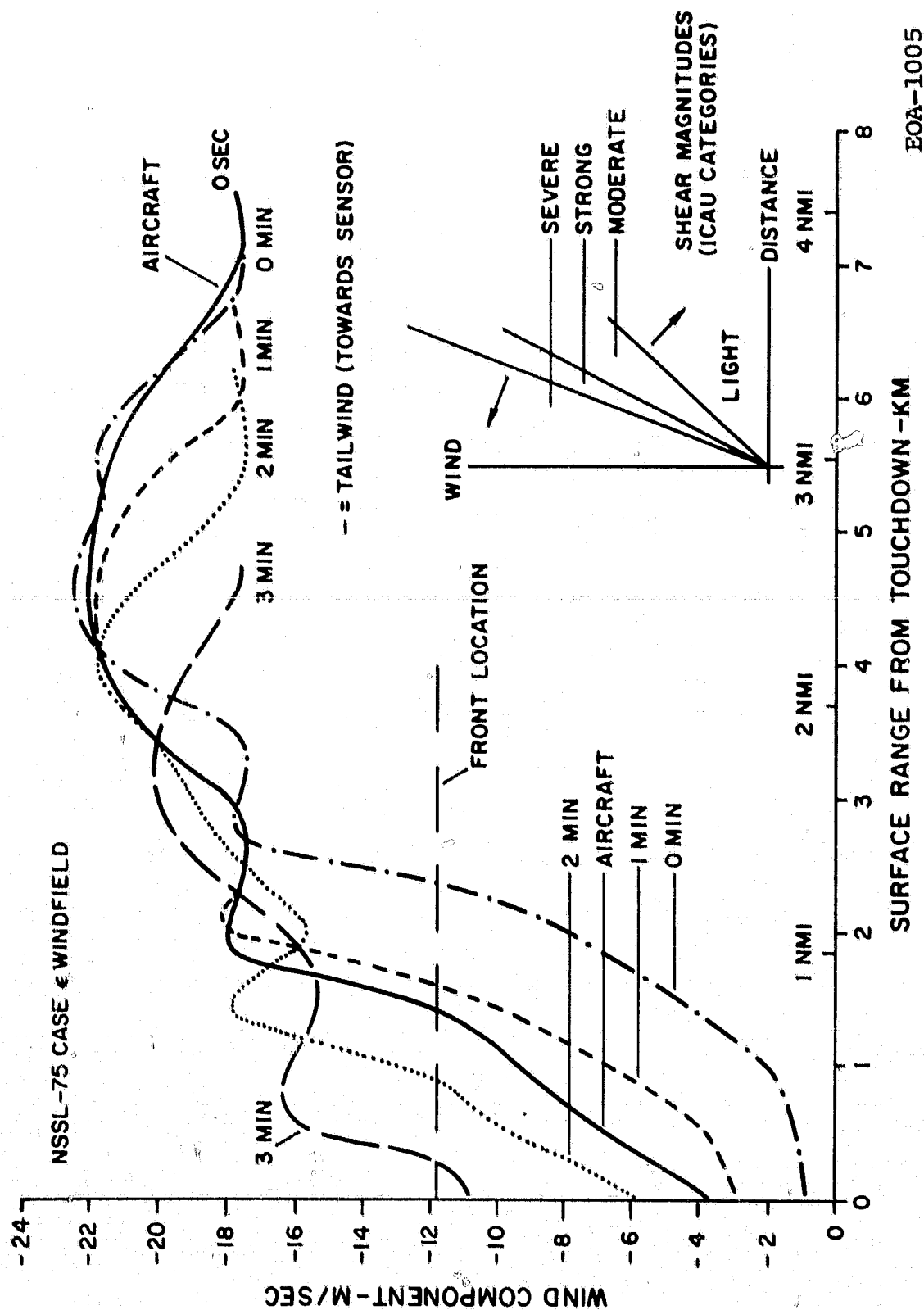


Figure D-10. Comparison of Aircraft Experienced Wind and Glide Slope Sensor Measurements

The front in this particular case is moving at a speed of 11.8 m/sec past the sensor. The aircraft time of flight from a range of 7500 m to touchdown is 113 seconds. At zero time, the Doppler observed by the glide slope sensor matches the aircraft Doppler for the first few thousand meters beginning at zero flight time. Similarly, at 1 minute the sensor observed Doppler is similar to the aircraft experienced Doppler near touchdown. At 2 minutes, the front is beginning to move past the sensor; and at 3 minutes, the sharp wind change associated with the front has moved past the sensor.

Several points can be made based on the data of Figure D-10. First, a glide slope sensor with zero minimum range capability adequately predicts the airspeed changes experienced by an aircraft flying the same slope in spite of temporal differences. Secondly, a surveillance sensor scanning 360° in azimuth and updating on the order of once each minute would adequately track this particular front (frontal speed 11.8 m/sec) as it moved through the airport area.

Because of the finite minimum range time of the CAT and other CO_2 pulse Doppler LIDARS (approximately 15 μs for CAT), the second situation examined assumed the sensor to be displaced down the runway by a distance of 2000 meters. The data for this case are shown in Figure D-11.

The sensor LOS was directed to pass through the aircraft glide slope at a point immediately above the middle marker as shown in the sketch in the lower right hand corner of the figure. Note that range is referenced to the touchdown location. Again, the sensor adequately predicts the airspeed changes along the glide slope. It should be observed that one reason the wind field is adequately measured by the displaced sensor is that the wind field is vertically striated (see lower curve of Figure D-9). For a horizontally striated wind field, as represented by the wind field of Figure D-8, this is not true.

The horizontally homogeneous wind field depicted in Figure D-8 was used to examine the Doppler characteristics measured by a glide slope sensor located at touchdown and also displaced from touchdown as the beam was scanned in azimuth. A significant difference between this wind field and that discussed earlier is that it is horizontally homogeneous and therefore is striated in horizontal layers not dissimilar to what might be expected from a thermal inversion and the shallow slope of a warm front. (Note in Figure D-8 the bulge in horizontal wind at the 150 meter altitude region.) This characteristic of the wind field causes significant changes in the measured Doppler as the sensor location is displaced.

Figure D-12 depicts the Doppler wind field obtained when the LIDAR beam is scanned at an elevation of 3 degrees between ± 45 degrees in azimuth for a sensor at touchdown.

Figure D-13 presents the same information for a sensor displaced from the touchdown location by 1524 meters in the down runway direction, and as indicated on the figure, scanned through a point on the glide slope directly above the middle marker. For compatibility with Figure D-12, the sensor offset from touchdown (approximately 1524 m) was subtracted from the range magnitude and the range of azimuth angles was varied to encompass approximately the same physical area as depicted in Figure D-12.

Comparing the two figures, the effects of the horizontally striated wind field causes the peak wind Doppler contour (12 m/sec) to occur at different ranges and to be stretched in range. If the atmosphere were truly homogeneous, this distortion could be processed out. As previously mentioned, in the atmospheric boundary layer, this is not often a correct assumption.

The difference between the two scans in terms of the wind Doppler they predict for an aircraft flying down the glide slope is shown in Figure D-14. It is seen that the displaced sensor erroneously predicts the Doppler onset rate. This particular wind field, truly horizontally homogeneous, would be easily sensed by a conically scanned VAD type LIDAR system.

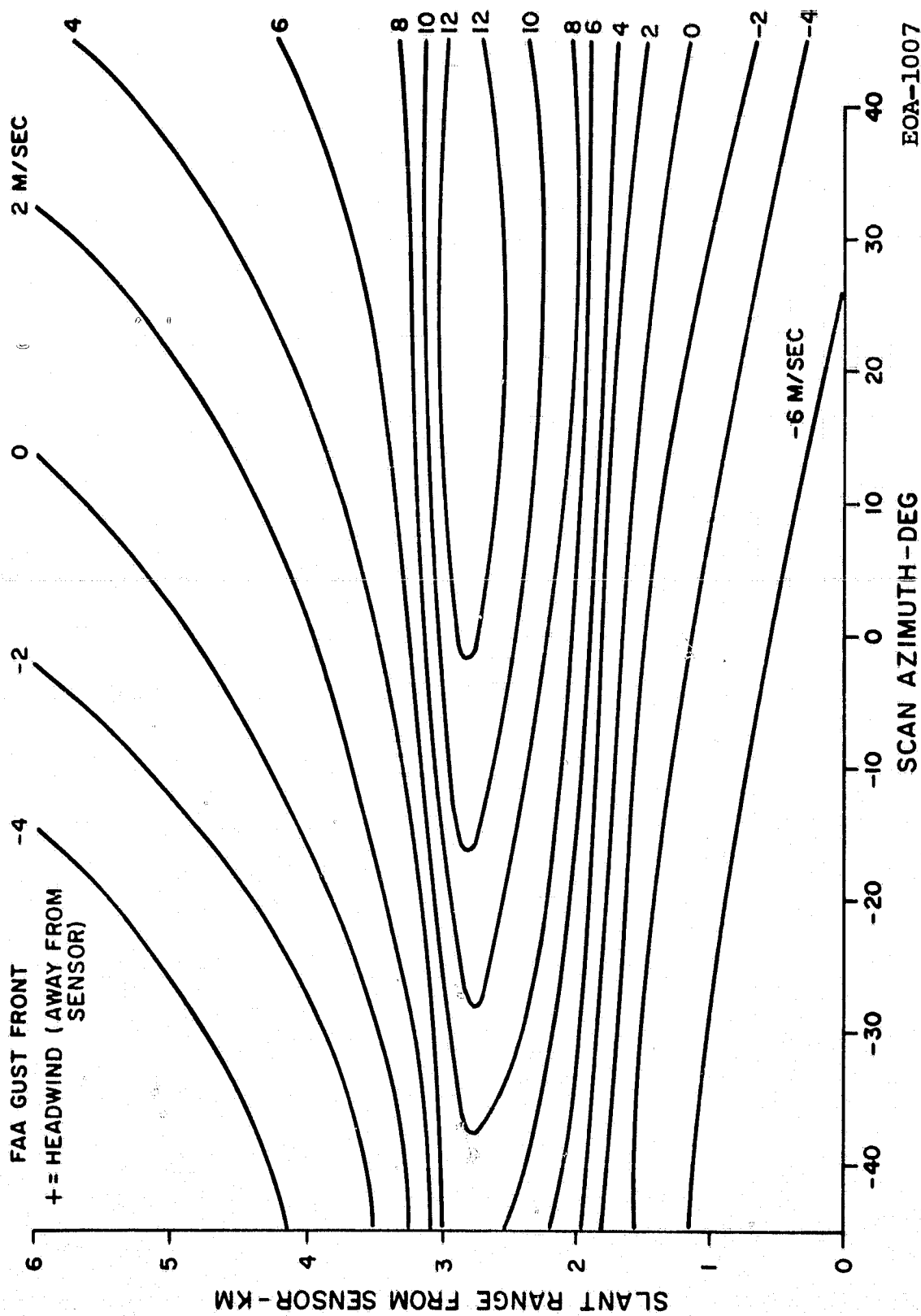


Figure D-12. Doppler Wind Field Sensed by Azimuth Scanning Touchdown Sensor

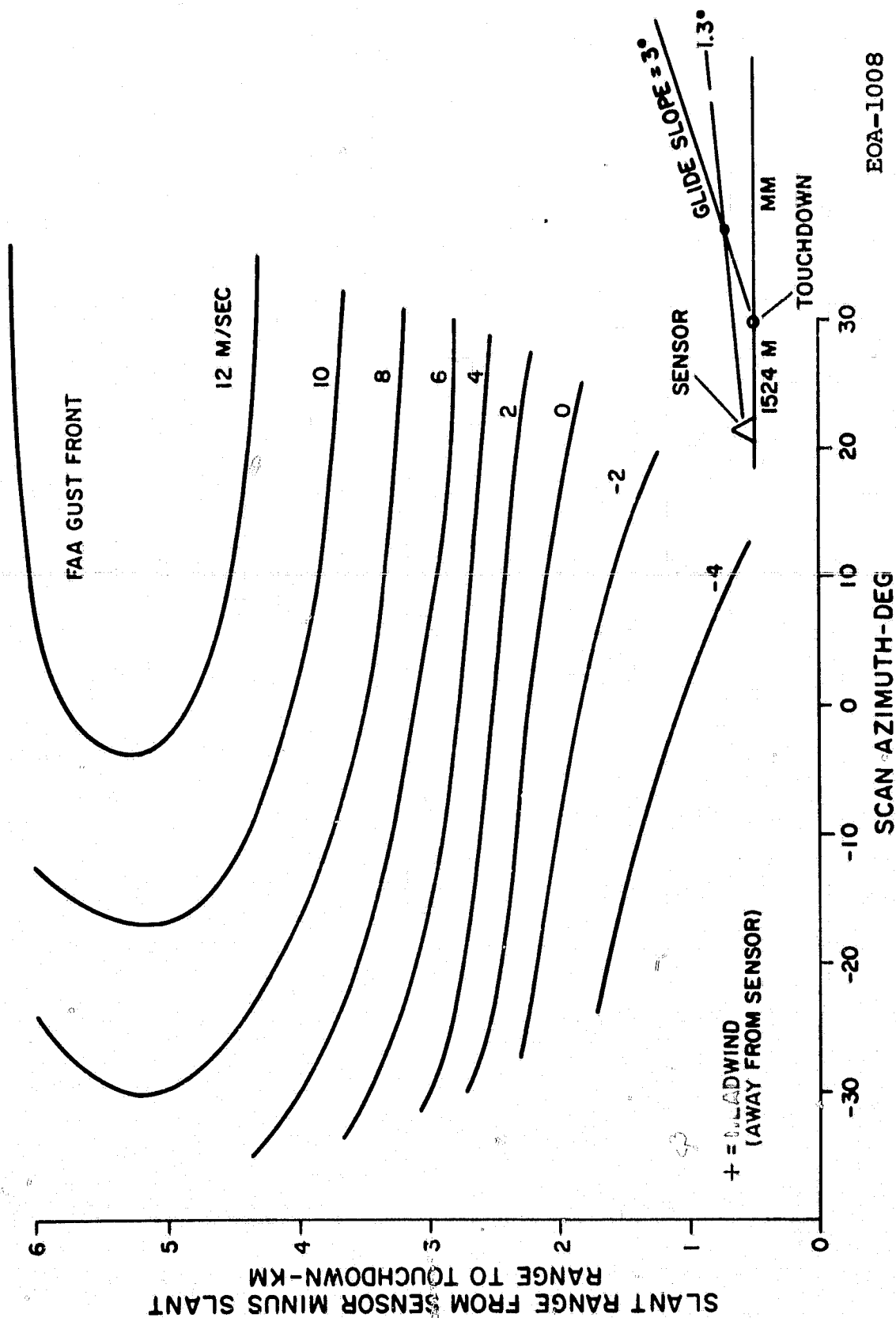


Figure D-13. Doppler Wind Field Sensed by Azimuth Scanning Displaced Sensor

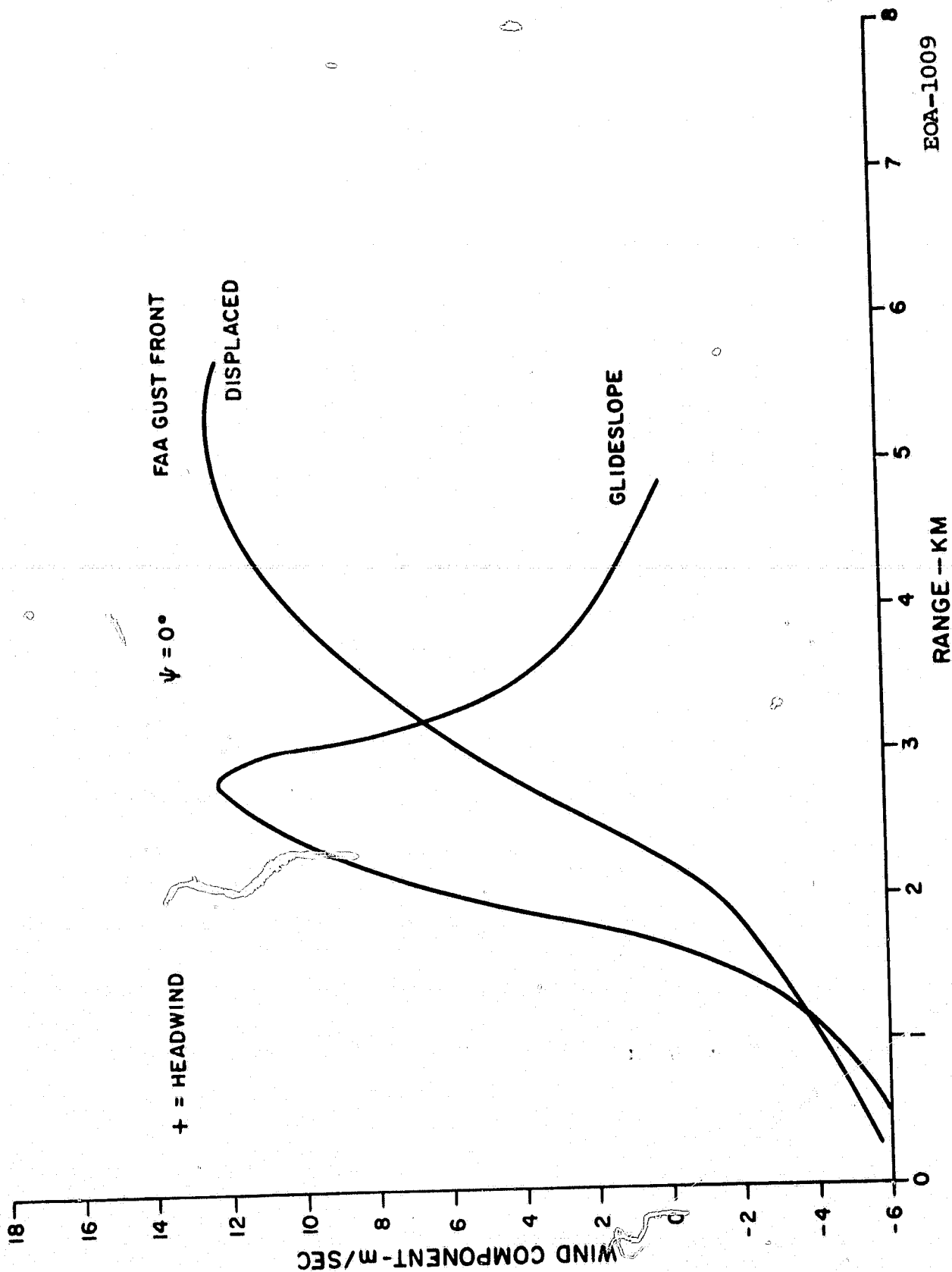


Figure D-14. Doppler Wind Prediction of Two Sensors

The possibility of utilizing an adaptive glideslope sensor consisting of a system normally directed up the glideslope, but periodically scanned in azimuth was also examined. The primary mission of the adaptive system would be to provide detail wind-shear information along the approach path but a secondary capability of warning of the approach of frontal systems from the side would also be provided.

The adaptive glideslope system would be located just off the runway at the runway midpoint. At this location both ends of the runway could be scanned depending on the direction of use. The nominal scan elevation angle would be directed to intersect the glideslope at some nominal range similar to the sketch shown on Figure D-13.

The feasibility of an adaptive system depends upon the ability to collect lateral information while performing the main function of tracking the expected air speed changes along the approach path.

A typical scan history might provide a duty cycle of 80 percent, i.e. 80 percent of the time would be spent performing the primary mission of providing glideslope data and 20 percent would be spent in providing lateral (approaching windfield) information. During the lateral mode a uniform azimuth scan rate at a fixed elevation angle (perhaps the same angle as in the glideslope mode) would be utilized.

Figure D-15 presents the maximum angular scan rate possible as a function of range for 12 inch and 18 inch aperture LIDARS based on lag angle considerations. The maximum scan rate for a 12 inch aperture system is 25 deg/sec for a 10 kilometer range and 12.5 deg/sec for a 20 kilometer range. The time required to scan 360 degrees in azimuth is 14.4 seconds (10 km system). With an 80 percent duty cycle this amounts to 57.6 seconds for tracking along the

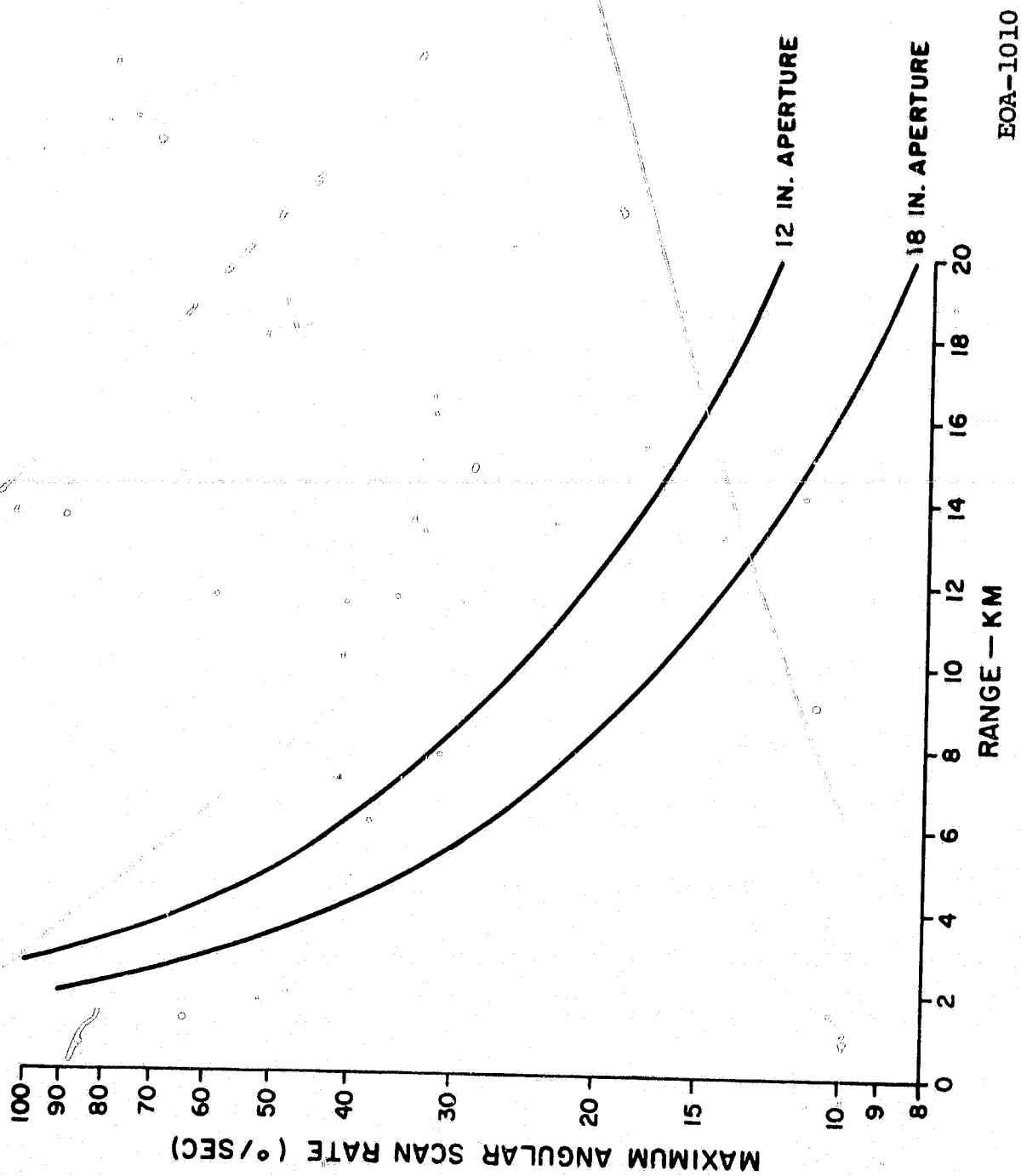


Figure D-15. Maximum Scan Rates Limited by Lag Angle Losses (3 dB)

glideslope followed by a 14.4 second azimuth scan or a total time of 72 seconds. For a 20 km system, a total of 144 seconds is required with 28.8 being used for the azimuth scan. Table D-2 lists the separation of sample points for various PRF values.

TABLE D-2
SAMPLE SEPARATIONS FOR AZIMUTHAL SCAN

<u>PRF</u>	<u>Angular Separation (mrad)</u>		<u>Linear Separation (m)</u>	
	10 km	20 km	10 km	20 km
200	2.3	4.6	23	92
100	4.7	9.4	47	188
50	9.3	18.6	93	372
20	23.3	46.6	233	932
10	46.6	93.2	466	1864

In order to predict the time of arrival of windshifts, frontal systems must be tracked as they approach. This requires at least three and preferably four looks at the frontal system during approach. Table D-3 summarizes the number of looks possible as a function of the cross runway approach speed of the storm. Note that the number of looks is independent of the sensor range due to a corresponding change in cycle time and maximum scan rate.

TABLE D-3
NUMBER OF STORM OBSERVATIONS

<u>Storm Approach Speed</u> (MPH)	<u>Number of Looks (Scan Cycles)</u>
10	30
20	15
30	10
40	7
60	5

Table D-3 shows that, even for storms that approach at high speed, the number of looks is adequate to track the storm during approach.

The drawback to the adaptive scan system is that it causes periodic interrupts to the wind shear data along the approach path. Based on the data of Figures D-7 and D-8 which show the Doppler windfield changes as a function of time and the previous analysis concerning lateral storm transport, the Doppler wind speed versus range measured by the sensor is not expected to vary considerably during the 14.4 seconds spent performing the azimuth scan (10 km range case).

The adaptive scan system appears to be a reasonable approach to providing coverage to both ends of a runway while simultaneously providing warning of frontal wind shifts approaching from across runway direction. A system with a maximum range capability of 10 kilometers provides an adequate number of looks for frontal systems approaching even at high speeds. Other than providing improvement in velocity resolution, pulse repetition frequency increases from 20 Hz to 200 Hz are not expected to affect the results indicated.

CONCLUSIONS

A study of the application of a CAT type CO₂ pulse Doppler LIDAR as a wind shear sensor has been examined. The study has shown that the resolution characteristics of such a sensor operating at a pulse length of 2 μ s are reasonably compatible with the minimum wind shear gust measuring requirements predicted by available data. Such a sensor could be applied to general wind field Doppler surveillance by locating the sensor at the airport center and scanning in azimuth out to maximum range. Adequate update capability is available with a 12" aperture system. At a maximum range of 10 km the system can update every 14 seconds, thus allowing the tracking of wind shear storms through the airport area.

Other deployment alternatives include providing glide slope wind Doppler information. In this case, the present CAT sensor must be displaced from the touchdown location by the minimum range capability of the system (approximately 2250 meters). Data from such a system would be in excellent agreement with actual aircraft experienced Doppler provided the wind field is vertically striated. In a horizontally striated wind field the glide slope sensor could be used, but would have to be scanned in elevation and range to obtain wind Doppler data along the actual glide slope. It should be noted that in cases of horizontally homogeneous wind fields (low level inversion and most warm fronts) the CW CO₂ Doppler LIDAR is also a viable sensor. Future application of the pure glide slope sensor could lead to fully automated landing capability where the feedback of the LIDAR obtained wind Doppler could be used in real time for insertion into the autopilot/autoland system. The latter could provide near all weather capability and therefore only one runway (both ends) might be instrumented to service an entire airport thereby reducing the system cost.

8. REFERENCES

- (1) NTSB-AAR-74-14
- (2) NTSB-AAR-76-B
- (3) NTSB-AAR-76-14
- (4) Fichtl, George H., Wind Shear Near the Ground and Aircraft Operations, J. of Aircraft, Vol. 9, No. 11, November 1972.
- (5) Barr, N. M., et al, Wind Models for Flight Simulation Certification of Landing and Approach Guidance and Control System, Report No. FAA-RD-74-206, December 1974.
- (6) Goff, R. W., Thunderstorm-Outflow Kinematics and Dynamics, NOAA TM ERL NSSL-75, December 1975.

APPENDIX E
CAT FLIGHT A TEST DATA ANALYSIS

DIVISION
Operation
Department

EQUIPMENT
EDL - Sudbury
Electro-Optics

To File
From A. Jelalian
Subject CAT Flight A Test Data
Analysis

Classification unclassified

Contract No.

Distribution

File No.

Memo No. 72:AVJ:136

Date 23 October 1972

The S/N equation for a ground target may be expressed as

$$S/N = \frac{\eta_o \eta_{SYS} \eta_{ATM} E_T D^2 \sigma}{32h\nu K \left[R^2 + \left(\frac{\pi D^2}{4\lambda} \right)^2 \right]} \quad (\text{Reference 1})$$

where

η_o = detector quantum efficiency (0.08)
 η_{SYS} = system efficiency (0.2)
 η_{ATM} = atmospheric efficiency
 E_T = energy per pulse (5mj) assumed
 D = optics diameter (1 ft)
 σ_o = effective target cross-section (3.5×10^{-1})
 $h\nu$ = planck's constant x transmitter frequency (1.9×10^{-20})
 K = filter mismatch ratio (1)
 R = target range (ft)
 λ = operating wavelength (3.3×10^{-5} ft)

Target Cross-section

Target cross-section measurements were previously performed in the laboratory (Reference 2) for a belt sander.

This resulted in σ being equal to $\sigma = 3.5 \times 10^{-1} A_B$ at a depression angle of 45° . Assuming a lambertian scattering function and computing this value for a scattering angle of 10° --typical of the glide slope angle during the Edwards dive bombing tests, $\sigma = 6.4 \times 10^{-2} A_B$. Sand from the Edwards Dry Lake area has been collected and reflectivity and scattering tests were performed to provide more accurate target information. Results from this test indicated that the Edwards Dry Lake reflectivity was 0.022 per steradian for measurements around the nominal 10° depression angle of the dive bombing tests.

The target cross-section σ may be expressed as

$$\sigma = 4\pi \rho(\pi) A_B$$

where: $\rho(\pi)$ = target reflectivity (ster^{-1})

A_B = area of the transmitter beam

Additionally σ_o the effective target cross-section may be expressed as

$$\sigma_o = \frac{\sigma}{A_B}$$

and may therefore be calculated to be 0.27. For the theoretical comparisons utilized in the data to follow, this reflectivity data was not available and a σ_o was computed from the flight test data (see Calculation Table II).

In-flight data taken on 8/29/72 and 9/6/72 over Edwards Dry Lake, California and Carson Sink, Nevada respectively, were analyzed for the purposes of determining system performance during the flight tests. (See Figs. E-1 and E-2.) A typical run consisted of the aircraft climbing to 15--20K feet and then descending at an approximately 10° dive angle to the desert floor.

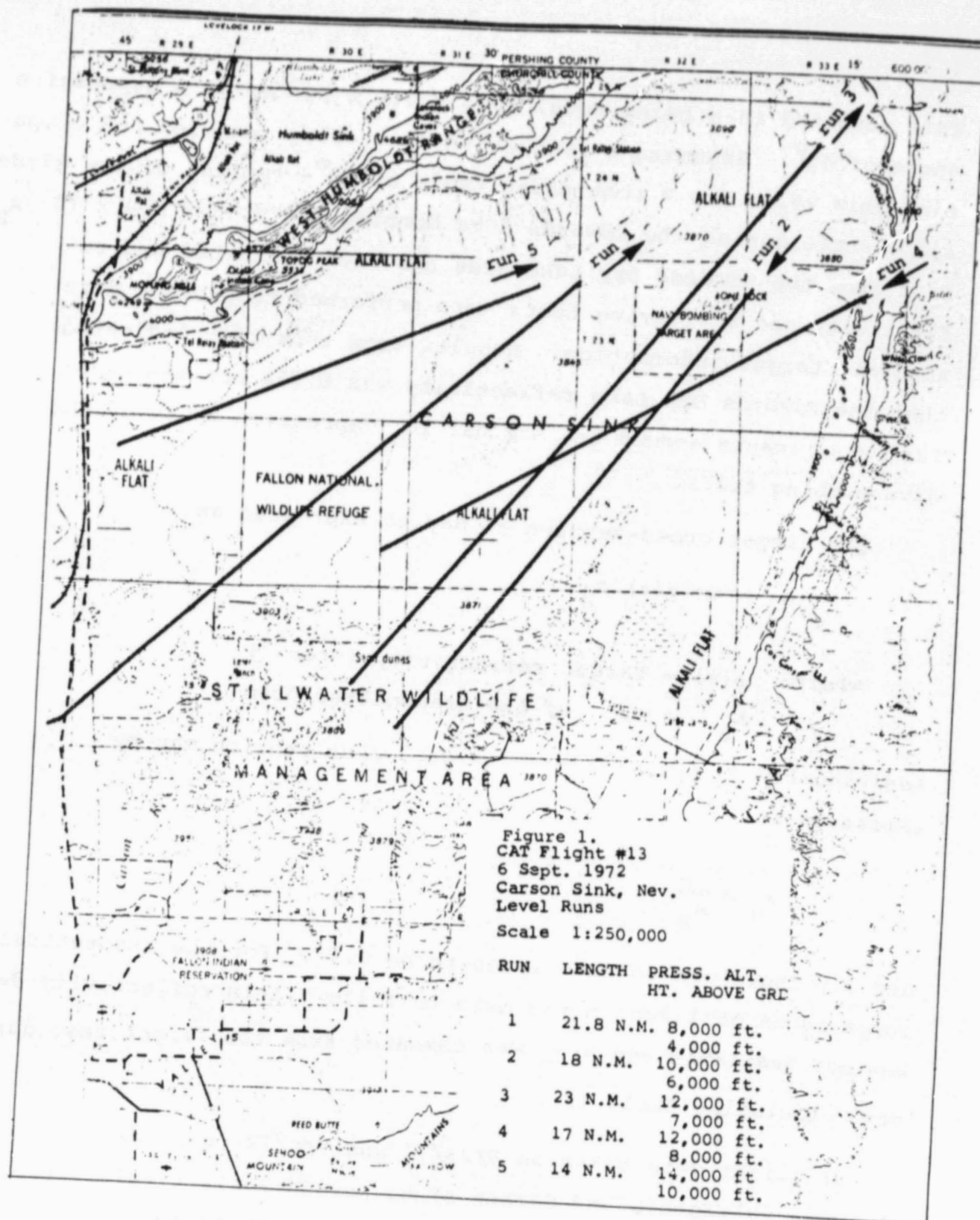
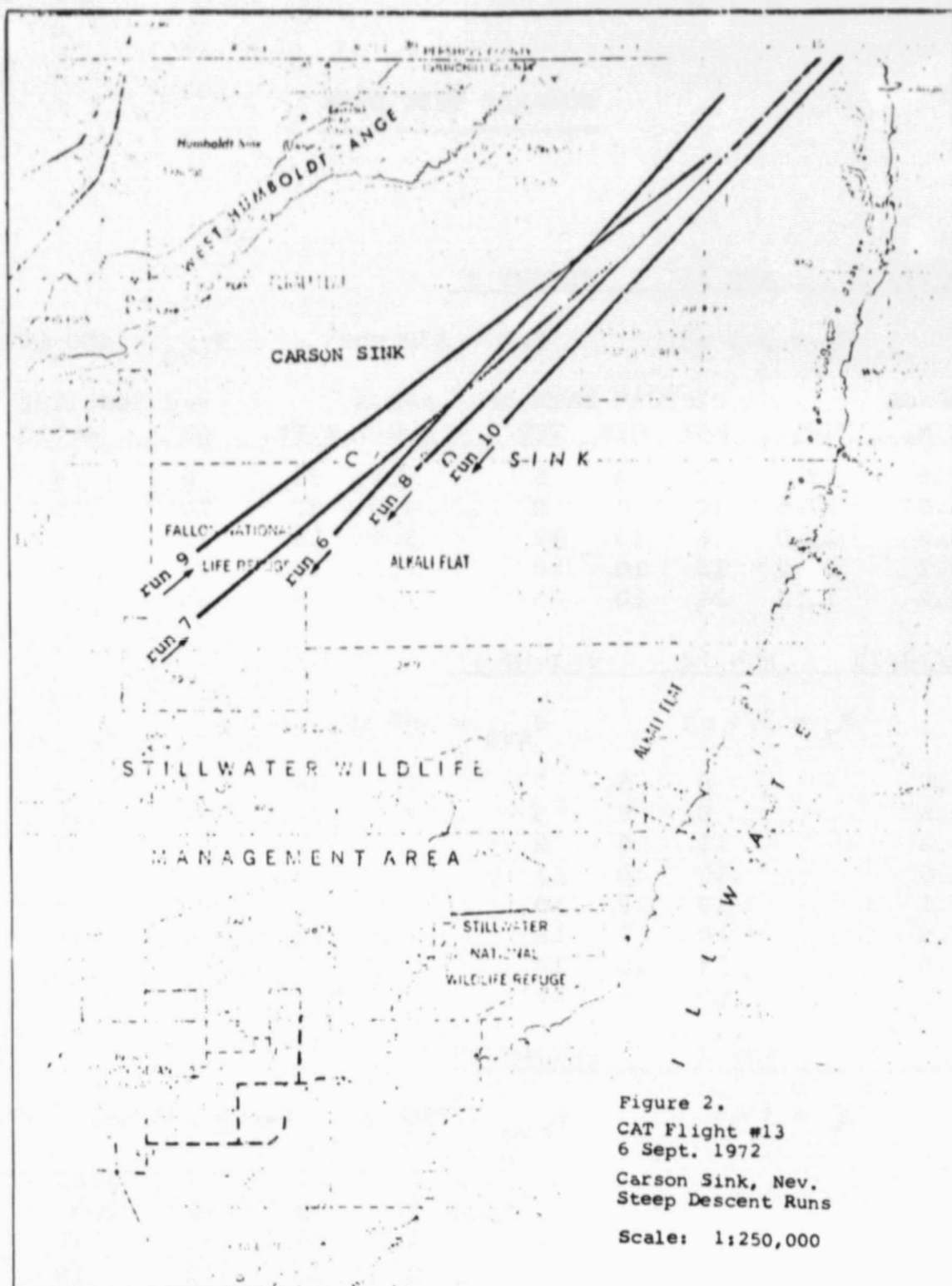


Figure E-1. CAT Flight No. 13, Level Runs

EOA-1012



EOA-1013

Figure E-2. CAT Flight No. 13, Steep Descent Runs

EDWARDS TEST DATA

8/29/72 RUN 15 FLIGHT 9

$E_T = 3.1 \text{ mj}$

PRF = 130 pps

$P_{AVG} = 400 \text{ mW}$

RANGE		PICTURE DATA dB			RANGE		s/N INFLIGHT	
N.Mi.	K.Ft.	MAX	MIN	TYP	N.Mi.	K.Ft.	dB	RATIO
5.5	33	10	4	6	5.5	33	6	4
4.6	27.6	10	6	8	4.5	27	10	10
3.5	21.0	16	10	12	3.5	21	12	16
3.2	19.2	12	10	10	2.5	15	22	162
2.2	13.2	22	10	20	1.5	9	25	316

8/29/72 RUN 12 FLIGHT 9

$E_T = 3.4 \text{ mj}$

$P_{AVG} = 440 \text{ mW}$

5.8	8	6	7	6	36	7	5
5.6	8	6	5	4.8	28.8	12	16
4.8	12	6	8	3.8	22.8	15	32
4.0	15	10	11	3.3	19.8	20	100
3.1	19	12	10	2.5	15.0	18	63
2.5	18	7	16	2.0	12.0	24	250
2.0	24	10	18				
1.6	26	8	22				

9/6/72 RUN 7 FLIGHT 13

$E_T = 5 \text{ mj}$

$P_{AVG} = 700 \text{ mW}$

PRF = 140 pps $\tau = 8 \mu s$

2	12	35	3140
3	18	30	1000
5.8	34.8	15	31
8	48	10	10
10	60	8	6.3
14	84	3	2

During this descent, S/N ratio as a function of range was recorded from real time observation of the A-scope display.

Utilizing data in calculation Tables I and II and the S/N ratios measured in flight, the data in Figures E-3, E-4 and E-5B are plotted. Photographs of in-flight data for Flight 13, Run 7 on 9/6/72 are presented in Figure E-5A.

Normalizing the atmospheric attenuation data to the one-mile range point for arbitrary values of absorption of 0.5 dB/RTKM and 1.0 dB/RTKM noted in Figure E-6, one may observe that the 1.0 dB/RTKM attenuation coefficient closely approximates the actual flight test data in Figures E-4 and E-5B. Calculation based upon the temperature and humidity noted for this flight and utilization of the McCoy, Rensch, and Long data, Reference 3, also computed to be approximately 1 dB/RTKM at sea level, why and if this effect exists across the total path is surprising and should be evaluated. Future evaluations will be directed at this area.

CALCULATION TABLE I

R (K FT)	R^2 10^8 FT^2	$\left(\frac{\pi D}{4\lambda}\right)^2$ 10^8 FT^2	$\left(R^2 + \frac{\pi D^2}{4\lambda}\right)^2$ 10^8 FT^2	$\left(\frac{1}{R^2 + \frac{\pi D^2}{4\lambda}}\right)^2$ $\times 10^{-9} \text{ FT}^{-2}$	c^* $\times 10^7$	α_1^R	α_2^R	A $e^{-\alpha_1^R}$	B $e^{-\alpha_2^R}$	Z_2 $ce^{-\alpha_2^R}$ $\times 10^7$	Z_1 $\frac{A}{Z_2 B}$ $\times 10^7$
5	0.25	5.7	5.95	1.7	4.5	0.35	0.7	0.72	0.5	2.3	1.4
10	1.0		6.7	1.5	4.0	0.7	1.4	0.5	0.25	1.0	2
15	2.3		8.0	1.25	3.3	1.05	2.1	0.35	0.12	0.33	2.9
20	4.0		9.7	1.03	2.7	1.4	2.8	0.25	0.07	0.188	3.6
25	6.3		12.0	0.8	2.1	1.75	3.5	0.17	0.03	0.063	5.7
30	9		14.7	0.68	1.8	2.1	4.2	0.12	0.015	0.027	8
35	12.5		18.2	0.55	1.45	2.45	4.9	0.08	0.0074	0.011	10.8
40	16		21.7	0.46	1.22	2.8	5.6	0.08	0.0037	0.0045	21.6
50	25		30.7	0.32	0.84	3.5	7.0	0.03	0.0009	0.00075	33

$$* c = \frac{\eta_o \eta_{\text{SYS}} D^2}{32 h \nu K \left[R^2 + \left(\frac{\pi D}{4\lambda} \right)^2 \right]}$$

$$\alpha_1 = 0.5 \text{ dB/RTKM}$$

$$\alpha_2 = 1.0 \text{ dB/RTKM}$$

$$S/N = Z E_T \sigma$$

$$Z_1 = ce^{-\alpha_1^R}$$

$$Z_2 = ce^{-\alpha_2^R}$$

CALCULATION TABLE II

$$S/N = ce^{-\alpha R} E_T \sigma_o$$

R	$ce^{-\alpha R} \times 10^7$	8/29 S/N [1dB/RTKM] THEOR.	9/6 S/N [1dB/RTKM] S/N [0.5dB/RTKM] THEOR.
5	2.3	805	8300
10	1.0	350	3600
15	0.33	116.0	1180
20	0.188	66	680
25	0.063	22	230
30	0.027	9.5	97
35	0.011	3.9	40
40	0.0045	1.6	16
50	0.00075	0.26	2.7
			11,600
			7,200
			3,400
			2,420
			1,300
			775
			430
			340
			80

DATA NORMALIZED TO FLIGHT TESTS MEASUREMENTS @ 10K RANGE

EDWARDS	8/29	S/N ≈ 350 @ 10K	$E_T = 3.1 \text{ mJ}$	EST. $\sigma_o = 0.0113$
EDWARDS	8/29	S/N ≈ 350 @ 10K	$E_T = 3.4 \text{ mJ}$	EST. $\sigma_o = 0.0105$
CARSON SINK	9/6	S/N ≈ 3600 @ 10K	$E_T = 5.0 \text{ mJ}$	EST. $\sigma_o = 0.072$

σ_o FOR SOIL TAKEN FROM EDWARDS WAS 0.27.

$$\therefore S/N = ce^{-\alpha R} E_T \sigma_o = 10^7 \times 3.1 \times 10^{-3} \times 0.27 = 8400$$

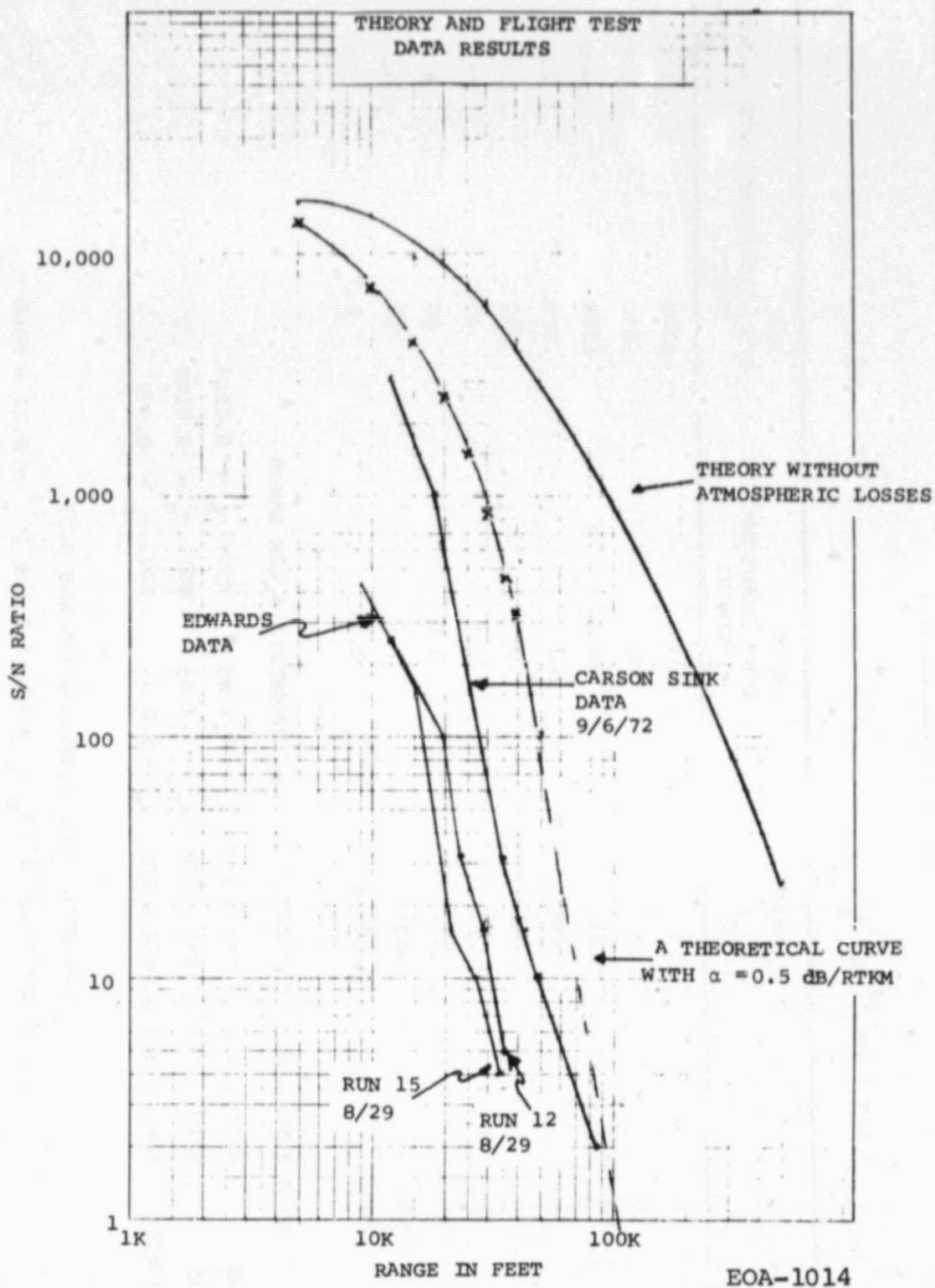


Figure E-3. Theory and Flight Test Data Results

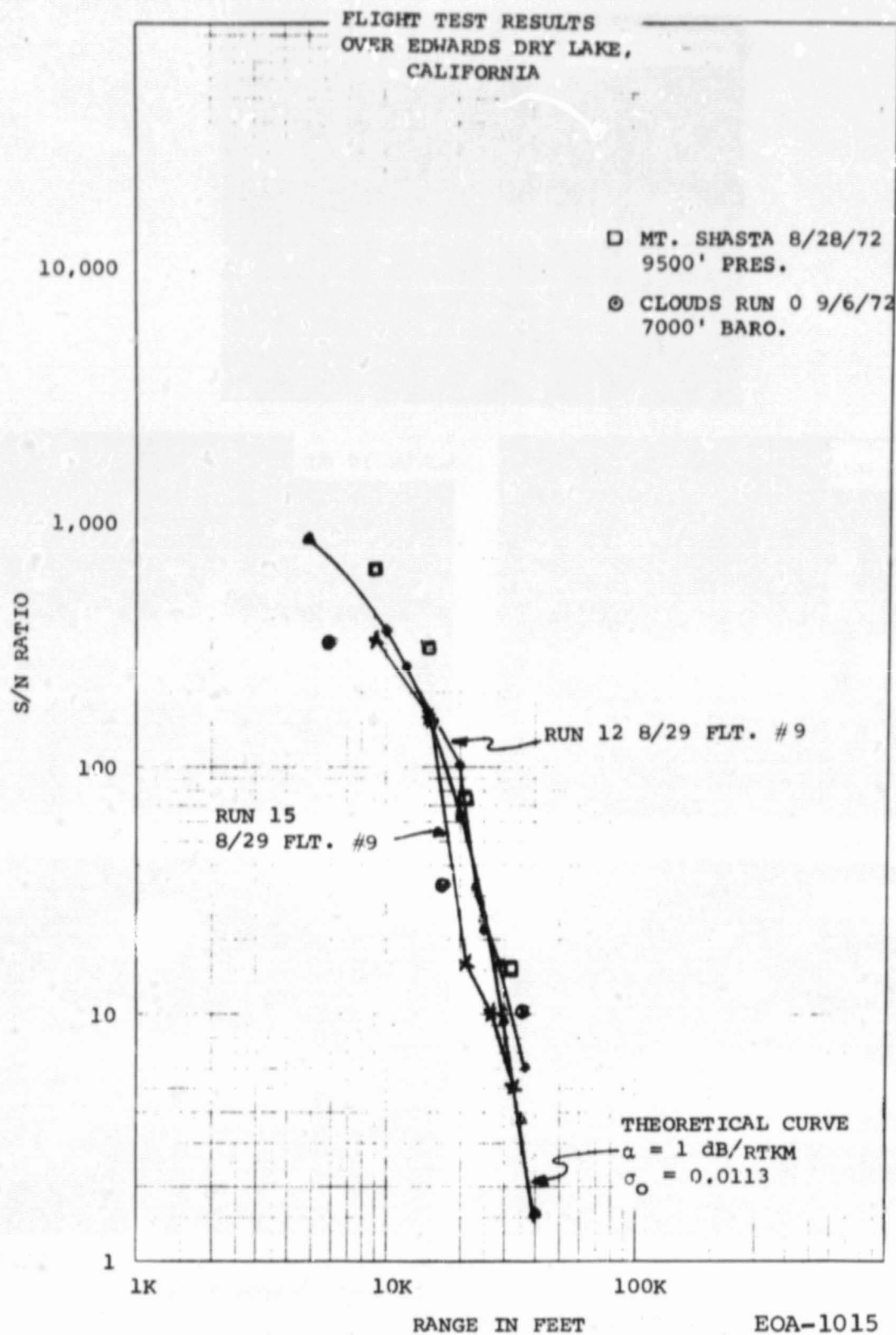
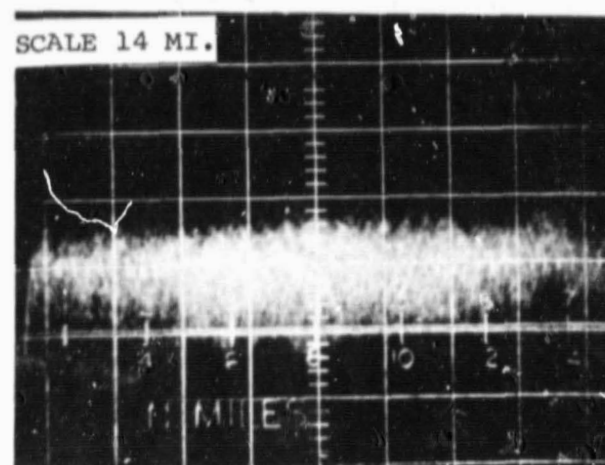
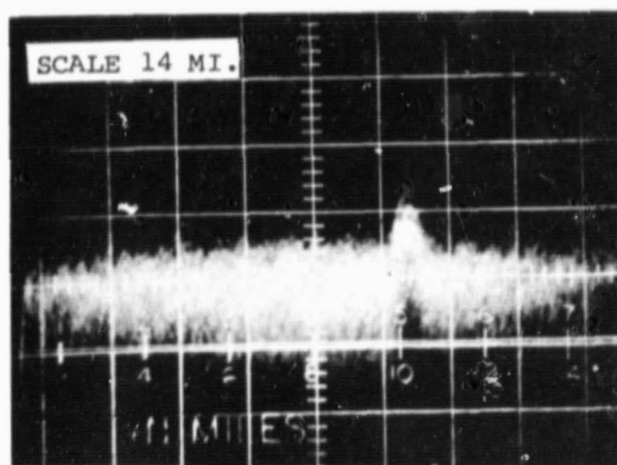
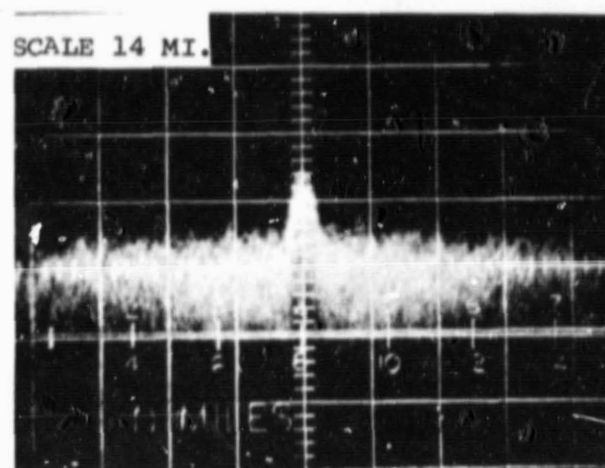
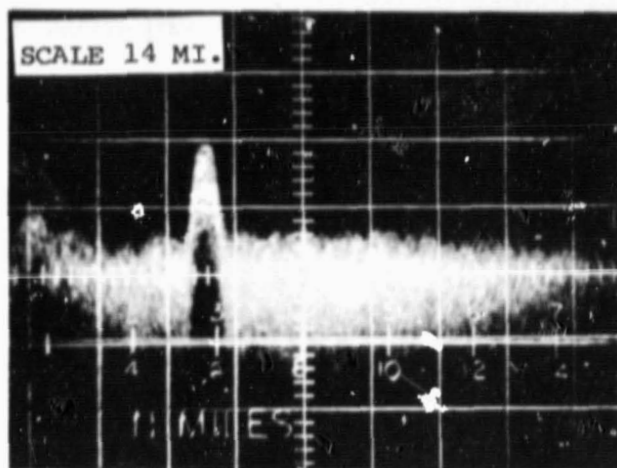
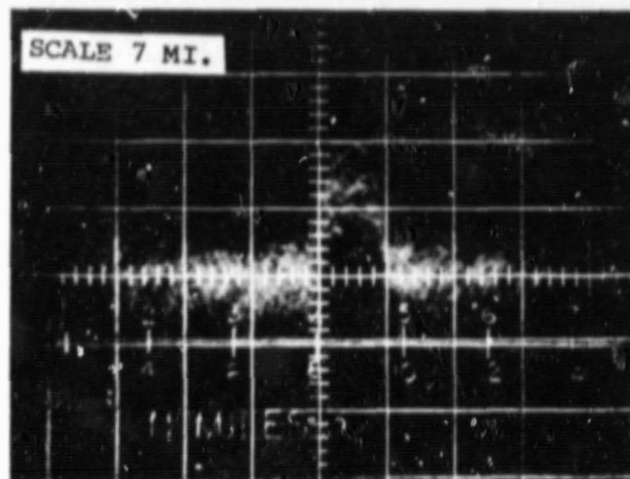


Figure E-4. Flight Tests Results Over Edwards Dry Lake, California



EO-586

FLIGHT 13 RUN 7 9/6/72 OVER CARSON SINK
 VERTICAL AXIS 10dB/CM
 HORIZONTAL SCALE 7 or 14 MILES

Figure E-5A. Flight 13, Run 7, 9/6/72 Over Carson Sink

FLIGHT TEST RESULTS OVER CARSON SINK, NEVADA

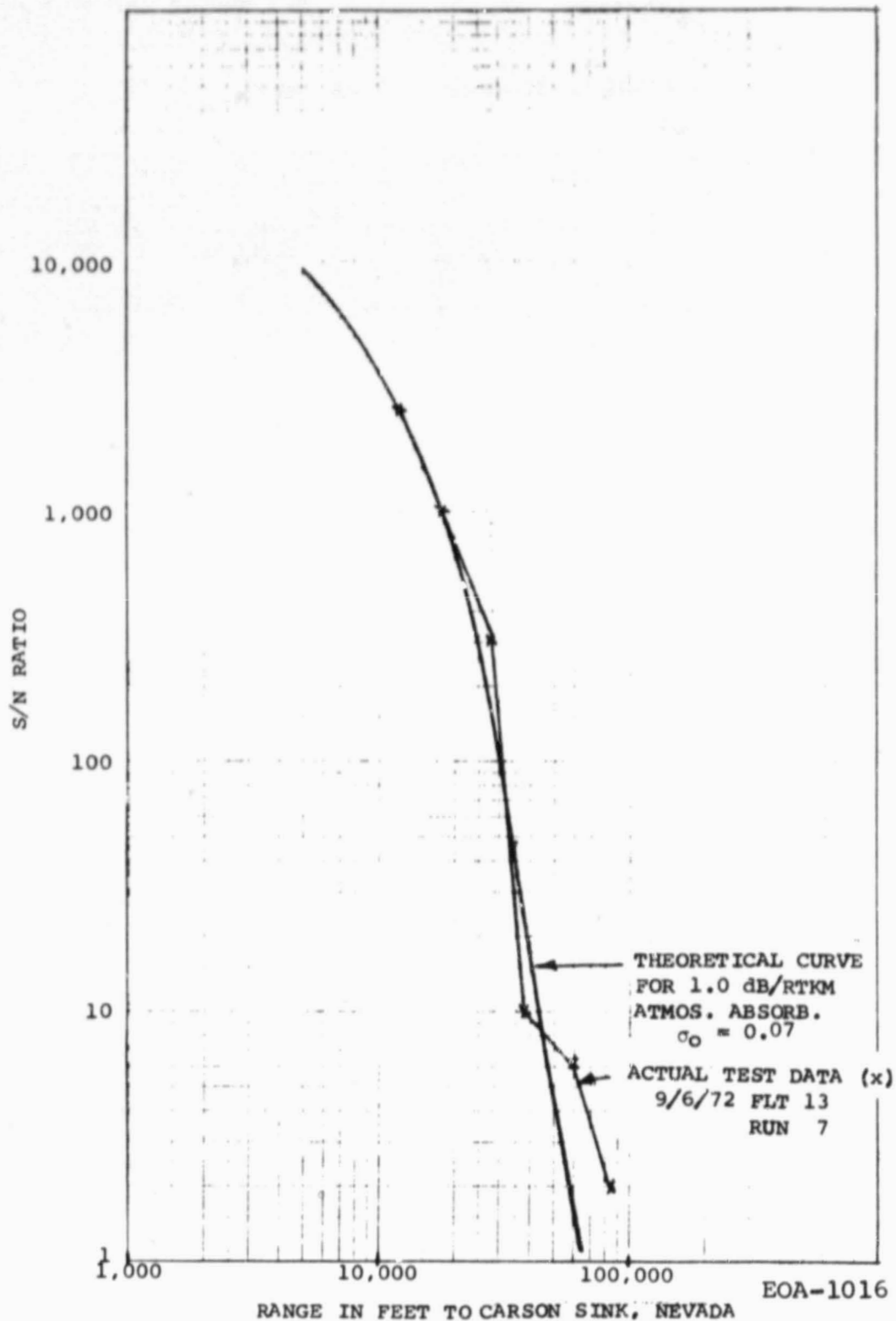


Figure E-5B. Flight Tests Results Over Carson Sink, Nevada

ATMOSPHERIC ABSORPTION VS. RANGE

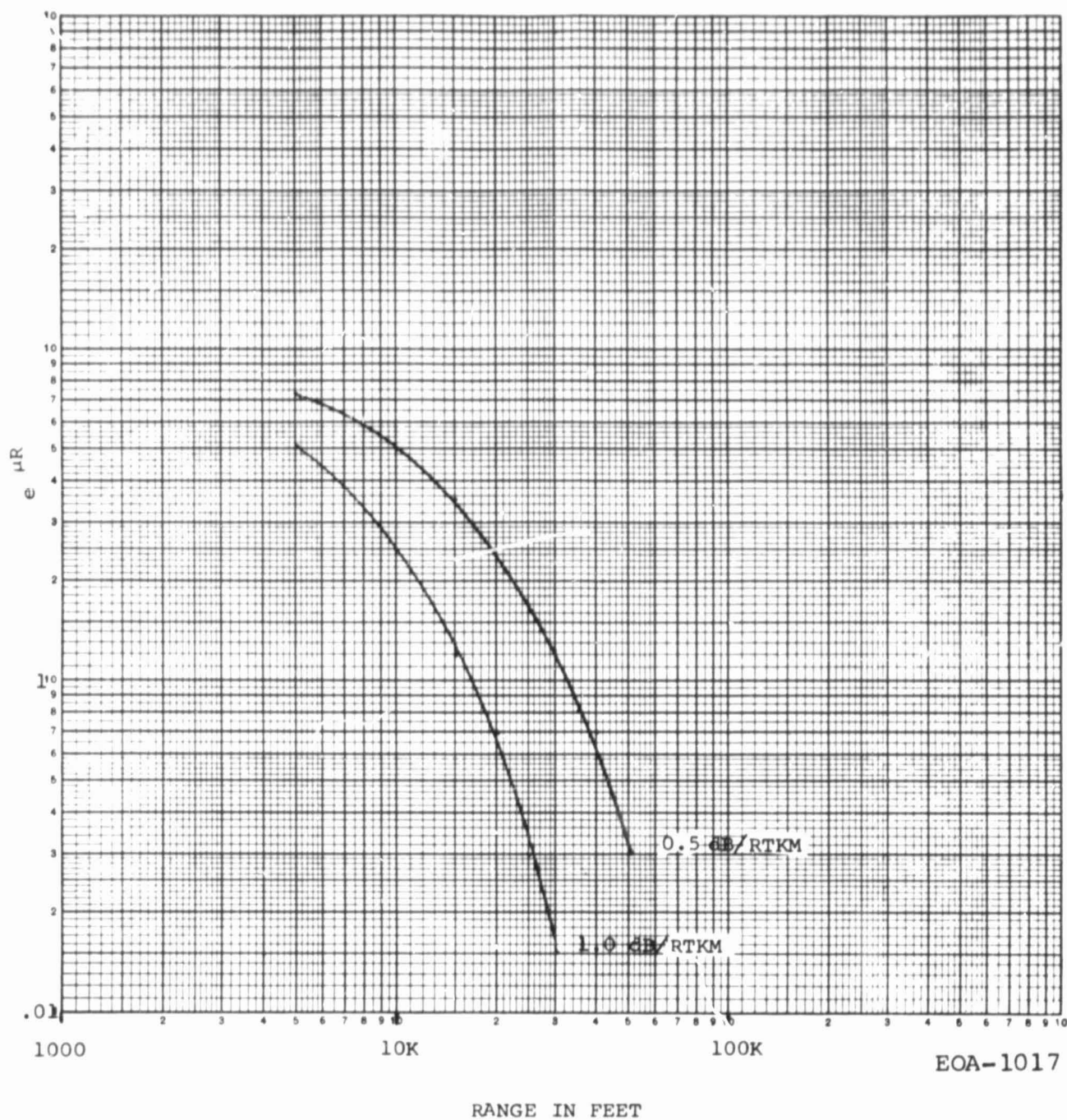


Figure E-6. Atmospheric Absorption vs Range

Soft Target Analysis

The S/N ratio for a pulsed unfocused system may be obtained from Reference to be

$$\left. \frac{S}{N} \right|_{\text{ATM}} = \frac{\eta_o \eta_{\text{SYS}} \eta_{\text{ATM}} \beta(\pi) \lambda E_T \left[\text{TAN}^{-1} \frac{4\lambda L_2}{\pi D^2} - \text{TAN}^{-1} \frac{4\lambda L_1}{\pi D^2} \right]}{2h\nu K}$$

where

η_o = detector quantum efficiency (0.08)

η_{SYS} = system efficiency (0.2)

η_{ATM} = atmospheric efficiency

$\beta(\pi)$ = atmospheric scattering function (ft^{-1})

E_T = transmitted pulse energy (5mj)

λ = transmission wavelength (3.3×10^{-5} ft)

L_2 = range and range cell distance

L_1 = range

D = optics diameter (1 ft)

$h\nu$ = 1.9×10^{-20} joules/photon

K = bandwidth mismatch factor

This equation may be reexpressed as

$$S/N = K_2 \left[\text{ARCTAN} (fct) \right] E_T \eta_{\text{ATM}} \beta(\pi)$$

For the 8 microsecond pulse case $\beta(\pi) \text{ m}^{-1}$ may be determined from the S/N measurement when normalized to a 5 mj pulse energy by using the following range vs. $\frac{1}{z}$ constants where $\beta(\pi) \text{ m}^{-1} = \text{S/N} \frac{1}{z}$.

Range	$\frac{1}{z_2}^*$	$\frac{1}{z}$
K ft.	10^{-8}	10^{-8}
6	0.3	0.67
12	0.85	4.5
18	2.36	27.8
24	6.4	160
30	21.8	1450

$\frac{1}{z_2}$ has 1 dB/RTKM Atmospheric Absorption.

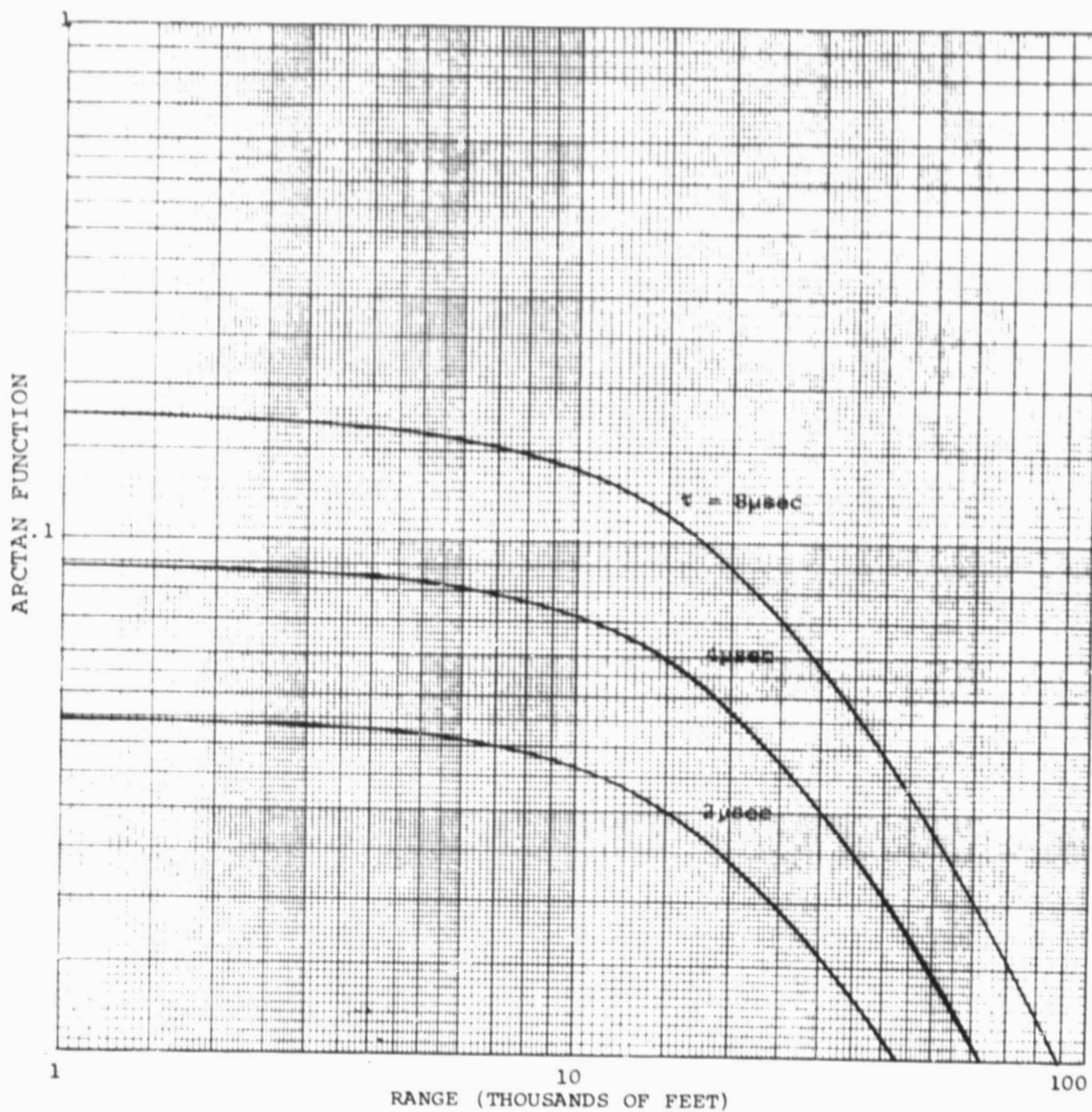
Assuming that a S/N ratio is measured at one mile, the atmospheric scattering function $\beta(\pi)$ may be obtained by multiplying by the $\frac{1}{z}$ constant. If the atmosphere is assumed to have a 1dB/RTKM atmospheric absorption, this effect may be removed by multiplying by $6.7 \times 10^{-9} \text{ m}^{-1}$.

The ARCTAN function may be computed for pulse widths of 2, 4, and 8 microseconds. This is plotted in Figure E-7.

$$\text{Letting } A = \frac{4\lambda L_1}{2\pi D} \quad \text{and} \quad B = \frac{4\lambda L_2}{2\pi D}$$

R K.Ft.	A	θ_A DEG.	A + 1000' $\tau=2\mu s$	$\theta_{2\mu s}$ DEG.	A + 2000' $\tau=4\mu s$	$\theta_{4\mu s}$ DEG.	A + 4000' $\tau=8\mu s$	$\theta_{8\mu s}$ DEG.
2	0.084	4.8	0.126	7.2	0.168	9.5	0.252	14.1
4	0.168	9.5	0.290	11.8	0.252	14.1	0.336	18.6
8	0.336	18.6	0.378	20.7	0.42	22.6	0.505	26.6
10	0.42	22.6	0.46	24.7	0.5	26.6	0.59	30.6
15	0.63	32.2	0.67	33.8	0.71	35.4	0.8	38.7
20	0.84	40.0	0.88	41.4	0.93	43	1.01	45.2
30	1.26	51.6	1.3	52.4	1.34	53.2	1.43	55

	$\theta_2 - \theta_A$			$\theta_4 - \theta_A$			$\theta_8 - \theta_A$	
	DEG.	RAD.		DEG.	RAD.		DEG.	RAD.
2	2.4	0.042		4.7	0.082		9.3	0.163
4	2.3	0.04		4.6	0.08		9.1	0.159
8	2.1	0.037		4.0	0.07		8.0	0.139
10	2.1	0.037		4.0	0.07		8.0	0.139
15	1.6	0.028		3.2	0.056		6.5	0.115
20	1.4	0.0245		3.0	0.052		5.2	0.091
30	0.8	0.014		1.7	0.03		3.4	0.06



EOA-1018

Figure E-7. Arctan Function ($\text{Arctan } 4\lambda L_2/\pi D^2 - \text{Arctan } 4\lambda L_1/\pi D^2$) vs Range (L_1)

On flight tests 8/29 and 9/6, if the atmosphere had a 1 dB/KM absorption, the following data should be (1) normalized to 5 mj and (2) multiplied by 6.7×10^{-9} to obtain $\beta(\pi)$.

CONDITIONS

DATE: 8/29/72 FLIGHT 9 RUN 0 $E_T = 3 \text{ mj}$

HAZE LAYER, MOFFETT TO SAN FRANCISCO

Ht. K.Ft.	S/N 1 mi.	S/N @ 1 N.Mi. NORM. TO				
		5 mj	1.5 N.Mi.	2 N.Mi.	2.5 N.Mi.	3.0 N. Mi.
7	5	8.3	2.5	1.25	--	--
7.4	8	13.3	4	2	1.2	--
9.4	8'	13.3	5	3.2	1.6	1
11.45	4	6.6	2.5	2	1	--
13.5	3.2	5.3	2.5	2	1	--
16	3.2	5.3	3.2	1.6	--	--
17	1	1.7				

DATE: 8/29/72 FLIGHT 9 RUN 13

AIR RETURNS ON CLIMB OUT FROM DIVE BOMBING

Ht. K.Ft.	S/N 1 mi.	S/N NORM. TO 5 mj
2.4	10	16
2.5	32	51
2.7	16	26
2.9	10	16
3.5	6.3	10
4.0	8	13
4.6	5	8
4.9	5	8
5.3	3	4.8
5.6	4	6.4
6.7	4	6.4
8.2	4	6.4
9.1	2.5	4
10	2.5	4
12.3	2.5	4

X DATE: 9/6/72 FLIGHT 13 RUN 0

$E_T = 6.5$ mj

MOFFETT - SAN FRANCISCO

<u>Ht.</u> <u>K.Ft.</u>	<u>S/N</u> <u>1 Mi.</u>	<u>S/N NORM.</u> <u>to 5 mj</u>	
1	3200	2500	INVERSION
1.5	320	250	
2.0	10	7.8	
3.0	10	7.8	
3.3	10	7.8	
3.5	10	7.8	
3.9	10	7.8	LT. HAZE
4.0	6.3	5.0	
4.4	6.3	5.0	
4.5	1.8	1.4	SLIGHT HAZE
4.7	1.8	1.4	
4.9	1.6	1.2	
5.4	1.6	1.2	

0 DATE: 8/31/72 FLIGHT 10 RUN

$E_T = 5.8 - 9.2$ mj

assume 5.8 mj

K = 0.86

SAN JACQUIN VALLEY

<u>Ht.</u> <u>K.Ft.</u>	<u>S/N</u> <u>1 Mi.</u>	<u>S/N NORM.</u> <u>to 5 mj</u>
3.3	10	8.6
3.4	10	8.6
3.6	10	8.6
4.1	10	8.6
4.2	10	8.6
4.5	10	8.6
4.6	10	8.6
4.9	10	8.6
5.2	10	8.6
11.7	10	8.6
12.0	10	8.6
12.3	3	2.6
12.9	2.5	2.16
13.5	4	3.45
14.1	6.3	5.45
15.8	1.6	1.38

Plotting the flight test data obtained at 9.4K barometric for 8/29/72 and normalizing the atmospheric theoretical data to $S/N = 8$ which was the actual measurement at 1 mile, the atmospheric absorption values of 1 dB/RTKM and 0.5 dB/RTKM yield S/N ratios tabulated below and plotted on Figure E-8B. Some typical flight test runs at different altitudes looking horizontally into the clear air, may be noted in Figure E-8A.

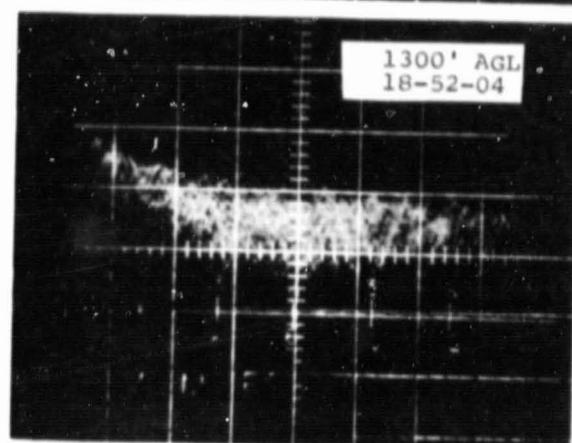
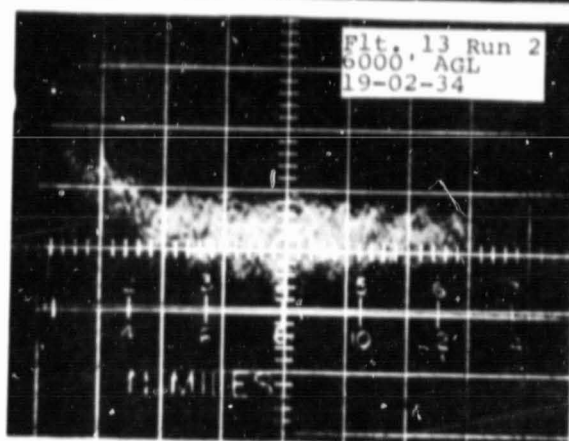
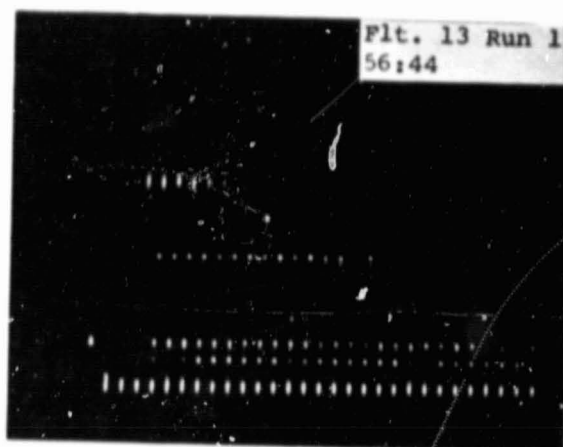
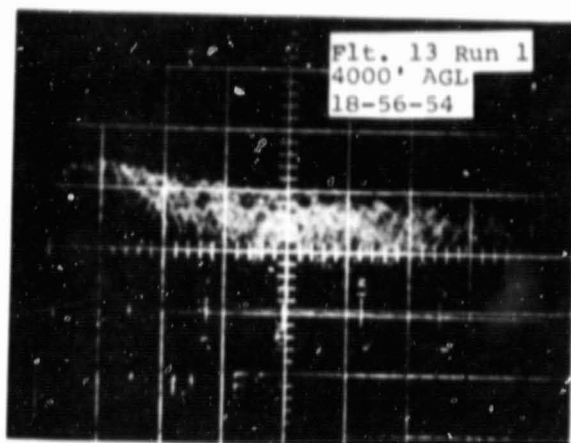
8/29/72 SOFT TARGET

RANGE K	9.4K Ft. S/N (ACTUAL)	$e^{-\mu r}$ at 1 dB/RTKM NORM. to 8	$e^{-\mu r}$ at 0.5 dB/RTKM NORM. to 8
6	8	8	8
9	5		
12	3.2	2.9	4.4
15	1.6		
18	1	1.04	2.2
24		0.38	1.07
30		0.11	0.58

The atmospheric data at a one-mile range in front of the aircraft noted on pages E-19 and E-20 is plotted in Figure E-9 and indicates the altitude effect upon S/N ratio for a 5 mj transmitter. Correspondingly, this is related to the atmospheric scattering function $B(\pi)$ noted on the right-hand scale.

A-Scope
 Vert. 10 dB/CM
 Horiz. 7 Nmi.
 Pull Scale

Vertical Axis
 15 Ft/CM
 Horiz. Axis
 7 Mi. Pull Scale



EO-589

Figure E-8A. Atmospheric Measurement at Altitude

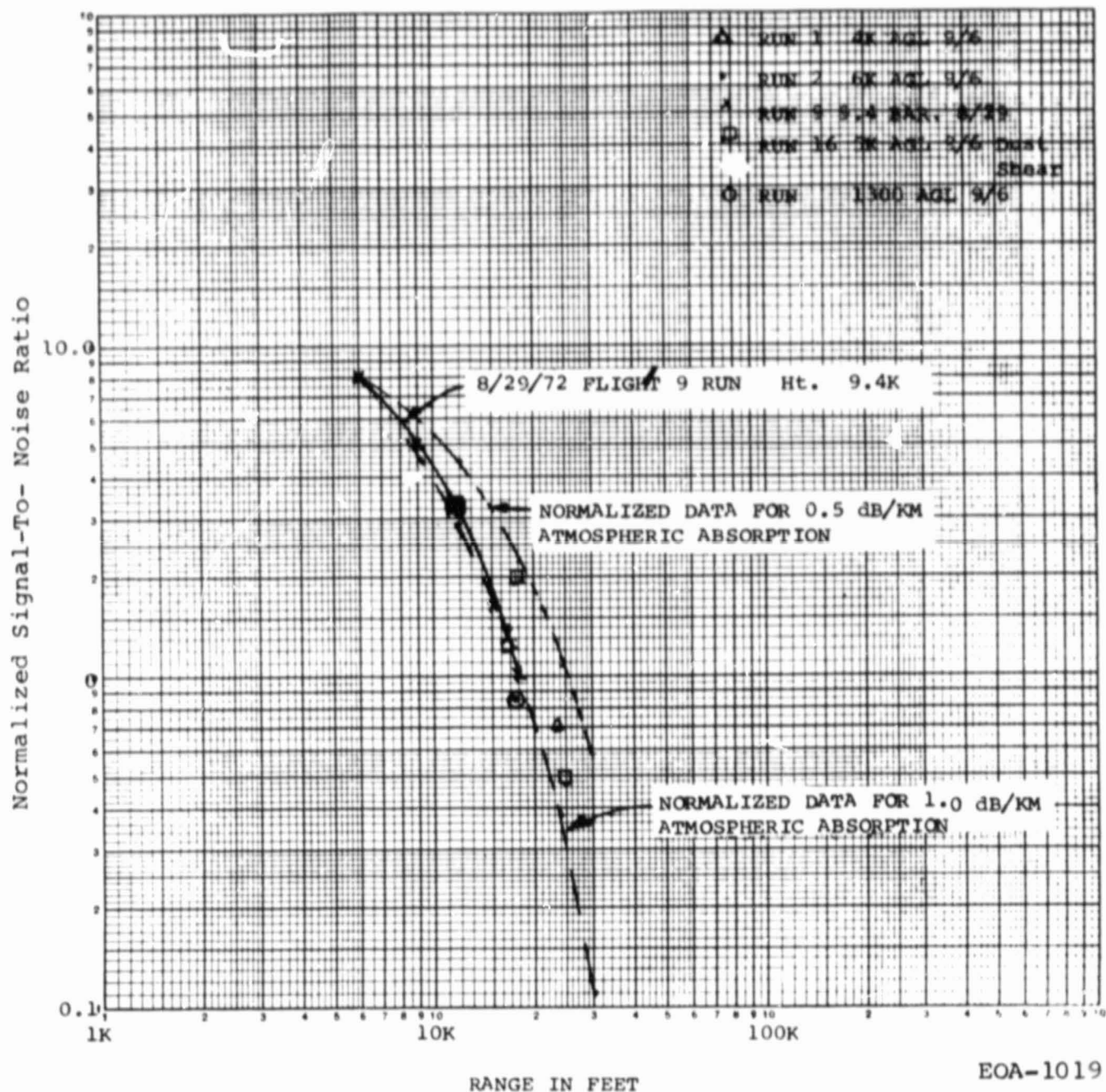
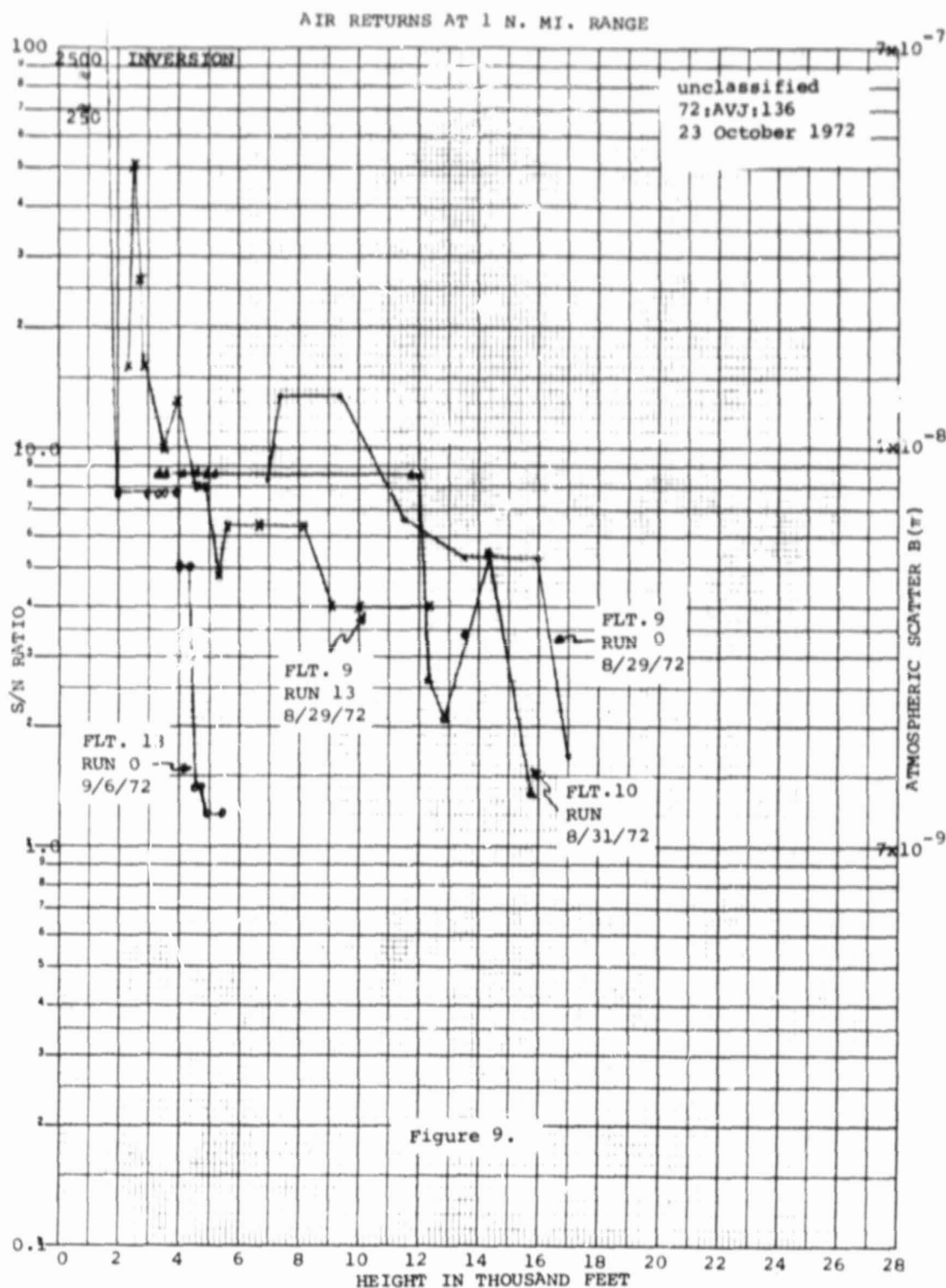


Figure E-8b. Dependence of SNR on Atmospheric Absorption



EOA-1020

Figure E-9. Altitude Dependence of SNR

REFERENCES

- (1) Sonnenschein, C. M., and Horrigan, F. A.; "Signal-to-noise Relationships for Coaxial Systems that Heterodyne Backscatter from the Atmosphere", Applied Optics, Vol. 10, p. 1600, July 1971.
- (2) Seavey, R. E.; "Reflectivity Measurements of Sand Paper at 10.6μ ", Memo 72-RES-6, 1 June 1972.
- (3) McCoy, John H., Rensch, David B., and Long, Ronald K.; "Water Vapor Continuum Absorption of Carbon Dioxide Laser Radiation near 10μ ", Applied Optics, Vol. 8, No. 7, p. 1471, July 1969.

APPENDIX F

CAT FLIGHT B TEST
DATA ANALYSIS

CONTENTS

<u>SECTION</u>	<u>PAGE</u>
1 INTRODUCTION	F-5
2 RETURNS FROM GROUND AT EDWARDS AFB	F-15
2.1 Description of Data	F-16
2.2 Signal-to-Noise Ratio Measurements.	F-20
2.3 Comparison with Theoretical Signal-to-Noise Ratio	F-22
2.3.1 Atmospheric Attenuation as Possible Cause of Difference.	F-26
2.3.2 Atmospheric Turbulence as Possible Cause of Difference.	F-28
2.3.3 Focussing or Aperturing as Possible Cause of Difference.	F-29
2.3.4 Theoretical Model of Best Fit to Data	F-32
2.4 Reading the Signal-to-Noise Ratio	F-35
2.4.1 Noise Level	F-36
2.4.2 Signal Level.	F-38
2.5 Pulse Integration	F-44
3 AIR BACKSCATTER RETURNS.	F-47
3.1 Signal-to-Noise Ratio Measurements.	F-48
3.2 Comparison with Theoretical Signal-to-Noise Ratio	F-52
3.3 Causes of Signal Fluctuations	F-56
4 TURBULENT CLOUD TESTS.	F-60
4.1 Returns from Turbulent Clouds	F-60
4.2 Correlation of Laser Return with Flight Turbulence.	F-63
5 MISCELLANEOUS TARGETS.	F-69
5.1 Signal-to-Noise Ratio Measurements.	F-69
5.2 Reflectivity.	F-71
5.3 Cirrus Clouds	F-73
6 EVALUATION	F-75
ATTACHMENT 1	F-80
ATTACHMENT 2	F-83

ILLUSTRATIONS

<u>FIGURE</u>		<u>PAGE</u>
F-1	Rogers Dry Lake at Edwards AFB, Site of the Calibration Test Runs	F-7
F-2	Clear Air at High and Low Altitudes which Produced Signals	F-8
F-3	Turbulent Clouds over Owens Valley.	F-9
F-4	Altitude Profile of CAT Flight B2	F-11
F-5	Altitude Profile of CAT Flight B4	F-12
F-6	Altitude Profile of CAT Flight B6	F-13
F-7	Altitude Profile of CAT Flight B8	F-14
F-8	Sequence Camera Photos of A-Scope and RVI During Dive at Edwards.	F-17
F-9	Signal-to-Noise Ratio Measurements Against Ground at Edwards AFB	F-21
F-10	Comparison of Theoretical and Experimental Results for Edwards Tests	F-25
F-11	Atmospheric Attenuation Coefficient for Dives at Edwards	F-27
F-12	Theoretical SNR of CAT Laser Against Ground	F-31
F-13	Calculated Atmospheric Attenuation for Edwards Dives.	F-33
F-14	Fit of Theoretical Curve D to Measurements at Edwards	F-34
F-15	Matching of Theoretical Noise Curve to Experimental Results	F-39
F-16	Peak SNR Measurements of All Sequence Camera Photographs During Dive at Edwards.	F-40
F-17	Sequence Camera Photos of A-Scope and RVI Showing Backscatter Returns	F-49
F-18	Signal-to-Noise Ratio Measurements Against Air.	F-51
F-19	Theoretical SNR of CAT Laser System Against Air	F-55
F-20	Fit of Theoretical Air Backscatter SNR Curve to Measurements.	F-57
F-21	Cumulus Clouds in Bishop Area	F-61
F-22	CAT Flight Test - Cloud Turbulence Correlation.	F-66
F-23	Signal-to-Noise Ratios for Various Targets.	F-72
F-24	Signal-to-Noise Ratios from Cirrus Clouds	F-74
F-25	Required Improvement in SNR for Operational CAT Laser Radar	F-77

TABLES

<u>NUMBER</u>		<u>PAGE</u>
F-1	Parameters.	F-23
F-2	Signal Levels in Sequence Camera Exposures.	F-43
F-3	Laser Returns from Clouds in Owens Valley, Flt. B4. .	F-64
F-4	Laser Returns from Clouds in Owens Valley, Flt. B8. .	F-65
F-5	In-Flight Recorded Accelerations.	F-68
F-6	Target Reflectivities at 10.6 Microns	F-70
F-7	Required S/N Improvement for Operational CAT System .	F-76

SECTION I

INTRODUCTION

The data from the January 1973 Clear Air Turbulence Laser Radar flight test series (series "B") are analyzed in this report. The data are in the following forms:

- a. Sequence camera photographs of the A-scope and Range/Velocity Indicator (RVI). The photographs are spaced at 1.2 second intervals. Each exposure lasts 0.1 second and contains the returns from approximately 14 pulses. The A-scope plots intensity vs. time (range) on single pulses and the RVI plots frequency vs. range for the integrated output of 50 pulses.
- b. Intensity/Velocity Indicator. The output from this display is recorded on tape. The IVI plots intensity vs. frequency at a selected range for the integrated output of 50 pulses.
- c. Polaroid photos of the A-scope taken during flight and in-flight notes of signal-to-noise ratio.
- d. Voice recordings. The conversations during flight were recorded on tape.
- e. Flight data print-outs. The ground and air velocities, wind speed and direction, pitch and roll angle, altitude, heading, latitude and longitude, temperature, dew frost point and acceleration were recorded at ten and one second intervals.

The data analysis here is concerned with the sequence camera output only, because this was largely sufficient to describe the system performance. There were two exceptions: (1) the flight data print-outs were used to verify the findings of the sequence camera data

analysis and (2) the IVI data were included in the analysis of the cloud turbulence tests.

The January 1973 flight tests fall basically into four groups:

1. Dives at Edwards AFB against a uniform dry lake to check out and calibrate the laser system.
2. Measurements of backscatter returns from air at various altitudes.
3. Turbulent cloud tests to evaluate the laser returns from turbulent air.
4. Measurements from miscellaneous targets including a mountain, the ground prior to landing, and cumulus, dust and cirrus clouds.

Each of these groups is analyzed in a separate section, from Sections 2 through 5. The conclusions from each group of tests are discussed at the beginning of each section. Section 6 estimates the improvement required for an operational Clear Air Turbulence laser radar.

Photographs of targets in the first three groups are in Figures F-1 through F-3. Figure F-1 shows the dry lake at Edwards AFB which was the target of the calibration test dives. Figure F-2 shows the air from which backscatter returns were detected at high and low altitudes. In Figure F-3, the type of clouds in the turbulence tests through the Owens Valley is shown.

The data from the flight test were also analyzed by A. Jelalian (Raytheon memo EM73-1115). The analysis here examines the sequence camera data in more detail and does not include any of the particle sampling data of Blifford which are in A. Jelalian's memo. The two analyses essentially complement each other and reach similar conclusions.

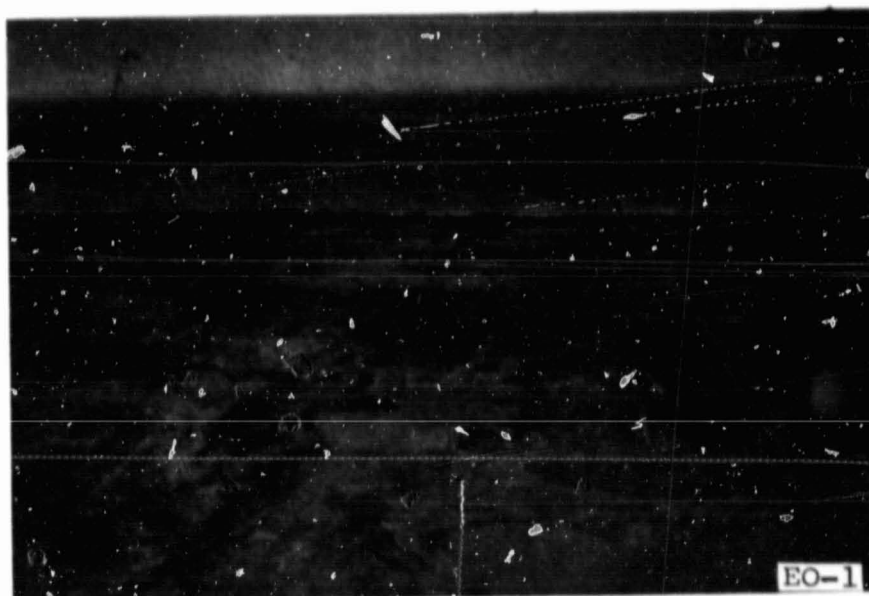


Figure F-1. Rogers Dry Lake at Edwards AFB,
Site of the Calibration Test Runs

ORIGINAL PAGE IS
OF POOR QUALITY

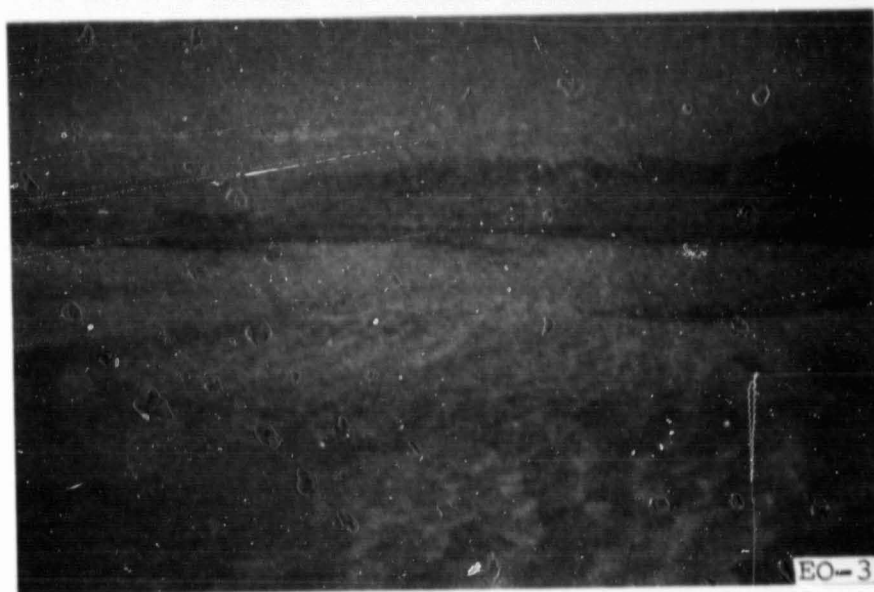


Figure F-2. Clear Air at High and Low Altitudes which Produced Signals. TOP: At 22 Kft near San Francisco, Faint Return on Range/Velocity Indicator. BOTTOM: Over Sand Hills near Imperial Valley, Calif., SNR's up to 20 dB per pulse.



Figure F-3. Turbulent Clouds over Owens Valley. TOP: Owens Valley. BOTTOM: Type of Clouds Penetrated

In review, the CAT laser radar consists of a coherent carbon dioxide laser at 10.6 microns transmitting pulses at a 140 to 160 pps rate adjustable in width from 2 to 10 microseconds, a 12 inch Cassegrain telescope, a heterodyne receiver with a cooled infrared detector, and signal processing electronics. Previous reports on the program should be consulted for further details. The laser radar was tested on a ground range and in an earlier flight test, series "A", in August/September 1972. The results from these earlier tests are examined in previous memos.*

The January 1973 flight test series consisted of eight flights in California spanning the time period from January 4 through 19. Of these, Flights B2, B4, B6 and B8 were productive. The other flights encountered problems with amplifier malfunction, window fogging, bad weather, etc. The altitude profiles target areas and run numbers of the productive flights are shown in Figures F-4 through F-7.

*See, for example, Raytheon Memo 72-DAK-69

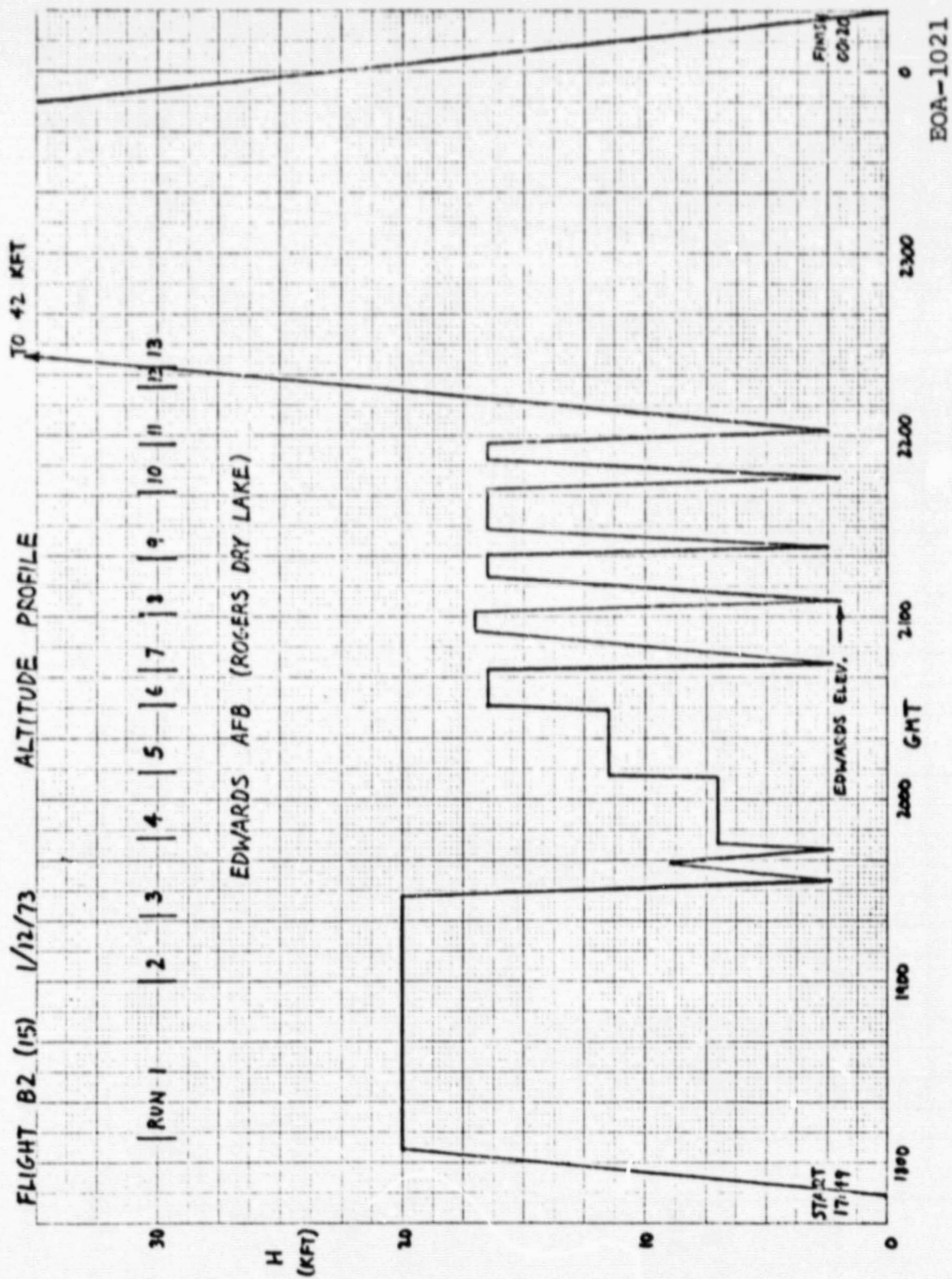


Figure F-4. Altitude Profile of CAT Flight B2

ORIGINAL PAGE IS
OF POOR QUALITY

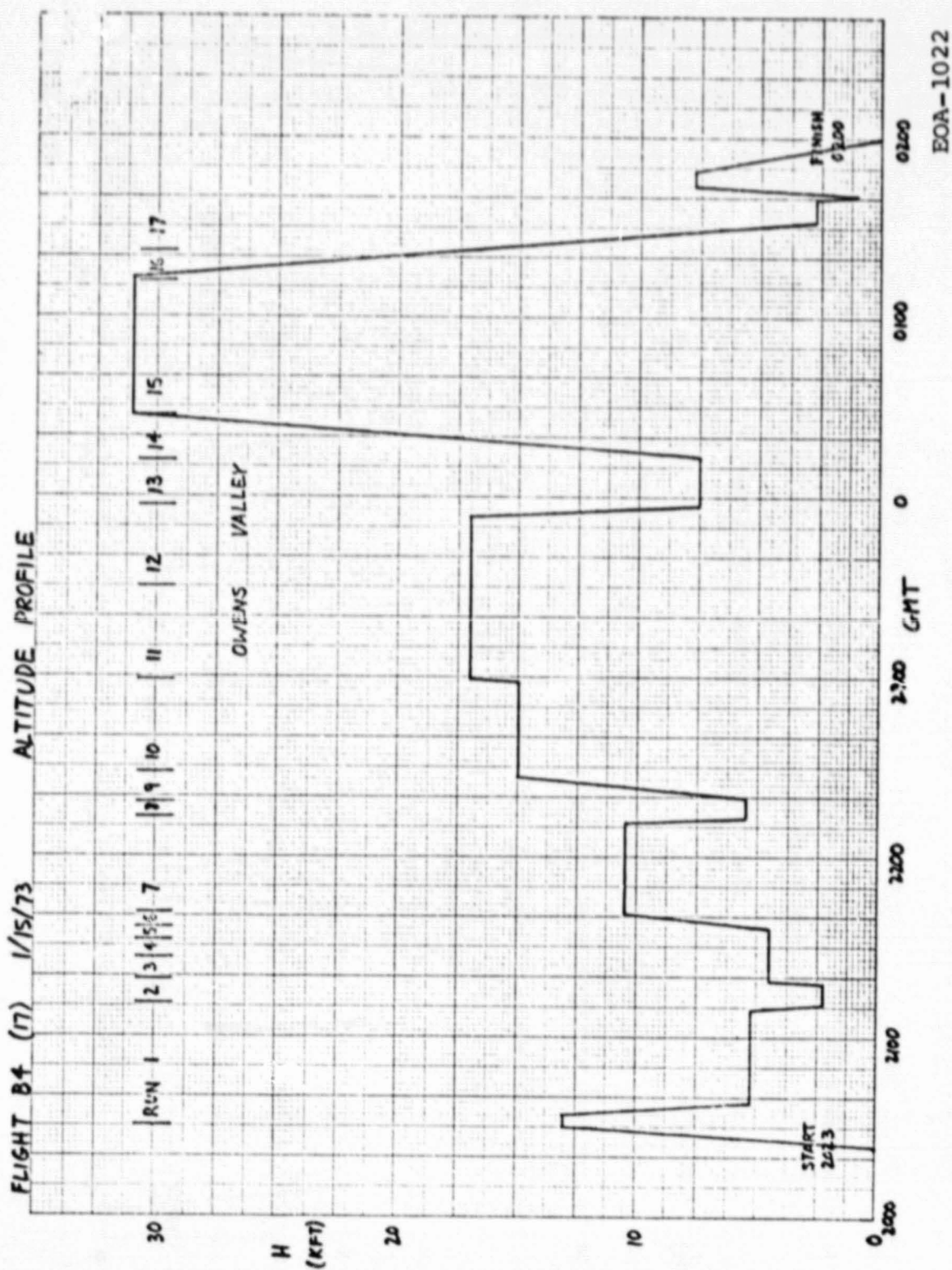


Figure F-5. Altitude Profile of CAT Flight B4

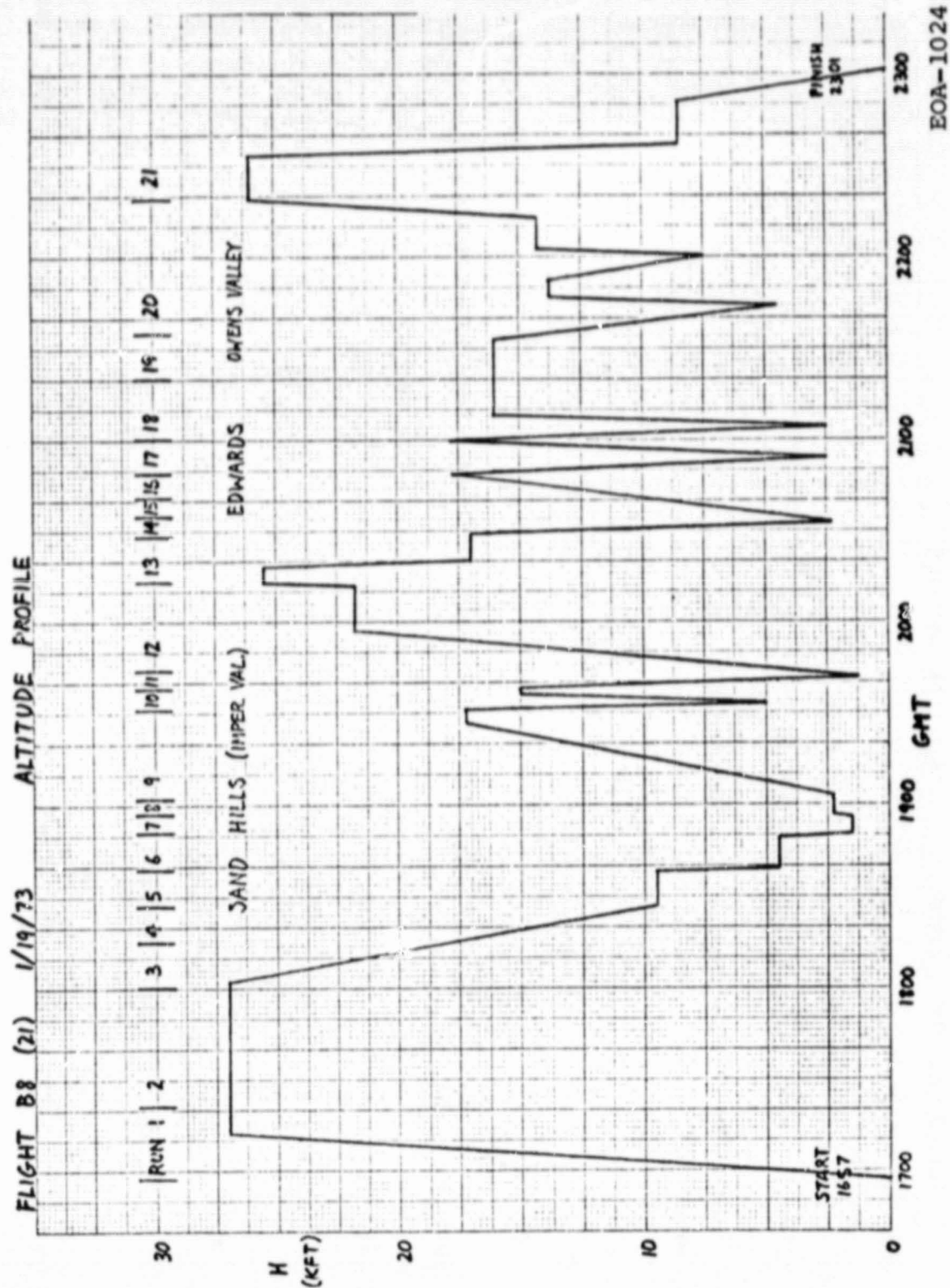


Figure F-7. Altitude Profile of CAT Flight B8

SECTION 2

RETURNS FROM GROUND AT EDWARDS AFB

The purpose of the flight tests at Edwards AFB was to check out and calibrate the CAT laser system. The aircraft engaged in steep descents against a uniform target, Rogers Dry Lake, with the laser operating continuously. The resulting measurements of signal-to-noise ratio were compared with various theoretical models of the laser system for the calibration. To calibrate the target, a sample of the dry lake bed was taken back to the lab and reflectivity measurements were made at the same angle of viewing.

The conclusions of the Edwards tests are:

1. The CAT laser system worked well, providing consistent results with signal-to-noise ratios as high as 42 dB. The data best fit the theoretical curve with the receiver focussed around 6000 feet, and with only 2 dB of unexplained loss.
2. The measured signal-to-noise ratios follow roughly the same slope as the 1972 test returns but are ~17 dB higher. The improvement is due to a higher laser output and the substitution of the HgCdTe detector.
3. The wide variations in signal level from pulse to pulse, at times exceeding 30 dB, are caused primarily by atmospheric scintillation. The other sources - target scintillation, frequency tuning of the receiver and laser instability - have smaller effects.
4. There may be no improvement in signal-to-noise ratio by pulse integration. The variation in signal level from

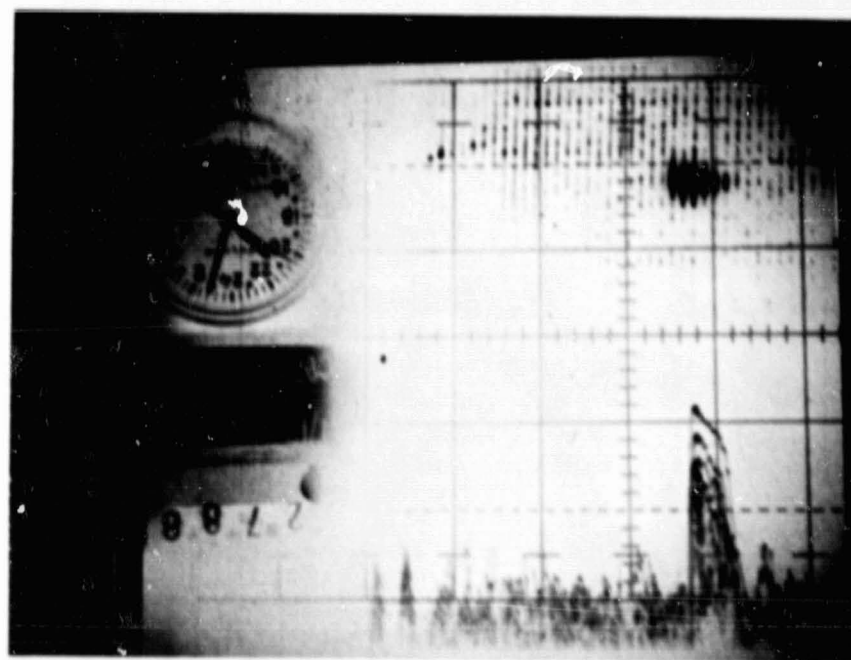
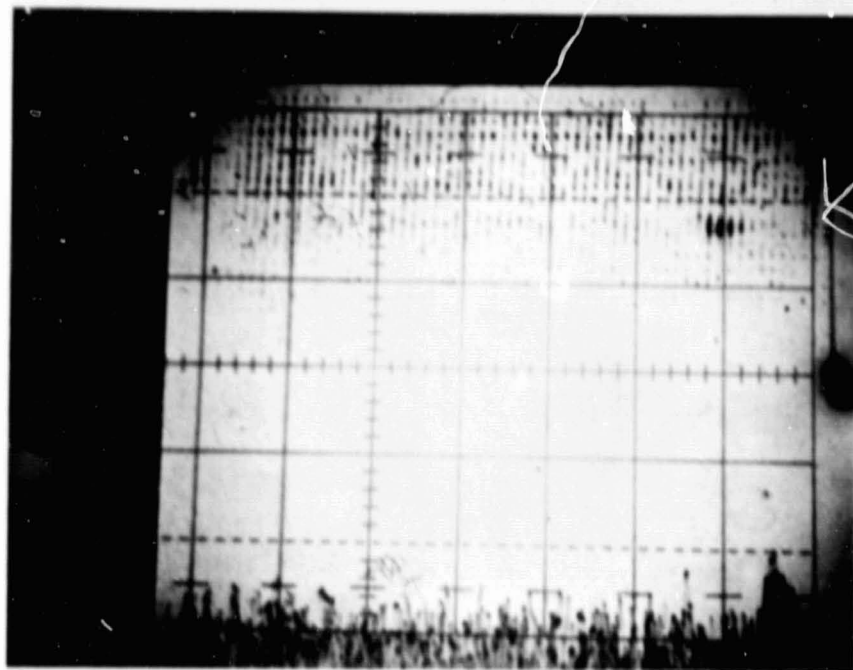
atmospheric scintillation was so great that the SNR for an integrated series of pulses was hardly better than the peak single-pulse SNR. This conclusion may not extend to the thinner air at higher altitudes where the CAT laser will be operating.

2.1 DESCRIPTION OF DATA

The signal-to-noise ratios during the flights were recorded by photographing the A-scope display of intensity vs. range with a sequence camera. The exposures were spaced at 1.2 second intervals and lasted 0.1 second to cover 14 to 16 pulses each. Since the reading of signal-to-noise ratio from the A-scope photographs is not at all obvious, especially when signal levels varied by as much as 30 dB on a single photograph, some consideration was given to the proper criterion for reading the ratio. The criterion and reasons for the wide signal variation are explained in Section 2.4.2.

Sample sequence camera photographs during one of the dives are shown in Figure F-8. The intensity (power) is plotted on the ordinate at 10 dB/box (log scale) and the range on the abscissa at 2 nautical miles/box on the A-scope. Each line represents the return on an individual pulse. The range-velocity indicator (RVI) display is shown at the top of each photograph and the 24-hour clock in the upper left corner, shown upside-down to properly orient the A-scope. The zero-range line is just to the right of the clock.

The return from the ground is obvious in each photograph, even at the maximum display range of 16 nautical miles. The RVI display confirms the presence of the signal indicated on the A-scope. (The slight offset between A-scope and RVI signals at the maximum range is due to a calibration inaccuracy.) The approach of the ground target with succeeding photographs is dramatically shown. The target return progresses from 11 nautical miles (SC photo 2753) to 2.4 nautical miles (SC photo 2838) in 102 seconds for an average

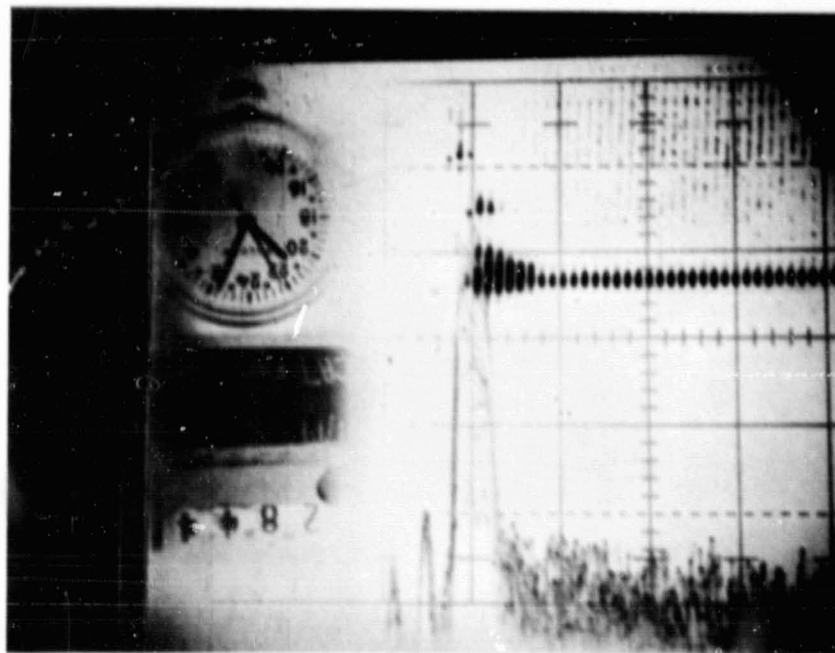
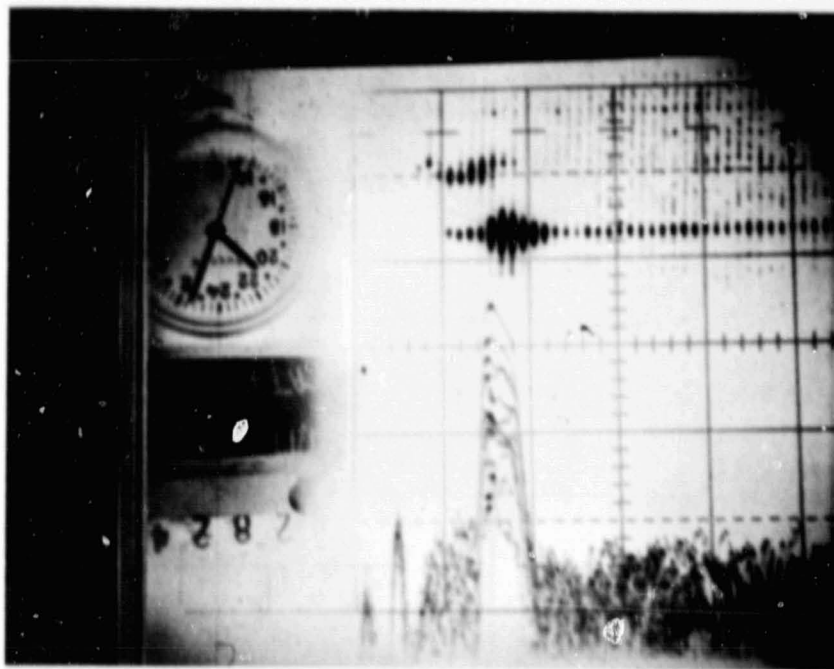


EO-590

Figure F-8. Sequence Camera Photos of A-Scope and RVI During
Dive at Edwards (Run 18 of Flight B8, 1/19/73)
(Sheet 1 of 2)

ORIGINAL PAGE IS
OF POOR QUALITY

F-17



EO-591

Figure F-8. Sequence Camera Photos of A-Scope and RVI During
Dive at Edwards (Run 18 of Flight B8, 1/19/73)
(Sheet 2 of 2)

range rate of 303 knots. The velocity of the aircraft as listed in the data print-outs is approximately 300 knots during this dive. The excellent matching of velocities shows that the laser beam was hitting the same general area of the dry lake throughout the dive.

The width of the signal is just under a nautical mile (measured at a few dB below the peaks), or 10 microseconds in time. This is roughly the pulse length, nominally set at 8 microseconds during the dive. Since the bandwidth at 250 KHz was higher than the matched filter value, the pulse shape is roughly preserved in the traces. They show a decay of 4 dB from beginning to end of the pulses as in SC photo 2824, which is in agreement with pre-flight measurements. The photographs also show that the laser power is down by at least 30 dB from the peak outside the borders of the pulse.

The RVI display shows an interesting effect toward the end of the dive. A second signal appears on the RVI offset in frequency from the ground return, for example in SC photo 2824. This second return is from the atmosphere. It extends from the minimum measurable range out to the ground return where it abruptly ends. It is much weaker in the early photographs of the dive which is to be expected since the air is thinner at the higher altitudes. There is no return on the A-scope because the latter was set at the frequency of the ground return. The frequency offset of the two signals is due to a ground wind. It is measured to be 1.8 MHz which corresponds to a velocity component along the beam of 32 ft/sec. The ground wind speed as listed on the data print-outs was roughly 60 ft/sec., and it was 60 degrees away from the aircraft heading. Therefore, its component along the laser beam is $60 \cos 60^\circ$ or roughly 30 ft/sec., which is in excellent agreement with the value of 32 ft/sec. deduced from the RVI display. This is a verification that the RVI display properly showed a difference in velocity, in this case between the wind and ground.

2.2 SIGNAL-TO-NOISE RATIO MEASUREMENTS

Good test data were obtained on three of the dives at Edwards:

Run 7 of Flight B2 (1/12/73)
Run 9 of Flight B2 (1/12/73)
Run 18 of Flight B8 (1/19/73)

On other dives the A-scope for the sequence camera did not work properly due to a faulty amplifier. There were occasional in-flight read-outs and Polaroid photos of the other A-scope, but these were not necessary since the three good dives yielded sufficient information.

The signal-to-noise ratio is given by the number of dB increments between the signal and noise levels. As explained in Section 2.4.1 the rms noise level is 3.4 dB below the baseline for most of the photographs*, and the proper signal level as defined by the standard signal-to-noise ratio equation is best represented by the peak signal. On some photographs all the signals were degraded. These were rejected as instances when the receiver was not tuned to the signal frequency due to the manual tuning procedure.

The signal-to-noise ratio was measured for the three good dives and plotted against range in Figure F-9. The highest signal-to-noise ratio exceeded 40 dB. Note how well the measurements from the different flights fall into a smooth, nearly straight-line channel. This excellent correlation adds justification to the selection of the peak signals for the signal-to-noise ratios. The signal-to-noise ratios for 1972 flight tests at Edwards are also shown for

*In earlier reports the rms noise value was judged by eye to be at the baseline, so the earlier plotted values of signal-to-noise ratio were about 3 dB too small.

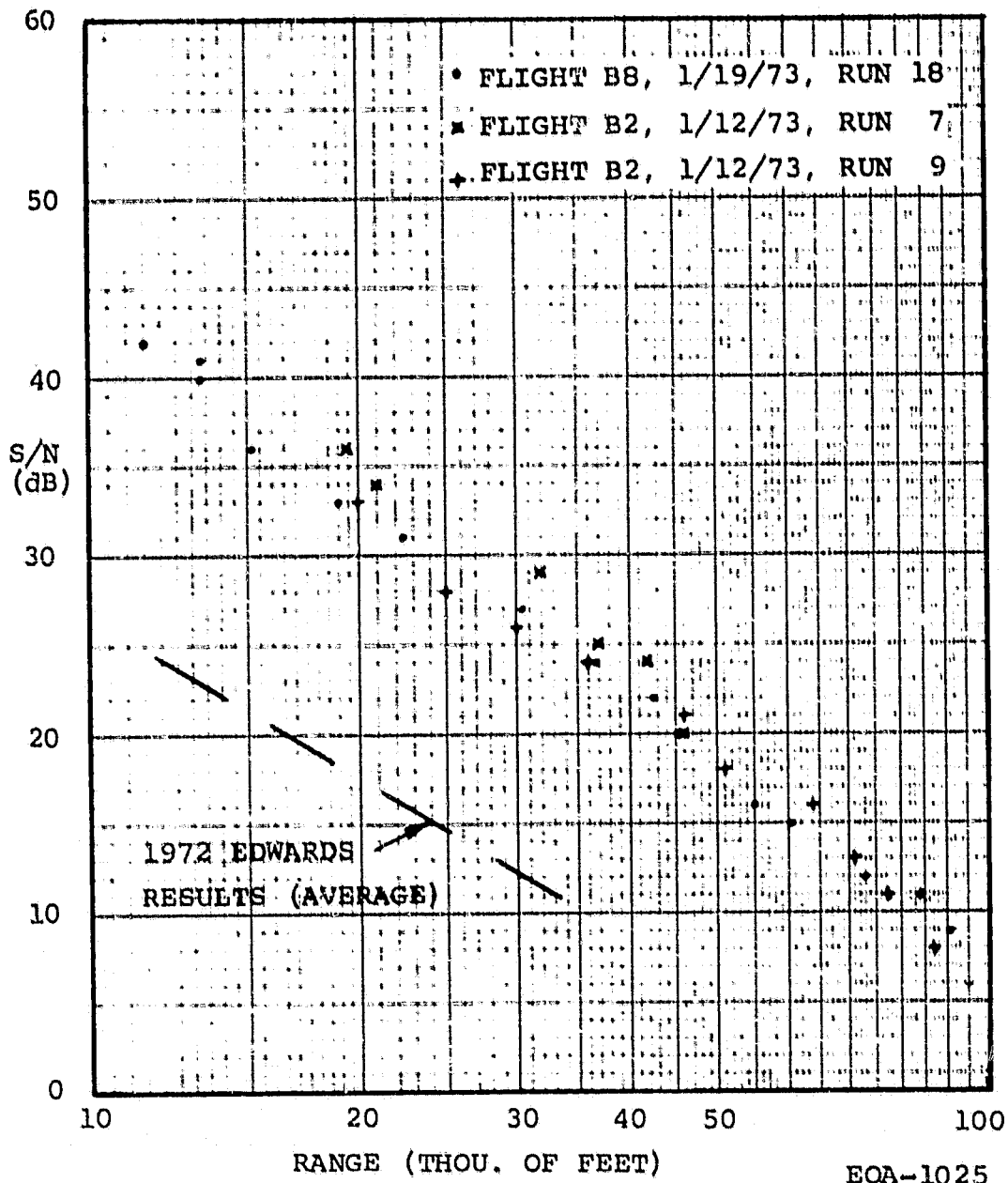


Figure F-9. Signal-to-Noise Ratio Measurements Against Ground at Edwards AFB During 1973 CAT Flight Tests

ORIGINAL PAGE IS
OF POOR QUALITY

comparison. The line is a rough average since the spread of those measurements was quite large, but it does show that the improvement for 1973 was roughly 17 dB. This improvement can be accounted for by two changes in the laser system - a better way of cooling the laser and the substitution of the mercury cadmium telluride detector for the copper-doped germanium detector.

2.3 COMPARISON WITH THEORETICAL SIGNAL-TO-NOISE RATIO

The signal-to-noise ratio equation for the CAT laser system, which is coherent and pulsed with a common aperture for transmission and reception, is given by:

$$\frac{S}{N} = \frac{E \sigma^i \eta_d \eta_s \eta_a d^2}{16 h \nu [R^2 + (\pi d^2 / 4 \lambda)^2 (1 - R/R_f)^2]} \quad (F-1)$$

against a target filling the beam. The detector is photovoltaic and the receiver is assumed to be matched to the pulse length. The symbols are defined and values specified in Table F-1.

The CAT laser system is supposed to be unfocussed (i.e., focussed at infinity), so that $R_f = \infty$. The physical size of the aperture is 12 inches but the effective size as defined by the $1/e^2$ intensity value is closer to 10 inches. The losses exclusive of the atmosphere and detector are estimated to be:

Optics (scattering, absorption, blockage)	3 dB
Extended diffuse target*, Gaussian LO, heterodyne inefficiency	5
Target depolarization	1
Receiver electronics (including bandwidth mismatch)	<u>4</u>
TOTAL	13 dB

*There is a loss of 3.4 dB with an extended diffuse target. This loss factor is explained and calculated in a paper by D. Fried, "Antenna Gain statistics" for a Heterodyne Receiver Laser Radar Viewing a Resolvable Target", Report No. TR-116, Optical Science Consultants, Oct. 1973.

TABLE F-1

PARAMETERS

<u>Parameter</u>	<u>Symbol</u>	<u>Value</u>
Signal-to-noise power ratio	S/N	
Laser pulse energy	E	12 mJ
Modified target cross section	σ'	0.05 ster ⁻¹
Target range	R	
Range of focus (beam & FOV)	R_f	
Aperture diameter	d	10 in
System efficiency	η_s	0.05
Detector quantum efficiency	η_d	0.25
Atmospheric transmission	η_a	
Wavelength	λ	1.06×10^{-5} m
Energy per photon	h ν	1.9×10^{-20} J

Thus, the system efficiency factor η_s is 0.05.

The critical parameter for the calibration is the target cross section, σ' . A sample of the dry lake was taken back to the lab, soaked in water and dried to simulate the dry lake condition. The reflectivity was then measured incoherently at 10.6 microns as a function of angle. At 10 degrees from the horizontal the back-scatter reflectivity is:

$$\rho(\pi) \approx 4 \times 10^{-3} \text{ ster}^{-1}$$

To convert this value to the target cross section, the basic definitions of the parameter are utilized:

$$\frac{\text{Reflected Intensity (W/ster)}}{\text{Incident Power (W)}} = \frac{\sigma'}{4\pi} = \rho(\pi)$$

So,

$$\sigma' = 4\pi \rho(\pi) = 0.05 \text{ ster}^{-1}$$

By substitution of the values in Table F-1 into Equation (F-1), the signal-to-noise ratio without atmospheric losses ($\eta_a=1$) is calculated. It is plotted against range in Figure F-10. The experimental results are included for comparison, and the difference is indicated by a dashed line. There are several possible causes of this difference:

1. Atmospheric attenuation;
2. Atmospheric turbulence;
3. The receiver or transmitter focussed at some finite range;
4. The effective aperture smaller than 10 inches.

Only factors varying with range can explain the difference.

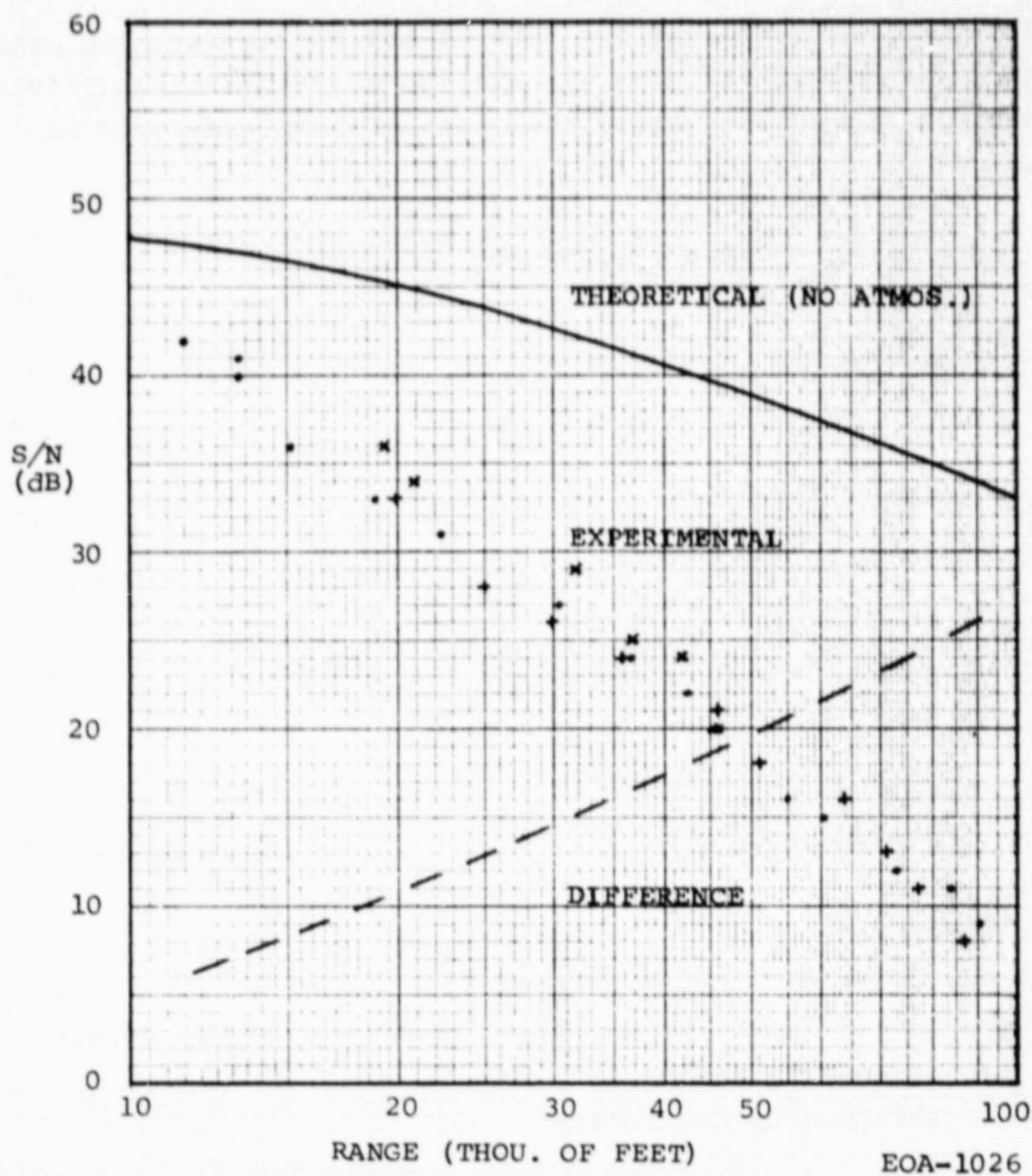


Figure F-10. Comparison of Theoretical and Experimental Results for Edwards Tests, Flights B2 (15) and B8 (21)

2.3.1 ATMOSPHERIC ATTENUATION AS POSSIBLE CAUSE OF DIFFERENCE

The atmosphere accounts for some of the difference, but does it account for all of it? The attenuation coefficient required to explain the difference is calculated with a formula derived as follows:

$$\eta_a = \exp \left(\int 2\mu(R) dR \right)$$

$$\frac{d\eta_a}{dR} = 2\eta_a\mu(R)$$

$$\text{So, } \mu(R) = \frac{1}{2} \frac{(\delta\eta_a)/\eta_a}{\delta R} = \frac{1}{2} \frac{\delta(\log_e \eta_a)}{\delta R} = \frac{2.30}{2} \frac{\delta(\log_{10} \eta_a)}{\delta R}$$

Since $S/N \propto \eta_a$ and μ in dB/km = $(10/2.30) \mu$ in km^{-1} ,

$$\mu(R) = \frac{1}{2} \frac{\delta(S/N)}{\delta R} \quad (\text{F-2})$$

where $\delta(S/N)$ is the change in SNR in dB not accounted for by a change in range, $\mu(R)$ is in dB/km and δR in km. Thus, the required attenuation coefficient is determined by measuring the slope of the difference curve plotted on a linear graph of S/N in dB vs. range and dividing by 2. This was done with the result plotted in Figure F-11 as the long dashed line. The range was converted into altitude by the formula,

$$H = H_0 + R \sin \phi = 1.97 \text{ Kft} + R \sin 7^\circ$$

where H_0 is the altitude of the dry lake and ϕ the depression angle of the laser beam.

To decide whether this variation of attenuation coefficient is

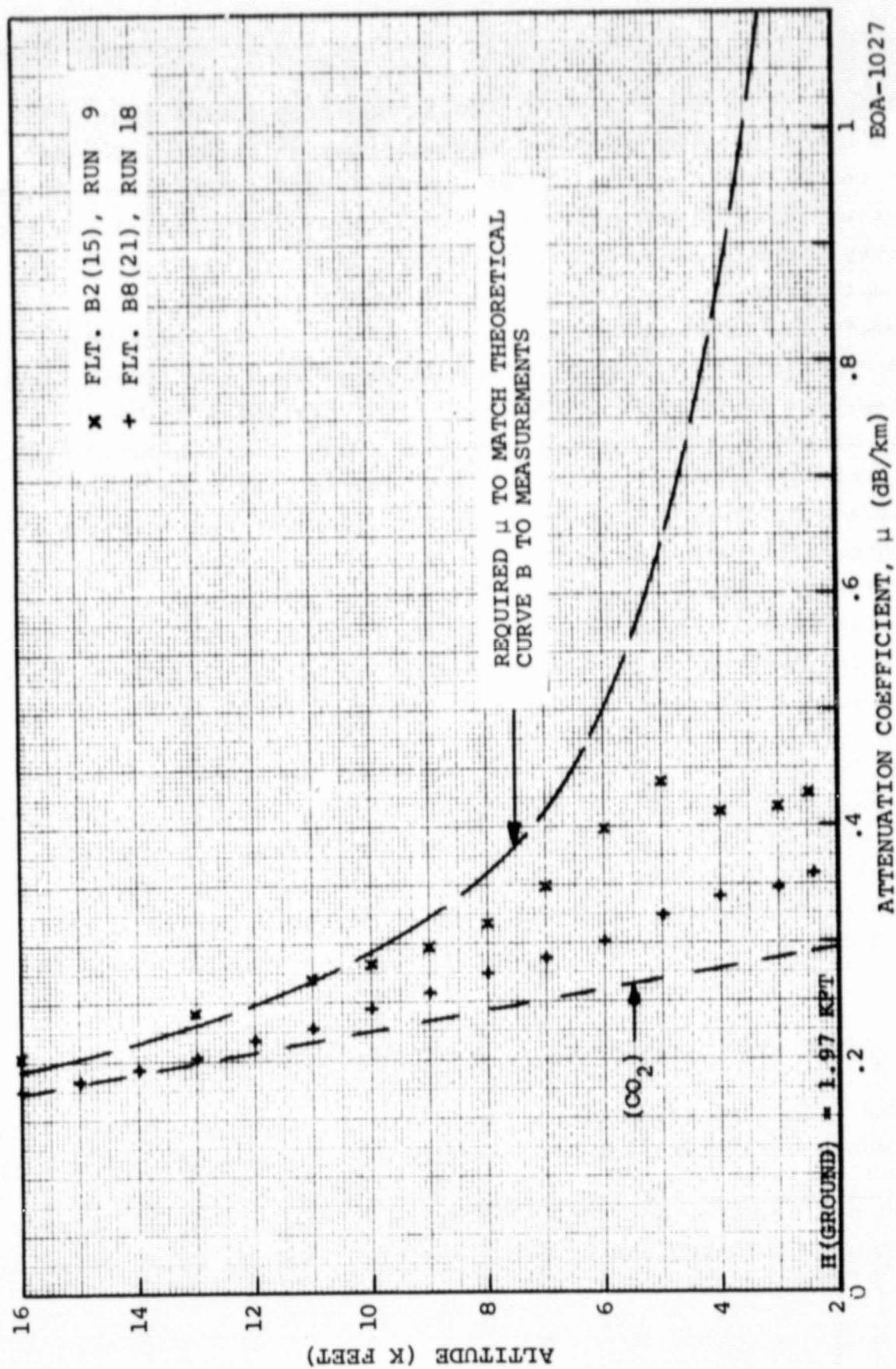


Figure F-11. Atmospheric Attenuation Coefficient for Dives at Edwards

realistic, it is compared with the attenuation coefficient calculated from temperature and humidity data measured in flight. The two major constituents of the atmosphere attenuating CO₂ laser radiation are carbon dioxide and water vapor. Aerosols are a third constituent but they are believed to have a lesser effect in clear weather. The attenuation due to the carbon dioxide was measured by P. Yin and R. Long* as a function of its concentration and an attenuation curve varying with altitude was drawn based upon the results. The contribution is plotted in Figure F-11 as the short dashed line. The effect of water vapor depends upon the temperature, relative humidity and total atmospheric pressure. These parameters were measured in-flight and recorded on the data print-outs. The way in which these parameters influence the attenuation of 10.6 micron radiation was measured by J. McCoy, D. Rensch, and R. Long**. A calculation of the attenuation from water vapor is shown in Attachment 1, and the result for the two days of good data is plotted in Figure F-11. The pluses and crosses show the expected overall attenuation coefficient.

A comparison of the required attenuation coefficient to explain the difference between theoretical and experimental SNR (long dashed line in Figure F-11) and the calculated coefficient (pluses and crosses) shows that the atmospheric attenuation cannot account for all of the difference, especially as evidenced by the huge attenuation required at low altitudes. Therefore some other explanation is required.

2.3.2 ATMOSPHERIC TURBULENCE AS POSSIBLE CAUSE OF DIFFERENCE

The effect of atmospheric turbulence is examined in Section 2.4.2. It is shown that turbulence can and probably did degrade the signal

*P. Yin and R. Long, App. Op., Vol.7, No.8, Aug. 1968, pp. 1551-3.

**J. McCoy, D. Rensch and R. Long, App. Op., Vol.8, No.7, July 1969, pp. 1471-7.

substantially during the dive over Rogers Dry Lake. However, the effect of turbulence is to degrade the signal by widely varying amounts. For some pulses the degradation can be more than 30 dB, but for others it may be less than 1 dB. In fact, for a sample of 14 pulses in each SC photograph the highest signal is likely to be degraded by less than 1 dB. Since just the highest signals were measured in reading the signal-to-noise ratio, these measurements then had little degradation from atmospheric turbulence.

2.3.3 FOCUSING OR APERTURING AS POSSIBLE CAUSE OF DIFFERENCE

To examine the effects of focussing the receiver or having an effective aperture less than 10 inches, the signal-to-noise ratio is calculated with Equation (F-1) for selected conditions of focus. The range of focus and aperture size are parameters in that equation. However, that equation applies to the situation where the beam and receiver are focussed at the same range. If the beam and receiver are focussed at different ranges, which is a realistic possibility in the CAT system, the equation must be modified. The beam is believed to have been properly collimated (focussed at infinity) because little change in beam size with range was observed at the test site. The receiver is focussed independently by varying the focus of the LO beam.

The signal-to-noise ratio is usually degraded when the transmitted beam and receiver are focussed at different ranges as opposed to a common range of focus. An approximate way to calculate the degradation factor is to assume the beam and receiver field-of-view are uniform cones. Then the degradation is given by the part of the beam outside the receiver field-of-view at the target, since this part does not contribute to the signal. The degradation factor is given by:

$$F \approx \frac{\text{Area of FOV}}{\text{Area of Beam}}$$

if Area of FOV < Area of Beam

$$\approx 1$$

if Area of FOV \geq Area of Beam

which is to be multiplied by the term on the right of the SNR Equation (F-1). (The factor F is actually greater than one when the beam is smaller than the field-of-view because the receiver is really more sensitive at its center where the beam is concentrated. The improvement can be as much as 3 dB at ranges much greater than the range of focus, but it will be neglected in the analysis.) The area of the beam or field-of-view is given by:

$$\text{Area} \approx \frac{\pi}{4} d^2 \left[\left(\frac{R}{R_f} - 1 \right)^2 + \left(\frac{\lambda R}{d^2} \right)^2 \right]$$

Therefore, the degradation factor is:

$$F \approx \frac{\left(\frac{R}{R_{fr}} - 1 \right)^2 + \left(\frac{\lambda R}{d^2} \right)^2}{\left(\frac{R}{R_{ft}} - 1 \right)^2 + \left(\frac{\lambda R}{d^2} \right)^2} \leq 1$$

where R_{fr} and R_{ft} are the ranges of focus of the receiver and transmitted beam. When the beam is unfocussed, the degradation factor is unity at ranges beyond twice the receiver focal range.

The signal-to-noise ratio was calculated and plotted in Figure F-12 for the following cases of receiver and transmitter focus and various aperture sizes:

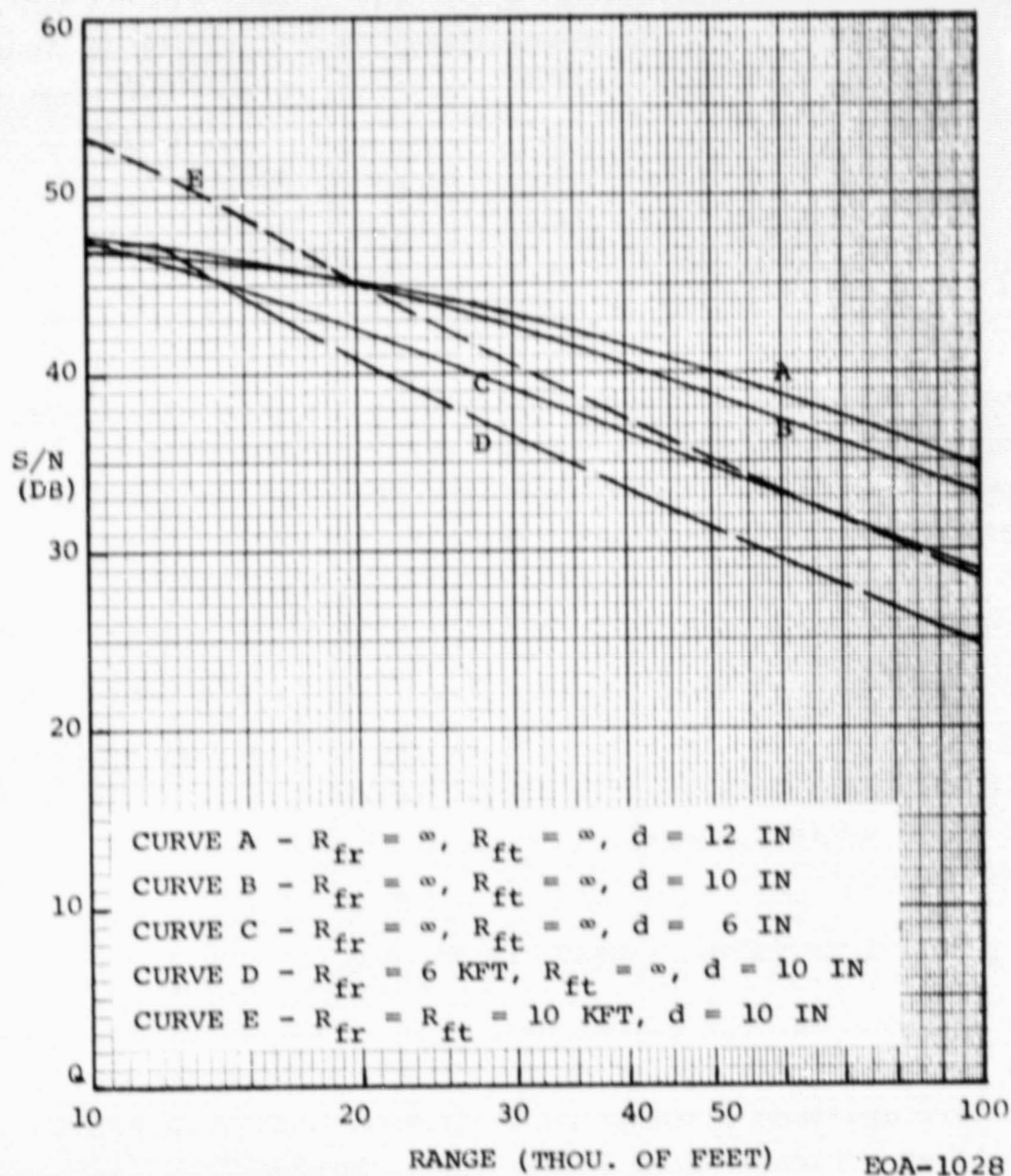


Figure F-12. Theoretical SNR of CAT Laser Against Ground (Rogers Dry Lake), No Atmospheric Loss

ORIGINAL PAGE IS
OF POOR QUALITY

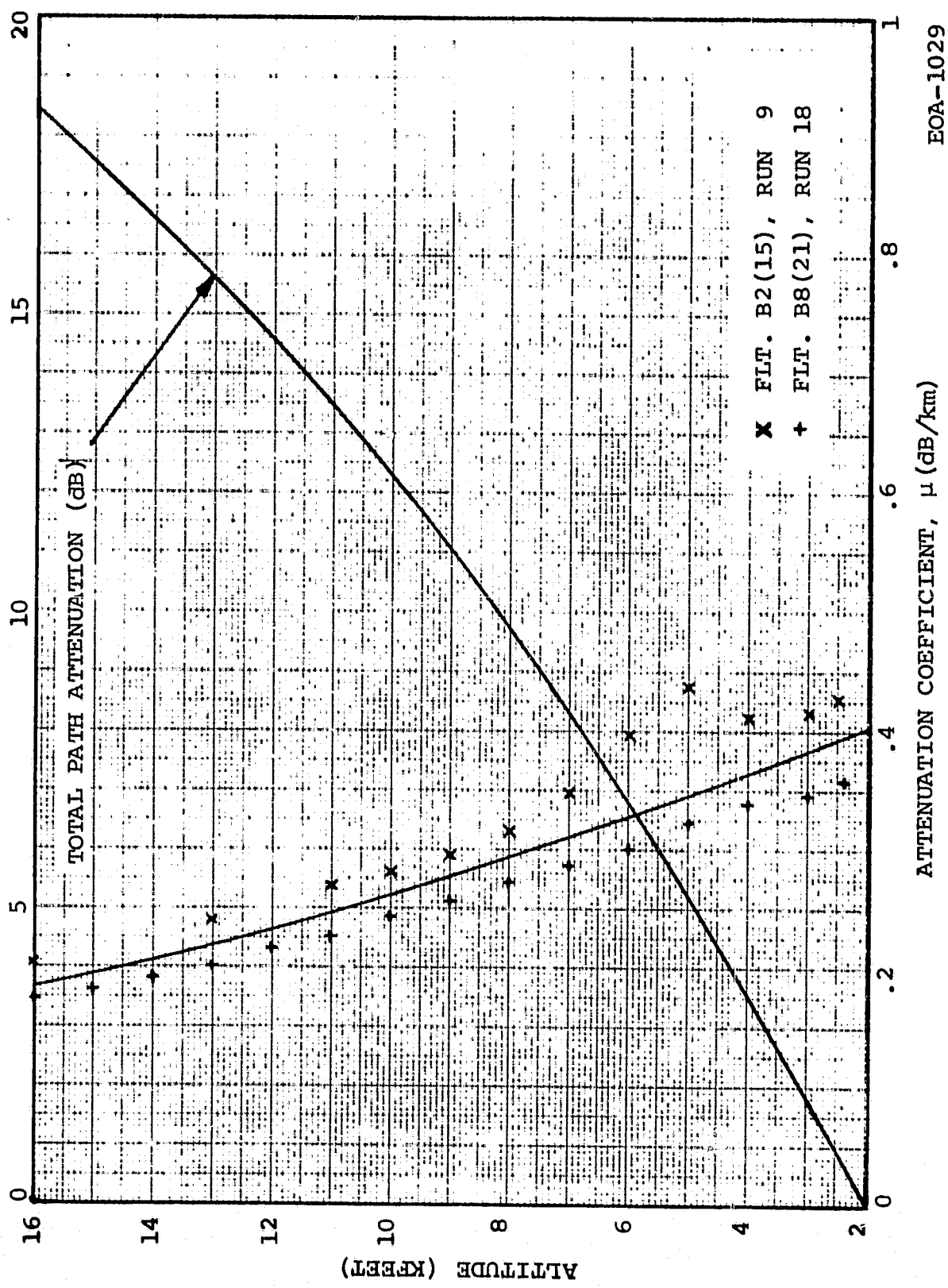
	<u>Receiver Focus</u>	<u>Transmitter Focus</u>	<u>Effective Aperture Diameter</u>
A.	∞	∞	12 inches
B.	∞	∞	10
C.	∞	∞	6
D.	6 Kft	∞	10
E.	10 Kft	10 Kft	10

Other cases were calculated but not plotted to avoid confusion in the graph. To discover how well the various theoretical models fit the experimental data, the missing ingredient of atmospheric attenuation has to be included. The attenuation is given by a line of best fit to the values calculated in Section 2.3.1 from the in-flight data and plotted in Figure F-11. This line of best fit is drawn in Figure F-13.

By including the atmospheric loss, the theoretical models can be compared to the experimental data. It is found that one model fits the data extremely well, as will be explained in the next sub-section.

2.3.4 THEORETICAL MODEL OF BEST FIT TO DATA

By applying (1) the atmospheric loss in Figure F-13 to the SNR curve D in Figure F-12, which is a receiver focussed at 6000 feet and an effective aperture diameter of 10 inches, and (2) a total system loss of 15 dB, which is 2 dB larger than the predicted loss (see Section 2.3), the signal-to-noise ratio curve in Figure F-14 results. The focus of the beam is unimportant because the curve remains essentially the same beyond 12 Kft (twice the receiver focal range) for any focus of the beam beyond 6000 feet. The SNR measurements on the three good data flights are also indicated in the graph. The excellent fit of the theoretical model to the experimental data points is obvious. Therefore, the Edwards data show that the



EOA-1029

Figure F-13. Calculated Atmospheric Attenuation for Edwards Dives
Line-of-Sight Angle $\approx 7.5^\circ$.

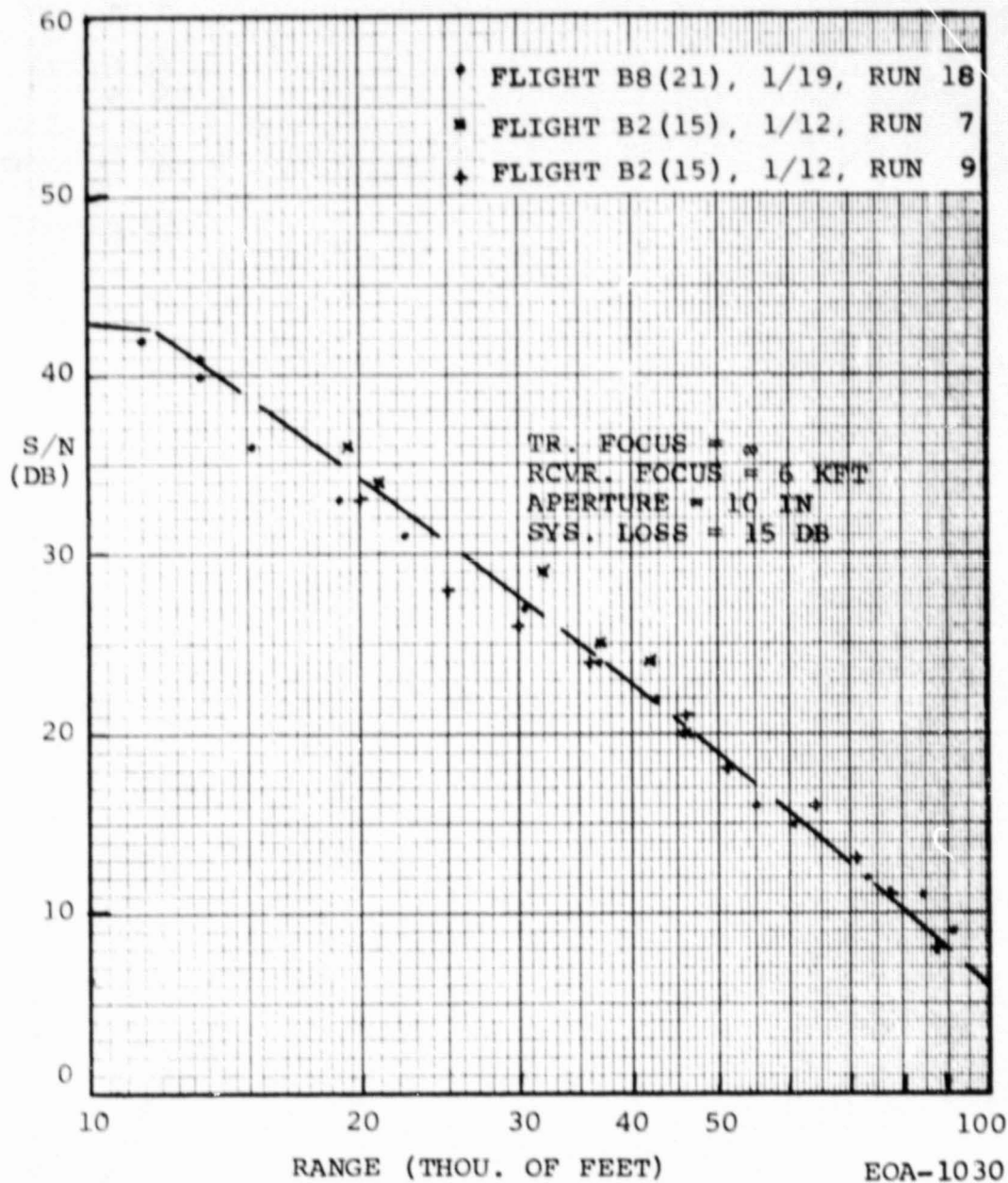


Figure F-14. Fit of Theoretical Curve D (With Atmospheric Loss and Additional 3 dB System Loss) to Measurements at Edwards

receiver was focussed at 6000 feet, the beam at 6000 feet or beyond, the effective aperture was 10 inches in size, and the system loss was 15 dB.

The likelihood that the CAT system fits this would depend upon the existence of factors which would make it fit the model. First, the effective aperture size was estimated to be 10 inches in size, so this value is quite acceptable. Secondly, the beam size was measured at several ranges out to two miles and was found to remain constant with range, so it was focussed way beyond 6000 feet. Third, a system loss of 15 dB is only 2 dB larger than the predicted value. The added loss may stem from the electronics which was assigned only 4 dB in spite of a mismatch of the bandwidth to the frequency width of the signal, or from the irregular distribution of the LO beam. Finally a receiver focus at 6000 feet is entirely possible based upon the focussing technique.

2.4 READING THE SIGNAL-TO-NOISE RATIO

Since the measurements of signal-to-noise ratio form the basis of the entire CAT flight test data analysis, the proper way to read this ratio deserves some close examination. The signal-to-noise ratios were read off sequence camera exposures of the A-scope which displayed signal and noise levels on a log intensity vs. time (or range) plot. Each exposure of the sequence camera lasted 0.1 second so that traces from approximately 14 pulses were imaged on each photograph.

Since the intensity is on a log scale, it would appear to be a simple matter to read the signal-to-noise ratio by measuring the number of dB increments between the signal and noise levels. However, it is not so simple for two reasons:

1. The proper noise level must be identified:

2. The signal levels in each photograph varied considerably, sometimes by more than 30 dB during the calibration dives at Edwards.

Therefore, the proper criteria for reading the signal and noise levels had to be established. Also, the wide variation in signal had to be explained.

2.4.1 NOISE LEVEL

The proper noise level in the normal SNR equation is the rms or 1 σ level. The problem is to identify this level on the A-scope plots.

The one, two and three sigma noise levels are exceeded for certain percentages of the samples assuming the noise is Gaussian:

1 σ :	31.7%	1.5 σ :	13.4%
2 σ :	4.6%	2.5 σ :	1.24%
3 σ :	0.25%	3.5 σ :	0.05%

Thus, the various σ levels can be determined by identifying the levels on the A-scope which are exceeded by the above percentages of the time. Now, the 1, 2, and 3 σ noise levels are not separated by these ratios on the A-scope display, that is, the 1 and 2 σ levels are not separated by 3 dB and the 1 and 3 σ levels by 5 dB as the ratios would suggest, because the square of the current is plotted on the A-scope rather than the current itself. The parameter plotted on the ordinate is:

$$\log_{10} \text{Power} \sim \log_{10} (\text{current})^2$$

Since the σ levels (and associated statistics) apply linearly to the current rather than the power, the real separations in dB between the various σ levels are double the ratios of currents, or

$$\begin{aligned}
 P_{2\sigma}/P_{1\sigma} &= 6.0 \text{ dB} \\
 P_{2.5\sigma}/P_{1\sigma} &= 8.0 \\
 P_{3\sigma}/P_{1\sigma} &= 9.5 \\
 P_{3.5\sigma}/P_{1\sigma} &= 10.9
 \end{aligned}$$

Therefore, the procedure for locating the 1σ level on the A-scope display is to find the level which is exceeded 4.6% of the time (if we use the 2σ level as the reference) and subtract 6.0 dB from that. As a check, the use of the 2.5, 3 and 3.5 σ levels as the reference and subtracting 8.0, 9.5 and 10.9 dB respectively, should yield the same A-scope level for 1σ . This comparison was, in fact, made with excellent correlation as will be explained.

In order to correlate percentages with absolute numbers, the total number of sampling intervals must be determined. The range gate of the receiver extended from 2 to 16 nautical miles for a total time span of 160 microseconds. The integration time of the receiver was approximately 2 microseconds since the bandwidth was 250 kHz. (The integration time is roughly verified by measuring the width of noise pulses on the A-scope.) Hence, there are $\sim 160/2$ or ~ 80 sampling intervals per pulse. Since each exposure of the sequence camera covers 14 pulses, the total number of noise sampling intervals per photograph is:

$$\frac{160}{2} \times 14 \approx 1100$$

Therefore, the numbers of times the various σ levels are exceeded are:

1 σ :	350	1.5 σ :	150
2 σ :	50	2.5 σ :	14
3 σ :	2.7	3.5 σ :	0.55

To (1) locate the 1 σ level and (2) check out the above theory, the numbers of noise pulses exceeding various intensity levels were measured on three sequence camera photographs and plotted in Figure 2-15. Then an attempt was made to fit the theoretical curve based upon the numbers listed above (with the separations of the σ levels in dB as determined earlier). An excellent fit was obtained when the 2 σ level is located at 2.6 dB above the baseline. Since the 1 σ noise level is 6.0 dB below the 2 σ level, the 1 σ noise level is (6.0 - 2.6) or 3.4 dB below the baseline for the portion of flight covering those particular sequence camera exposures. The noise was found to be quite consistent during each flight and between flights, so the 3.4 dB figure is rather general. As a check, the number of times the noise exceeds various levels can be compared with the values plotted in Figure F-15 for any sequence camera photograph. One exception is the latter portions of the dives at Edwards when the receiver overloaded due to the very high signals and a larger noise level resulted.

2.4.2 SIGNAL LEVEL

Typical signal returns for the dives at Edwards were shown in Figure F-8. It is apparent that the amplitude varied widely over the 14 pulses of each exposure - by more than 20 dB. The highest return is at 35 dB above the baseline in SC Photograph 2824, and the lowest return is at 12 dB. The amplitude also varied widely from one SC photograph to the next, as shown by a plot of all the peak signal-to-noise ratios of each photograph for a single dive at Edwards in Figure F-16. The photos were exposed at 1.2 second intervals. So, which amplitude

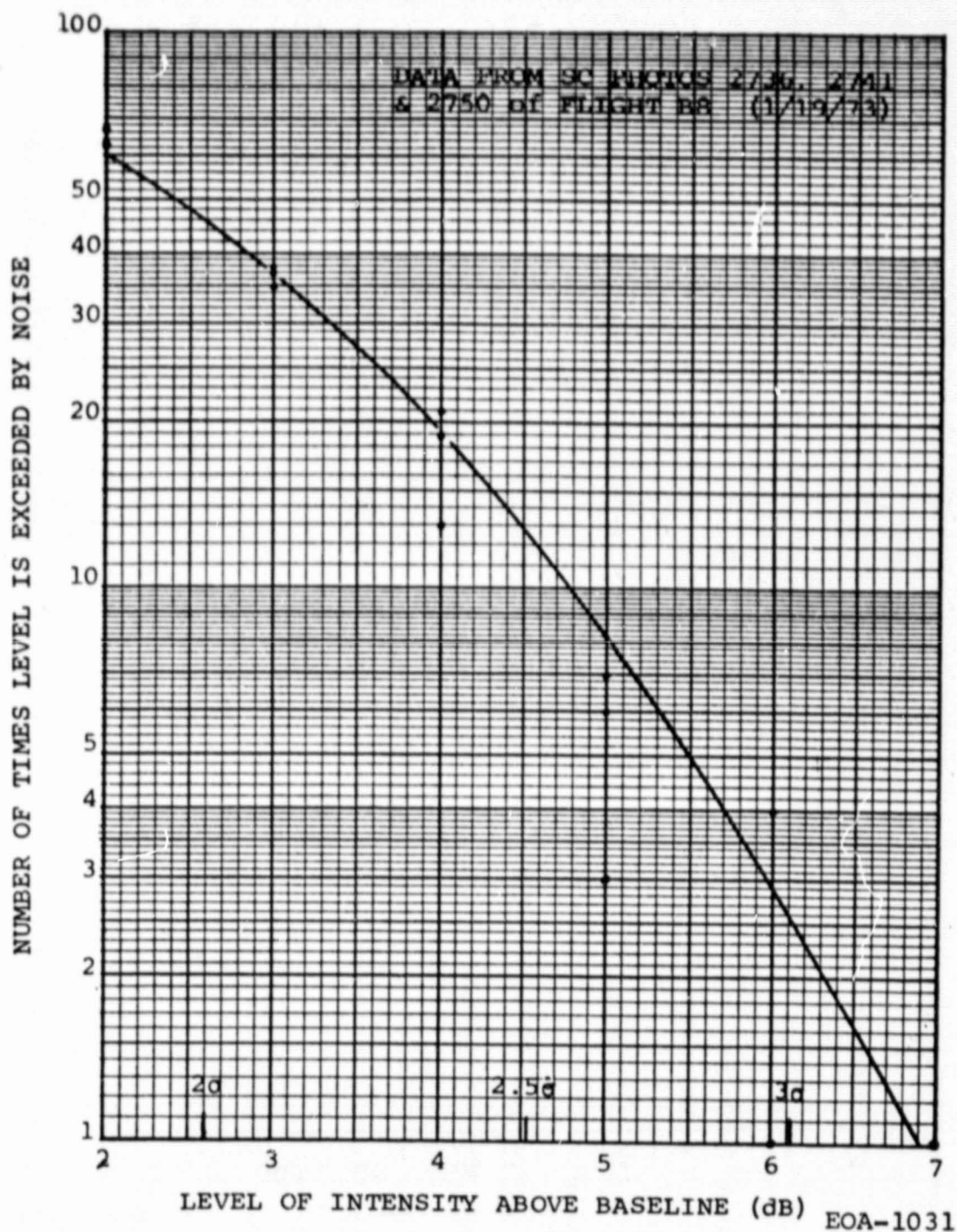


Figure F-15. Matching of Theoretical Noise Curve to Experimental Results

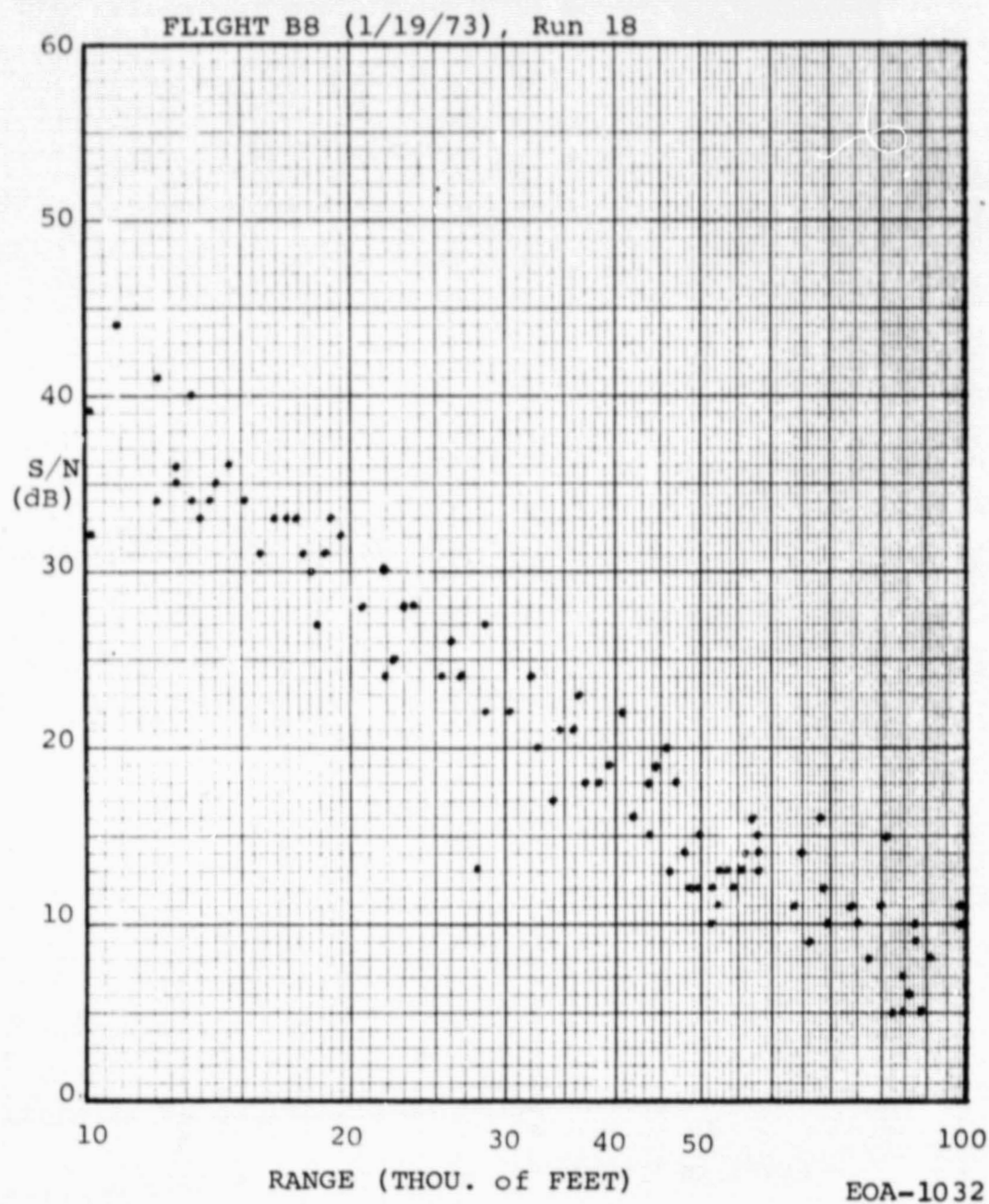


Figure F-16. Peak SNR Measurements of All Sequence Camera Photographs During Dive at Edwards

should be selected for the data analysis? In order to answer this question the causes of the wide signal variations are identified.

Possible causes are:

1. Target scintillation. Since the target consists of a collection of small specular reflectors, variations in amplitude from pulse to pulse out of the coherent receiver can be expected.
2. Atmospheric scintillation. The coherent receiver requires a plane wave input for its peak signal. Distortion of the wavefront by atmospheric turbulence (a variable refractive index) degrades the signal.
3. Frequency tuning. The frequency setting of the A-scope receiver was manually tuned during flight because the exact frequency was not known in advance and varied during each dive. The manual tuning procedure caused the receiver to periodically miss the signal.
4. Laser output variations. The high aircraft vibration during the dives may have caused the amplitude and frequency stability to vary or the laser output to be spread over several frequency modes.

Other causes which have a lesser effect are the LO shot noise and fluctuations in the photon arrival rate, and variations in the ground reflectivity (the dry lake is not precisely uniform).

The third cause - frequency tuning of the receiver - tended to produce drastic reductions of all the signals in the affected photographs and was, therefore, easily recognizable by comparison with other photographs. The tuning procedure consisted of varying the frequency setting manually in order to keep it on the signal. Since

the exposure time of the sequence camera was only 0.1 second, it is unlikely that the tuning is the source of any of the variations within a photograph.

The fourth cause - laser output variations - is not considered to be a significant source of the large SNR variations because the amplitude was found to remain steady at other times and a multi-frequency output probably would have shown up in the RVI or IVI display. However, this source is not to be ruled out, especially if the other sources cannot satisfactorily explain the variations.

The most probable causes are the target and atmospheric scintillation (causes 1 and 2 above). In order to verify that they are in fact responsible, the variations from these causes as predicted by theory are compared with the spread in the measured signal.

Measurements of the signal level of all pulses in two sequence camera photographs are listed in Table F-2. The intensities appear to follow a log normal distribution because the signal levels in dB, rather than the numerical ratios, are normally distributed. For example, the mean (average) of the logarithms is very close to the median (middle) of the logarithms in both photos which is a characteristic of a normal distribution - on SC photo 2824 the mean is 22.0 dB and the median is 22 dB, on SC photo 3057 the mean is 17.3 dB while the median is 17 dB. The same is obviously not true of the numerical ratios. A more rigorous analytical treatment involving the determination of moments can be applied to check out how well the data fit a normal distribution, but this would require an enormous amount of data points.

The significance of the distinction between normal and log normal distributions is that atmospheric scintillations are probably log normal while target scintillations are generally Rayleigh. The reasons

TABLE F-2

SIGNAL LEVELS IN SEQUENCE CAMERA EXPOSURES

SC Photo 2824 Flt. B8, Run 18		SC Photo 3057 Flt. B8, Run 18	
<u>10 Log (Above Baseline)</u>	<u>Numerical Ratio (Rel. to Baseline)</u>	<u>10 Log (Above Baseline)</u>	<u>Numerical Ratio (Rel. to Baseline)</u>
35 dB	3000	31 dB	1300
31	1200	24	250
29	800	22	160
27	500	21	130
26	400	19	80
23	200	17	50
22	150	16	40
20	100	14	25
17	50	11	12
16	40	9	8
15	30	6	4
13	20		
12	16		
Geometric mean = 22.0 dB		Geometric mean = 17.3 dB	
Arithmetic mean = 502 (27.0 dB)		Arithmetic mean = 187 (22.7 dB)	

are explained in memos by C. DiMarzio.* Since (1) the measurements appear to be log-normally distributed, and (2) the predicted variations from target scintillation are much lower than the observed variations, the conclusion is that the atmosphere is the primary cause of the variations. The atmospheric turbulence around the aircraft may be the main contribution to this effect.

If turbulence is the primary cause, then the highest value of the signal-to-noise ratio on each sequence camera photograph should be read since this is the closest value to the signal-to-noise ratio in an unperturbed atmosphere. In fact, the probability is 50 percent that the peak signal of 14 pulses in a sequence camera photograph will be within 7 per cent of the signal level for an unperturbed atmosphere.* As partial verification, the peak signal-to-noise ratios of numerous photos during a dive form a smooth, nearly straight line graph with range as shown in Figure F-9.

Although atmospheric turbulence is the primary cause of the signal variations there is still a contribution from target scintillation. Assuming that the target consists of an infinite number of diffuse scatterers, the peak signal of 14 pulses will generally be approximately 3 dB above the average. The fact that this spread was not observed is another indication that target scintillation was not the principal cause of the signal variation.

2.5 PULSE INTEGRATION

The pulse repetition rate of the CAT laser is around 160 pps. Since many pulses will hit basically the same air target in looking for Clear Air Turbulence, there is a possibility of improving the signal-to-noise ratio by integrating consecutive pulses. For signals of constant height and Gaussian noise, the improvement ratio is ideally the number of pulses. For example, if 50 pulses are integrated, the signal-to-noise ratio should be improved by 17 dB.

*Raytheon E/O Department Memo 73-CAD-08 and another to be published.

This amount of improvement will not exist for the CAT laser system. The key assumption of a constant signal level is not correct because atmospheric and target scintillations vary the signal widely, as shown by the returns at Edwards. In order to produce any improvement in the signal-to-noise ratio, the sum of the signal currents from N pulses must exceed \sqrt{N} times the peak signal current since the noise current is a factor of \sqrt{N} larger. For the dives at Edwards, the improvement was insignificant. This conclusion was reached after performing a pulse integration analytically on the signal levels in the two sequence camera photographs listed in Table F-2. The parameter in the table (Numerical Ratio) is the signal power level in arbitrary units. Thus,

$$P_s = K_1 \gamma$$

$$i_s = K_2 \gamma^{1/2} = K_3 \gamma^{1/2} i_n$$

where P_s and i_s are the signal power and current, γ the "numerical ratio" listed in the table, i_n the noise current, and K_1 , K_2 and K_3 are constants. The signal-to-noise ratio for a single pulse is:

$$\left(\frac{S}{N}\right)_1 = \left(\frac{i_s}{i_n}\right)^2 = K_3^2 \gamma$$

For integrating M pulses,

$$\left(\frac{S}{N}\right)_{\text{int}} = \left(\frac{\sum i_s}{\sqrt{M} i_n}\right)^2 = \frac{K_3^2}{M} (\sum \gamma)^2$$

assuming that the integration process is 100 percent efficient.
For SC photo 2824,

$$\sum \gamma = 225$$

$$M = 13$$

So

$$(S/N)_{int} = 3900 K_3^2$$

The peak single-pulse SNR is:

$$(S/N)_{1, peak} = 3000 K_3^2$$

So the improvement in signal-to-noise ratio from integrating 13 pulses is only:

$$\frac{(S/N)_{int}}{(S/N)_{1, peak}} = \frac{3900 K_3^2}{3000 K_3^2} = 1.3$$

or 30%. For SC photo 3057,

$$\begin{aligned} \Sigma \sqrt{\gamma} &= 111 \\ M &= 11 \end{aligned}$$

$$(S/N)_{int} = 1100 K_3^2$$

$$(S/N)_{1, peak} = 1300 K_3^2$$

and

$$\frac{(S/N)_{int}}{(S/N)_{1, peak}} = 0.86$$

So there is actually a loss of 14% in the SNR from integrating 11 pulses. Therefore, pulse integration does not really help in these two cases. At the higher altitudes where the CAT laser radar will be operating, the air is thinner and atmospheric scintillation is not as severe, so there should be a larger improvement. How much improvement is an unknown.

SECTION 3

AIR BACKSCATTER RETURNS

The eventual target of the Clear Air Turbulence laser radar is clear air. Therefore the returns from this target are of interest.

Returns from air were observed throughout the test series, at altitudes as high as 22,000 feet and at ranges as far as 6 miles. However, the sequence camera was not operated all the time, in fact, it was on only during 20 per cent of the good data flights on the average, and much of that was for the dives at Edwards or the Owens Valley runs. Therefore, the sequence camera seldom recorded data at the higher altitudes where some clear air returns were observed on the Intensity/Velocity Indicator (IVI). Hence the data analysis here is confined to the lower altitude returns, i.e., below 10,000 feet.

The conclusions of the analysis are:

1. The SNR curve for the receiver focussed around 6000 feet appears to give the best fit to the measurements. Based upon the system loss of 15 dB determined from the Edwards data, the backscatter coefficient σ at five altitudes between 2 and 10 Kft varied from 0.7 to 7×10^{-9} per meter per ster. These values are roughly an order of magnitude less than the coefficients observed in the 1972 test series, probably due to the difference in air between summer and winter.
2. The signal amplitude fluctuated wildly with range on individual pulses, although the envelope remained reasonably constant from pulse to pulse. Numerous causes were postulated. The primary one appears to be target scintillation.

3. Pulse integration may have significantly improved the signal-to-noise ratio at the higher altitudes, but a more careful comparison of the IVI and A-scope returns is necessary before the improvement factor can be determined.

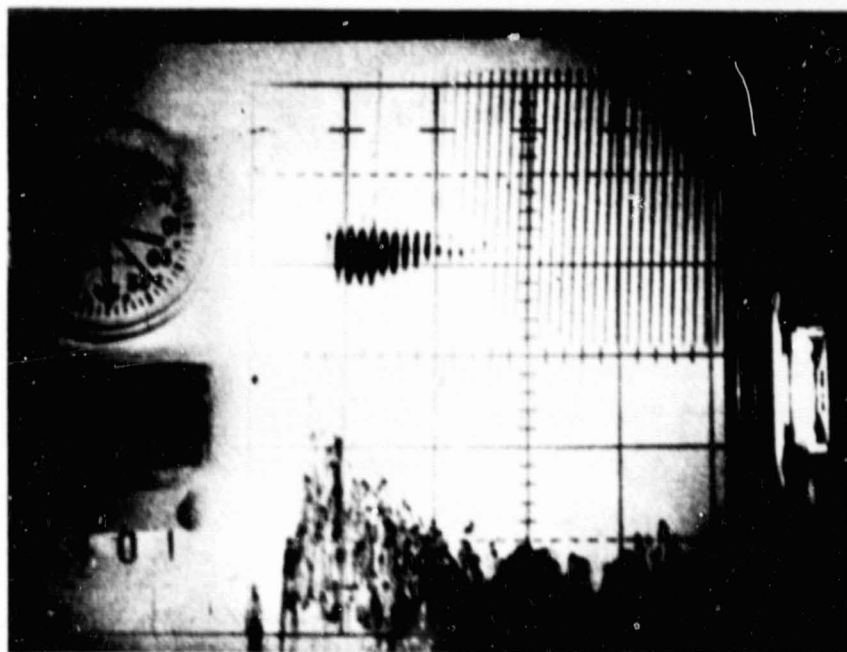
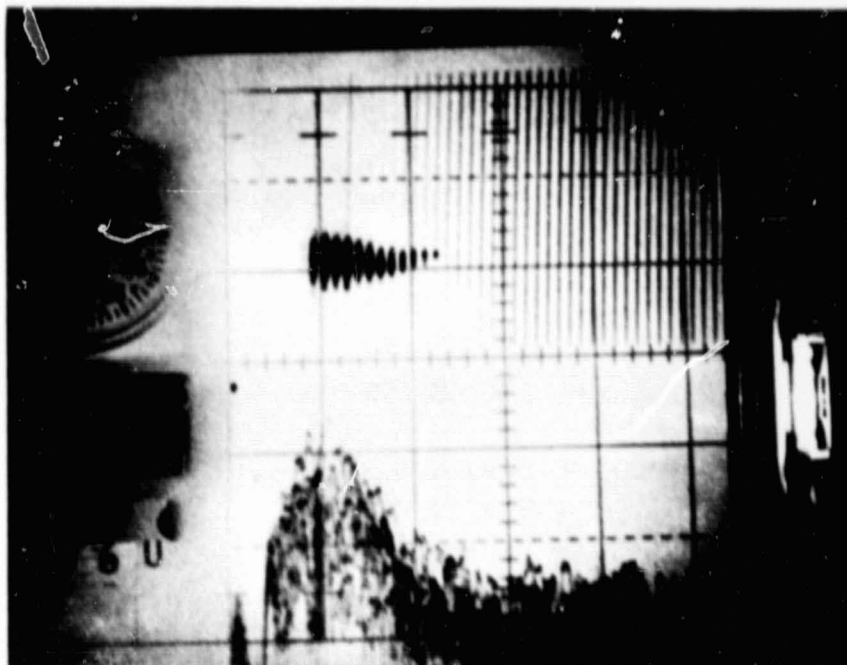
3.1 SIGNAL-TO-NOISE RATIO MEASUREMENTS

Typical A-scope plots of returns from air as recorded by the sequence camera are shown in Figure F-17. The intensity is plotted on the ordinate at 10 dB/box and the range on the abscissa at 2 nautical miles/box. (Although the zero range is the first vertical line at the left, just to the right of the clock, the low initial return in the first box should be disregarded since there is a delay in the receiver response.) The range/velocity indicator (RVI) output is plotted as the blackened area above the A-scope. The signal return is shown in the RVI to be slightly over one MHz in width at roughly the 5 percent borders.

The sequence camera photographs show that the backscatter return is contained within a well-defined envelope on the A-scope displays even though the signal returns on individual pulses fluctuate wildly with range. The signal-to-noise ratio was measured from the envelope. Reasons for the fluctuations are discussed in Section 3.3.

There were only a few times during the flight series when the backscatter was observable and the sequence camera was operated. These times are:

<u>Flight & Run</u>	<u>Approximate Time (GMT)</u>	<u>Altitude</u>
B2 (1/12), 3	19:41	4.7Kft
5**	20:23**	11.5**
B8 (1/19), 1*	17.11*	up to 24*
4*	18.17*	15*



EO-592

Figure F-17. Sequence Camera Photos of A-scope and RV1
Showing Backscatter Returns on Run 8 of
Flight B8

<u>Flight & Run</u>	<u>Approximate Time (GMT)</u>	<u>Altitude</u>
7*	18:50*	5*
8	18:58	2
9	19:05	4
20	21:42	6
20	21:56	9
21	22:55	3.6

*A-scope for sequence camera was not functioning properly.

**Target may not have been air.

In some of the above cases the air may not have been so clean. In fact, there were dust storms in the vicinity of one or two of the low altitude returns, although the signals were not from the dust storms.

The signal-to-noise ratios for Flight B8 as measured off the A-scope are plotted in Figure F-18. The signal level is measured from the envelope of the signal return (see Figure F-17). The proper rms noise level is 3.4 dB below the baseline as explained in Section 2.4.1. The axes of the graph were scaled to match the SNR plots in Section 2.

The highest signal-to-noise ratio is 20 dB, observed at low altitude at a range of two miles. The furthest range of measurement is 6 nautical miles. There is little consistency in the reduction of signal-to-noise ratio with altitude - for example, the return is greater at 8.8 Kft (designated by dots) than at the lower altitude of 3.6 Kft (designated by triangles). These measurements were made at well-separated locations. Also, the variation with range is not consistent - compare, for example, the circles and triangles. This inconsistency contrasts with the excellent correlation of returns from the ground on different dives at Edwards (see Figure F-9). The cause is probably the variation in particle density along the beam.

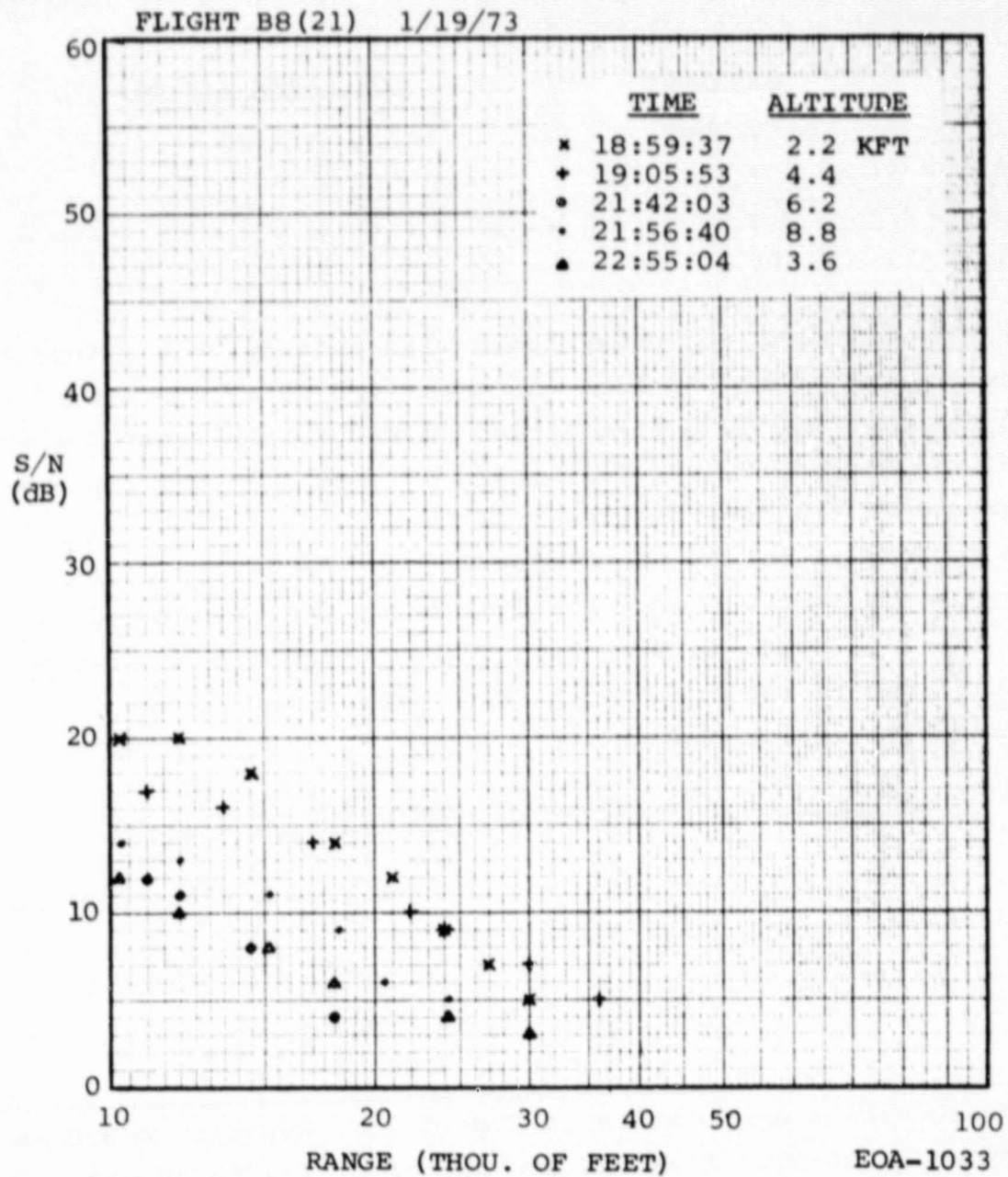


Figure F-18. Signal-to-Noise Ratio Measurements Against Air

Measurements against air were also made in the 1972 flight test series ("A" series).* The signal-to-noise ratios at a range of two miles were:

<u>Altitude</u>	<u>S/N (1972 series)</u>
7 Kft	4 dB
7.4	6.5
9.4	8.5
13.5	6.5

The rise in signal-to-noise ratio with increasing altitude suggests a haze layer around 10 Kft. A comparison of values around 7 Kft for the 1972 and 1973 test series shows that the improvement for 1973 was roughly 7 dB. This is 10 dB less than the improvement observed in the Edwards' tests of 17 dB (see Section 2.2). The discrepancy is due to the difference in scattering coefficient between summer and winter - the 1972 tests were conducted in August and the 1973 tests in January. The air tends to be clearer in winter than in summer, causing the backscatter coefficient to be less in the winter tests.

3.2 COMPARISON WITH THEORETICAL SIGNAL-TO-NOISE RATIO

The theoretical signal-to-noise ratio for a coherent pulsed laser radar against air is given by:**

$$\frac{S}{N} = \frac{EB\lambda \eta_d \eta_s \eta_a}{h\nu} \left(\tan^{-1} X_2 \tan^{-1} X_1 \right) xF$$

*Measurements are plotted in Figure 7 of Raytheon E/O Department memo 72-DAK-69. A correction factor of 3.4 dB should be added to the values in the graph due to improper reading of the rms noise level (see Section 2.4.1).

**Derived in article by C. Sonnenschein & F. Horrigan, App. Op. Volume 10, No. 7, July 1971, pp. 1600-4.

for a photovoltaic detector, where

$$X_{1,2} = - \frac{\pi d^2}{4\lambda R_f} + \left(\frac{4\lambda}{\pi d^2} + \frac{\pi d^2}{4\lambda R_f^2} \right) R_f \left(\frac{\lambda c \tau}{\pi d^2} + \frac{\pi d^2 c \tau}{16\lambda R_f^2} \right)$$

$F \approx 1$ for beam \leq receiver FOV

If the beam is unfocussed, it is smaller than the FOV at ranges greater than twice the range of receiver focus. The symbols are defined in Table F-1 of Section 2 with the following additions:

β is the backscatter coefficient in units of meter⁻¹ ster⁻¹

c is the velocity of light = 3×10^8 m/sec

τ is the receiver integration time ≈ 4 μ sec

The values are the same as listed in Table F-1 except for the system loss factor which is:

$$\eta_s \approx 0.2 \text{ (7 dB)}$$

The loss factor is 6 dB smaller due solely to definitions - the diffuse target factor (3.4 dB) and the mis-match of bandwidth to pulse length (~ 2.5 dB) are taken into account in the SNR equation rather than in the loss factor.

The two atmospheric parameters - the backscatter and attenuation coefficients - have not been assigned values. The attenuation coefficient is determined from the in-flight temperature, humidity and altitude measurements by the techniques outlined in Attachment 1. It determines the atmospheric transmission by the formula:

$$\eta_a = e^{-2\mu R}$$

where μ is the attenuation coefficient. The backscatter coefficient β is the biggest unknown. Very few data exist at 10.6 microns, and there may be none for altitudes above ground level. A rough value of β at ground level in winter is:

$$\beta_{10.6} \sim 10^{-8} \text{ m}^{-1} \text{ ster}^{-1}$$

It may easily be an order of magnitude higher or lower depending upon particle content. Particle density counts were made on some flights but the calculation of backscatter coefficient from the particle counts is not possible without information on the size, shape and refractive index of the particles. Also, there is no assurance that the particle samples, which are drawn in through a curved pipe protruding from the side of the aircraft, are truly representative of the air in the laser beam. A comparison of the particle counts and the backscatter returns as a function of altitude was made to see if there is a correlation.*

The theoretical signal-to-noise ratio was calculated with the aid of a computer and plotted in Figure F-19 for a backscatter coefficient of 10^{-8} per meter per steradian and no atmospheric loss. Five conditions of focus and effective aperture size are shown which are the same five conditions as examined for the Edwards data in Section 2. Note that the curves are virtually identical to the Edwards' signal-to-noise ratio curves except for a downward displacement of 23 dB, which indicates that the SNR equation against air can be approximated by the SNR equation against the ground with the appropriate reflectivity. The equivalent reflectivity of air in terms of the backscatter coefficient is:

$$\sigma'_{\text{air}} \approx 2.5 \times 10^4 \beta$$

or

$$\rho(\pi) \approx 2 \times 10^3 \beta$$

for the CAT laser radar, where β is in units of (meter-ster) $^{-1}$.

*See Raytheon memo EM 73-1115 by A. Jelalian

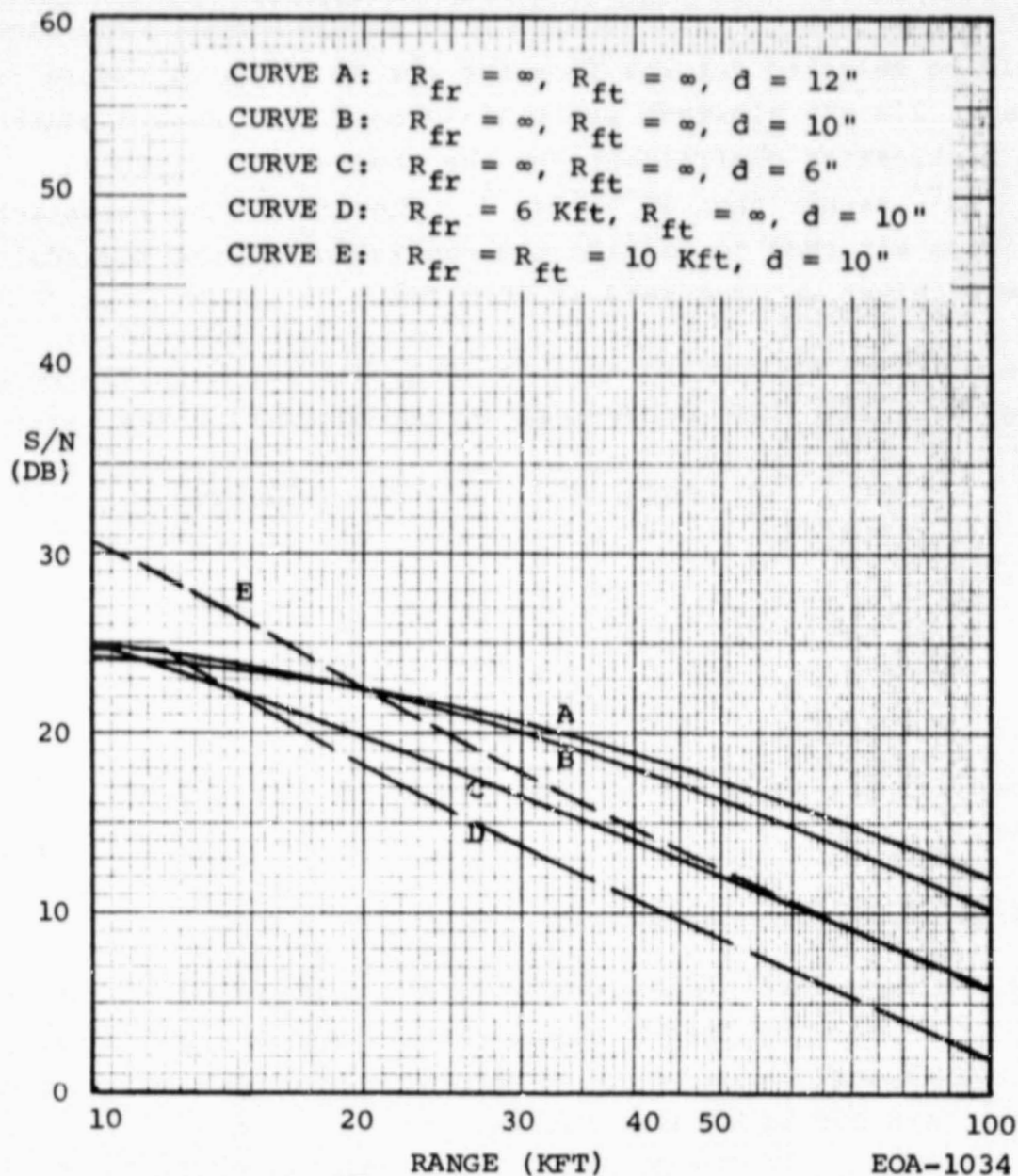


Figure F-19. Theoretical SNR of CAT Laser System Against Air (No Atmospheric Attenuation)

The curve of best fit for the Edwards data is the SNR plot for receiver focussed at 6000 feet, a receiver aperture of 10 inches, and a total system loss of 15 dB (curve D in Figure F-19). The same curve* fits well to selected returns from the air as shown in Figure F-20. The data at 2.2 Kft altitude at 18:59:37 on flight B8 are plotted, and the backscatter coefficient for the theoretical curve is $7 \times 10^{-9} \text{ m}^{-1} \text{ sr}^{-1}$ rather than $10^{-8} \text{ m}^{-1} \text{ sr}^{-1}$. Therefore, the backscatter returns from air tend to confirm the conclusion of the Edwards' tests, that the receiver was focussed at 6000 feet.

The backscatter coefficients for the data plots in Figure F-18, assuming the system loss determined in the Edwards' tests, are:

<u>Time</u>	<u>Altitude</u>	<u>$\beta_{10.6\mu}$</u>
18:59:37	2.2 Kft	$7 \times 10^{-9} \text{ m}^{-1} \text{ sr}^{-1}$
22:55:04	3.6	0.8
19:05:53	4.4	4
21:42:03	6.2	0.7
21:56:40	8.8	1

These coefficients apply to well-separated locations across California in winter.

3.3 CAUSES OF SIGNAL FLUCTUATIONS

The sequence camera photographs of the A-scope show that the backscatter return fluctuated rapidly with range on individual pulses. These fluctuations, which reach 20 dB over the 14 pulses of each photograph, are due to various causes:

- a. Target scintillation. The amplitude variations from target scintillation follow a Rayleigh distribution and could produce a complete nulling of the signal, depending upon the relative positions of the scatterers in a volume element.

*The equivalent system loss against air is 9 dB since there is a difference of 6 dB in the SNR equations due to differences in definitions as explained earlier.

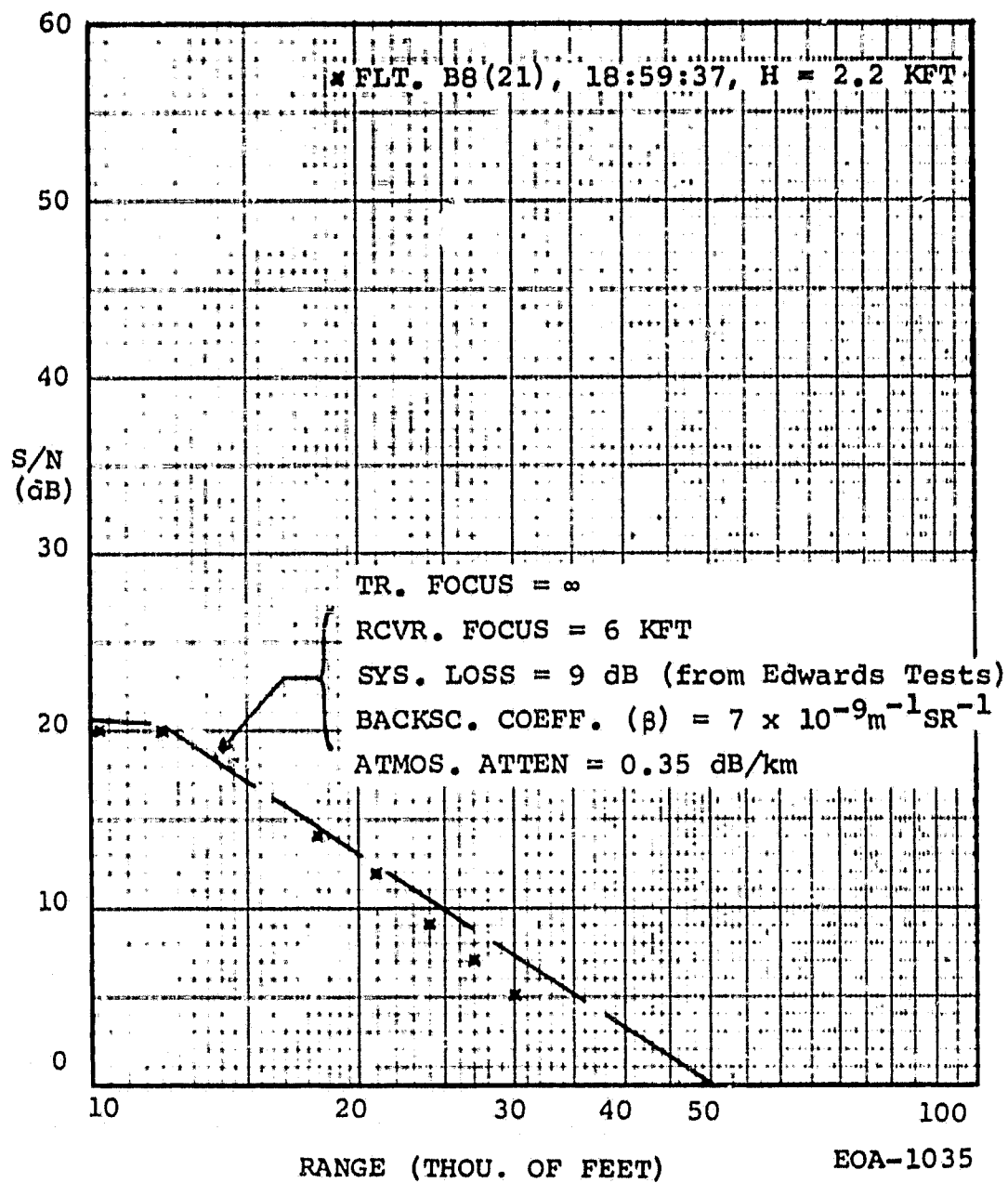


Figure F-20. Fit of Theoretical Air Backscatter SNR Curve to Measurements

ORIGINAL PAGE IS
OF POOR QUALITY

- b. Atmosphere scintillation. Distortion of the wavefront by variable refractive indices along the beam degrade the signal for a coherent receiver. However, atmosphere scintillation is not a major cause of the fluctuations because its effect is to reduce the signal at all ranges rather than at selected ranges which the data show. If turbulence near the laser were the major cause, the returns on individual pulses would be smoothly varying functions with range at various amplitudes.
- c. Laser instabilities. This is also ruled out as a major source of the signal variations for the same reason. The effect of a frequency or amplitude wander or multiple frequencies is to degrade the signal equally at all ranges rather than at the selected ranges actually observed.
- d. Variations in the particle content. If the signal return is primarily from a few large particles, then wide amplitude fluctuations would result from variations in the number of particles per sampling volume. However, such variations are not expected to result in a smooth, well-defined envelope as observed in SC photo 999. Also, the high signal levels indicate large numbers of particles are present.
- e. Doppler variations. Variable winds along the path produce doppler variations which could shift the frequency outside the bandwidth of the receiver. Since the bandwidth is 250 kHz, a change of only 4 ft/sec shifts the signal outside the receiver passband. However, since the wind patterns are not likely to change over the one second exposure time of each SC photo, the peaks and valleys should occur at approximately the same ranges on all the pulses, which was not observed.

- f. Noise. At the lower signal levels the noise during the signal is sufficient to produce noticeable variations in signal level. However, noise cannot account for the substantial fluctuations at the higher signal levels.

It is difficult to pinpoint which of the above possible causes is primarily responsible for the signal fluctuations, but if one had to be picked, it would be target scintillation. This contrasts with atmospheric scintillation as the primary cause of the signal fluctuations against a hard target at a given range (Rogers Dry Lake), discussed in Section 2.4.2.

The signal intensities were recorded not only on the A-scope but also on the IVI which plots intensity against frequency (velocity) at a given range. One important difference is that the IVI integrated 50 pulses while the A-scope was limited to single pulses. Hence, the effects of integration can be observed.* Preliminary indications are that pulse integration does improve the signal-to-noise ratio at high altitudes since some returns were observed on the IVI above 20,000 feet and there were no observable returns on the A-scope. However a more careful examination of the IVI output is necessary to determine the improvement factor.

*The calibrated IVI output was not available to me so I was not able to correlate IVI and A-scope returns - D.K.

SECTION 4

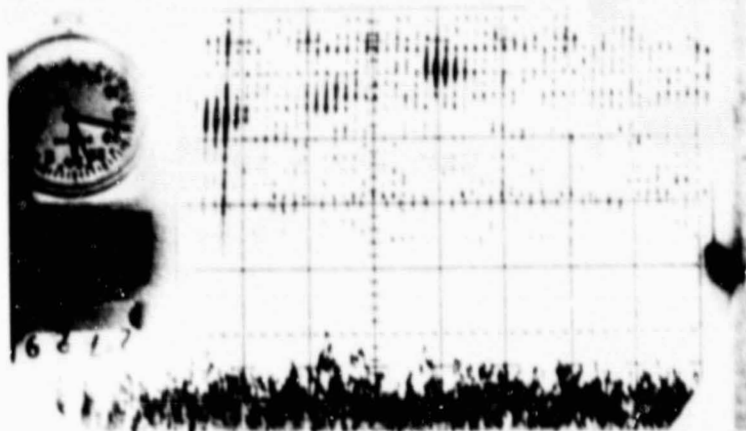
TURBULENT CLOUD TESTS

During the 1973 flight test program the aircraft flew into regions of severe air turbulence in order to evaluate the CAT laser performance against turbulence. The flights were conducted over the Owens Valley in California through cumulus clouds which were fed by high winds from adjacent mountain ranges. The laser operated continuously during these flights even though the aircraft encountered forces as great as 1.24G above normal.

The high turbulences were clearly shown on the laser radar displays well before they were reached. They appear as wide returns on the Range/Velocity Indicator (RVI). The time of encounter is predicted from the range and aircraft velocity, and the severity of the turbulence is shown by the width of the RVI signal. The aircraft generally avoided the turbulent clouds for safety reasons. Thus, only one correlation could be made between the Doppler spread of the laser return and the turbulence actually encountered. The flight turbulence was measured by accelerometers located in the aircraft.

4.1 RETURNS FROM TURBULENT CLOUDS

Typical sequence camera A-scope and RVI returns from clouds are shown in Figure F-21. The five photographs show the more interesting returns from the flights. The A-scope is on the bottom and the Range/Velocity Indicator (RVI) on the top. The scale is 2.64 MHz/div. vertically and 2 nau. miles/div. horizontally on the RVI and 10 dB/div. vertically on the A-scope. (For 10.6 micron radiation one MHz of doppler shift is equivalent to 17.4 ft/sec.) The A-scope return does not always correlate with the RVI signal because the A-scope shows the return only at a single frequency.

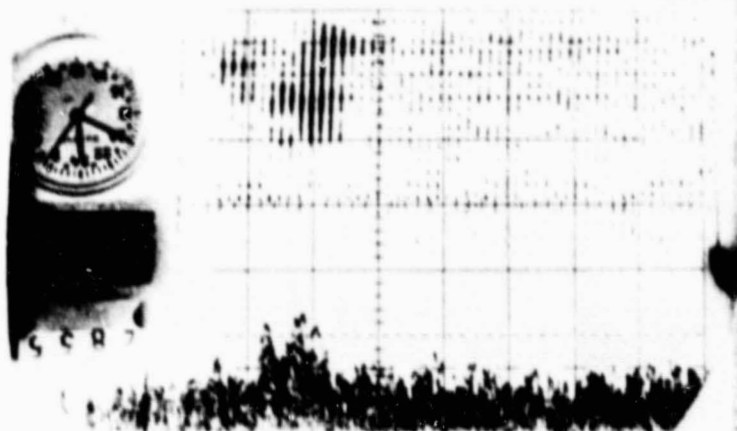


(a)

HORIZONTAL - 2 n mi/DIV
 VERTICAL - 10 $\frac{\text{dB}}{\text{DIV}}$ A-SCOPE
 2.64 $\frac{\text{MHz}}{\text{DIV}}$ RVI

#2729--THREE CLOUDS

#2835 to #2838--
 WIDE SPECTRAL RETURNS

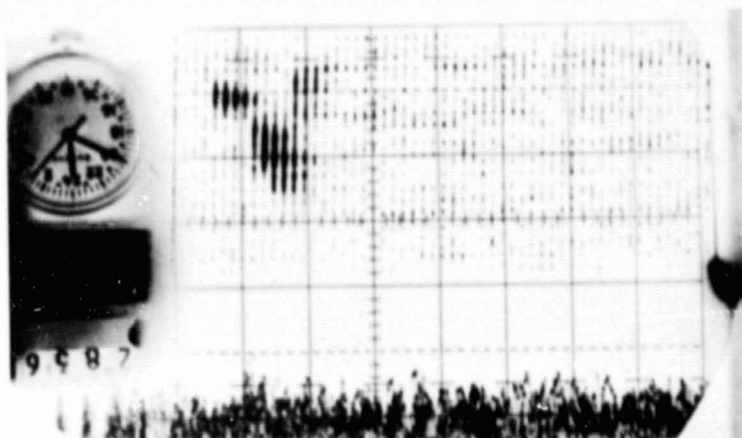


(b)

EO-566

CAT FLIGHT B8 - January 15, 1973 - Run 12

Figure F-21. Cumulus Clouds in Bishop Area - Altitude 17,000 Ft.
 (Sheet 1 of 2)

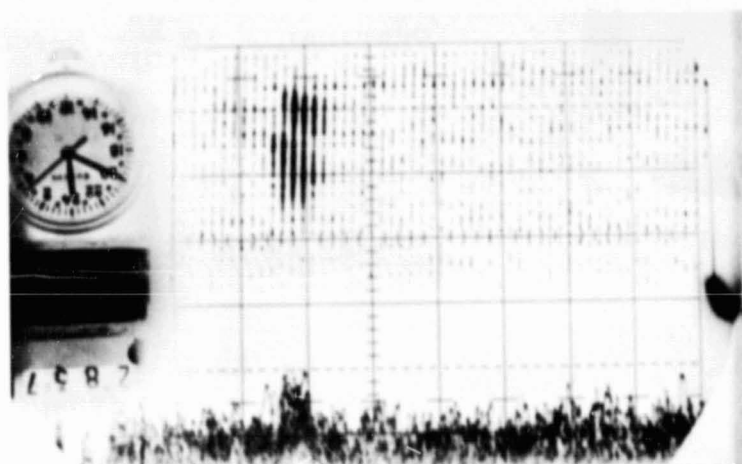


(c)

HORIZONTAL - 2 n mi/DIV

VERTICAL - 10 $\frac{\text{dB}}{\text{DIV}}$ A-SCOPE

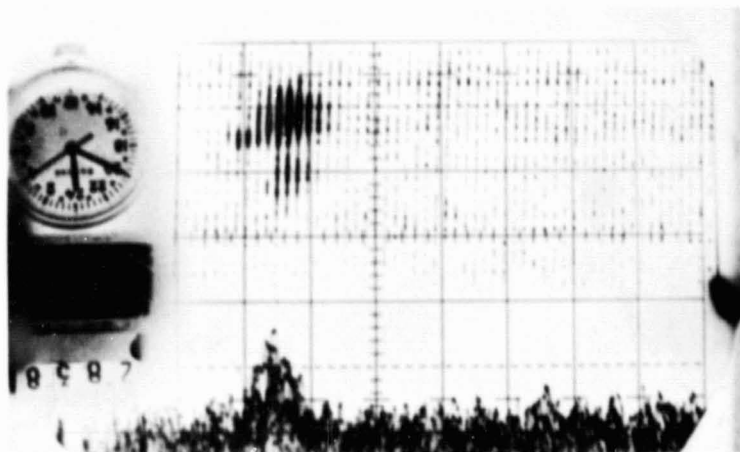
2.64 $\frac{\text{MHz}}{\text{DIV}}$ RVI



(d)

#2729--THREE CLOUDS

#2835 to #2838--
WIDE SPECTRAL RETURNS



(e)

EO-567

CAT FLIGHT B8 - January 15, 1973 - Run B8 - (continued)

Figure F-21. Cumulus Clouds in Bishop Area - Altitude 17,000 Ft.
(Sheet 2 of 2)

A study of the cloud returns indicates that:

- As many as three well-separated clouds were detected simultaneously by the laser radar (see Figure F-21a.)
- Doppler widths were as large as 5.5 MHz, showing a wind velocity spread of 60 mph in the space of a mile (see Figure F-21b.)
- Clouds were detected at ranges out to 9 nautical miles.
- Signal-to-noise ratios exceeded 20 dB.
- The extent of laser beam penetration into a cloud was as much as three nautical miles

One conclusion from these observations is that 10.6 micron radiation penetrates certain types of cumulus clouds well. A visual check showed the clouds to be opaque to visible radiation (see Figure F-3). In spite of the good penetration, the backscatter return was still high - in one instance when two clouds were detected simultaneously the signal-to-noise ratio was 13 dB from each one.

Clouds were detected on 37 occasions during the two flights along the Owens Valley, B4 and B8. The characteristics of the clouds as determined from the sequence camera photographs are summarized in Tables F-3 and F-4. The clouds were more turbulent on Flight B4 than on Flight B8 as the Doppler widths indicate.

4.2 CORRELATION OF LASER RETURN WITH FLIGHT TURBULENCE

The correlation between the CAT laser radar returns from a turbulent cloud and actual flight turbulence was successfully demonstrated and is shown in Figure F-22, which was taken from Progress Report 11. The Intensity/Velocity Indicator (IVI), which displays intensity against frequency (velocity) at a given range, is shown on the top and the aircraft acceleration on the bottom. The range of the IVI was set at 2.25 nautical miles. Flying at a recorded speed of 350

TABLE F-3

LASER RETURNS FROM CLOUDS IN OWENS VALLEY, FLT. B4 (17)

Run No.	Time of First Signal (Hr:Min:Sec.)	No. of First Photo	No. of Photos with Signal	Max. Range (N.Mi.)	Length (μsec)	Doppler Width (MHz)	Max. SNR in 300 KHz (DB)	Remarks
11 1	23:02:47	1935	7 out of 7	3.5	10	1		As many as 3 clouds appear
2	23:03	1949	21 out of 24	2.5	10	1		
3	23:04	1992	42 out of 46	4	10-20	1.5		Two clouds occasionally appear
4	23:05:32	2070	9 out of 9	2	10	2		
5	23:33:16	2129	13 out of 13	2	10	2	20	
6	23:34	2165	4 out of 8	3	7	2	18	
7	23:34	2177	2 out of 2	4	20	1.3	14	
8	23:34	2195	24	3	10-15	3	14	Signal some-times split
9	23:35:32	2240	11 out of 11	2.5	> 10	3	12	
10	23:39:35	2318	17 out of 17	2.5	8	3	15	
11	23:41	2405	38	5.2	10	2	> 20	
12	23:42	2447	23 out of 23	3	10	4	16	
13	23:43	2507	9 out of 10	2.5	> 8	4		
14	23:43	2516	3 out of 3	3	8	3	17	
15	23:43	2532	10 out of 10	2	10	2.5	20	
16	23:45:05	2591	17 out of 17	2	> 8	2.5	14	
17	23:46	2638	10 out of 11	2	> 8	2.5		
18	23:47	2720	2 out of 2	5.3	6	1.5		
19	23:47	2723	11 out of 17	2.7	8	2.5	20	Three clouds (SC 2729)
20	23:48	2760	6 out of 11	2	8	1.5	20	
21	23:49:37	2811	60 out of 70	< 5		up to 5.5	20	Three clouds appear sporadically
13 22	00:14:21	3163	2 out of 2	2.3	8	2	16	
23	00:29	3200	40 out of 40	2				

TABLE F-4

LASER RETURNS FROM CLOUDS IN OWENS VALLEY, FLT. B8 (21)

Run	No.	Time of First Signal (Hr:Min:Sec)	No. of First SC Photo	No. of Last SC Photo	Max. Range (N.Mi.)	Length (μsec)	Doppler Width (MHz)	Max. SNR in 300 KHz (DB)	Remarks
19	1	21:22:52	2885	2948	5.5	20	1	10	Two clouds appear, then merge
20	2	21:30:00	2973	2985	3	20	1		
	3	21:45:45	3236	3274	5	20	0.6	25	May be dust cloud
	4	21:49:39	3299	3341	5		1.5	19	Two clouds appear, SNR's for both
	5	21:57:51	3605	3636	5	12	1		Also air return (to 4 mi) + ground return (~ 8 mi)
10	6	21:59:23	3681	3686	5	20	1		
	7	22:01:06	3766	3774	7	10	0.5	4	
	8	22:04:48	3840	3857	7	12	1	5-17	
	9	22:06:02	3852	3883	3	20	1.5	5-12	
11	10	22:07:23	3929	3946	3	40	1.5	16	A second cloud appears sporadically
	11	22:09:04	4013	4014	3	10	1		
	12	22:09:13	4021	4048	9	10	0.5	7	A second cloud appears occasionally
	13	22:10:27	4084	4099	5	15	1	17	
14	14	22:11:55	4158	4171	6	15	1.5	12	Two clouds

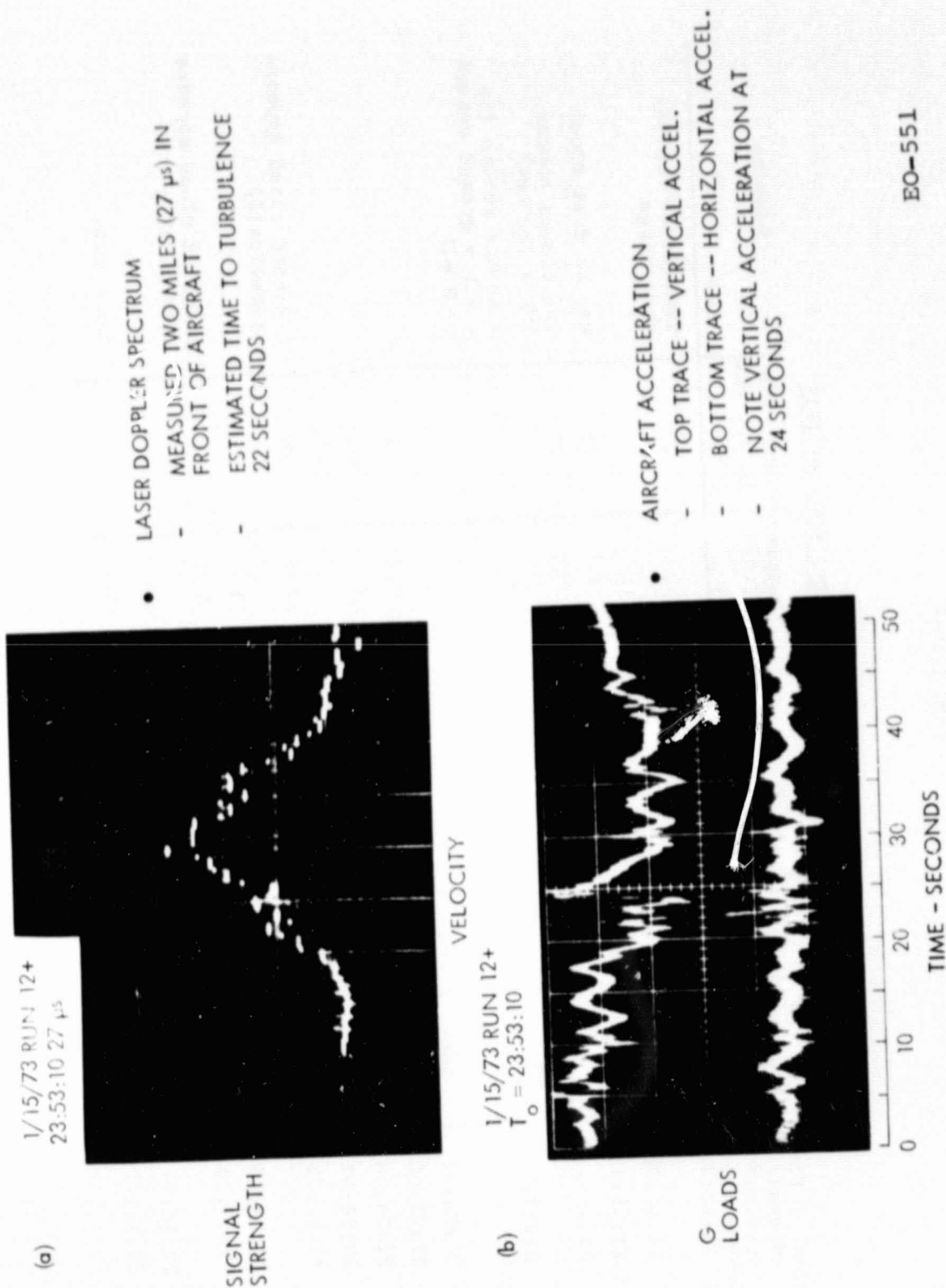


Figure F-22. CAT Flight Test - Cloud Turbulence Correlation

knots, the aircraft should encounter the turbulence 23 seconds later. The aircraft vertical accelerometer recorded a strong impulse 24 seconds afterward, showing excellent correlation between turbulence as predicted by the CAT laser radar, and the turbulence as experienced later by the aircraft.

The accelerometer scale can be calibrated by comparison with the digital accelerometer data in the in-flight data print-outs. The highest value of acceleration occurring in the time interval of the measurement is recorded. There are print-outs for ten-second, five-second and one-second intervals. The values for one-second intervals in the period depicted in Figure F-22 are listed in Table F-4. There is an excellent match if the printed values are plotted on a vertical scale of 0.32G per box with the zero-G level (rest state) set at 1.43 boxes above the centerline. Therefore, at the 24-second mark a downward force of 0.3G relative to rest changed to an upward force of 0.45G in less than a second. The largest upward force was 1.24G above normal, encountered at 23:43:12 on Flight B4.

TABLE F-5

IN-FLIGHT RECORDED ACCELERATIONS

Flight: B4

Time Period: 23:53:09 to 23:53:59 GMT

<u>Time</u>	<u>Vertical Acceleration</u>	<u>Time</u>	<u>Vertical Acceleration</u>
23:53:09	0.36 g	23:53:35	0.20 g
10	.37	36	.05
11	.41	37	-.04
12	.35	38	-.15
13	.46	39	.08
14	.56	40	-.12
15	.49	41	-.10
16	.42	42	-.05
17	.48	43	-.06
18	.38	44	-.26
19	.29	45	-.08
20	.36	46	-.06
21	.22	47	-.12
22	.28	48	-.20
23	.39	49	-.19
24	.27	50	-.10
25	.20	51	-.04
26	.37	52	-.05
27	.27	53	.07
28	.16	54	.05
29	-.01	55	.03
30	.02	56	.11
31	0	57	.05
32	.10	58	.05
33	.41	59	.16
34	.42		

SECTION 5

MISCELLANEOUS TARGETS

The returns from all targets other than Rogers Dry Lake at Edwards AFB, clear air and turbulent clouds are discussed in this section. These targets are:

Mountain (partially snow-covered)
Ground (prior to landing)
Dust clouds
Cumulus clouds
Cirrus clouds

In general, the returns followed approximately the same slope with range as the the Edwards data. The reflectivities of the targets based upon the calibration from the Edwards tests are listed in Table F-6.

Continuous returns from cirrus clouds were detected out to 8 and possibly 14 nautical miles at altitudes between 30 and 40 thousand feet.

5.1 SIGNAL-TO-NOISE RATIO MEASUREMENTS

All the targets except for cirrus clouds were detected on the last flight, B8. The altitudes and times of detection are:

<u>Target</u>	<u>Altitude</u>	<u>Run</u>	<u>Time (GMT)</u>
Mountain	~10 Kft	20	21 hr:38 min
Ground (before landing)	~ 6	21	21:52
Dust cloud	~ 6	20	21:43
Cumulus clouds	~16	19	21:30

TABLE F-6

TARGET REFLECTIVITIES AT 10.6 MICRONS

<u>Target</u>	<u>Backscatter Reflectivity, $\sigma(\pi)$</u>
Ground (Edwards) ^a	5×10^{-3} ster ⁻¹ a
Ground (S.F. area)	5×10^{-3}
Mountain (snow?)	5×10^{-3}
Cumulus clouds	$\sim 8 \times 10^{-5}$ b
Dust cloud	$\sim 3 \times 10^{-4}$ b
Air ^c	$\sim 2 \times 10^{-5}$ c

Notes:

- a. Reference target. Measured by R. Seavey on flat, dried sample (see Raytheon memo 73-RES-2)
- b. These values may be low because any overflow of the return outside the 250 kHz bandwidth due to doppler spread was not taken into account.
- c. Equivalent reflectivity based upon parameters of the CAT laser radar and an air backscatter coefficient of 10^{-8} meter⁻¹ ster⁻¹. (See Section 3.2)

The mountain and clouds were in the Owens Valley area and the ground is in the general area of San Francisco. The dust and cumulus clouds were also detected on other occasions during the flight test series.

The measurements of signal-to-noise ratio against these targets are plotted in Figure F-23. The Edwards data are also plotted for comparison. The signals from the hard targets, the mountain and ground, were of similar amplitude to the signals from the dry lake at Edwards, indicating that the dry lake was not an unusual target from the viewpoint of reflectivity. Note also that the slopes of the miscellaneous target data tend to follow the slope of the Edwards data, which was most closely fit by the 6000 foot focused receiver curve.

The cumulus and dust clouds are turbulent and tended to spread the return signal over a frequency band larger than the bandwidth. Therefore the measured signal-to-noise ratios are too low by a few dB.

5.2 REFLECTIVITY

The reflectivities are determined by comparison to the calibrated Edward's data. Assuming the system losses remain the same, the reflectivities are in the same ratio as the signal-to-noise ratios. A correction factor is applied for the difference in atmospheric attenuation. Figure F-13 of Section 2 shows a typical variation of attenuation coefficient with altitude. Based upon these data the attenuation coefficients are estimated to compare with the Edwards coefficients as follows: for mountain, roughly 0.1 dB/km lower; for ground in San Francisco area, roughly 0.1 dB/km higher; for cumulus clouds at 16,000 feet altitude, approximately 0.15 dB/km lower; and for the air around dust clouds, roughly 0.1 dB/km higher.

The reflectivities as determined from the measurements are listed in Table F-6. It is interesting to note that the reflectivities of the ground - Rogers Dry Lake at Edwards, a mountain, the area around

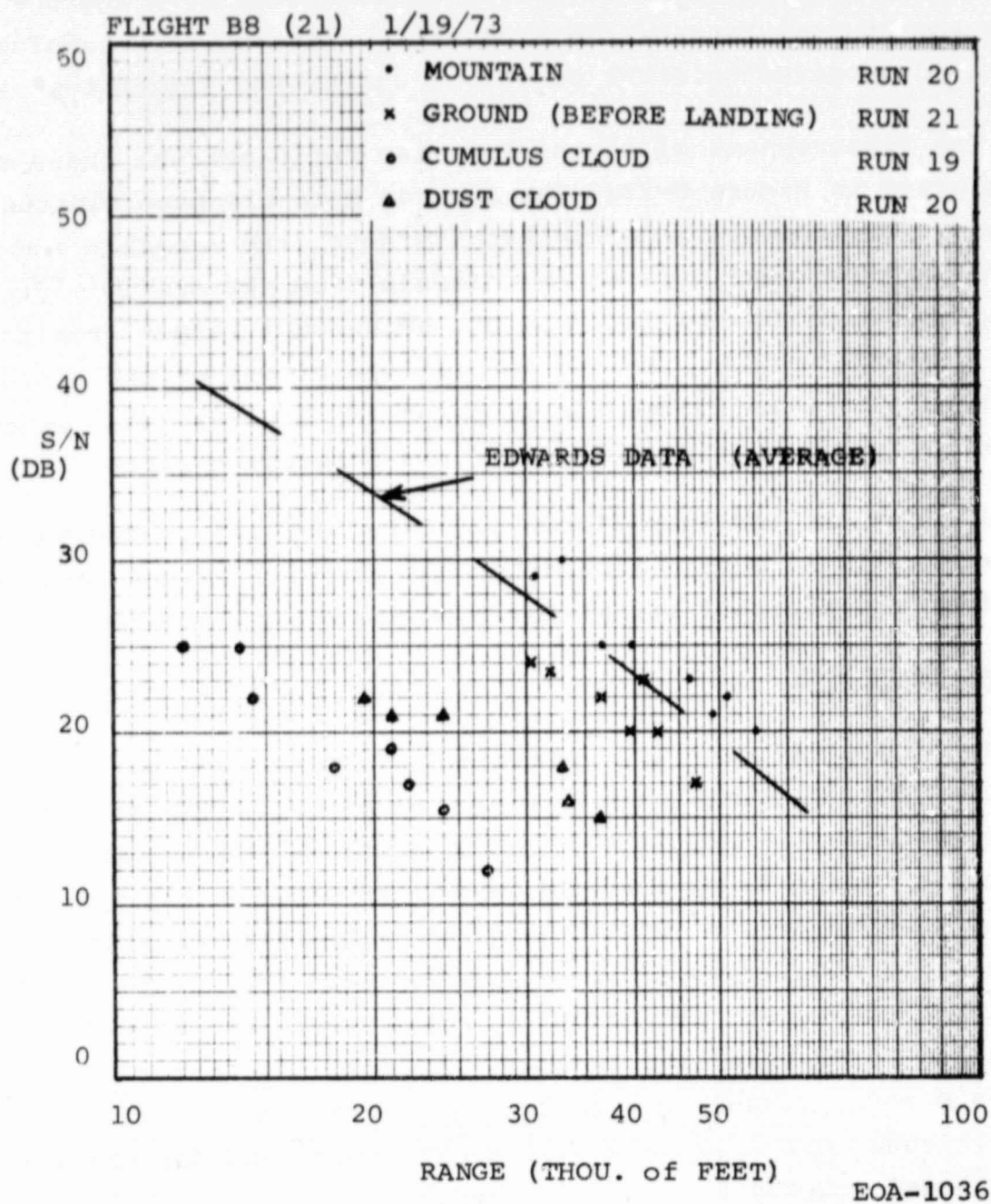


Figure F-23. Signal-to-Noise Ratios for Various Targets

San Francisco - are all the same in spite of the differences in surfaces. The reason for this similarity is not known.

5.3 CIRRUS CLOUDS

Cirrus clouds were detected on numerous occasions during the flight series, particularly on Flight B6 on January 16 toward Gary, Indiana. When the aircraft flew in the clouds continuous returns were received out to 8 and possibly 14 nautical miles. From the sequence camera record,

A-scope showed returns out to 6 miles
RVI showed distinct return out to 8 miles
RVI showed faint return out to 14 miles.

The RVI has greater range because it integrates pulses. The altitude of the aircraft was 30 to 40 thousand feet.

The signal-to-noise ratios are plotted in Figure F-24. They reach as high as 20 dB which is within 5 dB of the peak return from cumulus clouds. Note that the return at 19:10 marked by dots is low initially but extends out to a further range than the other two returns, indicating a lower density cloud and greater penetration of the laser radiations. A signal through 8 miles of cirrus cloud shows excellent penetration by 10.6 micron radiation.

FLIGHT B6 (19) 1/17/73

Run 2

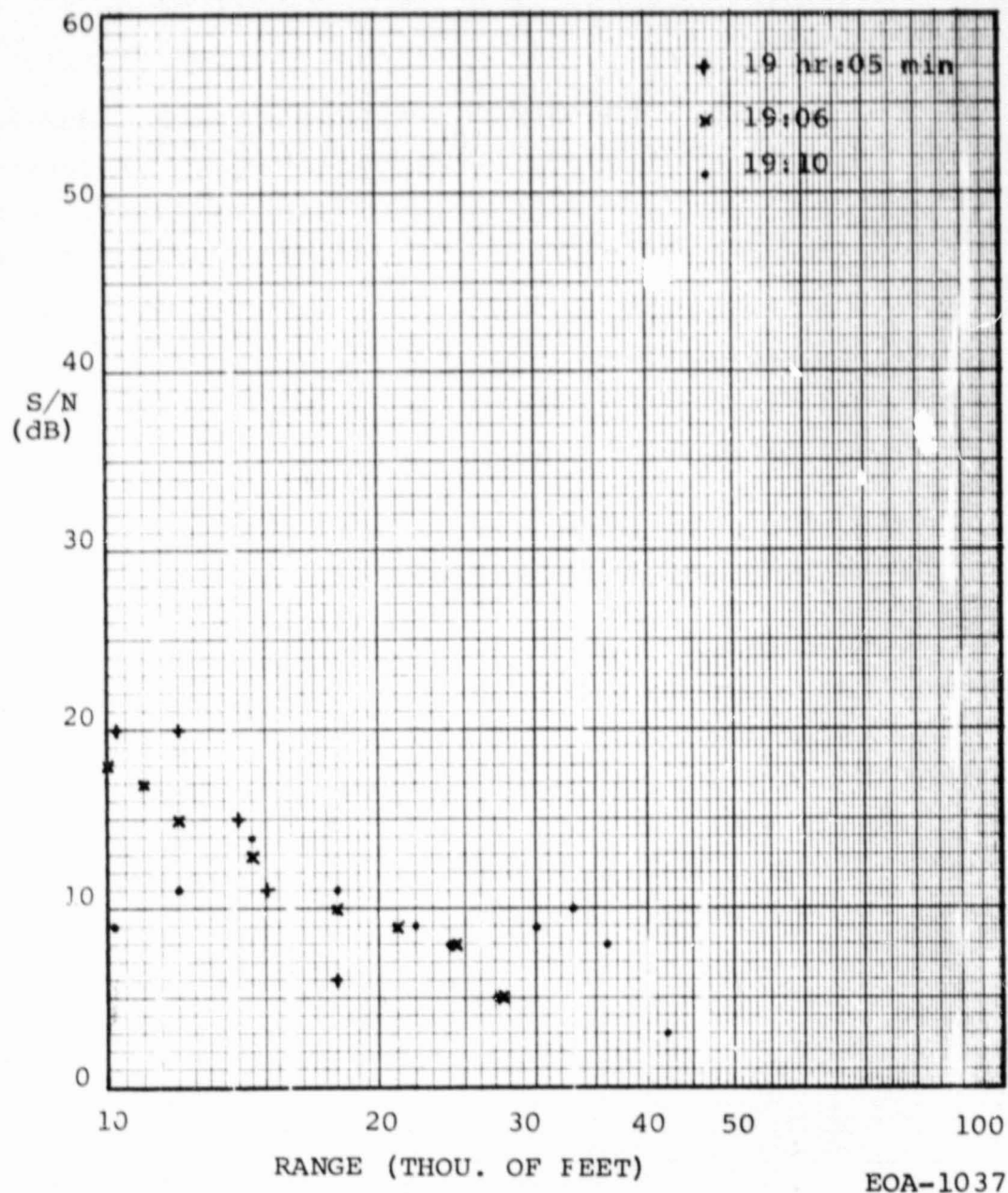


Figure F-24. Signal-to-Noise Ratios from Cirrus Clouds

SECTION 6

EVALUATION

The January 1973 flight test series demonstrated that the CAT laser operated consistently during all types of flight conditions within 2 dB of its theoretical performance and that it could detect and measure turbulence in front of the aircraft. The question to be answered here is how much improvement is still required to detect Clear Air Turbulence at high altitude.

A. Jelalian derived the required improvement to be roughly 20 dB in Raytheon memo EM-73-1115. Although a somewhat different approach was used, the same conclusion was reached that roughly 20 dB of system improvement is necessary.

The determination of the required improvement is outlined in Table F-7. The actual flight test results were used as the starting point, viz., that the signal-to-noise ratio against air was roughly 15 dB at low altitude at 2 nautical miles range as shown in Figure F-18. From there the required improvements are determined to be:

- ~ 11 dB for a detection range of 5 nautical miles
- ~ 18 dB for a detection range of 10 nautical miles
- ~ 26 dB for a detection range of 20 nautical miles

at an altitude of 40,000 feet. Since the desired detection range is 10 to 20 nautical miles, the required improvement in SNR is roughly 20 dB.

The required improvement is plotted against range and altitude in Figure F-25.

TABLE F-7

Required S/N Improvement for Operational CAT System

		<u>Required Increase in CAT System</u>	
		<u>Each</u>	<u>Cumulative</u>
1.	Measured SNR from air was roughly 15 dB at low altitude (~3Kft) for a range of 2 miles in winter	-7 dB	-7 dB
2.	A SNR of 8dB is probably sufficient in an operational system, judging by the SC A-scope returns		
3.	Improvement from focussing receiver at infinity rather than at 1 mile is 0dB at a range of 2 miles	0	-7
4.	For operation at 40,000 feet altitude, the backscatter coefficient is estimated to be roughly 12dB lower.*	+12	+5
5.	a. For operational range of 2 miles, need 0dB more	0	5
	b. For operational range of 5 miles, need 6dB more**	+6	or 11
	c. For operational range of 10 miles, need 13dB more**	+13	or 18
	d. For operational range of 20 miles, need 23dB more**	+23	or 28

*Extrapolated from data in Figure 15 of Memo 73:AJ:039

**Assuming an atmospheric attenuation coefficient of 0.1 dB/km at 40,000 feet in winter

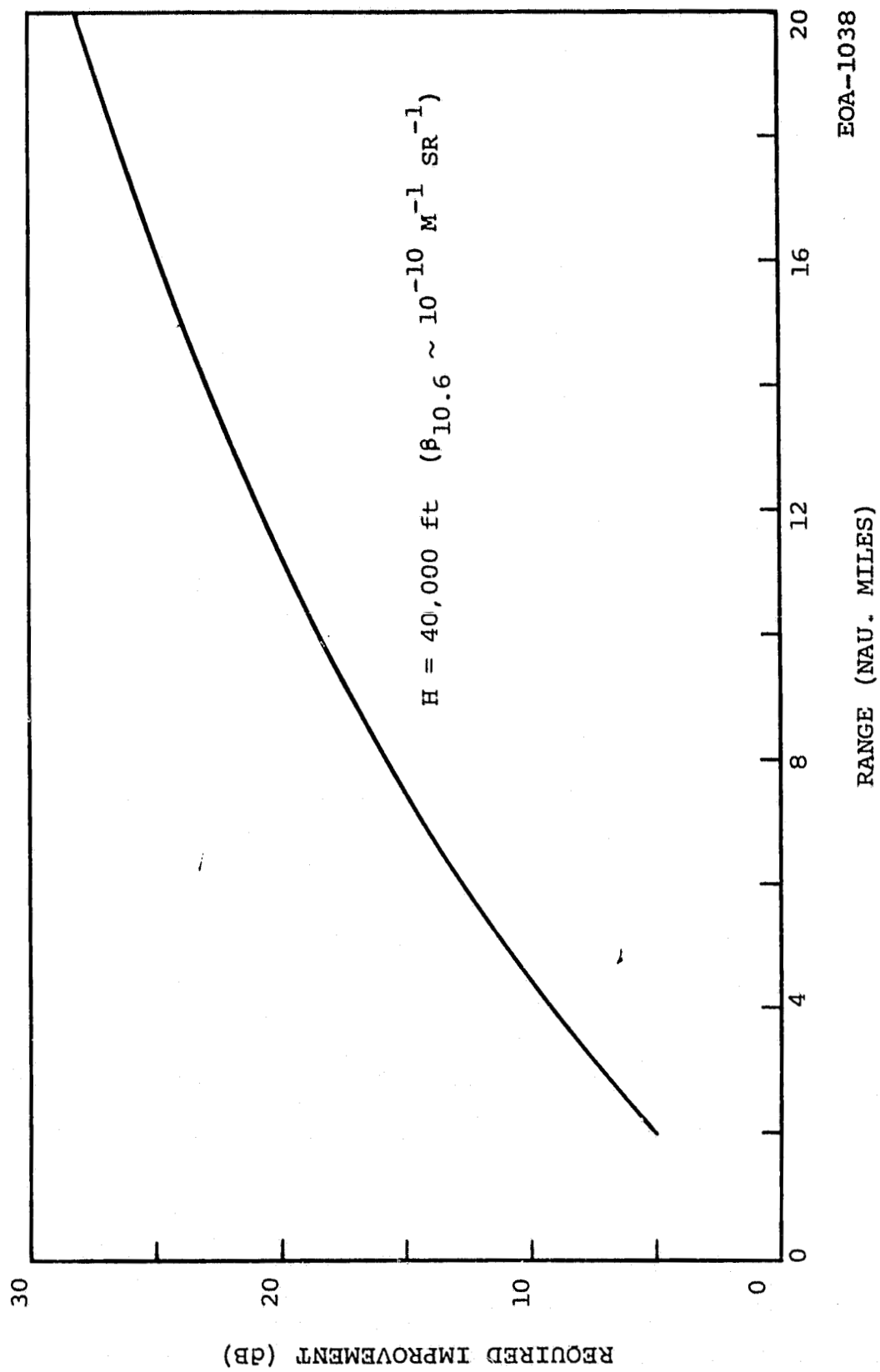


Figure F-25. Required Improvement in SNR for Operational CAT Laser Radar

The assumptions in the above analysis are:

- a. The receiver was focussed at 6000 feet during the January tests; also that it can be properly collimated in future systems.
- b. The backscatter coefficient is a factor of 16 lower at 40,000 feet ($\beta \sim 10^{-10}$ per meter-ster) and a factor of 5 lower at 20,000 feet ($\beta \sim 4 \times 10^{-10}$ per meter-ster), compared with ground level.
- c. The atmospheric attenuation coefficient is 0.1 dB/km each way at 40,000 feet and 0.15 dB/km at 20,000 feet.
- d. A SNR of 8 dB is sufficient for detection, and any reduction from frequency - broadening of the signal beyond the bandwidth due to turbulence is not detrimental.

The SNR improvement can come from a variety of sources. The logical ones are:

1. Reduce the losses. The observed loss exclusive of the detector is 15 dB which is detailed as follows:

Optics (beamsplitter, GE window, lenses)	3 dB
Extended diffuse target, Gaussian beam	5 dB
Target depolarization	1 dB
Receiver electronics	4 dB
Unexplained	2 dB

It may be possible to eliminate up to 5 dB of these losses but a couple dB is more likely.

2. Pulse integration. The SNR can be improved by the number of pulses if the integration is perfect and the signal amplitude remains constant. However, the signal amplitude varies widely, and analytical integration of the

Edwards returns showed that there was virtually no improvement in integrating 50 pulses. At higher altitudes the air turbulence, which is the primary cause of the signal variation, is less severe. Hence, there may be substantial improvement from integration, though by less than the number of pulses.

3. Increase the laser output. If all else fails, the improvement must come from this source.
4. Other system improvements. Two possibilities are the detector and the aperture. The quantum efficiency of the HgCdTe detector in the test was approximately 0.25, so there is little room for improvement here. Enlarging the effective aperture from 10 to 15 inches only increases the signal-to-noise ratio at 10 miles by 3 dB in theory, and perhaps less in practice due to turbulence limitations.

Therefore, pulse integration and increasing the laser output are the most promising areas for realizing the 20 dB improvement in signal-to-noise ratio.

ATTACHMENT 1

CALCULATION OF ATMOSPHERIC TRANSMISSION

The method of determining the transmission of CO₂ laser radiation from the temperature, humidity and altitude is explained here. The atmospheric attenuation during the dives at Edwards AFB discussed in Section 2 and the air backscatter measurements in Section 3 is of interest.

The two major attenuators of CO₂ laser radiation are water vapor and carbon dioxide. A third attenuator is aerosols, primarily water droplets, but their effect is generally less significant at 10.6 microns unless a dense haze or fog is present.

1.1 ATTENUATION BY WATER VAPOR

To determine the attenuation from water vapor, the relative humidity, temperature and pressure are required. The parameters monitored in flight are the static temperature, dew frost temperature and altitude. The relative humidity is calculated from the static and dew frost temperatures by the formula:

$$RH = 10^{x-y} \quad (F-3)$$

where

$$x-y = \frac{A}{B} \cdot \frac{T_d - T_s}{\left(1 + \frac{T_d}{B}\right) \left(1 + \frac{T_s}{B}\right)}$$

and

$$A = 7.5$$

$$B = 237.3$$

where T_s and T_d are the static and dew frost temperatures. The water vapor content, measured in terms of its partial pressure, is given by:

$$p = RH \times \text{Partial pressure of H}_2\text{O for 100\% humidity}$$

$$\approx RH \times 5.2 \times 10^{0.0259T_s} \quad (\text{F-4})$$

for the temperature region of interest. The attenuation of 10.6 micron radiation due to water vapor was measured by J. McCoy, D. Rensch and R. Long¹ to follow the formula,

$$\mu_{\text{H}_2\text{O}} = 4.32 \times 10^{-6} p (P+193p) \quad (\text{F-5})$$

Here, $\mu_{\text{H}_2\text{O}}$ is the attenuation coefficient due to water vapor, in km^{-1}

p is the partial pressure of H_2O , in Torr

P is the total pressure, in Torr

As an approximation over the altitudes of interest,

$$P \approx 760 \times 10^{-0.0172H} \quad (\text{F-6})$$

where H is the altitude in thousands of feet above sea level.

1.2 ATTENUATION BY CARBON DIOXIDE

The second significant attenuator of CO_2 laser radiation is carbon dioxide. P. Yin and R. Long² have calculated the absorption at the center of the P(20) line as a function of altitude. From their data,

$$\mu_{\text{CO}_2} \approx 0.072 - 0.002H \quad (\text{F-7})$$

for January, where the altitude H is in thousands of feet. The approximation is valid up to an altitude of 12 km (40,000 feet).

1.3 TOTAL ATTENUATION

The round-trip atmospheric transmission along a slant path is given by:

$$\eta_a = \exp \left(2 \int_0^R \mu(R') dR' \right) \quad (\text{F-8})$$

where R is the path length and R' is the range along the path. The

attenuation coefficient $\mu(R')$ is:

$$\mu = \mu_{H_2O} + \mu_{CO_2} \quad (F-9)$$

where μ_{CO_2} is given by equation (F-7) and μ_{H_2O} is given by equations (F-6), (F-4) and (F-3). The atmospheric transmissions were determined by this technique in Sections 2 and 3.

REFERENCES

1. J. McCoy, D. Rensch, R. Long, App. Op., Vol. 8 No.7, 7/69, pp. 1471-8
2. P. Yin and R. Long, App. Op., Vol. 7, No. 8, 8/68 pp. 1551-3

ATTACHMENT 2
SEQUENCE CAMERA DATA

A review of the targets, signal-to-noise ratios and other parametric data in the sequence camera films of the A-scope and RVI is given in this Attachment. The flights covered are B8(21) on January 19 which contained the most information and B2(15) on January 12 which included the dives at Edwards. The time history of Flight B8 is given on pages F-85 through F-90 and the signal-to-noise ratios on pages F-91 through F-95. Flight B2 is covered on pages F-96 through F-100.

All signal-to-noise ratios in this Attachment must be raised by 3.4 dB. The rms level of the noise was improperly located in the early days of the data analysis and was subsequently found to be 3.4 dB below the A-scope baseline (see Section 2.4.1).

SUMMARY SHEET OF TARGETS ON SEQUENCE CAMERA FILM,
FLIGHT B8 (21), 1/19/73

<u>RUN</u>	<u>SC PHOTOS</u>	<u>TARGET(S)</u>
1	TO 127*	CLEAR AIR
2,3	147-163*	CIRRUS CLOUD**
4	185-267*	CLEAR AIR**
5	274*	
6,7,8	280-972*	DUST CLOUD, GROUND, CLEAR AIR (OVER SAND HILLS NEAR IMPERIAL VALLEY)
8,9	982-1471	CLEAR AIR, DUST CLOUD
11,12	1670-2073*	DUST CLOUD, GROUND**
14	2106-2387*	GROUND, DUST OVER GROUND**
17	2438-2589*	GROUND, CLEAR AIR** (EDWARDS)
18	2696-2850	GROUND, DUST CLOUD** (EDWARDS)
19	2885-2948	TWO CUMULUS CLOUDS (OWENS VALLEY)
	2973	CUMULUS CLOUD (OWENS VALLEY)
20	3025-3074	MOUNTAIN (OWENS VALLEY)
	3093-3225	CLEAR AIR, DUST CLOUD**, GROUND** (OWENS VALLEY)
	3236-3341	TWO CUMULUS CLOUDS (OWENS VALLEY)
	3503-3826	CLEAR AIR, MOUNTAIN, CUMULUS CLOUD** (OWENS VALLEY)
	3840-3857	CUMULUS CLOUD** (OWENS VALLEY)
	3862-3883	CUMULUS CLOUD** (OWENS VALLEY)
	3929-3946	TWO CLOUDS**
	4084-4099	CUMULUS CLOUD
21	4323-4342	CIRRUS CLOUD**
	4352-4416	CIRRUS CLOUD**
	4552-4988	GROUND (NEAR MOFFETT), CLEAR AIR, CUMULUS CLOUD**

*-SCOPE NOT FUNCTIONING PROPERLY

**PROBABLE TARGET

CAT FLIGHT TEST DATA REDUCTION
 REVIEW OF SEQUENCE CAMERA FILM

FLIGHT B8 (21), 1/19/73

GMT ^b	SC Photo ^b	Signal
17:11 (Run 1)		Clear air returns were observed during flight up to altitudes of 24 Kft. However, no signals appear on A-scope, only slight signals on RVI, ~ 0.5 MHz wide (see for example SC 0094).
17:12:08	127	Last (?) trace of RVI signal appears, H = 24 Kft. Possible returns on 133, 137-8.
17:26:11 (2, 3)	147	Slight backscatter return on RVI, probably from cirrus cloud. No A-scope correlation. 0.2-1 MHz width, H = 27 Kft.
	163	Last trace of signal
18:16:19 (4)	185	Slight signal on RVI, flight over sand dunes, no clouds noted. No A-scope correlation. ~ 0.2 MHz, H = 15.3, level flight
	267	Last trace of signal
18:30:27 (5)	274	Signal appears on RVI at range of 12-16 mi., H = 9.44, level flight
18:38:07 (6)	280 ^a	Signal appears at 5-6 mi.
	281	Second signal appears at 11 mi. on RVI, ~ 3 MHz away from first signal. Closer target may be a dust cloud, further target the ground. Still no A-scope correlation. Depression angle $\approx 5^\circ$. A 3 MHz separation indicates ~ 30 knots, data sheets show a 40 knot wind 7° away from the aircraft velocity vector, hence there is an approximate correlation.
	301	Far signal (ground) disappears
	325	Near signal ends
	341	Near signal returns in strength. Indicates aircraft is passing back and forth through a dust cloud, confirmed by in-flight notes. Signal on RVI extends out to ~ 6 mi, still no A-scope signal. A-scope apparently is not working.
18:49:07 (7)	635	A second signal appears at 8 mi., offset ~ 2 MHz from the first. The backscatter return (first) snakes through ~ 0.5 MHz, indicating a shear. Data indicates beginning of descent (sand hills near Imperial Valley).
	637	A third weaker signal appears at very close range (≤ 2 mi), ~ 2 MHz away from the strong backscatter return, its separation varies to 4 MHz away in SC 700's, finally disappears ~ SC 800.
	647	The two strong signals merge into one in range, extending out to 6 miles. Ground signal comes as close as 5 mi.
	680	Ground signal disappears (but reappears momentarily on SC 699 and 700). Data sheets indicate end of dive. Backscatter return continues on RVI, strong and wide (~ 3 MHz).

GMT	SC Photo	Signal
58:15 (8)	968	<u>A-scope finally works.</u> Shows high SNR for back-scatter
	969	See Table 1 for SNR, H = 2.2 Kft.
	971	See Table 2 for SNR
58:19	972	Air return finally disappears
18:59:17	982 ^a	Backscatter signal out to ~ 4 mi, H = 2.2, V = 217 knots.
	993	See Table 3 for SNR
	998	See Table 4 for SNR
	999	See Table 5 for SNR. Low SNR's at ranges less than 2 mi. may be due to receiver malfunction.
	1110-13	Slight break-up of air return into two separate doppler segments
19:03:07 (9)	1142	First appearance of well-separated doppler signal, ~ 3 MHz apart. One signal extends out to 7 mi. on RVI (SC 1246), the other to ~ 2 mi.
	1255	Long doppler signal snakes across RVI. Correlation of snaking effect by A-scope
	1275	See Table 6 for SNR. H ~ 4.4.
07:38	1364	One signal (out to 6 mi) finally ends
	1471 ^c	(End of reel. Next one started a half hour later.)
	(Reel 2)	
19:39:13 (11)	1670	Signal appears on A-scope out to ~ 6 mi, probably a dust cloud. Signal snakes in frequency through ~ 0.3 MHz. H ~ 10 Kft, in middle of 50° dive.
	1671	A second signal appears at 12 mi, offset ~ 2.5 MHz from the first, probably the ground. No A-scope correlation (it does not appear to be functioning).
41:30 (12)	1785	Ground signal disappears (receiver is overloading).
	1945	Occasional second signal appears at 5-8 mi. around this time.
55:49	2073	Air return finally disappears
20:29:05 (14)	2106	Signal (probably the ground during the dive) at 9.4 mi. Width ~ 0.7 MHz, ~ 1 mi long.
	2122	Signal begins to appear on A-scope, however, its amplitude is much lower than expected. Suspect A-scope still not functioning properly.
	2239	Two separate signals appear - dust moving over ground
34:37	2387	Last trace of all signals.
20:50:26 (17)	2438	Ground first appears at end of scale for Run 17 at Edwards. Values appearing on A-scope are approximately an order of magnitude lower than values called out during flight. The SC A-scope is still not functioning right.
	2589	Ends dive. Only air return out to 4 + mi. remains.
21:01:06 (18)	2696	Ground first appears at end of scale for Run 18 at Edwards. A-Scope now working. See Table 7 for SNR.

GMT	SC Photo	Signal
		Slight dust cloud attenuates beam. Dust return is especially apparent when ground is ≤ 4 mi away. It is offset ~ 1.5 MHz from ground return, data sheets indicate a ~ 30 knot ground wind $\sim 70^\circ$ away from aircraft heading, hence its doppler separation should be ~ 1 MHz. Printed data: V held at ~ 300 knots (± 10 knots for most of dive), $\varphi_{ind} = 4.4^\circ - 6.8^\circ D$ with typical value of $6^\circ D$, therefore laser is pointed $\sim 6^\circ + 1.5^\circ = 7.5^\circ$ down.
21:22:52 (19)	2885 ^a	Signal appears at 5 mi, probably from cloud. Notes indicate Owens Valley, just past Mt. Whitney. Cloud length ~ 1.7 mi, doppler width ~ 1 MHz, H = 14.4 Kft V = 308, $\varphi_{ind} = 2.7^\circ U$, heading remains constant at this time ($\pm 2^\circ$). See Table 8 for SNR.
	2912	Second cloud appears at 5.5 mi, same doppler shift.
	2913	SNR of second cloud ≈ 10 dB at 5.5 mi.
	2916	SNR of cloud #1 ≈ 10 dB at 2 mi, SNR of cloud #2 ≈ 8 dB at 5 mi.
	2922	Both clouds merge.
24:03	2948	Cloud return disappears as aircraft closes in on it. Slight turbulence was encountered shortly thereafter (~ 0.16 G).
21:30:00	2973	Cloud return appears at 3 mi on 12 out of 13 frames, ~ 1.7 mi in length, 1 MHz wide. H = 16.3, V = 302, $\varphi = 1.7^\circ U$, heading constant for 80 sec afterward.
21:38:15 (20)	3025 ^a	Strong signal at 8 mi. Probably a mountain because $\varphi = 2.5^\circ D$. Return is very strong and narrow (~ 1.3 mi). See Table 9 for SNR.
	3040-5	Return starts to recede and approach again. Data sheets indicate a 30° roll is starting.
	3073-4	Signal suddenly disappears. Indicates target was a mountain the plane was heading for and had just looked over a ridge. Distance of closest approach ≈ 5 mi.
21:41:17	3093	Signal appears at close range, extends out to ~ 4 mi. Apparently an air backscatter return. H = 6.2, V = 330.
	3120	See Table 10 for SNR.
	3128	See Table 11 for SNR.
	3132	See Table 12 for SNR.
	3141, 44, 52	S/N ~ 8 dB at minimum range.
42:43	3173 ^a	Signal is disappearing. H ≈ 6 Kft.
21:43:14	3177 ^a	Strong signal appears at 3 mi. Data shows slight dive, prior to an ascent. Plane starts at 5.7 Kft, dives to 4.35, then rises again. Length ~ 2.5 mi (SC3209). See Table 13 for SNR.

GMT	SC Photo	Signal
-----	----------	--------

In-flight notes indicate dust cloud in Owens Valley

	3187	Second signal at same range but different doppler shift (~ 3 MHz away) appears. Probably the ground. It may have been off scale in frequency on earlier photos.
44:09	3219	Ground return disappears.
	3225	Air return disappears. Data indicate plane in turn.
21:45:45	3236 ^a	Signal appears at 4-5.5 mi, ~ 0.6 MHz wide, probably a cloud.
	3265-74	See Table 14 for SNR. Signal sporadically disappears and reappears. Receiver overloading.
21:49:39	3299	Signal appears at 4 mi, probably the dust cloud. Just completing turn. Doppler width ~ 1.5 MHz.
	3314	Second signal appears, ~ 1.5 mi further away, same doppler shift.
	3315	SNR of #2 is 5 dB at 4 mi when SNR of #1 is 15 dB at 1.5 mi.
	3316	SNR of #2 is 9 dB at 3.5 mi when SNR of #1 is 10 dB at 1.5 mi.
	3319	Signal for first cloud disappears as plane gets close to it. SNR of #2 is 10 dB at 3 mi.
	3325	SNR = 13 dB at 2 to 3 mi.
	3326	SNR = 18 dB at 2 mi.
	3329	SNR = 19 dB at 1.7 mi.
50:27	3341	Signal disappears.

21:55:51	(Reel 3) 3503 ^a	Backscatter signal out to 3.5 mi, ~ 0.6 MHz wide, H = 9 Kft, V = 284, $\phi_{indic} \approx 10^\circ$, constant heading.
	3505	See Table 15 for SNR
	3507	See Table 16 for SNR.
	3510	See Table 17 for SNR.
	3515	Signal extends out to 6 mi on RVI.
	3538	S/N = 11 dB at 2.7 mi.
	3545	See Table 18 for SNR. H = 8.8.
	3546	A second signal suddenly appears at ~ 4.5 mi, 2 MHz away but lasts for only two photos.
07:44	3548	S/N = 14 dB at 2 mi.
	3602	Second signal appears at 9 mi, 2 MHz away. Plane is in turn (10° in 20 sec).
	3605	Third signal appears just beyond first signal (range ~ 4-5 mi) offset ~ 1 MHz in frequency.
	3607	Positions of three signals:

Signal	Range	Frequency Offset from #1
1	2-4 mi	-
3	4-5	~ - 1 MHz
2	8-9	~ - 2

GMT	SC Photo	Signal
58:27	3636	Frequency spread of three signals has doubled. Aircraft heading = 335° at 58:16, 352° at 58:55. Last trace of signal #3.
	3645	A-scope finally on Signal #2. S/N = 16-21 dB at 7.4 mi. High sharp signal indicates hard target. Signal #3 has disappeared but Signal #1 at minimum range is still present to attenuate signal #2.
	3646	S/N = 16 dB at 7 mi.
	3650	S/N = 19 dB at 7 mi.
	3652	Signal #2 abruptly disappears. Target appears to have been a mountain that the plane had just turned from.
	3681	A second signal appears at 5 mi, 2 MHz away.
	3686	Second signal disappears.
	3739	A second signal appears at 5.5 mi, ~ 0.2 MHz away, S/N ~ 4 dB, signal on only one photo.
	3766	A second signal appears at 7 mi at same frequency.
	3767	S/N of close signal $\approx 8 - 14$ dB, S/N of far signal ≈ 4 dB at 7 mi.
	3774	Second signal disappears.
22:02:19	3826	First signal finally, but gradually, disappears. Data sheets indicate plane is ascending. H = 14 Kf (plane was at 7.5 Kft two minutes earlier). So near return (signal #1) was clear air backscatter.
22:04:48	3840 ^a	Signal at 7 mi, looks like cloud, ~ 12 μ sec long, ~ 1 MHz wide. H = 14 Kft, V = 320, $\phi = 0^{\circ}$.
	3841	S/N = 5 - 17 dB at 7 mi.
	3857	Signal disappears.
22:06:02	3862	Slight backscatter signal at minimum range. Its rather sudden appearance plus its high amplitude later indicates probable cloud. S/N = 6 dB at 2 mi. H = 14.2 Kft.
	3870	S/N = 12 dB at 2.6 mi.
	3883	Signal disappears.
22:07:23	3929	Signals appear at 3 and 7.5 mi. Closer signal increases on subsequent photos, further signal disappears.
	3939	S/N = 16 dB at 1.7 mi, extends out to 5 mi.
	3942	Close signal disappears, segment remains at 6 mi, ~ 8 μ sec long.
07:44	3946	Signal disappears.
22:10:27	4084	Signal appears at 5 mi, probably a cloud. See Table 19 for SNR.
	4099	Signal disappears.
22:34:01 (21)	4323 ^a	Signal appears out to 4 mi. Looks like air backscatter but is quite strong, may be cirrus cloud. H = 22.4, $\phi_{ind} = 4.9^{\circ}$. See Table 20 for SNR.

34:23	4330	See Table 21 for SNR.
	4342	Signal disappears.
22:34:33	4352	Backscatter return appears on A-scope, no RVI correlation. $H = 20$, $\phi_{ind} = 5-7^{\circ}D$.
	4354	Slight signal on RVI. Snakes in frequency through ~ 0.4 MHz. Doppler width ~ 0.2 MHz.
	4359	$S/N \approx 5$ dB at 2.4 mi (A-scope), RVI signal at 3.2 mi.
	4376	$S/N \approx 6$ dB at 2 mi.
	4416	Signal disappears.
22:52:01	4552 ^a	Signal appears at 9 mi, probably the ground because plane is beginning its descent for landing. $H = 6.7$, $\phi_{ind} = 4-9^{\circ}D$. Doppler width ~ 1 MHz. See Table 22 for SNR.
		Air backscatter also present, but 2 MHz away, 0.5 MHz wide. Data indicates wind speed of ~ 20 knots, $\sim 20^{\circ}$ from flight direction, which correlates with observed doppler shift.
52:47	4590	Ground return disappears. Data indicates plane pull-up. Backscatter return continues.
	4618	See Table 23 for SNR. $H = 2.5$.
	4627	Second signal appears at 7 mi, appears to be a cloud. $H = 3.5$, $\phi_{ind} = 3.8^{\circ}U$.
	4630	$S/N = 12$ dB at 6.3 mi. Strong backscatter return.
	4637	Second signal disappears.
	4644	Long backscatter return, to ~ 6 mi. $H = 3.5$.
	4650	See Table 24 for SNR.
4666 & 82		$S/N = 12$ dB at 2 mi from air. $H = 3.5$, $\phi_{ind} \sim 5^{\circ}U$.
54:58	4703	Second signal appears at 5 mi. Data indicates start of turn.
	4705	$S/N = 9$ dB at 6 mi.
	4706	Second signal disappears.
	4708	See Table 25 for SNR. $H = 3.6$.
	4710	$S/N = 10$ dB at 1.3 mi from air.
55:29	4729	Second signal appears at 5 mi. Data indicates start of climb ($\phi = 8.7^{\circ}U$), therefore probably a cloud.
	4733	Second signal disappears.
	4736	$S/N = 11$ dB at 2 mi from air.
	4738	Second signal appears at 7 mi.
	4744	Second signal disappears.
59:15	4927	Second signal appears at 6 mi, offset in frequency by 1.5 MHz, $\phi = 0^{\circ}$, $H = 1.6$. Probably the ground.
	4934	$S/N = 22$ dB at 4.5 mi. $H = 1.4$, $\phi_{ind} = 0-2^{\circ}D$.
	4936	Ground return disappears.
	4451	Ground return reappears at 5 mi, offset from backscatter return by 1.5 MHz.
	4966	Ground return disappears. $H = 0.6$ Kft.
23:00:23	4988	END

NOTES

- a. Sequence Camera started.
- b. SC clock time may differ from time GMT. SC photos are 1.2 seconds apart.

Table B8-1
(Clear air)

<u>R</u> (n.mi)	<u>S/N</u> (dB)
2	12
2.7	7
3.6	5
4	4
4.7	3
6	1

Table B8-4
(Clear air)

<u>R</u>	<u>S/N</u>
1.7	17
2	15
3	10
4	5
4.6	3

Table B8-2
(Clear air)

<u>R</u>	<u>S/N</u>
1.7	12
2.4	10
3	5
4	2
5	1

Table B8-5
(Clear air)

<u>R</u>	<u>S/N</u>
1	9
1.2	10
1.5	14
1.7	17
2	17
2.4	15
3	11
3.5	9
4	6
4.5	4
5	2

Table B8-3
(Clear air)

<u>R</u>	<u>S/N</u>
1.7	15
2	15
2.4	13
3	12
4	5
5	1

Table B8-6
(Clear air)

<u>R</u>	<u>S/N</u>
1.8	14
2.2	13
2.7	11
3.6	7
4	6
5	4
6	2

Table B8-7 (Ground, Edwards)

<u>SC Photo</u>	<u>R</u>	<u>S/N</u>
	<u>(n.mi)</u>	<u>(dB)</u>
2736	15	5*
41	14	7*
50	12	8*
53	11	9
56	10	11*
67	9	12
71	9	13*
88	7.5	17*
95	7	19*
99	6	21*
2805	5.2	22
07	5	24*
19	4	25
21	3.7	28*
23	3.3	29
24	3.2	30*
30	3.1	30
33	3	30
34	2.5	33*
38	2.4	32
43	2.2	37*
44	2.2	38*
46	2	41

Table B8-8 (Cloud)

<u>SC Photo</u>	<u>R</u>	<u>S/N</u>
2888	4.5	9*
94	4	12*
98	4	13*
99	3.6	14*
2904	3	15*
22	3.5	16*
28	2	18
37	2.4	19*
39	2	20
40	2.3	22*
45	2	22*

Table B8-9 (Mountain)

<u>SC Photo</u>	<u>R</u>	<u>S/N</u>
3026	9	17*
31	8.3	19*
35	8	18*
37	7.6	20*
50	6.5	22*
52	6	22*
57	5.4	27*
62	5	26*

*Plotted on graph

Table B8-10
(Clear air)

<u>R</u>	<u>S/N</u>
1.8	5
2	5
2.4	3
3	0

Table B8-11
(Clear air)

<u>R</u>	<u>S/N</u>
1.7	6
2	5
2.4	2
3	0

Table B8-12
(Clear air)

<u>R</u>	<u>S/N</u>
1.6	8
1.8	9
2	8
2.4	5
3	1

Table B8-13
(Dust cloud?)

<u>SC Photo</u>	<u>R</u>	<u>S/N</u>
3178	6	12*
82	5.5	13*
83	5.4	15*
3204	4	18*
09	3.5	18*
17	3.2	19*

Table B8-14
(Cloud-dust?)

<u>SC Photo</u>	<u>R</u>	<u>S/N</u>
3238	5.3	9
46	3.3	10
53	2.5	13
54	2.5	18
60	1.5	20
61	1.7	25

*Plotted on graph

Table B8-15
(Clear air)

<u>R</u>	<u>S/N</u>
1.6	10
2	8
2.5	5
3	3
4	0

Table B8-16
(Clear air)

<u>R</u>	<u>S/N</u>
1.8	10
2	10
2.5	5
3	3

Table B8-17
(Clear air)

<u>R</u>	<u>S/N</u>
1.8	11
2	10
2.5	6
3	4
4	0

Table B8-18
(Clear air)

<u>R</u>	<u>S/N</u>
1.7	11
2	10
2.5	8
3	6
3.4	3
4	2

Table B8-19
(Cloud)

<u>SC Photo</u>	<u>R</u>	<u>S/N</u>
4092	3.3	13
96	3	14
98	2.7	17

Table B8-20
(Cirrus cloud?)

<u>R</u>	<u>S/N</u>
1.8	10
3	3
4	0

Table B8-21
(Cirrus cloud?)

<u>R</u>	<u>S/N</u>
1.7	11
2.2	9
4	2

Table B8-22
(Ground)

<u>SC Photo</u>	<u>R</u>	<u>S/N</u>
4555	7.7	14*
59	7	17*
61	6.5	17
65	6	19*
68	5.3	20*
70	5.2	20
75	5	21*
78	5.3	21*
80	6.8	20*

Table B8-23
(Clear air)

<u>R</u>	<u>S/N</u>
1.8	8-10
2.5	5
3	4-6
4	1

Table B8-24
(Clear air)

<u>R</u>	<u>S/N</u>
2	10
2.5	8
3	6
4	2

Table B8-25
(Clear air)

<u>R</u>	<u>S/N</u>
1.7	9
2	7
2.5	5
3	3
4	1
5	0

*Plotted on graph

CAT FLIGHT TEST DATA REDUCTION
REVIEW OF SEQUENCE CAMERA FILM

FLIGHT B2(15), 1/12/73

GMT ^a	SC Photo	Signal
19:28:58 (Run 3)	0080 84	Ground return first sighted at 180 μ sec Correlation on A-scope S/N = 9 dB at 140 μ sec S/N = 14 dB at 134 μ sec
29:33	108	Target starts receding and finally disappears
19:29:49	113	Ground return first sighted at 170 μ sec See Table 15-1 for SNR Signal width \sim 1 MHz, $\phi \sim 60^\circ$, $V \approx 340$ knots, $P = 1.8$ W
	327	Signal finally disappears (receiver out of saturation)
19:40:45	443	Air backscatter return. $H = 4.7$ Kft, $\phi = 2.2^\circ$, $V = 278$, apparent Doppler width \sim 1 MHz S/N = 4 dB at $R = 20$ μ sec
	470	S/N = 8 dB at 20 μ sec
	473	See Table 15-2 for SNR
43:34	584	Last trace of signal
20:22:43 (5)	770	Air backscatter return, out to 25-30 μ sec on RVI (saturation much further), occasional A-scope correlation $H = 11.5$ Kft, $\phi = 2.4^\circ$, $V = 310$ S/N = 2 dB at 15 μ sec
	819	Last trace of backscatter return
	904	
20:42:42 (7)	916e	Ground return See Table 15-3 for SNR
47:45	1172	Still have trace of receiver saturation. SC off
21:19:28 (9)	1233	Ground return First appears at end of scale (194 μ sec) on RVI See Table 15-4 for SNR Apparent Doppler width \approx 1 MHz, $H = 16.5$, $V = 316$, $\phi \sim 60^\circ$
22:35	1395	SC turned off with trace of saturation
21:43:56 (10)	1489	Ground return First appears at 70 μ sec. See Table 15-5 for SNR
	1520	Last signal appears
21:58:57 (11)	1644	Ground return at \sim 70 μ sec See Table 15-6 for SNR
59:51	1696	Last signal (at $R = 54$ μ sec)
22:29:13	1772	Signal appears at close range, looks like return from cirrus cloud. A-scope correlation. $H = 38$ Kft (up to 38.55), $V = 366$, $\phi \approx 2^\circ$

GMTa

SC Photo

Signal

1787, 9	RVI signal out to end of scale (200 μ sec) but may be receiver overload.
1788	Signal definitely out to 67 μ sec
1796	See Table 15-7 for SNR
1797	Signal out to 80 μ sec on RVI, perhaps to end of scale. Doppler width \sim 0.7 MHz
1814	S/N \approx 16 dB at 20 μ sec
1819	See Table 15-8 for SNR
1836	See Table 15-9 for SNR
1839	Last signal
23:49:24 1872e	Signal on A-scope at close range, looks like back-scatter (RVI obscured). Appears on a few scattered photos - 1872-74, 92, 1901, 2, 7, 8, 10, 14, 15, 20, 30-31, 40. Occasional correlation by RVI. (Gap in data sheet.)

NOTES

- a. SC clock time appears to differ from true GMT (as indicated on printed data sheets) by roughly a half minute. Time is read as Hr:Min:Sec
- b. Pitch angles are printed angles minus depression angle of laser beam. (1.50)
- c. Signal-to-noise ratios are ratios of peak signal to peak noise. They are approximately 5 dB lower than peak signal to rms noise ratios which were originally read.
- d. $R(\text{Kft}) = 0.5 \times R(\mu\text{sec})$, $R(\text{n.mi.}) = 0.081 \times R(\mu\text{sec})$.
- e. Sequence Camera started.

SNR MEASUREMENTS FROM SC FILM

TABLE 15-1

SC PHOTO	R (μ sec)	S/N ^d (dB)
121	103	14
124	90	15
126	30	19
129	73	20
132	72	23
137	70	23
166	57	23

TABLE 15-3 (Run 7)

SC PHOTO	R (μ sec)	S/N (dB)
916	88	11
917	82	17
918	80	17
919	84	16
920	82	17
921	84	20
922	81	16
924	83	17
925	83	15
926	84	21*
927	87	18
931	92	16
933	92	17*
939	74	22*
941	71	22
943	64	26*
954	42	21*
958	39	33*

*Plotted in Figure F-9.

TABLE 15-2

R (μ sec)	S/N (dB)
20	4
25	
30	
40	
50	

TABLE 15-4 (Run 9)

SC PHOTO	R (μ sec)	S/N (dB)
1239	170	6
42	175	5*
47	168	6
53	154	7
54	155	8*
56	144	9
61	138	10
68	142	10*
78	129	13*
90	110	13
97	102	15*
1302	92	18*
26	72	21*
27	71	22
39	60	23*
46	50	25*
51	40	30*
68	36	28

*Plotted in Figure F-9.

TABLE 15-5

SC PHOTO	R (μ sec)	S/N (dB)
1491	65	0
96	60	1
97	57	5
1502	54	6
08	51	6

TABLE 15-6

SC PHOTO	R (μ sec)	S/N (dB)
1651	70	3
52	66	5
57	51	7
61	44	8
66	43	10
67	42	11
68	44	13

TABLE 15-7

R (μ sec)	S/N (dB)
20	13
25	11
30	6
40	1

TABLE 15-8

R (μ sec)	S/N (dB)
20	14
25	10
30	4
35	1

TABLE 15-9

R (μ sec)	S/N (dB)
20	10
25	7
30	2

APPENDIX G

Detailed Operating Instructions and System
Adjustment and Processor Use for
the CAT System

A. OPERATING INSTRUCTIONS

Part 1 Turning the System On

Van temperature should be between 65° and 75°F. Higher temperatures will cause misalignment of the lasers and amplifiers as well as cause processor failure.

Block the detector with the sighting mirror. The procedure for bringing the system up is as follows:

- A. Turn on the 400 Hz generator and transfer switch. This applies power to the racks holding the Honeywell laser supplies and synchronizer, as well as the power amplifier drive circuits.
- B. Reset the synchronizer. The synchronizer is generally left on and starts up as soon as 400 Hz power is applied. Sometimes the reset may need pushing a little later if the processor is misbehaving or if proper screen current on the amplifier drive circuit cannot be attained.
- C. Turn on the Honeywell laser power supplies to standby and block the beam path at the laser.
- D. Turn on the pump and cooler for the system.
- E. Turn on the optical spectrum analyzer.
 - " " " racks power switches.
 - " " " power supply for the telescope pyro detector.
 - " " " power supply for the receiver (28V).
 - " " " power meter.
 - " " " locking loop and set to ground. Using the limit knob, reduce the voltage to about 300V.
 - " " " E/O power switch.
 - " " " RX power switch

DO NOT turn on the detector bias.

Much of the above is left on and will come on with the rack power.

Turn on the -40V and Fil. -450V (Power Amplifier Modulator Rack).

Making sure the voltage control knob on the Universal Voltronics Rack is set to "0", push the HV on button.

- F. Turn on the processor rack.
" " " monitor rack.
- G. Turn on the computer (See manual).
- H. Open exhaust door for system vacuum pump and turn on the pump.
- I. Fill the detector with LN_2 .
- J. After about 5 - 10 minutes of cooler operation, turn on the Honeywell laser. Overvolting may be required.
- K. Turn on the Sylvania laser, making sure first that the detector is blocked with the sighting mirror.
- L. Wait about 15 or 20 minutes for lasers to stabilize. Use this time to position system on target and prepare for data taking.
- M. Adjust the tuning of the Honeywell laser (alignment) using an asbestos block and adjusting for maximum brightness at P20 (or desired transition). Use the lowest adjustment screw on back of Honeywell laser first and then the screw to the right if the spot can't be made bright. Do not adjust upper left hand screw (pivot screw). The lasing unit used to control the centering of the Honeywell laser is to be left off as this unit will not operate properly when the laser pulser circuit is on. Honeywell power output should be over 7 watts and the current drawn from the Northeast supplies should be between 18 and 21 mA.
- N. Tune the Sylvania laser (alignment) with about 300 volts set on the locking loop (grounded) using a Number 3 Optical Engineering image plate and UV light. Tune for darkest spot P20 or darkest spot which is desired transition.
- O. Remove beam blocks from both lasers, turn up voltage on the locking loop to the maximum (limit knob) and switch from grounded to closed. Voltage will sweep down and then up to around 400V or so where the

lasers will become locked together and locked light will come on. Viewing the RF output on the spectrum analyzer below set to 10 MHz 300 kHz BW, the video filter off, and in the zero position, a line will be visible that should be made as smooth and straight as possible by adjustment of the loop gain. The injection controls on the locking loop will have no effect when the lasing loop is off. Other controls on the locking loop should not be used. Do not adjust the gain knob beside the voltage limit knob. Check to see that only P20 or the desired transition is lit in the optical spectrum analyzer.

- P. Power amplifier operation is as follows: Turn on gas valve on tank, check to see there is pressure reading on the high pressure gauge (tank) and the tube pressure should be between 12 and 14 Torr.
- Q. Push on the 1600V on the power amplifier modulator rack. All voltages should read on the voltage monitor meter. Slowly increase the Universal Voltronics output control while watching the tube current and the screen current meters. Slowly increase the screen current drive knob as the voltage is increased. Do not red line the screen current. Operating voltage is 12 KV, a little over 60 mA tube current, and a little under 20 mA screen current. The amplifier tubes will be lit.
- R. While watching the scope beside the synchronizer that displays the output pulse waveform and pulser waveform, turn on the Spellman High Voltage Supply under this scope. As voltage comes up, a pulse shape should be seen on the scope. Decay slope should be smooth and regular. View the vertical output of the spectrum analyzer with the locking loop plugged into it on the upper scope in the monitor rack. This line should be straight and smooth. If it is not, the ball spider and/or the output power beam will need adjusting. Check to see that the beam leaving the diagonal mirror has a hole in the center of the beam. Use wax chart graph paper.

Refer to waveform section for Step R and S.

- S. If the spectrum analyzer vertical output display (A-Scope) is not as in waveform section, adjust the ball spider by turning opposing tuning keys in the same direction. This will cause the ball to move up, down or sideways changing the A-scope display. Null the A-scope display so that the ball is centered on the secondary. (Look into the telescope primary.) The final tweak may be slight.

Also check from time to time during the ball tweeking that the wires are not too tight. Loosen one key of the tight axis if this is the case. Watch the A-scope display for a minute or two to make sure the display does not change.

- T. Determine the output power by placing a CRL power head between the telescope and system. Move the head around to find the maximum average power. Without moving the head have someone turn off the Spellman Power Supply and read the leakage power. Subtract the leakage from the power and divide by the PRF to find the output in joules. Enter this value in the log. Always make sure that the detector bias is off and the detector is blocked when making this measurement. Check output power from time to time during calibration runs. Output power should be between 1.3 and 2.1 watts average power.
- U. Open detector up by folding down sighting mirror. Make sure there is LN_2 in the detector. Bias the detector by turning on the bias switch and turning up the control knob until the voltage reads 0.4 on the meter and the current reads two divisions before 6 mA. The local oscillator power may need adjustment to make the readings. Use only slight adjustments of the LO attenuator. A dark band should be seen on the RVI display.
- V. Turn on the pulser and check to see that the pulse starts no more than $5\mu S$ before the output pulse on the waveform scope.
- W. The system is now operational. For extended operation watch:
- the gas supply
 - the waveforms and timing (check the A-scope by turning off the pulser only)
 - the detector bias and cool
 - the output power (after blocking the detector).
- X. Remember before you make any changes to the system alignment or check power, remove the bias and block the detector. Make it a habit to always check that first.
- Y. Avoid blocking the LO beam with your finger while adjusting the receiver. See system adjustment and processor use.
- Z. In case of an emergency, refer to the Emergency Shutdown Procedure. Memorize it.

Warning: Never push the reset or change pulse length of the output pulse or the PRF when the Spellman HV supply and/or the power amplifier supplies and modulator are on.

WAVEFORM SECTION II

The following waveforms are normal during system operation:

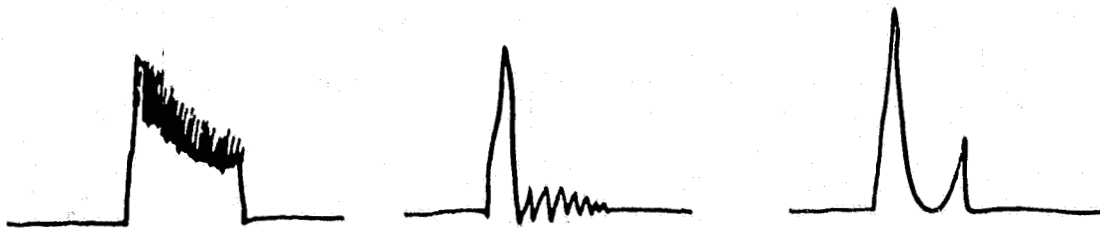
Output pulse shape:

Normal



Output pulse shape:

Wrong



Troubleshooting Case:


1. Check optical spectrum analyzer to see that only P20 or desired transition is lit. Retune the lasers for brightest spot and relock the lasers. Check amplifier alignment.
2. Check amplifier alignment and alignment of ball using A-scope display, if okay, retune lasers.
3. Check A-scope display and adjust ball. Check amplifier alignment. May need to retune lasers.

A-Scope Display

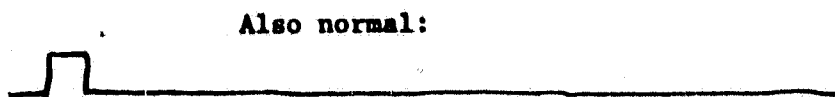
Normal: (Sync pulse)



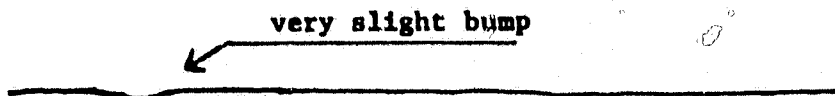
Vertical output of spectrum analyzer
(10 dB log)



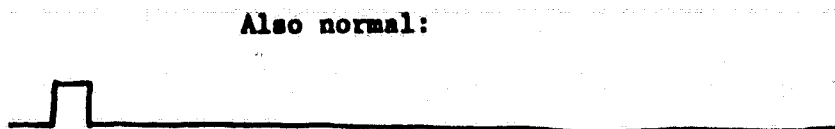
Also normal:



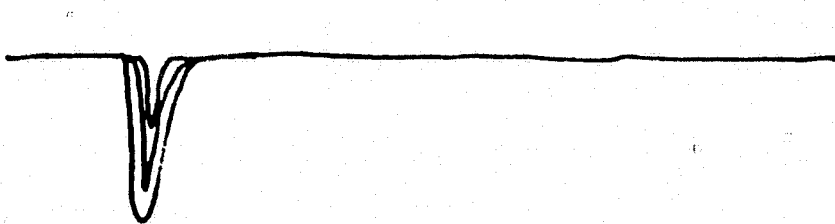
very slight bump



Also normal:



Wrong:

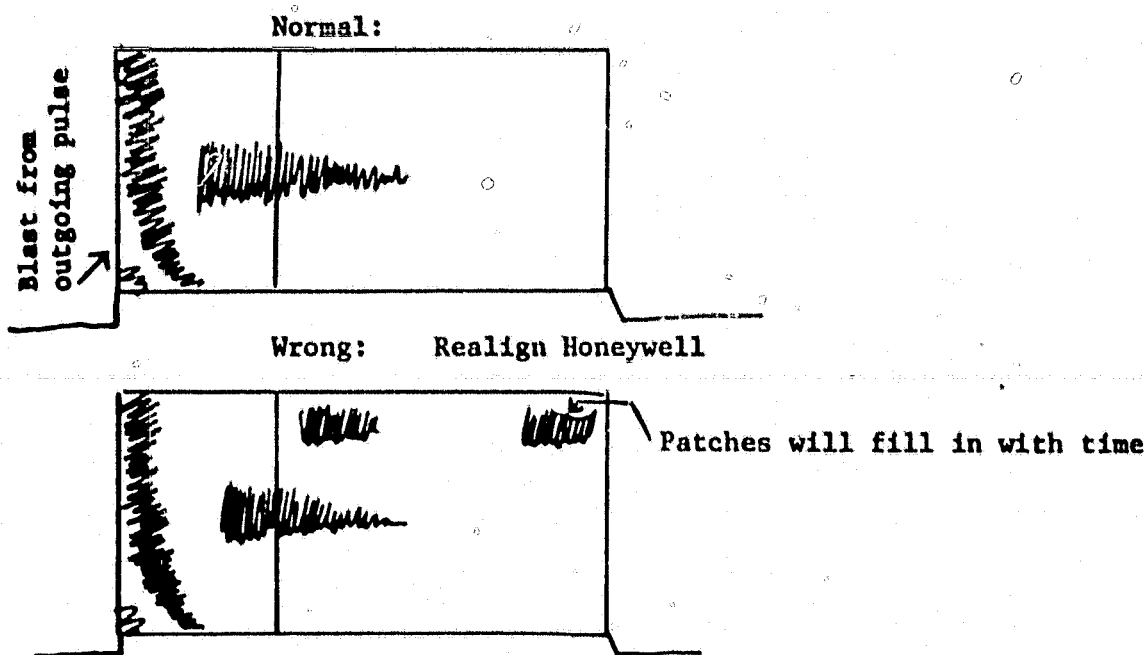


Adjust spider ball

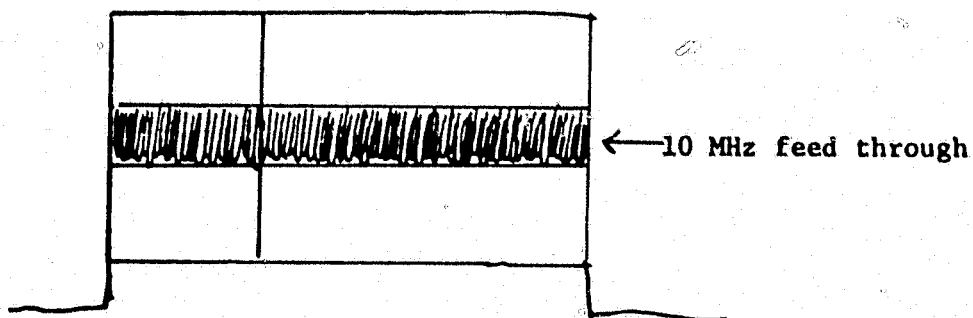
May also require
adjustment of lasers
and output beam

RVI Display

The following condition in the RVI display will require retuning of the Honeywell laser and will probably show up in the output pulse shape as Case 3.

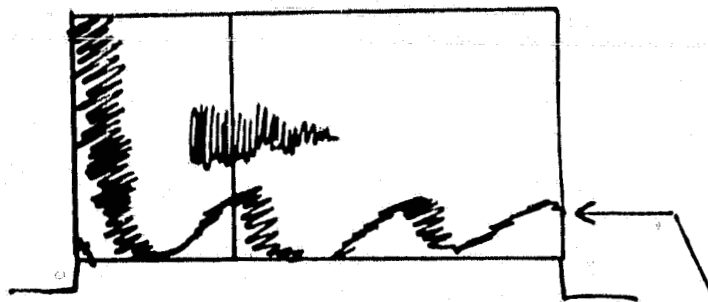
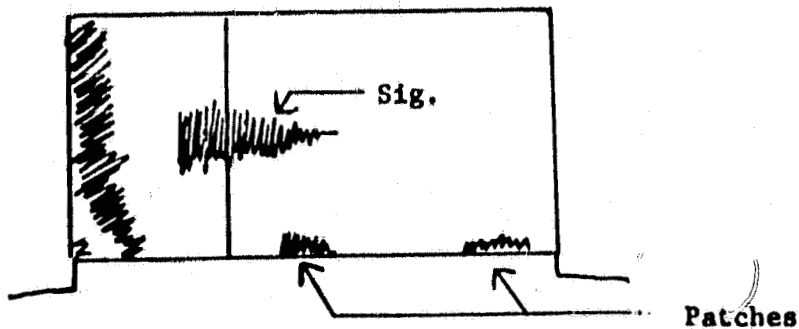


The following display will be seen with 40 dB or less attenuation if the pulser is off.



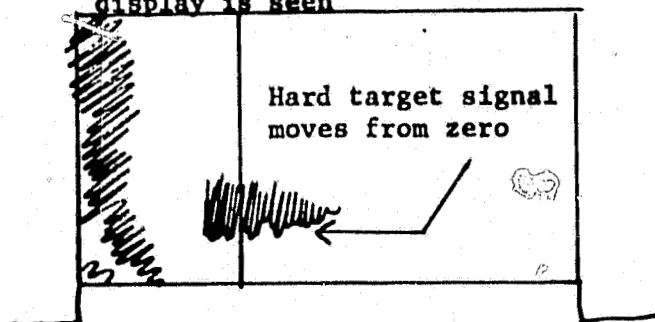
RVI Display Continued

The following display will be seen if the pulser voltage is too low:



Bad case of low pulser voltage.
Check pulser display below
output pulse display.

Check pulser timing or pulser
timing jitter if the following
display is seen

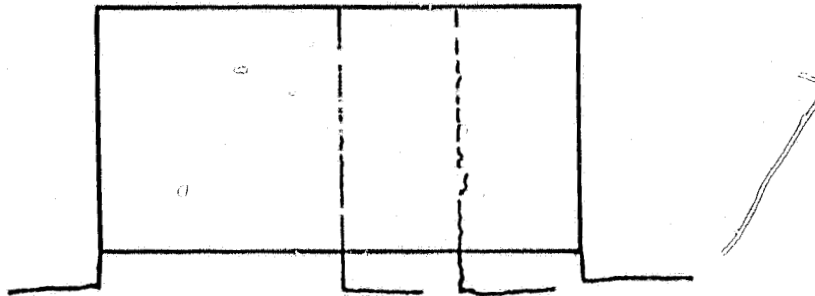


Hard target signal moves or
jitters from zero most commonly
down. Also seen on IVI. Try
turning off, then on, pulser
and resetting timing.

RVI Display Continued

If RVI display goes to a straight bright line, turn off the 5 volt supply (gray panel with switch) and turn on again.

If RVI display and IVI display jitter:



Push the synchronizer reset.

Warning:

Never push the reset or change pulse length of the output pulse or the PRF when the Spellman HV supply and/or the power amplifier supplies and modulator are on.

Spot Shape of Output Pulse

Before telescope:

Correct

(Number 7
Plate)

Wrong



After Diagonal:

Correct

(Wax Chart
Paper)

Wrong



Danger: Never adjust the amplifier alignment when you are not watching an image on a plate.

Power density of the beam at the telescope output is eye safe.

B. SYSTEM ADJUSTMENT AND PROCESSOR USE

The following relates some detail on system adjustments and use of the processor for making signal and noise measurements.

Part A. System Adjustments. Refers to Steps R and S of Operating Instructions

Alignment of Output Beam through the Telescope

If the telescope should become misaligned so that the beam does not strike the diagonal properly or falls on the center of the secondary, proceed as follows:

- (a) Check the alignment of the amplifier using a No. 7 optical engineering plate. Move the beam around to find the extremes of the aperture and center the beam. Using a No. 7 plate, see that the shadow of the hole in the diagonal, after the beam leaves the diagonal, is centered on the beam. If it is way too high or low, beyond slight adjustments of the amplifier alignments, then the telescope height adjustment must be made. This is done with the two vertical leveling screws at either edge of the mounting bracket on the telescope. Lock the screws up after the adjustment is made. If the shadow of the hole is to the right or left, slide the diagonal in and out to adjust. The diagonal will also rotate which will allow up, down adjustment of the beam on the secondary. To center the beam on the secondary, hold the No. 7 or No. 8 plate in front of the secondary and view its reflection in the primary mirror. Rotate the diagonal until the beam is centered up, down. Left, right adjustment is made using the horizontal spider holding the diagonal. Grasp the bolt on the outside of the telescope and slide it forwards or backwards. The spider ball should fall in the shadow of the diagonal hole.

Never attempt to adjust the secondary mirror spider or focal position. This will destroy the telescope collimation.

Laser Alignment

- (b) Prior to locking the two lasers together, careful adjustment of the laser's alignment is required to achieve full output power as well as avoid misalignment of the Honeywell beam into the amplifier tubes. The system alignment is going to be best at P20. Using a block of asbestos blocking the Honeywell beam, view the intensity of the glowing spot. Experience will tell how bright it should be. As the lower left hand adjustment on

the Honeywell is moved, the intensity of the spot will change and may go faint to bright again. There are two major bright points as the laser is tweaked. One is P20 and the other is P22. As the spot is brightened up by laser tweaking, check to see that P20 shows on the optical spectrum analyzer. If it's not, rotate the adjustment very slowly, causing the spot to go faint, then bright again. Check for P20. If the spot does not get bright again, reverse direction and check at each bright point for the P line. Peak up the spot intensity on P20.

The Sylvania laser alignment should be done with 300 volts set on the locking loop in the grounded state. Use a No. 3 plate and UV light to view the spot. Carefully tweak the laser's uppermost screw until the spot is darkest on the plate. Check for P20. If it's not, try again. Use the other adjustment screws if required. Removing all the beam blocks and UV light, turn up the locking loop voltage limit knob and close the loop. The loop should lock a little above the voltage set originally during laser tweaking.

Receiver Alignment Check Part (d) first

- (c) If maximum signal to noise is critical and/or if calibrated targets are not producing expected signals, a slight change in receiver alignment might be required. In general, tweaking of the receiver gains only 1 or 2 dB increase in signal if it was off a bit. Tweaking may be done on the wind or target signal. In general, it's easier on the wind signal until beam absorption causes signals so small it's hard to see wind on the RVI display. When wind is visible, while watching the RVI display, rotate the uppermost adjustment on the recombining beam splitter until the signal is the brightest and extends the farthest on the RVI. Repeat the adjustment on the uppermost adjustment knob of the gold mirror between the brewster plate and beam splitter. Tweak the knobs no more than one-half turn either way from their original position and use fairly rapid motions at first to see visible changes on the RVI. Caution: Don't let your fingers slip off the knob of the beam splitter into the local oscillator beam. Loss of LO while bias is applied to the detector is not good. Do not attempt to align the receiver on a faint signal. It's easy to get lost and end up with a totally misaligned receiver. On target signals, apply attenuation until the signal on the RVI begins to fade. While watching the signal, tweak the receiver for maximum brightness and least flashing.

Receiver Alignment after Telescope Removal

- (d) This procedure is used after amplifier alignment most often because the brewster plate has been removed. After replacing the brewster plate to its original reference marks, and while the isolator wafer is still out of the magnet assembly, adjust the plug-in half wave plate for the modulator until maximum power leaves the modulator. (This would already have been done during amplifier alignment.) Tweak the amplifier until the CW beam (amplifier off) is centered, leaving the brewster plate. Attach the short rail to the front of the system where the telescope bolts on and put the 20" fl lens on the rail. Position the spinning sandpaper target at 45° to the focused beam and 20" away. Adjust the position of the lens to center it on the beam. Focus the beam on the target while the target is spinning. View the output of the receiver signal on the spectrum analyzer. It should be above or below 10 MHz depending on the direction of rotation. Tweak the receiver for maximum signal to noise. The CW power leaving the amplifier tubes will be about 1 watt. The signal this should produce on the spectrum analyzer will be about -9 dBm. Noise should be -78 dBm. To find receiver efficiency, use the following equation:

$$\text{efficiency} = \frac{8.52 \times 10^{-11} \text{ } 10^S}{\text{Power CW}}$$

Where S = the sum of the noise and signal divided by 10.

To find dB of receiver losses, take the log of the above equation and multiply by 10.

Never forget to return the modulator half wave plate to its original position where about 50 to 70 milliwatts leave the modulator CW. The wafer will be damaged if CW power exceeds 100 mW. Make this adjustment while the magnet assembly is out of the system. The above measurement is made with the magnet less the wafer in the system. After the wafer had been returned to its assembly and the half wave plate has been readjusted and removed from the modulator, replace the isolator to its position in the system against its hard stops. With the amplifier tubes on and the modulator on, tweak the output beam until the beam is centered.

Amplifier Alignment

- (e) Remove the isolator and take out the wafer. Reassemble the isolator without the wafer and replace the magnet assembly into the system. Make sure that the beam is aligned through the

modulator. For this the modulator half wave plate will need adjusting for maximum transmission. Make sure the beam enters and leaves the centers of the isolator tubes and is aligned through the side stepping mirrors. Using the mirror adjustments, steer the beam into the beam expander and get the beam to pass through on axis. The beam expander should not need to be moved around unless it has been bumped so hard it was relocated. During this alignment, go slowly and think out each step to achieve a beam on axis end. When the beam is aligned up to and through the expander, tape a small piece of wax paper to the output polarizer of the modulator and allow the CW beam to pass for a fraction of a second to mark the paper. Avoid burning the paper and causing smoke. Go to the receiver end of the system and remove the receiver electronics, the quarter wave plate and brewster plate. Align the cathatometer so that the cross hairs track the optical axis down the amplifier tubes as it's focused close to and far away looking into the output tube.

This alignment may take some time and require placing pointers at the amplifier input to see where the axis is. While shining a light on the wax paper target at the modulator, focus the cathatometer on this target; with luck, it will be visible, and the spot probably off to the side. While watching the spot, have someone adjust the four X and Y axis adjustments on the input mirrors to the amplifier. These adjustments should be made differently. Go beyond with one X axis adjustment and bring it back with the other X axis adjustment and so on. When the spot looks centered, remove the target and let the beam pass through the amplifiers. See if it looks good coming out of the amplifiers and make small adjustments to the input mirrors to achieve this. If it can't be made to come through, try again. Cross hairs over the input amplifier tube aperture may help. When the CW beam looks good leaving the amplifier, go to Part (d) Receiver Alignment after Telescope Removal.

Processor Use

- (f) This section provides guidelines to achieve consistent results when making signal-to-noise measurements on the IVI display.

IVI scope should be set to 0.5 V/div. Processor should be set to 0.25 Sec. integration period, 25 pulse integrations. Set the range pointer to the target range desired. The deflection of the IVI display is to be measured. Check that the zero lies one div. up from the bottom, using the scope input ground switch.

The desired deflection (peak) is to the center line. Attenuation will be used to achieve this. When the signal peaks fall consistently on the third division up from zero (watch for a few minutes), record the attenuator settings.

Move the range pointer out to where there is no signal on the RVI (around 100μ S) and remove attenuation until the noise floor is centered on the IVI display. Record this attenuation value. If the RVI display goes to a line, turn off, then on, the 5 volt supply. If any display does not look normal, push the reset on the synchronizer. Never do this when the modulator and/or power amplifier are on. See the detailed operating instruction, RVI display, on the wave form section.